Kinetic Phase-Tuning in the Synthesis of Iron and Chromium Metal-Organic Frameworks

Dominic James Bara

University of Glasgow

Submitted in fulfilment of the requirements for the Degree of Doctor of Philosophy

School of Chemistry

University of Glasgow

April 2020

Abstract

Metal-Organic Frameworks (MOFs) are solid-state materials which display exceptional permanent porosity and unprecedented structural diversity. These unique properties have garnered significant attention for potential applications, including gas storage, catalysis, and drug delivery.

This thesis focuses on kinetic phase-tuning in the synthesis of Fe and Cr-MOFs and aims to explore novel strategies for phase-control, as well as assessing their biocompatibility for therapeutic applications such as drug delivery.

The introduction chapter discusses reticular chemistry and other key concepts relating to the synthesis of MOFs, as well as exploring some of the synthetic methods employed for high valent MOFs and their subsequent development for biomedical applications. In Chapter 2, a comprehensive investigation of self-assembly in the Fe–biphenyl-4,4′-dicarboxylate system is conducted by exploring the use of coordination modulation - the addition of monotopic ligands which can compete with the bridging linkers during the self-assembly process - as a tool for phase control. It was found that coordination modulation can reliably tune between the kinetic product, non-interpenetrated MIL-88D(Fe), and the thermodynamic product, two-fold interpenetrated MIL-126(Fe). Coordination modulation slows self-assembly and therefore selects the thermodynamic product MIL-126(Fe), while also offering fine control over defectivity and inducing mesoporosity. Interpenetration control is also demonstrated using the 2,2′-bipyridine-5,5′-dicarboxylate linker; it is energetically prohibitive for it to adopt the twisted conformation required to form the interpenetrated phase, although multiple alternative phases are identified due to additional coordination of Fe cations to its N donors. In addition, oxidation modulation - the deliberate use of metal precursors in different oxidation states to that found in the resulting MOF - is employed as a novel method to kinetically control self-assembly. Combining coordination and oxidation modulation enables the synthesis of pristine MIL-126(Fe) with surface areas close to the predicted maximum for the first time, suggesting that combining the two may be a powerful methodology for the controlled self-assembly of high-valent MOFs.

Chapter 3 details work conducted on the synthesis of Fe-terephthalate MOFs, utilising the two methodologies that were developed in the previous chapter - coordination and oxidation modulation - to control the phase that crystallises. An extensive crystallisation study was performed by variation of key parameters such as synthesis time, temperature, quantity of

modulator, and Fe precursor. The results have established synthetic routes to various MOFs containing the common metal hydroxide chain and oxo-centred trigonal secondary building units (SBUs), as well as gaining insight into the kinetic and thermodynamic relationships between the different phases. The thermodynamic relationship between two topologically identical frameworks - MOF-235(Fe) and MIL-88B(Fe) – could subsequently be ascertained, with MOF-235(Fe) being the thermodynamically preferred product when using chloride salts as the metal precursor. MOF-235(Fe) differs from MIL-88B(Fe) in that it contains non-coordinating $[FeCl_4]^-$ counterions, and as such a novel analogue of MOF-235(Fe) could be obtained when using $Fe(BF_4)_2$ which provides suitable $[BF_4]^-$ anions. The role of the counterion was found to be crucial for directing the structure and has broad implications for other MOF syntheses. In addition, these synthetic efforts yielded suitably large crystals of a prototypical flexible MOF - MIL-53(Fe) - which enabled study of its flexibility by single-crystal X-ray diffraction.

In Chapter 4 the synthesis of Cr-MOFs is explored using coordination modulation as a strategy for phase control. The ligand exchange rate of Cr^{3+} is much slower than for Fe^{3+}, making it more challenging to obtain crystalline materials as there is less 'error-checking', hence, modulation was considered a viable strategy for enhancing crystallisation. Two synthetic routes were established in this study and were found to reliably control the crystallinity and SBU in the resulting MOF: synthesis in water and pyridine with acetic acid as modulator yields frameworks with the trigonal $[Cr_3O(RCO_2)_6(H_2O)_2X]$ (X = monoanion) SBU, while synthesis in water with HCl yields those with chain $[Cr(OH)(RCO_2)_2]$ SBU. The ability to control the SBU in this manner is extremely useful and has enabled the synthesis of many novel Cr-MOFs in this study. A series of flexible dicarboxylate MOFs with MIL-88 topology were synthesised successfully using the acetic acid route, and their flexible behaviour was investigated by powder X-ray diffraction. Interestingly, synthesis with the longest linker - 4,4′-stilbenedicarboxylic - yields a two-fold interpenetrated framework (Cr-SDC) which, despite interpenetration, exhibits comparable flexibility to the MIL-88 frameworks. The use of higher connectivity linkers has also been explored, generating novel frameworks with greater rigidity and permanent porosities surpassing the dicarboxylates. The most notable of these frameworks is MIL-100(Cr)_BTB, containing benzene-1,3,5-tribenzoate (BTB) as linker, which demonstrates exceptional sorption capacity (4000 m^2g^{-1}). The HCl route enabled the synthesis of novel isoreticular analogues of MIL-53(Cr), two of which could be grown as large single crystals, which has never previously been reported for directly synthesised Cr-MOFs. The remarkable stability of Cr-MOFs suggests that many

of these frameworks could find use in demanding applications where their high porosities and flexible properties can be utilised.

MOFs have been widely studied for their potential use in biomedical applications, particularly as drug delivery systems, however these have typically been limited to frameworks consisting of either Zr^{4+} or Fe^{3+}, with those consisting of Cr^{3+} largely neglected due to the associated stigma relating to the toxicity of Cr^{6+}. In Chapter 5 the biocompatibility of several of the Cr-MOFs developed in Chapter 4 were tested using cell culture experiments. The results showed that all the MOFs were biocompatible within the doses expected to be used in drug delivery applications.

In summary, novel synthetic strategies for phase-tuning in Fe^{3+} and Cr^{3+} carboxylate systems have been developed, providing better control over the obtained phase, and enhancing crystallinity. These enhanced synthetic protocols have enabled discovery of novel MOFs, investigation of the flexibility, gas sorption, and biocompatibility of these and existing benchmark materials, and has revealed that Cr-MOFs are promising candidates for biomedical applications.

Contents

Abstract i

Acknowledgements vi

Declaration vii

Abbreviations viii

Chapter 1 1

1.1 Aims 3

1.2 Metal-Organic Frameworks 3

1.3 Trivalent Carboxylate MOFs 10

1.4 Synthesis of MOFs 20

1.5 Biomedical Application of MOFs 30

1.6 Conclusions and Outlook 33

1.7 References 34

Chapter 2 41

2.1 Introduction 44

2.2 Aims 47

2.3 Synthesis of Fe-BPDC MOFs (1) 48

2.4 Modulation of Fe-BPDC MOFs (1) 57

2.5 Synthesis of Fe-BPYDC MOFs (2) 70

2.6 Solvothermal Synthesis of Fe-BPDC MOFs (1′) 78

2.7 Conclusions 82

2.8 Experimental 84

2.9 References 88

Chapter 3 91

3.1 Introduction 94

3.2 Aims 96

3.3 Synthesis of Fe-terephthalate MOFs 97

3.4 Variation of the Fe-precursor 109

3.5 Flexibility of MIL-53(Fe) 114

3.6 Conclusions and Future Work 119
3.7 Experimental 121
3.8 References 124
Chapter 4 126
4.1 Introduction 130
4.2 Aims 132
4.3 Synthesis of Cr-biphenyl-4,4′-dicarboxylate Frameworks 133
4.4 Synthesis of Isoreticular MIL-88 Frameworks 140
4.5 Flexibility of MIL-88 and MIL-88-int Frameworks 146
4.6 Synthesis of Cr(OH)-dicarboxylate Frameworks 155
4.7 Synthesis with Higher Connectivity Linkers 165
4.8 Conclusions 178
4.9 Experimental 180
4.10 References 187
Chapter 5 191
5.1 Introduction 194
5.2 Aims 195
5.3 Biocompatibility of Cr-MOFs 196
5.4 Conclusions 202
5.5 Experimental 204
5.6 References 215
Chapter 6 217
6.1 Conclusions 219
6.2 References 225

Acknowledgements

Firstly, I would like to thank my supervisor Professor Ross Forgan for his guidance during my PhD and for being supportive in allowing me to pursue my scientific interests.

Thank you to all the members of the Forgan Group, past and present, for being not only superb colleagues but also great friends during my time in Glasgow. It has been an absolute pleasure to work with you all! I am especially grateful to our postdocs Nikos and Fatma for their guidance and friendship during the final years of my PhD, it has meant a lot to me.

I've had a great time working in the Chemical Biology Lab, and it would not have been the same without all the great people we've shared it with over the years, including the Liskamp, Jamieson, and Thompson groups. Big thanks also go to our lab manager Susan Gannon for maintaining the lab and being a constant source of good humour.

This thesis would not have been possible without crystallography, so I am very grateful to Dr Claire Wilson for all her help with data collections and refinements. I also want to thank Jim Gallagher and Peter Chung for their help with SEM over the years.

I also want to thank Emily Meekel for her contributions to some of the work described in my thesis during her final year project and summer placement in our group.

I would not have made it through my PhD without the love and support from my family and my wonderful girlfriend Sára, thank you for keeping me sane (not an easy task). I cannot wait to see you all soon once this coronavirus nightmare has ended!

Finally, I would like to acknowledge COVID-19 for driving the whole world insane during my thesis writing period. I am looking forward to returning to real life and normalcy ASAP.

The European Research Council, University of Glasgow, and Royal Society of Chemistry are acknowledged for their financial support.

Declaration

This thesis has been written and compiled by the author, Dominic James Bara, who has carried out the research at the University of Glasgow between 2016 and 2020 under the supervision of Professor Ross Forgan. Where collaborative results have been included in this thesis the input of others has been acknowledged. Parts of this thesis have been published in peer reviewed journals and at the start of each chapter reference to the relevant publications is given.

Abbreviations

Å	angstrom
~	approximately
°	degrees
°C	degrees Celsius
λ	wavelength
1,4-NDC	naphthalene-1,4-dicarboxylate
2,6-NDC	naphthalene-2,6-dicarboxylate
ABTC	3,3',5,5'-azobenzenetetracarboxylate
BDC	1,4-benzendicarboxylate (terephthalate)
BET	Brunauer–Emmett–Teller theory
BPDC	biphenyl-4,4′-dicarboxylate
CCDC	Cambridge crystallographic data centre
DCA	dichloroacetic acid
DCM	dichloromethane
DFT	density functional theory
DMF	*N*,*N*-dimethylformamide
DMSO	dimethylsulfoxide
EDTA	ethylenediaminetetraacetic acid
e.g.	for example
eq	equivalent
et al.	and others
EtOAc	ethyl acetate
EtOH	ethanol
g	gram
h	hour
HDF	human dermal fibroblasts
HEK-293	human embryonic kidney cells
HCl	hydrochloric acid
HRTEM	high-resolution transmission electron microscopy
IR	infrared spectroscopy
IRMOF	isoreticular metal-organic framework
K	Kelvin

M	moles per litre
MeOH	methanol
MIL	Matériaux Institut Lavoisier
mg	milligram
ml	millilitre
mM	milli moles per litre
mmol	millimole
MOF	metal-organic framework
MPa	megapascal
n/a	not applicable
nm	nanometre
NMR	nuclear magnetic resonance spectroscopy
no.	number
PBS	phosphate-buffered saline
PXRD	powder X-ray diffraction
RTCA	real-time cell analysis
SA	surface area
SCXRD	single crystal X-ray diffraction
SDC	4,4′-stilbenedicarboxylate
SEM	scanning electron microscopy
TEM	transmission electron microscopy
TFA	trifluoroacetic acid
TGA	thermogravimetric analysis
UiO	Universitetet i Oslo
UV-Vis	ultraviolet-visible spectroscopy
V	volume
vs	versus
VT-PXRD	variable temperature powder X-Ray diffraction

Chapter 1

Introduction

Contents

Chapter 1 1

1.1 Aims 3

1.2 Metal-Organic Frameworks 3

1.2.1 Introduction 3

1.2.2 Reticular Chemistry 4

1.2.3 Interpenetration 7

1.2.4 Summary 9

1.3 Trivalent Carboxylate MOFs 10

1.3.1 Background 10

1.3.2 MIL-88 and MOF-235 11

1.3.3 MIL-53 and MIL-68 13

1.3.4 MIL-101 and MIL-100 15

1.3.5 Soc-MOF 18

1.3.6 Summary 19

1.4 Synthesis of MOFs 20

1.4.1 Synthesis and Characterisation 20

1.4.2 Crystallisation Additives 21

1.4.3 Kinetic Phase-Tuning 25

1.4.4 Preformed Cluster Approach 27

1.4.5 Summary 29

1.5 Biomedical Application of MOFs 30

1.5.1 Cytotoxicity 30

1.5.2 Drug Loading and Release 30

1.5.3 Surface Coating 31

1.5.4 Summary 32

1.6 Conclusions and Outlook 33

1.7 References 34

1.1 Aims

The focus of this thesis is the synthesis of metal-organic frameworks (MOFs) constructed from Fe^{3+} and Cr^{3+}, which are controlled by tuning key synthetic parameters that dictate the phase, crystallinity, and other bulk properties of the resulting materials. In addition, the toxicity and internalisation of some of these MOFs will be investigated for their potential use in biomedical applications such as drug delivery. The purpose of this chapter is to introduce metal-organic frameworks along with the main concepts relating to their structures and physical properties. Further background on trivalent MOFs, framework synthesis, and the application of MOFs in drug delivery will also be explored to introduce the subject matter addressed by the remaining chapters.

1.2 Metal-Organic Frameworks

1.2.1 Introduction

Metal-Organic Frameworks (MOFs) are a sub-class of coordination polymers: structures consisting of inorganic nodes and organic molecules linked together to form repeating arrangements in 1, 2 or 3-dimensions. The crucial distinction between MOFs and other coordination polymers lies in their potential void space,[1] commonly referred to as 'pores', which can be occupied by a range of non-framework species. The interest in MOFs rests primarily in their porosity, which makes them highly desirable for various applications such as catalysis,[2] gas-storage,[3] and drug delivery.[4]

The keys to designing porous frameworks of this type lie in the knowledge of the metal-containing component, either a single metal ion or cluster, that will form under a given set of conditions, and then the selection of an appropriate linker to ensure the resulting framework is porous. The most widely known example of this type of framework design is MOF-5[5] which is formed by $Zn_4O(RCO_2)_6$ (Figure 1.1a) secondary building units (SBUs), which were already known to form as discrete entities when Zn^{2+} was reacted with monocarboxylates, and bridged by benzene-1,4-dicarboxylates (Figure 1.1b) to give a porous cubic network (Figure 1.1c). MOF-5 is typically synthesised by heating the starting materials at elevated temperature using non-volatile organic solvents such as *N*,*N*-dimethylformamide (DMF) and *N*,*N*-diethylformamide (DEF),[6,7] which will occupy the pores post-synthesis. The relatively strong Zn-O bonds in MOF-5 confer remarkable rigidity to the framework, the result being that it can be fully evacuated without any loss of intrinsic

structure and thus enabling the subsequent uptake of gas molecules.[5] The porosity of a MOF is commonly probed in this way, using an inert gas such as N_2, which requires these solvent molecules to first be evacuated; in many cases this can lead to framework collapse.

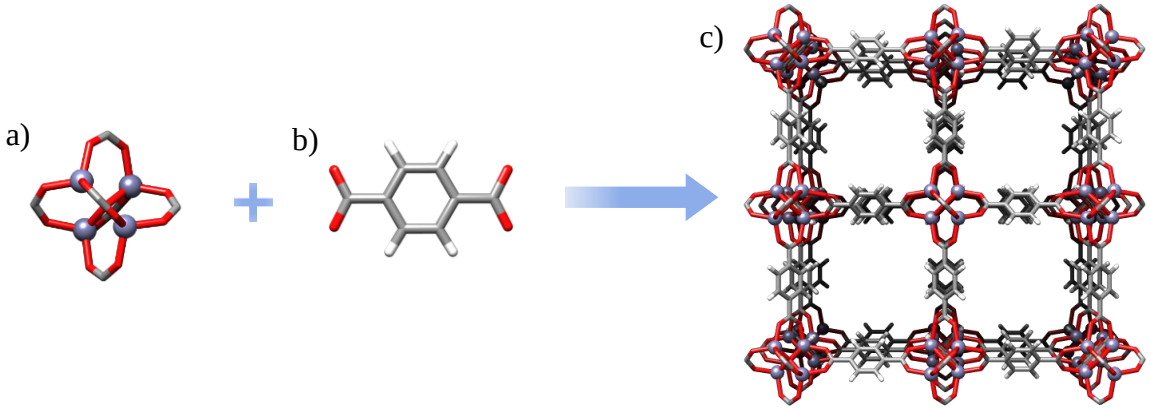

Figure 1.1. Building the structure of a typical MOF by combining a) a $Zn_4O(RCO_2)_6$ SBU, and b) a benzene-1,4-dicarboxylate linker, into c) the packing structure of MOF-5.[5]

1.2.2 Reticular Chemistry

The synthetic concept of combining geometrically well-defined components through strong bonds to form porous frameworks is known as 'reticular chemistry' and is the guiding principle of MOF design. A useful way of describing a MOF structure is to consider the underlying network, formally referred to as its topology.[8] The topology of a MOF can be visualised by simplifying the metal-containing components into nodes (vertices) with the bridging linkers as edges which connect them (Figure 1.2a). In the case of linkers which have connectivity higher than two, it is easier to consider the linkers themselves as nodes with multiple edges branching out, as is the case in HKUST-1, a MOF constructed from Cu(II) paddlewheel SBUs and benzene-1,3,5-tricarboxylate linkers (Figure 1.2b).[9] MOF structures can have the same topology even if the linker and metal-containing components are dissimilar, as long as the underlying net is fundamentally the same, and thus this way of analysing MOFs can be very useful when comparing topologically related frameworks.

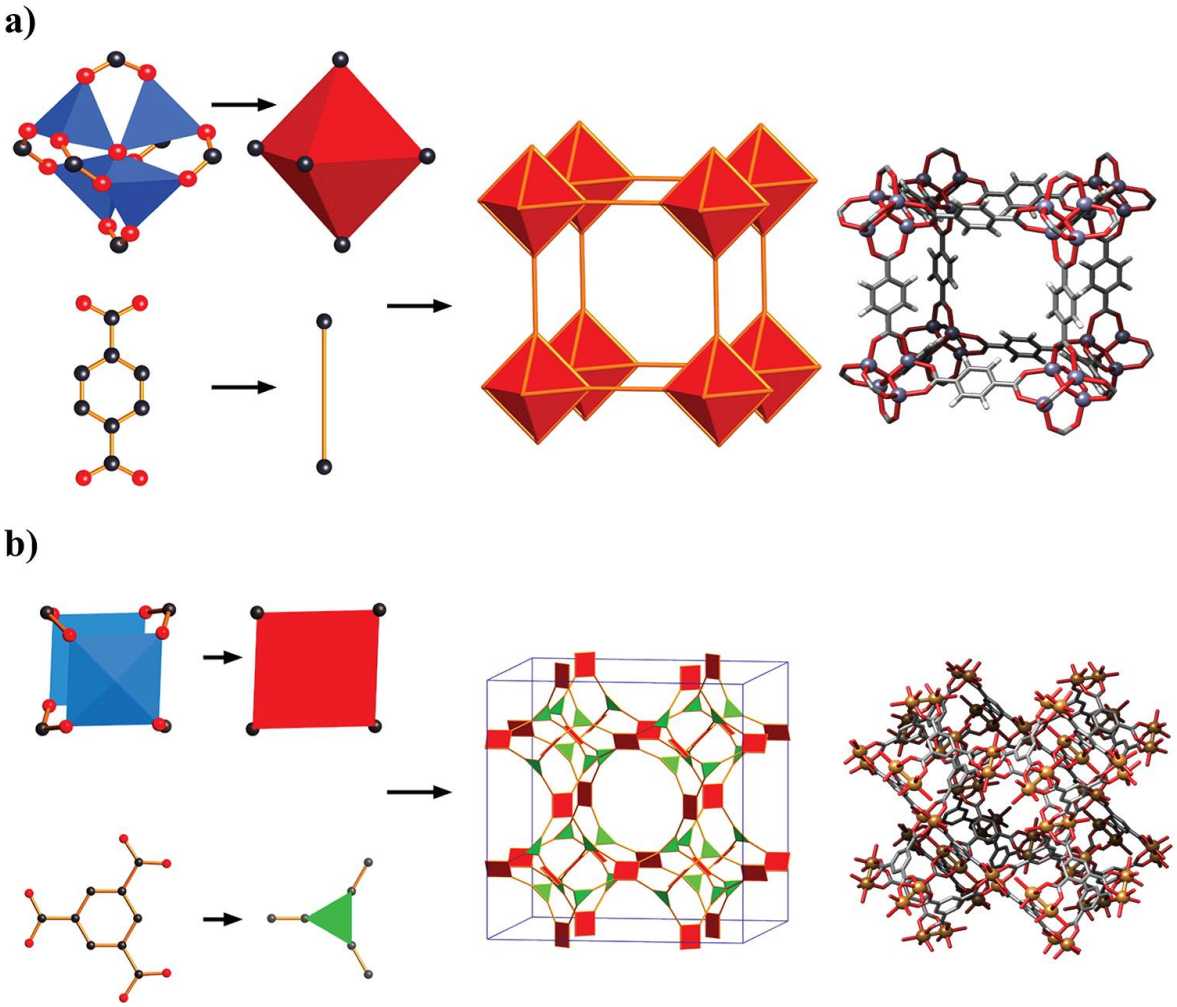

Figure 1.2. a) Components of MOF-5 simplified with $Zn_4O(RCO_2)_6$ as an octahedron and terephthalate as a rod, and their combination to form the net present in MOF-5. b) Components of HKUST-1 simplified with Cu_2 as a square and benzene-1,3,5-tricarboxylate as a triangle, and their combination to form the net present in HKUST-1.[8]

For a given SBU, the pore size of the resulting framework can be tuned by varying the linker length while maintaining the underlying topology, and such frameworks can be described as 'isoreticular' to one another. One example is the IRMOF series,[10] of which MOF-5 is the first member (IRMOF-1), where each member of the series is constructed from $Zn_4O(RCO_2)_6$ octahedra bridged by dicarboxylate linkers of varying length. As can be seen in Figure 1.3, the pore volume expands as the linker is extended by increasing its number of consecutive phenyl rings, going from IRMOF-1 (1 ring) to IRMOF-10 (2 rings) and to IRMOF-16 (3 rings). This concept is advantageous as it enables the pore size to be tailored for a given application in a predictable manner, while preserving the underlying net.

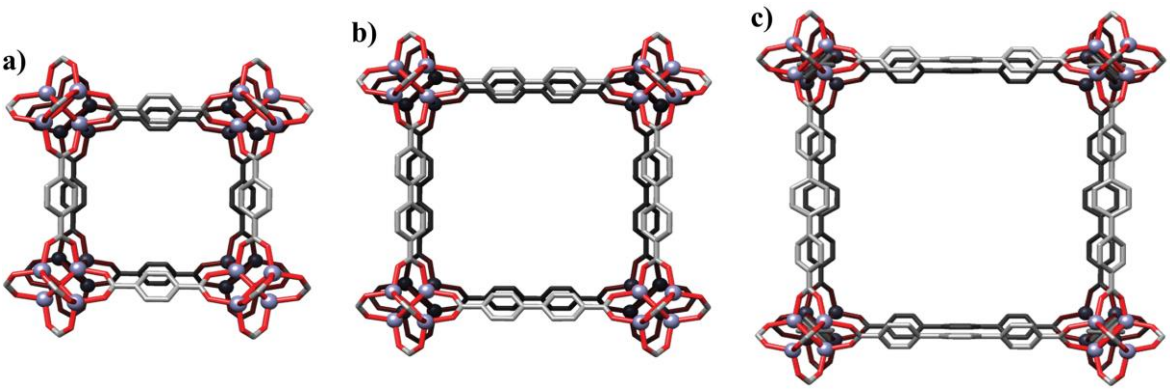

Figure 1.3. Pore expansion of members of the IRMOF series: a) IRMOF-1, b) IRMOF-10, c) IRMOF-16.[10]

In addition to tuning the pore size, the pore environment can also be modified by incorporation of functional groups onto the organic component. The linkers used to construct MOFs usually contain aromatic rings, which can easily be modified to add functionality to the resulting MOF without changing the underlying topology. This can be further exploited through post-synthetic modification (conducting reactions on the pre-synthesised MOF) to attach other pendant groups in order to confer desirable properties to the material. The benefit of this approach is that the post-synthetic modifications can often be conducted under milder conditions than direct synthesis, providing access to otherwise unobtainable materials. The versatility of this approach was demonstrated comprehensively by Cohen et al.[11,12] using IRMOF-3, whose terephthalate linker has an amino group in the 2-position, to attach a range of functional groups via a reaction between the amine on the MOF with a series of anhydrides and isocyanates (Figure 1.4). All of these modifications could be achieved with relatively high conversions (>40%) at room temperature and led to significant increases in their respective affinities towards hydrogen as well as their total hydrogen uptakes.[11] Such ease of modification is almost unheard of in other widely studied porous materials such as zeolites due to the lack of diversity in their building blocks.

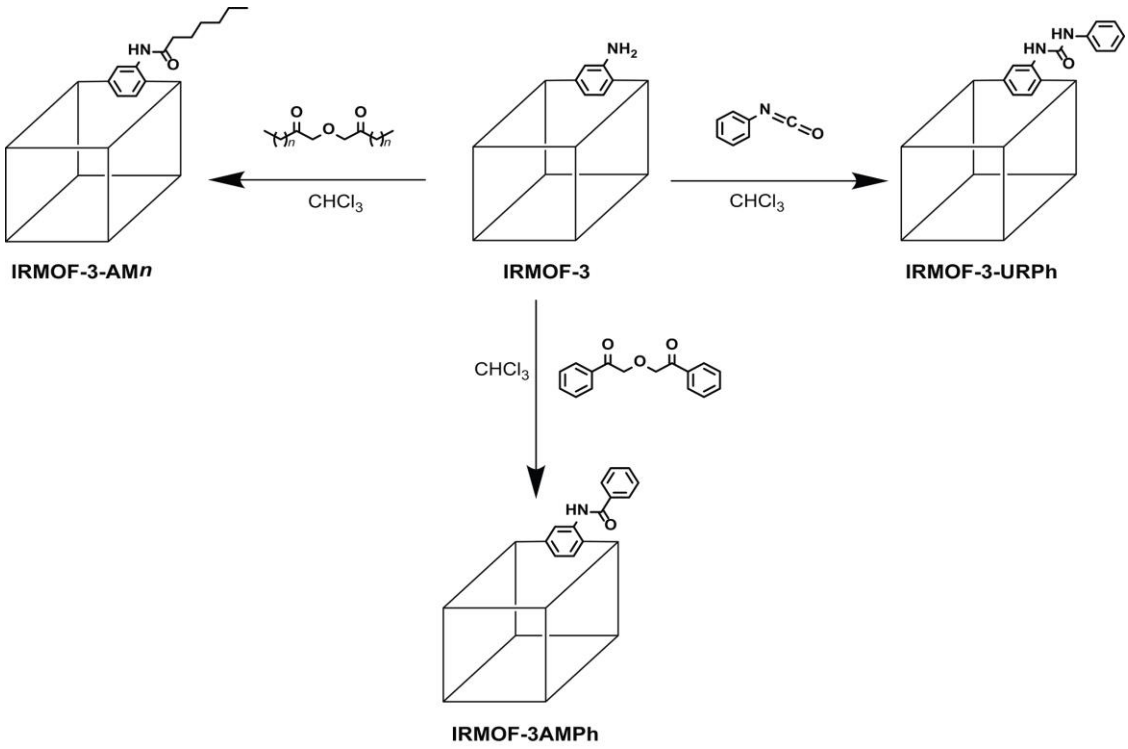

Figure 1.4. Schematic representation of post-synthetic modifications which can be conducted on IRMOF-3 to attach pendant groups onto the framework.[11]

1.2.3 Interpenetration

When sufficiently long linkers are used in MOF syntheses, there is a common tendency for the networks to interpenetrate,[13] where two or more single nets grow together into an interlocked structure that reduces the overall pore size (Figure 1.5a). A degree of porosity can often be preserved in two-fold interpenetrated structures, such as the indium framework SHF-61 (Figure 1.5b), but this reduces significantly as the order of interpenetration increases, for example in the three-fold interpenetrated [Ni(muconate)(bpa)($2H_2O$)]·$2H_2O$ (bpa = 1,2-bis(4-pyridyl)ethane, Figure 1.5c), eventually giving tightly packed coordination polymers without any void space.

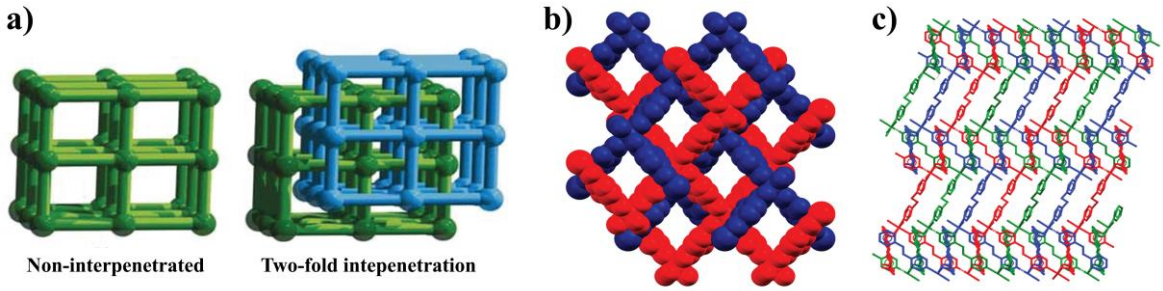

Figure 1.5. a) Schematic representation of a two-fold interpenetrated network,[14] b) two-fold interpenetrated (Me_2NH_2)[In($ABDC)_2$] (SHF-61),[15] c) three-fold interpenetrated [Ni(muconate)(bpa)($2H_2O$)]·$2H_2O$ (bpa = 1,2-bis(4-pyridyl)ethane).[16]

Because interpenetration greatly reduces the pore volume, it is often viewed as a detriment and synthetic strategies are therefore employed to prevent interpenetration, such as introducing steric bulk on the linker or varying the nature of the solvent. For example, interpenetration control by solvent was demonstrated in a zinc biphenyl-4,4'-dicarboxylate-2,2'-diol system where synthesis in *N*,*N*-diethylformamide (DEF) led to a non-interpenetrated framework, while using *N*,*N*-dimethylformamide (DMF) led to a two-fold interpenetrated framework.[17]

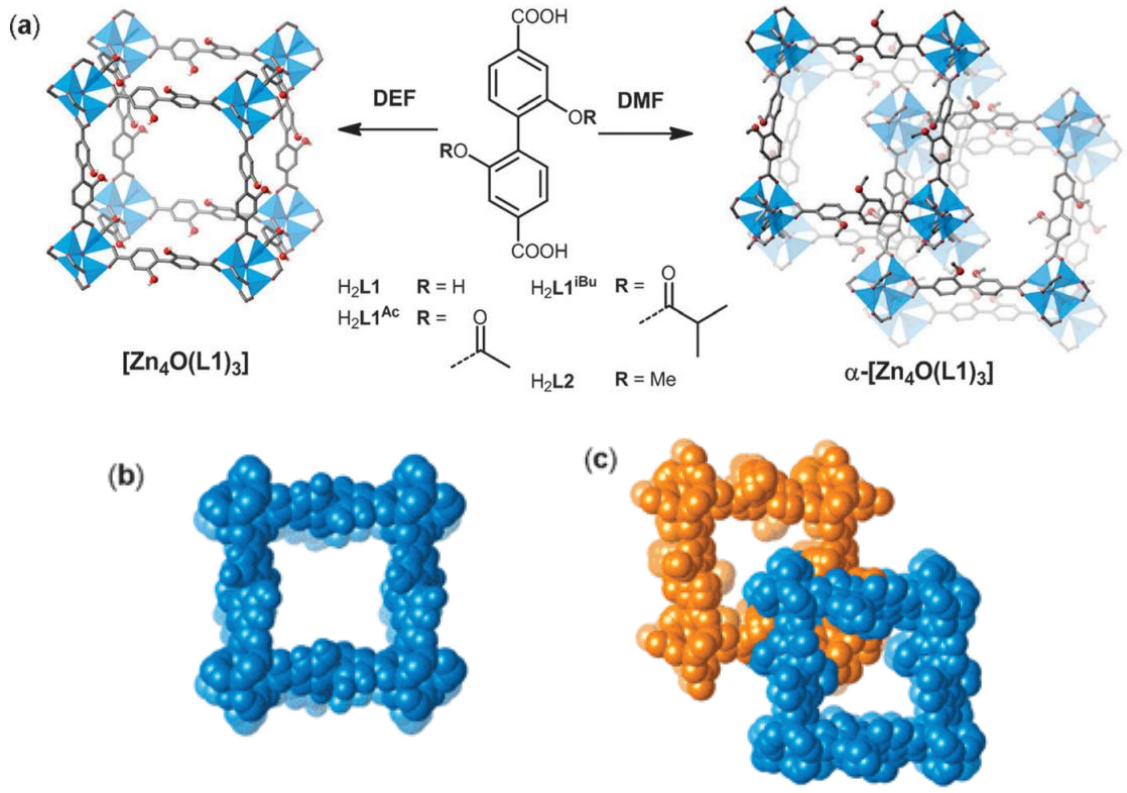

Figure 1.6. Schematic representation of the syntheses of $[Zn_4O(L1)_3]$ and α-$[Zn_4O(L1)_3]$. Space fill models of b) non-interpenetrated $[Zn_4O(L1)_3]$, c) interpenetrated α- $[Zn_4O(L1)_3]$.[17]

Despite being commonly viewed as detrimental, interpenetration can in fact lead to desirable properties absent from their non-interpenetrated counterparts. One example is increased selectivity in gas separations: the presence of multiple nets in close proximity provides sites with stronger van der Waals interactions between the guest and the MOF than are present in most non-interpenetrated frameworks. This can radically increase the binding affinity towards various guest molecules and is particularly relevant for the capture and storage of gases such as CO_2 and H_2, applications in which MOFs have been identified as promising candidates and which require adsorbents that perform well at low pressure.[18,19] The impact of interpenetration on CO_2 affinity has been explored using Grand Canonical Monte Carlo

(GCMC) simulations on a number of prototypical interpenetrated and non-interpenetrated MOFs.[20] While the non-interpenetrated frameworks displayed greater uptake at high pressure (up to 50 bar) due to their larger pore sizes, the interpenetrated MOFs performed better at lower pressure (up to 2 bar) due to the closer contact between adjacent nets. In addition, the interpenetrated frameworks displayed better selectivity for CO_2 over H_2.

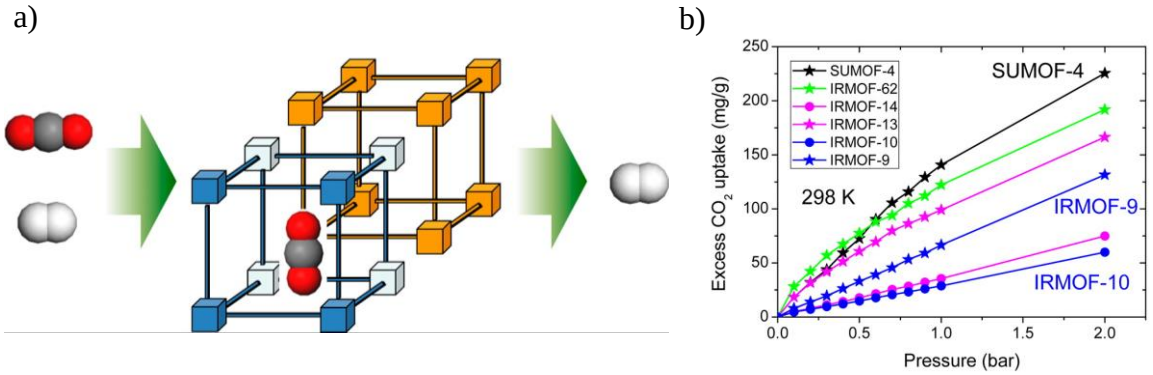

Figure 1.7. a) Illustration of CO_2/H_2 separation using interpenetrated MOFs, b) CO_2 adsorption isotherms of non-interpenetrated MOFs (IRMOF-10 and IRMOF-14) and interpenetrating MOFs (IRMOF-9, IRMOF-13, IRMOF-62, and SUMOF-4) at pressures up to 2 bar at 298 K.[20]

1.2.4 Summary

The unique properties of MOFs, namely their high degree of tunability and vast structural diversity, make them superior to other porous materials, but also impedes their development for practical applications. Although the concepts underpinning reticular chemistry are straightforward when applied to deconstructing known structures, in practice it is often troublesome to synthesise a desired framework *de novo* and thus MOF "design" is usually a *post hoc* rationalisation of experimental work actually guided by trial and error. In addition to interpenetration, which we have already discussed briefly, structure prediction can also be confounded by other phenomena, such as framework polymorphism, which will be addressed in Section 1.4.3 . These challenges are currently being addressed by computational and synthetic efforts to determine how synthesis conditions influence framework structure and why some phases form preferentially under a given set of conditions.[21,22] In the next section we will discuss trivalent MOFs, which are an essential subject of this thesis.

1.3 Trivalent Carboxylate MOFs

1.3.1 Background

MOFs containing divalent metals such as Cu^{2+} and Zn^{2+} have been studied very extensively, but generally suffer from poor chemical stability.[23] The archetypal example is MOF-5, which despite its high permanent porosity, was found to slowly degrade over time from atmospheric moisture, leading to a loss of crystallinity and porosity.[6] This effect is very common for M^{2+}-carboxylate frameworks, as water can displace the relatively labile metal-linker bonds. MOF hydrolysis presents a significant challenge for potential applications where humid environments are an inevitability, as the bulk properties of the material will decline over time. One way to enhance the stability of MOFs is to use higher valent metals which possess a greater charge density than M^{2+} ions and thus tend to form stronger M-carboxylate bonds.[23]

MOFs containing trivalent metals have been known since 2002 and compromise much of the MIL-family (Matériaux Institut Lavoisier) of materials synthesised by Férey et al.[23] The range of metals that can be used to make these materials includes the transition metals Cr^{3+}, Sc^{3+}, Fe^{3+}, and V^{3+}, as well as the 13th row p-block elements Al^{3+}, Ga^{3+}, and In^{3+}. MOFs constructed from yttrium and the lanthanides will not be covered as their coordination chemistry is divergent from the aforementioned metal ions.

The most common SBUs found in M^{3+}-carboxylate frameworks are the trigonal planar $[M_3O(RCO_2)_6(L)_2X]$ (L = neutral monodentate ligand, X = monoanion) cluster and the infinite chain of corner-sharing octahedra $[M(OH)(RCO_2)_2]_n$. Generally, the $[M_3O(RCO_2)_6(L)_2X]$ SBU is less common for the p-block elements, which more frequently adopt structures with the $[M(OH)(RCO_2)_2]_n$ SBU, however, there are examples with each of these SBUs for all of the M^{3+} metals. Some of the well-known frameworks constructed from each of these SBUs will be discussed here.

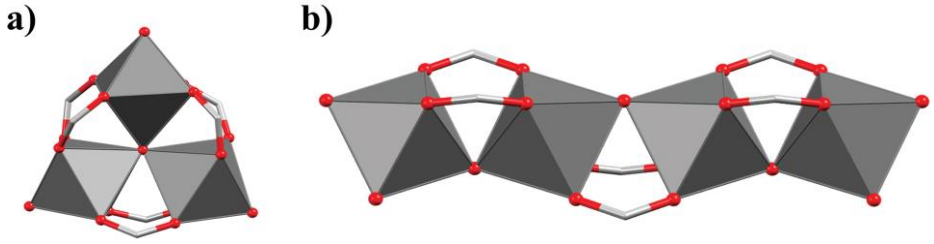

Figure 1.8. Polyhedral representation of the a) $[M_3O(RCO_2)_6(H_2O)_2X]$[24] (L = neutral monodentate ligand, X = monoanion), and b) $[M(OH)(RCO_2)_2]_n$ SBUs.[25]

1.3.2 MIL-88 and MOF-235

Two frameworks containing the $[M_3O(RCO_2)_6(H_2O)_2X]$ SBU are MOF-235[26] and MIL-88B,[27] both of which possess the same linker (1,4-BDC), topology (Figure 1.9a-b) but differ primarily in the fact that MOF-235 contains an $[MCl_4]^-$ anion inside the pores instead of a coordinating anion (X) at the cluster, which is replaced by another neutral solvent molecule (Figure 1.9c). MIL-88B has been reported for all of the transition metals mentioned,[27-31] while MOF-235 has only been reported with Fe^{3+} in addition to an amino-terephthalate variant with Al^{3+}.[26,32] The crystallisation of MOF-235 is contingent on the formation of a tetrahedral $[MCl_4]^-$ anion and has therefore only been observed when the corresponding metal chloride precursors are used. In addition, the presence of DMF during the synthesis also appears to be essential to form MOF-235; DMF is present as terminal ligands in MOF-235(Fe)[26] and has been found to be a prerequisite to promote the formation of MOF-235(Al)_NH_2 from *in situ* crystallisation studies.[33]

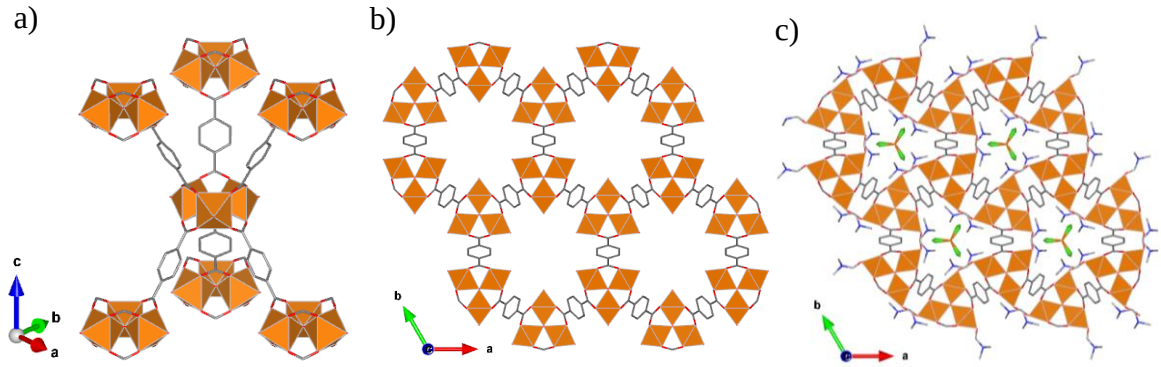

Figure 1.9. a) Representation of the hexagonal ABA layering in MIL-88B(Fe)/MOF-235(Fe), b) packing structure of the open form of MIL-88B(Fe) as viewed down the *c*-axis, c) packing structure of the open form of MOF-235(Fe) as viewed down the *c*-axis.

A remarkable property of MIL-88B, along with its isoreticular analogues, is its flexible nature, expressed in the ability to undergo large and reversible expansions/contractions without bond breaking. The mechanism that enables this flexibility is a continuous kneecapping-like motion of the carboxylates around the metal cluster (Figure 1.10a). Comparatively, MOF-235 does not exhibit this flexibility because of the strong interaction between the $[MCl_4]^-$ anion and the framework. A solvated sample of MIL-88 will typically adopt a large pore form, referred to as ‘open’, while a desolvated sample will adopt a narrow pore form designated as ‘dry’ or ‘closed’ (Figure 1.10b). An intermediate state, known as the ‘as-synthesised’ form (Figure 1.10b), is obtained prior to heating and is the most

susceptible towards the readsorption of solvents, while the dried forms become progressively difficult to reopen as the linker length increases, due to the increased interactions between adjacent linker molecules.[34]

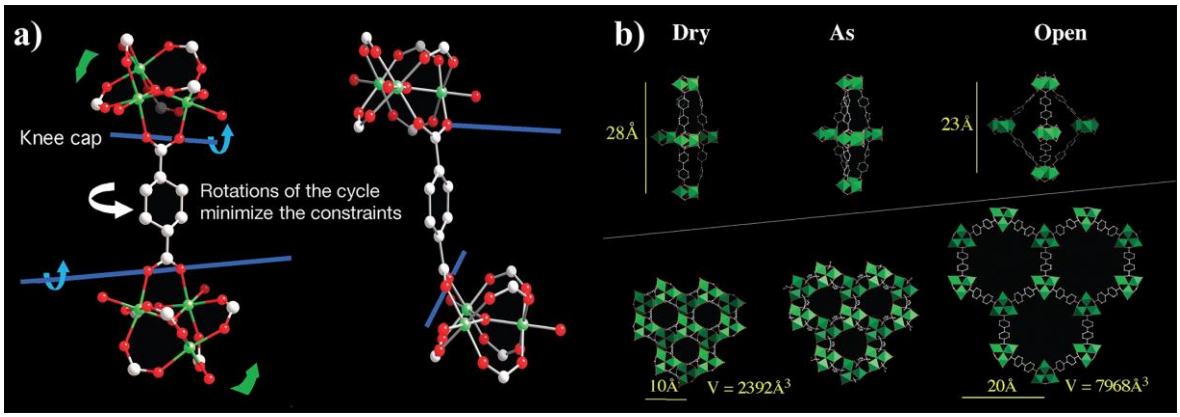

Figure 1.10. Schematic representation of the linker rotation and knee-capping motion associated with the flexing mode of MIL-88B, b) representation of the open (Open), closed (Dry) and as-synthesised (As) states of MIL-88, with MIL-88D used as the example.[34]

Other members of the MIL-88 series include MIL-88A with fumarate, MIL-88C with naphthalene-2,6-dicarboxylate (2,6-NDC), and MIL-88D with 4,4´-biphenyldicarboxylate (BPDC). The ratio of the volumes of the dried and solvated forms (V_{open}/V_{dry}) varies depending on the nature of the solvent as well as the linker length, going from 1.85 for MIL-88A to 3.3 for MIL-88D. Solvent molecules which can interact strongly with both the metal centres and the organic components, such as pyridine, appear to be the most effective at reopening the dried forms and often lead to the largest framework expansion.[34]

Functionalised variants of MIL-88B(Fe) and MIL-88D(Fe) have been prepared by using linkers with different substituent groups (Figure 1.11a).[29] These modifications introduce increased steric hindrance, leading to a reduction in the swelling amplitude (Figure 1.11b), defined by the transition between the open and closed (dry) forms ($=(V_{open}-V_{dry})/V_{dry}$), by restricting unit cell contraction. This has a large effect on the accessibility of the pores in these functionalised MIL-88 frameworks, both in terms of the gas uptake and how easily the closed form can be reopened. The nitrogen uptake of MIL-88B, which is insignificant for the unfunctionalised form, increases dramatically for the tetramethyl variant with a BET surface area (SA_{BET}) of 1216 m^2g^{-1}. For the MIL-88D frameworks, introducing steric hindrance to the linker greatly enhances the ease of swelling from the dried forms. While the dry form of MIL-88D could only be reopened fully through immersion in hot pyridine, the

dimethyl and tetramethyl variants could be reopened at room temperature in a number of solvents.

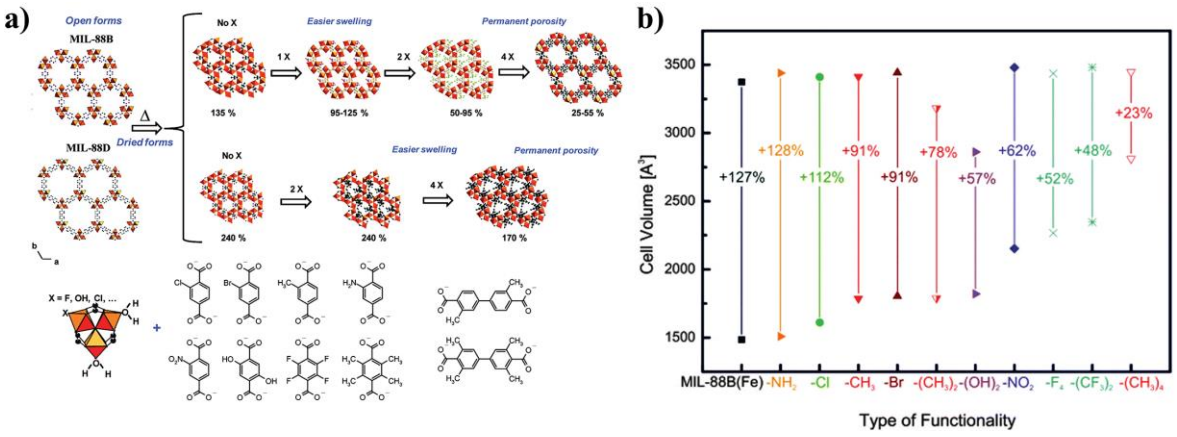

Figure 1.11. a) Schematic view of the flexibility of MIL-88B and MIL-88D modified solids as a function of the number of functional groups on the linker, with the swelling amplitudes given below each packing view (swelling amplitude = $(V_{open}-V_{dry})/V_{dry}$),[29] b) comparison of the absolute unit cell volumes and swelling amplitudes for MIL-88B with different functional groups.[35]

1.3.3 MIL-53 and MIL-68

For the $[M(OH)(RCO_2)_2]$ SBU, there are two common structures with terephthalate as linker: the polymorphs MIL-53 (also known as MIL-47 for V^{3+}/ V^{4+}) and MIL-68 with formula [M(OH)(1,4-BDC)]. MIL-53 is a flexible framework containing 1-D diamond-shaped channels parallel to the SBU chains (Figure 1.12a), while MIL-68 possesses a rigid Kagomé topology containing both hexagonal channels and triangular channels (Figure 1.12b). MIL-53 is the most common structure adopted by trivalent terephthalates and can form with all of the metals discussed here (Cr,[36] Sc,[30] Fe,[37] V,[38] Al,[39] Ga,[40] In[41]). MIL-68 has also been obtained with most of these metals (Sc,[42] Fe,[43] V,[44] Al,[45] Ga,[46] In[46]) but tends to be favoured when DMF is used as solvent, whereas MIL-53 can be synthesised in a wider range of solvents. There are many isoreticular variants of MIL-53, a notable example being the Al-fumarate framework[47] which has been produced and sold commercially by BASF (Basolite A520).[48] Extended frameworks include MIL-69 [Al(OH)(2,6-NDC)],[49] DUT-4 [Al(OH)(2,6-NDC)],[25] and DUT-5 [Al(OH)(BPDC)][25] (Figure 1.12c). Unlike MIL-53(M), DUT-4 and DUT-5 have an open pore structure yet do not exhibit any flexibility, and thus possess high permanent porosity.[25] Interestingly, despite the otherwise identical framework structures of DUT-4 and MIL-69, the latter possesses a narrow pore structure which is inaccessible to N_2, and these two frameworks do not interconvert via solvent

adsorption/evacuation.[25] Only one extended form of MIL-68 has been reported thus far, known as CYCU-3 (Figure 1.12d), which contains 4,4′-stilbenedicarboxylate (SDC) as linker and exhibits remarkably high permanent porosity (SA_{BET} = 2757 $m^2 g^{-1}$).[50]

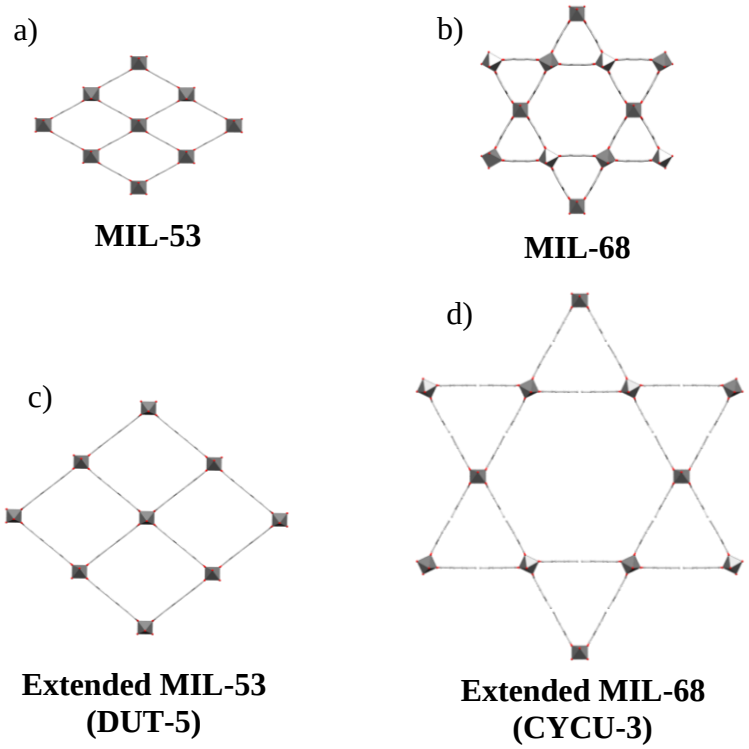

Figure 1.12. Structures viewed down the axis of the M(OH) chain: a) MIL-53,[36] b) MIL-68,[43] c) DUT-5,[25] d) CYCU-3.[50]

The flexibility of MIL-53 has been widely studied and is distinct from MIL-88 in that it undergoes stepwise transitions rather than the continuous mode reported for MIL-88. The prototypical example is MIL-53(Al), which crystallises with terephthalic acid inside its pores, giving a wide pore form known as MIL-53(Al)_as (Figure 1.13a) with 'as' denoting that it is the 'as-synthesised' form.[39] When this material is heated, the terephthalic acid is removed to give a slightly more open form when fully activated (i.e. there are no guests inside the pores) and known as MIL-53(Al)_ht (Figure 1.13a) to denote that it is the 'high temperature' form. MIL-53(Al)_ht readily adsorbs atmospheric moisture when cooled down to room temperature, and contracts to give a form with narrow pores. This hydrated material is named MIL-53(Al)_lt (Figure 1.13a) to denote that it is the 'low temperature' form, and this hydration/dehydration process is fully reversible. The mechanism for the flexibility is rotation of the $AlO_4(OH)_2$ octahedra, causing a corresponding effect on the BDC–Al–BDC angles in the network, which decrease from 75.0° in MIL-53(Al)_ht to 42.6° in MIL-53(Al)_lt. When looking down the axis of the Al(OH) chain, between MIL-53(Al)_ht and

MIL-53(Al)_lt there is an opposite rotation of 20.3° about the axis of the chain between adjacent $AlO_4(OH)_2$ octahedra.

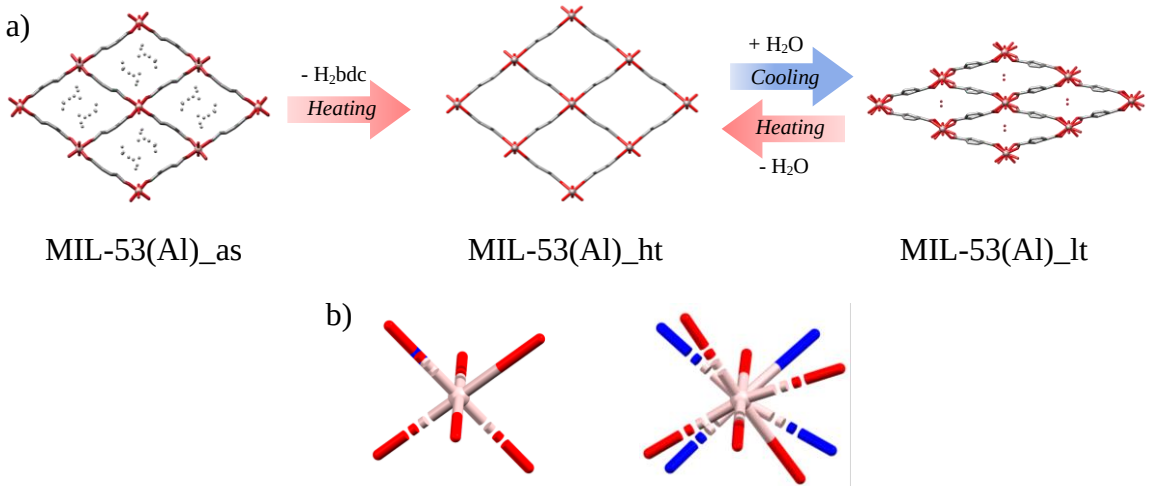

Figure 1.13. a) Diagram of the structural changes of MIL-53(Al)_as upon activation to remove H_2BDC and the subsequent hydration/dehydration of the activated form upon cooling/heating, b) view of two adjacent $AlO_4(OH)_2$ octahedra in MIL-53(Al)_ht (left) and MIL-53(Al)_lt (right) as viewed down the axis of the Al(OH) chain, the oxygens are coloured as red and blue for each $AlO_4(OH)_2$ octahedra.

The flexibility of MIL-53 varies depending on the nature of the metal and leads to quite divergent behaviour across the entire MIL-53(M) series.[39,40,51-54] For example, studies on the Fe and Cr analogues have shown that, despite their similar ionic radii, they exhibit completely different breathing during hydration/rehydration.[51] MIL-53(Cr) displays similar behaviour to MIL-53(Al), with analogous unit cells for the corresponding MIL-53(Cr)_as, MIL-53(Cr)_ht, and MIL-53(Cr)_lt forms. In contrast, the dehydration of MIL-53(Fe)_lt causes the structure to contract further (by ~87 $Å^3$) and adopt a fully closed form MIL-53(Fe)_ht when heated above 423 K. An intermediate anhydrous phase where half the pores are fully closed and half slightly open, MIL-53(Fe)_int, was also observed at relatively lower temperatures (323 K < T < 413 K). The underlying reason for these differences in behaviour are still not very well understood, but have been postulated to be related to both their ionic radii and electronic structures.[40,53]

1.3.4 MIL-101 and MIL-100

Some of the most interesting M^{3+} carboxylates are those possessing the zeolite MTN topology, namely the terephthalate (BDC) framework MIL-101 and the benzene-1,3,5-tricarboxylate (BTC) framework MIL-100.[55,56] MIL-100 is an interesting case as its structure

was first predicted by computational simulations and then the synthetic conditions were selected to target the Cr^{3+} analogue.[55] This approach can be exceptionally useful in cases such as MIL-100 where the unit cell is very large, and where it is also not possible to grow crystals large enough for SCXRD. Both frameworks are constructed from $M_3(\mu_3\text{-}O)(RCO_2)_6$ trimeric SBUs, which form tetrahedral cages by connection with six BDC linkers (MIL-101) or four BTC linkers (MIL-100) (Figure 1.14a). The tetrahedral cages comprise two types of larger cages via corner-sharing, one featuring pentagonal windows (small cage) and the other featuring pentagonal and hexagonal windows (large cage) (Figure 1.14b). These small and large cages are connected by face-sharing to yield the MTN topology (Figure 1.14c).

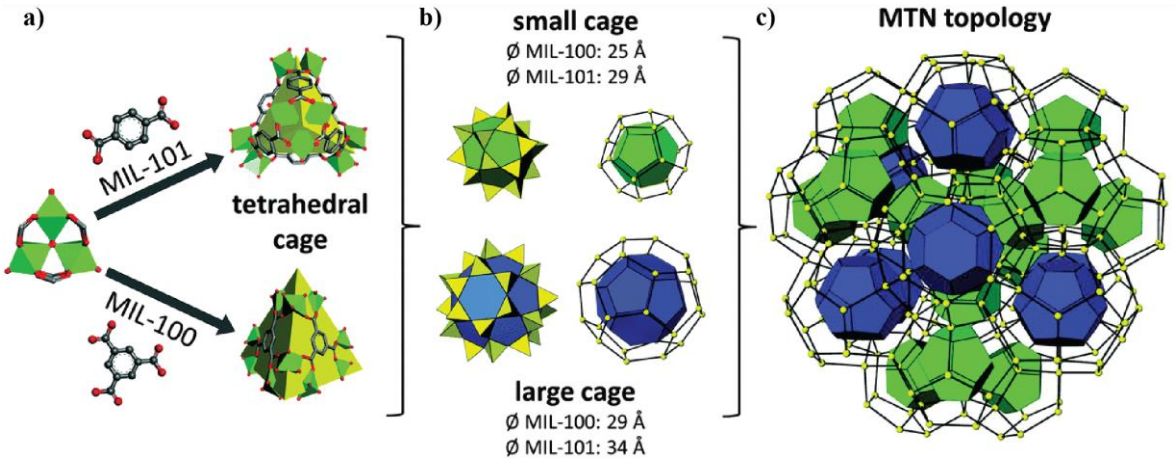

Figure 1.14. a) Polyhedral depiction of the tetrahedral cages in MIL-101 and MIL-100, b) simplified representation of the large and small cages built up from these tetrahedral cages, c) underlying MTN topology of MIL-100 and MIL-101.[57]

While both frameworks have been synthesised with a range of trivalent metals, the most significant are the original Cr^{3+} variants due to their high chemical stabilities. The combination of high porosity (SA_{BET} = 2500-4,500 $m^2\ g^{-1}$)[55,56,58] and stability expressed by MIL-100(Cr) and MIL-101(Cr) make them particularly desirable, as such MOFs are relatively rare. Nevertheless, some of the other notable analogues include MIL-100(Sc), which has demonstrated exceptional ability as a Lewis acid catalyst,[42] as well as the Fe^{3+} analogues of both materials, which have attracted interest for drug delivery and biomedical imaging due to their low toxicities.[59,60]

Functionalised variants of MIL-101 have been prepared for Cr^{3+}, Fe^{3+}, and Al^{3+} directly from functionalised terephthalate linkers,[58,61,62] as well as a number from post-synthetic modifications. The nature of the functional group has been shown to tune the CO_2 uptake in MIL-101(Al)_X (where X = the substituent(s) on the terephthalate)[61] and has also been exploited to graft other moieties to the framework post-synthetically. In contrast, stable

extended analogues have proven to be somewhat more challenging to obtain. The extended variant with naphthalene-2,6-dicarboxylate has been reported with both Fe^{3+} and Cr^{3+}, known as MIL-101(Fe)_NDC[58] and MIL-101(Cr)_NDC[63] respectively, as well as a 4,4´-biphenyl dicarboxylate analogue with Fe^{3+}, MIL-101(Fe)_BPDC.[58] Increasing the pore size typically reduces the stability of MOFs, and both Fe^{3+} analogues were found to degrade in a range of solvents and/or transform into denser phases.[58] Consequently, MIL-101(Cr)_NDC is the only example of an extended MIL-101 framework that displays high permanent porosity (SA_{BET} = 2100 m^2 g^{-1}) post-activation.[63]

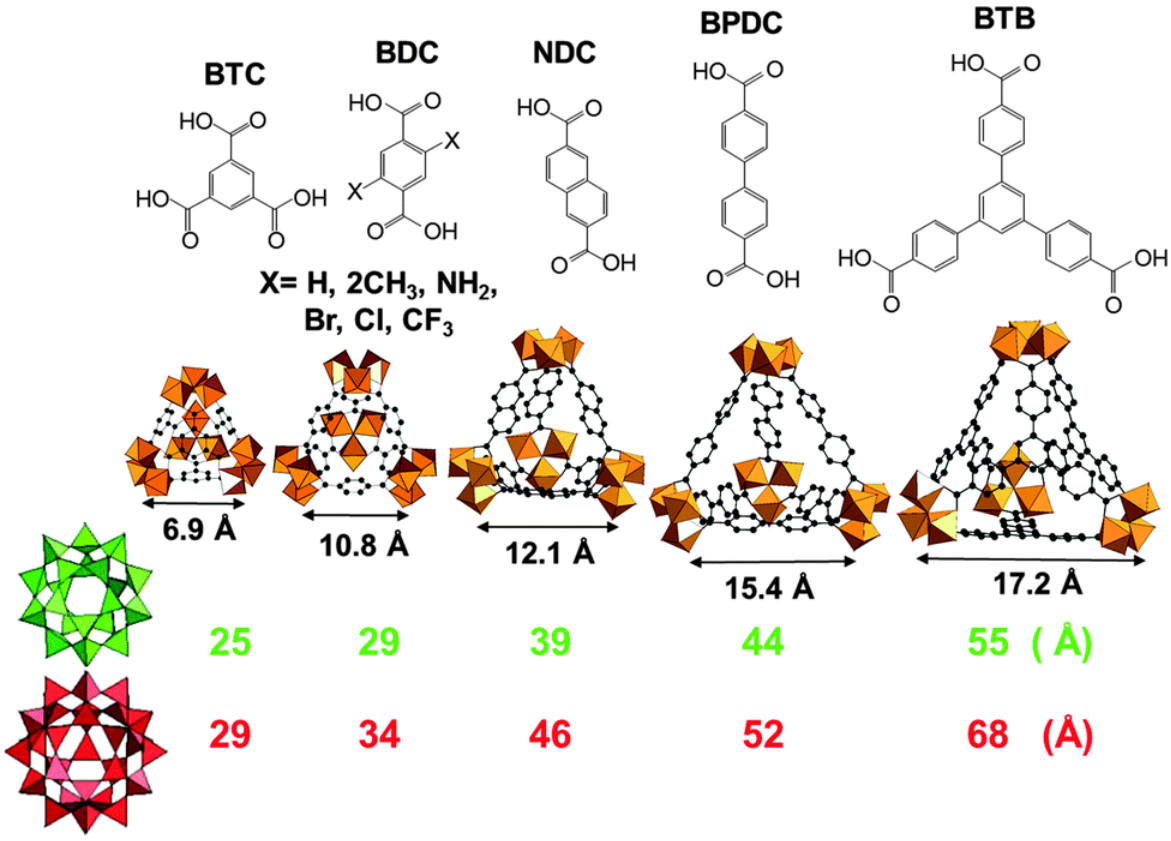

Figure 1.15. Schematic representation of the tetrahedral cages in each of the extended MIL-100/101 frameworks along with the corresponding diameters of the large (red) and small (green) cages in these solids.[58]

As with MIL-101, the development of extended isoreticular analogues of MIL-100 is particularly challenging. An Fe-analogue with 1,3,5-tris(4-carboxyphenyl)benzene (BTB) known as MIL-100(Fe)_BTB has been reported, but rapidly degrades in water and the surface area of the pristine material could not be accessed, either due to this degradation or collapse of the pores upon evacuation. It was rationalised by Zhou et al. that the trigonal planar nature of BTC helps to stabilise the tetrahedral cage in MIL-100, as the linker is required to undergo a slight bowl-shaped bending to conform to structure.[64] In contrast, it is

much more energetically unfavourable for a non-planar linker such as BTB to adopt this conformation, thus explaining why MIL-100(Fe)_BTB is unstable. With this rationale in mind, stable extended analogues of MIL-100 have been prepared using two trigonal planar tricarboxylate linkers: benzo-tris-thiophene carboxylate (BTTC) and 4,4',4''-s-triazine-2,4,6-triyl-tribenzoate (TATB).[64] These yielded two structures with MIL-100 topology, namely PCN-332 (BTTC) and PCN-333 (TATB). The latter of these frameworks possessed a cubic cell with a = ~127 Å and, unlike MIL-100(Fe)_BTB, huge accessible surface area (~4,000 $m^2 g^{-1}$). In addition, these materials displayed remarkable stability in aqueous media over a range of pH values (pH = 3-9) without an appreciable drop in crystallinity or gas-sorption capacity.[64]

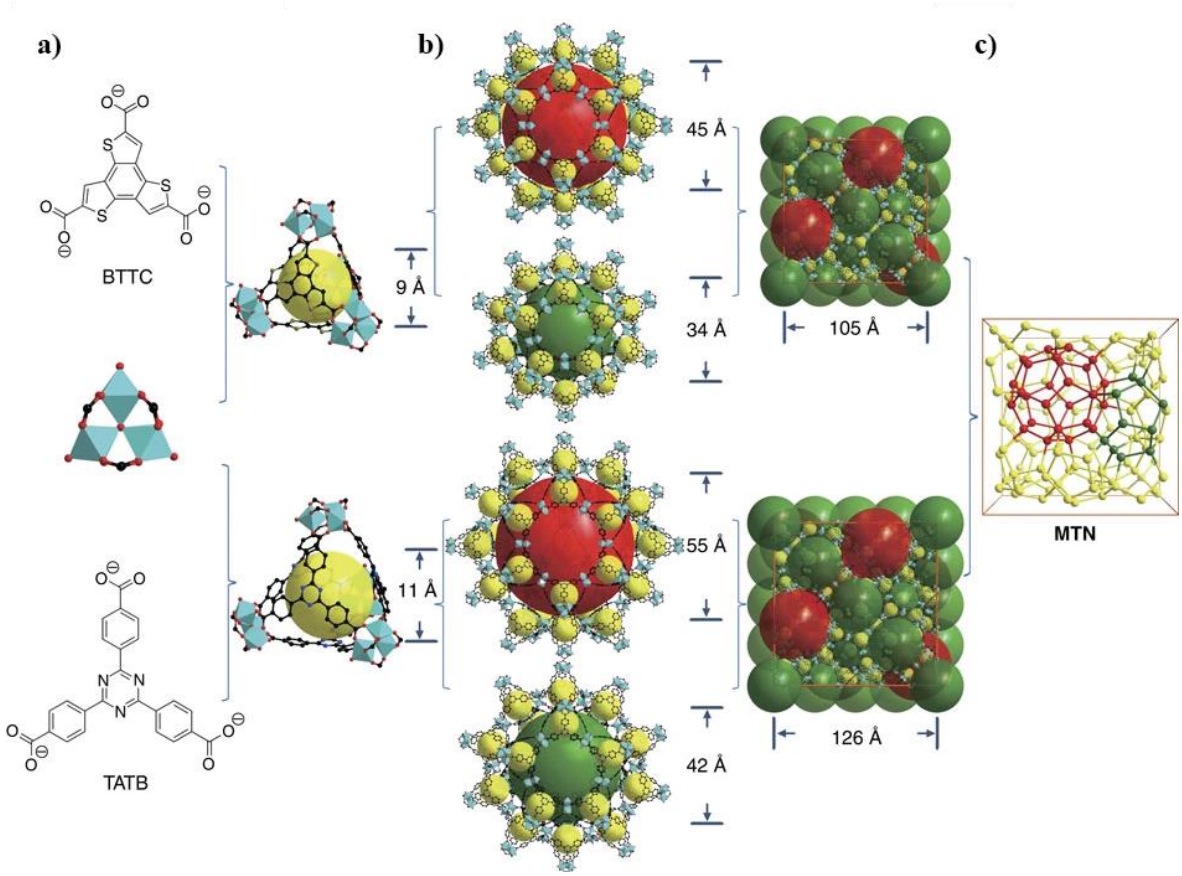

Figure 1.16. a) The ligands in PCN-332 and PCN-333, b) Tetrahedral (yellow), small (green), and large (red) cages present in PCN-332 and PCN-333, c) Simplification of PCN-332 and PCN-333 into the MTN topology.[64]

1.3.5 Soc-MOF

A well-known example of an M^{3+}-tetracarboxylate network is the soc-MOF (square octahedron cubic) topology, typically formed using 3,3',5,5'-azobenzenetetracarboxylate (ABTC). These M^{3+}-ABTC frameworks are known by many names: M-soc-MOF,[65] MIL-

127,[66,67] and PCN-250.[68] They have been synthesised with most of the M^{3+} metals (Al, Fe, Ga, In, Sc, V) and possess a cubic pore architecture (Figure 1.17a) with relatively high porosity (1000-2000 m^2g^{-1} depending on the metal).[30,65] Their high porosity and potential open metal sites have garnered interest for their use in gas separation, and the Ga^{3+} and Al^{3+} analogues have demonstrated remarkable selectivity for H_2S over CH_4 and CO_2, as well as exhibiting high stability under these conditions.[65] Just as remarkable are the extended analogues M-soc-MOF-1[69,70] with 3,3″,5,5″-tetrakis(4-carboxyphenyl)-*p*-terphenyl (TCPT) as linker[70] (Figure 1.17b). The Cr^{3+} analogue, obtained via metathesis from Fe-soc-MOF-1, exhibits much higher hydrolytic stability compared to the Al and Fe forms and impressively can undergo fully reversible water vapour uptake at room temperature - a desirable property for regulating humidity in confined spaces.[70]

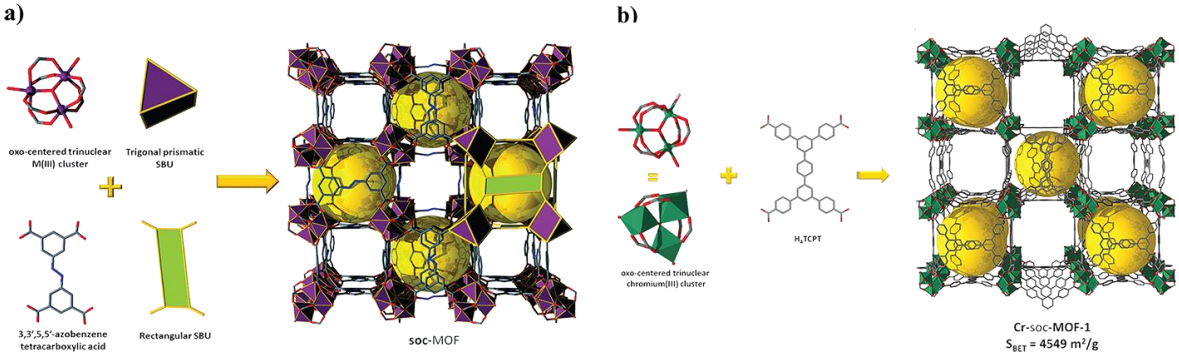

Figure 1.17. Topological representation of soc-MOF,[65] b) Packing structure of an extended isoreticular analogue Cr-soc-MOF-1.[70]

1.3.6 Summary

This section has given an overview of the predominant structure types which can be formed from trivalent metals and carboxylate linkers, and how they relate to key framework properties such as porosity, flexibility, etc. While most of these frameworks can be synthesised from more than one metal, there are multiple trade-offs such as stability, ease of synthesis, and cost of metal precursor, which all need to be considered. As we will discuss in Section 1.5 , Fe^{3+} MOFs have been reported to be biocompatible due to the endogenous nature of iron, and thus we have focused our attention to their synthesis in the next two chapters to aid in their development for biomedicine. Additionally, Cr^{3+} MOFs have proven to be the most stable of those discussed, exemplified by MIL-101(Cr), but also particularly challenging to synthesise,[23] and hence we have also directed our efforts towards developing reliable synthetic strategies in Chapter 4. As such, the considerations relevant to MOF synthesis will be explored in more depth in the next section.

1.4 Synthesis of MOFs

The synthesis of MOFs is an important topic which has developed a large degree of interest since their inception, as the vast majority of known structures, with some exceptions,[71] do not occur in nature. The conditions required to synthesise MOFs are not uniform, and range from simple mixing of starting materials, such as with ZIF-8, a zinc imidazolate framework[72] which can be obtained with good yield within 5 minutes by stirring an aqueous solution of the starting materials at room temperature,[73] to more complex and time-consuming protocols which require carefully controlled synthetic conditions. Furthermore, there may be other necessary steps such as linker synthesis, which are non-trivial and increases the overall cost and time required to obtain a final product.

1.4.1 Synthesis and Characterisation

The conventional method for MOF synthesis is the solvothermal method (Figure 1.18), which involves heating a sealed vessel containing the metal precursor and ligand(s) in a suitable solvent.[74] After the framework crystallises, the solid can be collected by filtering or centrifuging, usually followed by washing away unreacted starting materials. This type of synthesis can be conducted above the boiling point of the solvent and utilises vessels which are suitable for withstanding the pressure which builds up during heating. Solvent exchange is normally required to remove the non-volatile solvents employed in the synthesis with those that can be more readily removed via heating. Alternative methods for synthesis will not be covered here but include microwave heating,[75] mechanochemical synthesis,[76] and sonochemical synthesis.[74] Regardless of the synthesis method, there are multiple parameters which need to be tuned for a given framework, including reactant concentration, synthesis time and temperature, as well as the necessary activation protocol.

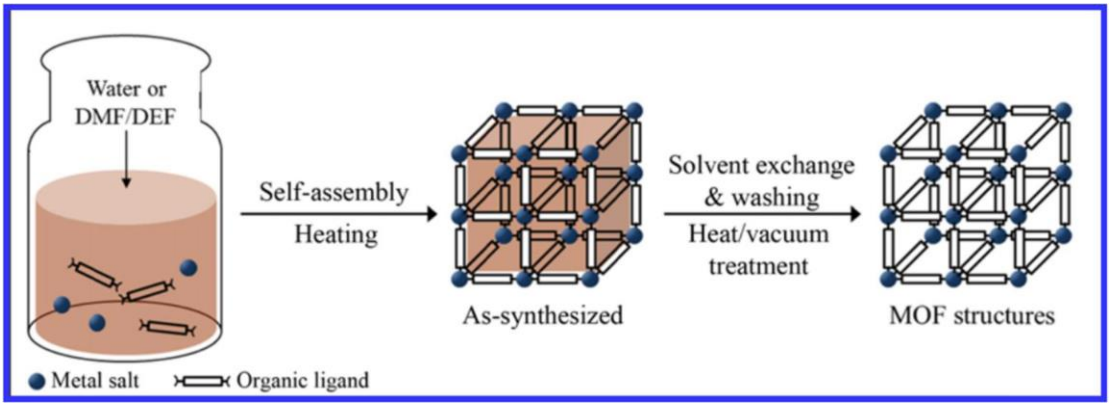

Figure 1.18. Schematic representation of solvothermal MOF synthesis and subsequent activation.[74]

The most common techniques to characterise MOF samples include powder X-ray diffraction (PXRD), which is primarily used for phase identification but can also be used to extract unit cell information and determine macroscopic features (crystallite size, orientation, etc.). Thermal gravimetric analysis (TGA) is also regularly employed to assess thermal stability, and when complemented by other techniques such as elemental analysis (EA) enables determination of sample composition. The most widely used technique to characterise porosity is gas sorption analysis, primarily consisting of N_2 adsorption isotherms to enable a reliable estimation of the surface area, pore volume, and pore size distribution of a given MOF. New MOF structures can be characterised by single crystal X-ray diffraction (SCXRD) to determine the crystal structure but requires crystals of adequate size and quality.

1.4.2 Crystallisation Additives

The main challenge encountered when synthesising high valent carboxylate MOFs is controlling the crystallisation process in order to achieve sufficiently crystalline material. The relative inertness of the metal-carboxylate bonds makes it difficult for self-assembly to proceed towards a well-ordered structure, as there is often not enough reversibility to ensure "error-checking" through rearrangement of the framework components. The concept of using crystallisation additives, species which can promote crystal growth and/or enhance crystallinity, was already well-established in zeolite chemistry,[77,78] a related class of porous materials that consist of aluminium, silicon and oxygen. In the context of zeolites these are referred to as 'mineralisers', which are typically hydroxides, carbonates, or halides, and their function is to aid in dissolving the starting materials, as well as dissolving poorly crystallised material that forms during the reaction and sometimes to template the structure itself.[56,79,80] In MOF synthesis, crystallisation additives are generally referred to as 'modulators' and play a similar role in enhancing crystallinity through promoting the formation of the SBU or other prenucleation species and introducing a degree of reversibility by competing with the linker.[23] They are typically monocarboxylates or mineral acids, although they can include any additive which is able to play a similar role in regulating MOF crystal growth. The use of monocarboxylates for this purpose is particular to MOF synthesis and is commonly referred to as 'coordination modulation'.[81] For simplicity, we will refer to all of these crystallisation additives as 'modulators' to denote their role in enhancing crystallisation.

The use of HF as a modulator was carried over from zeolite research by Férey et al. and has proven to be highly successful in aiding MOF crystallisation when using high valent metal

ions.[23] For example, the addition of HF enabled the growth of large single crystals of the aluminium framework MIL-53(Al) for the first time, along with the novel framework AlTCS-1 (TCS = tetrakis(4-oxycarbonylphenyl)silane)).[82] Similar improvements have also been observed with the zirconium-terephthalate framework UiO-66 (UiO stands for Universitetet i Oslo), which usually forms poorly crystalline and aggregated particles under solvothermal conditions in the absence of a modulator.[83] The addition of up to 3 equivalents of HF greatly enhanced the crystal quality and increased the crystal size, as evidenced by SEM imaging. Notably, HF has been used frequently to synthesise Cr-MOFs, which are some of the most challenging frameworks to crystallise due to the chemical inertness of Cr^{3+} and often require HF or another additive to facilitate their synthesis.[36,55,56,84]

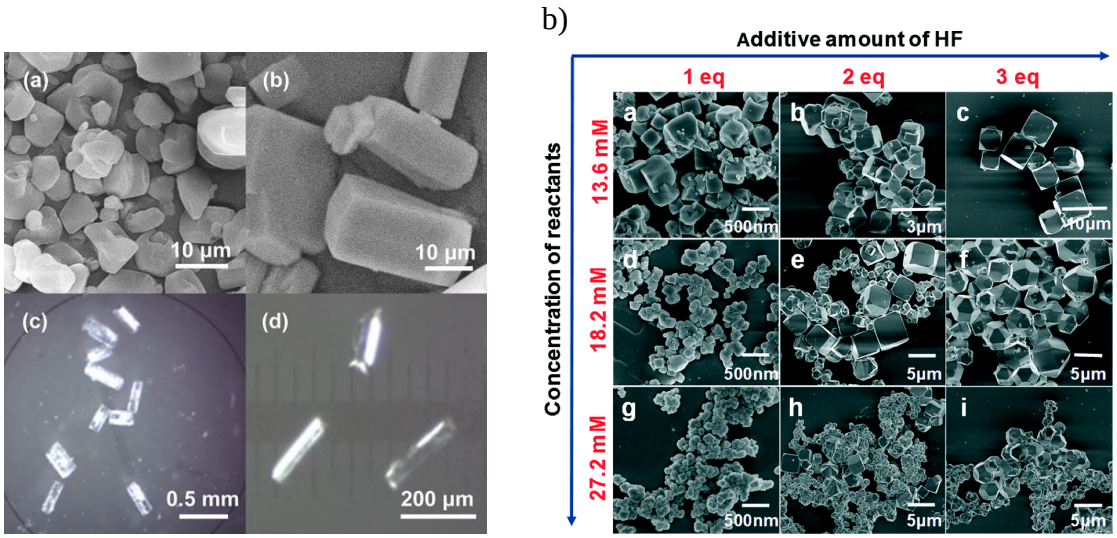

Figure 1.19. a) SEM images of MIL-53(Al) prepared using 0.39 (a) and 2.3 (b) molar equivalents of HF; Images of large single crystals of (c) MIL-53(Al) and (d) AlTCS-1 prepared using 4.4 molar equivalents of HF,[82] b) SEM images of UiO-66 prepared with varying molar equivalents of HF at three different reactant concentrations.[83]

Monocarboxylates have been used extensively as modulators in the syntheses of zirconium MOFs, where they have proven to be highly effective and, in many cases, essential for crystal growth.[85,86] Benzoic and acetic acid have been shown to be effective modulators in the crystallisation of the Zr-BDC (UiO-66) and Zr-BPDC (UiO-67) frameworks and led to increased crystal size and quality in both cases (Figure 1.20).[85] An explanation is that the addition of these monocarboxylates leads to the formation of discrete zirconium complexes in solution prior to nucleation, after which the dicarboxylate linker have to compete with these modulators, both coordinated and in solution, to cause nucleation. As the concentration of modulator is increased, the rate of nucleation decreases, and thus fewer crystallites are

formed. If a sufficient time is allowed for crystal growth, this will lead overall to larger crystallites. Additionally, the dynamic competition between the linker and modulator enables rearrangement into a more ordered structure, consistent with greater overall crystallinity. As such, the crystallites of Uio-66 and UiO-67 became larger and also less intergrown when the modulator concentration was increased, similar to HF. This enhancement in crystallinity was demonstrated by an increase in the specific surface area of the materials relative to unmodulated samples: from 270 m^2g^{-1} to 3000 m^2g^{-1} in the case of UiO-67 with 30 equivalents of benzoic acid.[85]

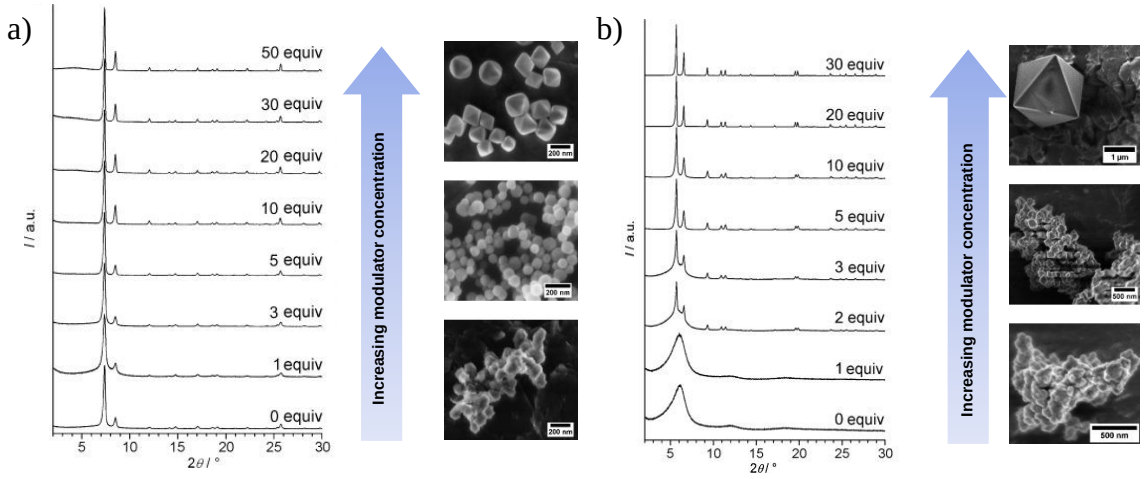

Figure 1.20. PXRD patterns of UiO-66 prepared with different molar equivalents of benzoic acid (relative to $ZrCl_4$) and SEM images of UiO-66 synthesized with 0, 10 and 30 equivalents of benzoic acid, b) PXRD patterns of UiO-67 prepared with different molar equivalents of benzoic acid (relative to $ZrCl_4$) and SEM images of UiO-67 synthesized with 0, 3 and 30 equivalents of benzoic acid.[85]

As was mentioned earlier, monotopic ligands which are added to the synthesis of MOFs are referred to as 'coordination modulators' and, apart from their ability to control self-assembly by competing with the bridging linkers, they can cap crystal facets and decorate the surfaces of crystallites by coordinating to metal sites (Figure 1.21).[81] This has proven to be an effective strategy for modifying crystallites to enhance their colloidal stability[87] and has also been used to attach anti-cancer therapeutics such as dichloroacetic acid.[88]

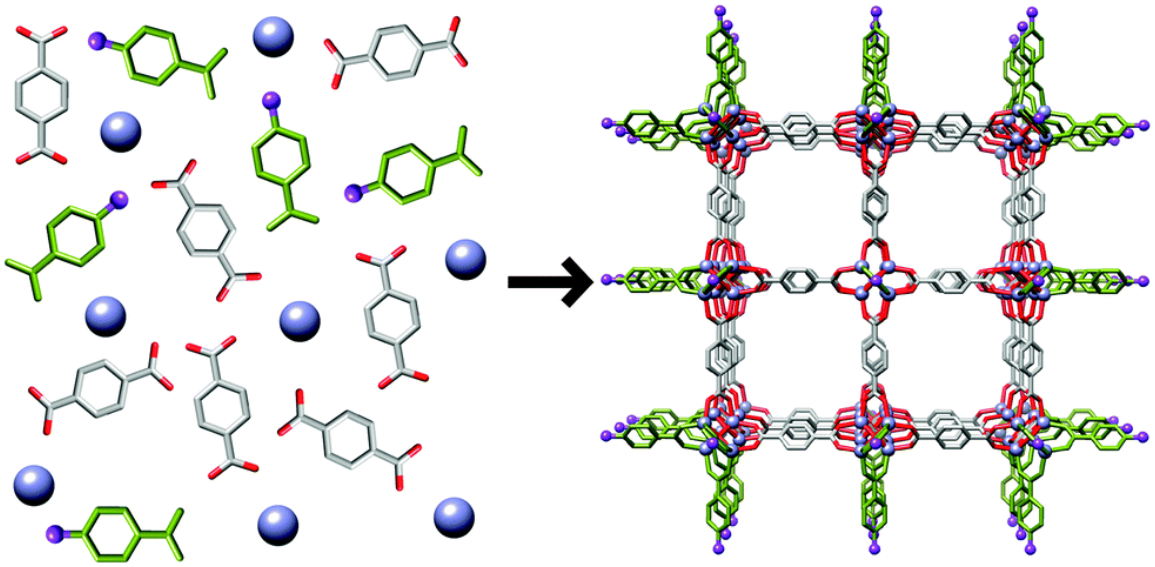

Figure 1.21. Schematic representation of coordination modulation, in this example monocarboxylates cap the surface of MOF-5.[81]

The incorporation of these monotopic ligands can also create defect sites within a framework, where they replace bridging linkers. The most well-known example is UiO-66 which has a 12-connected Zr_6O_8 cluster, and consequently can tolerate a large number of these defects and still retain a rigid porous structure.[89] Depending on the number and geometry of these missing linkers, they can also create missing cluster defects (Figure 1.22a). Modification in this way can be used to create hierarchically porous MOFs,[90] which can have enhanced gas sorption properties relative to the parent framework. The existence of these defects is often inferred from bulk-phase characterisation techniques, such as PXRD, gas-sorption data, and TGA,[89,91,92] but recent developments in low-dose high-resolution transmission electron microscopy (HRTEM) have enabled the direct visualisation of these defects in UiO-66.[93] Unlike conventional crystallography, which only gives an average unit cell across an entire crystal, this technique enables resolution of sub-unit-cells within a single crystallite, allowing individual defects to be mapped out and solved using electron crystallography (Figure 1.22b).[93] This innovative technique will no doubt enable a detailed study of defectivity in other MOF systems, which will result in a better understanding of the nature and tendency of different types of defects in these solids.

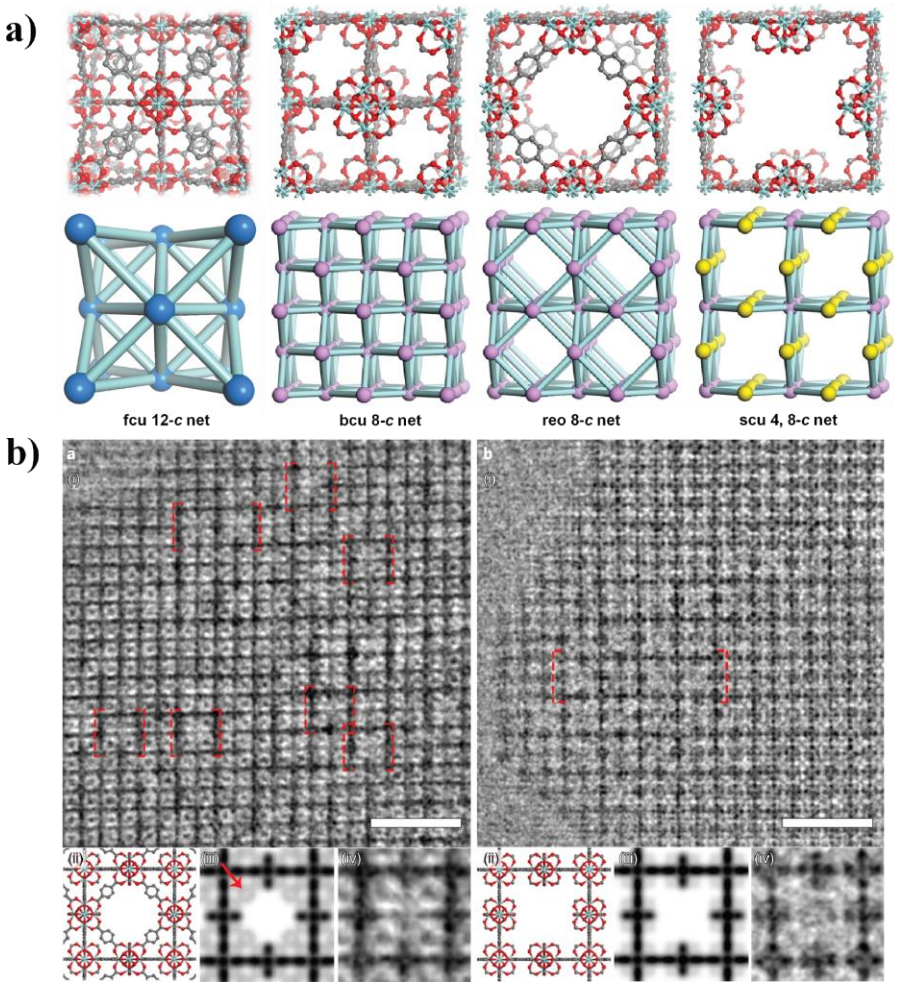

Figure 1.22. Crystal models (top) and topological representations (bottom) of the perfect (**fcu** 12-*c* net) and defective structures of UiO-66, b) HRTEM images (scale bars, 5 nm) of defective UiO-66, highlighting defective regions with **reo** (left) and **scu** unit cells.[93]

1.4.3 Kinetic Phase-Tuning

As was explored in Section 1.3 , there can be multiple phases obtained from the same metal source and linker, and thus the synthesis conditions can require more attention to ensure phase-purity. A good illustrative example is seen with the vanadium-terephthalate frameworks MIL-101(V), MIL-88B(V), and MIL-47(V).[28] All three MOFs can be synthesised from the same synthetic mixture, but the synthesis temperature and time could be controlled to tune between them. MIL-101(V) was identified experimentally as the kinetic product relative to its polymorph MIL-88B(V) (Figure 1.23a), as it dominates when lower temperatures and shorter reaction times are employed (Figure 1.23b). This is consistent with the structure of MIL-101 which is much more complex and possesses very large pores, which are energetically unfavourable, while MIL-88B has a simpler structure and has the default topology for connecting trigonal prisms. Unsurprisingly, MIL-88B(V) is therefore the

predominant phase at higher temperature but converts into MIL-47(V) (which is isoreticular to MIL-53) when the synthesis time is extended. The condensed $[M(OH)(RCO_2)_2]$ chain SBU in MIL-47/53 is a more stable framework component than the $[M_3O(RCO_2)_6(H_2O)_2X]$ SBU found in the other two frameworks, making it the overall thermodynamic product (Figure 1.23a).

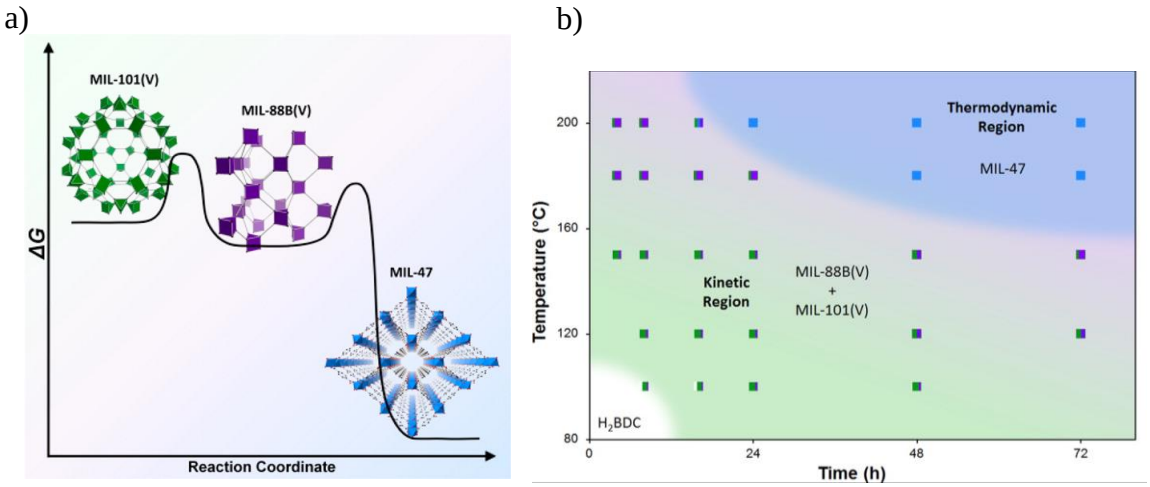

Figure 1.23. a) Diagram of the synthesis of vanadium-terephthalates, showing the relative free energy of each polymorph, b) product synthesis diagrams for vanadium MOFs with temperature and time.[28]

Modulators, which have already been discussed for tuning crystal size and functionality, can also be used to tune the phase by influencing the kinetics of self-assembly. Adding benzoic acid to the synthesis of MIL-101(Cr) decreases the crystal size when low equivalents were added, but at higher concentrations (≥5 molar equivalents) stimulates the growth of MIL-88B(Cr), which could be identified by SEM (Figure 1.24).[94] It is likely that the modulating role of benzoic acid, which facilitates rearrangement during self-assembly, enables MIL-101(Cr) to transform into the more stable MIL-88B(Cr). A similar phase tuning effect was also reported for the vanadium analogues when increasing the HCl concentration, lowering the pH and thus slowing down linker deprotonation, ultimately favouring MIL-88B(V) over MIL-101(V).[28] The same transformation is not seen in unmodulated syntheses of the Cr analogues when the heating time is extended, going straight from MIL-101(Cr) to MIL-53(Cr),[95] which suggests that benzoic acid also acts to stabilise the $[Cr_3O(RCO_2)_6(H_2O)_2X]$ cluster against decomposition into the $[Cr(OH)(RCO_2)_2]$ SBU found in MIL-53(Cr). A related example of phase tuning using acetic acid as a modulator has recently been demonstrated in the microwave synthesis of Zr-terephthalates.[96] The addition of 10 equivalents of acetic acid favoured the formation of MIL-140A, a thermodynamic phase

with formula [ZrO(BDC)],[31] over the kinetic phase UiO-66 at much lower temperature than had previously been reported.[96]

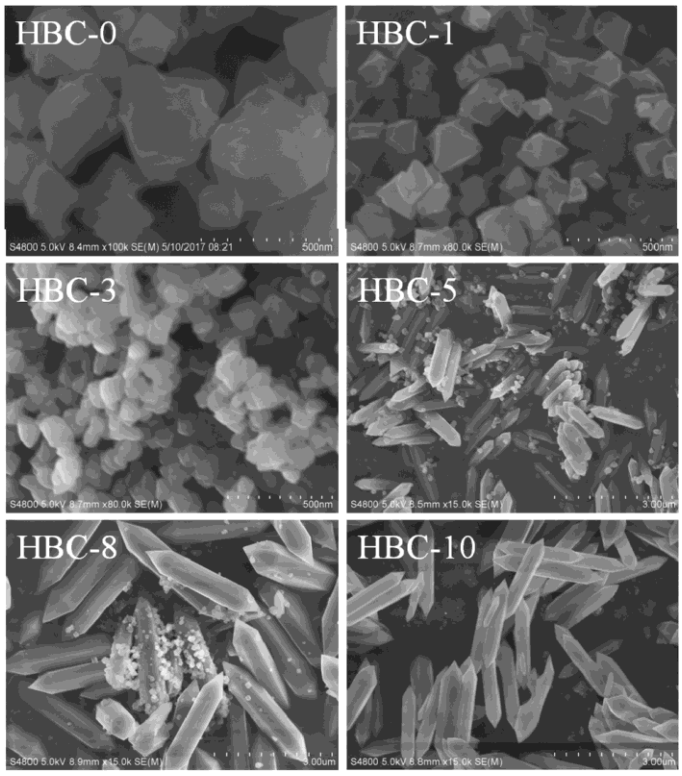

Figure 1.24. SEM images of products obtained from the synthesis of chromium-terephthalate with different molar equivalents of benzoic acid (HBC).[94]

1.4.4 Preformed Cluster Approach

As discussed in Section 1.2.2 , framework design relies on knowledge of the building blocks which will come together during the self-assembly process. This is still largely a trial-and-error process, which is contingent on the desired SBU forming under the synthesis conditions. One way to control this process is to use a preformed cluster, which is preserved in whole or part during self-assembly to provide the desired SBU and therefore control the topology of the product.

This approach was used to prepare the isoreticular Fe^{3+} MOFs MIL-88A (fumarate) and MIL-89 (muconate) using the robust[97] $[Fe_3(\mu_3\text{-}O)(CH_3COO)_6(H_2O)_3]Cl$ cluster as metal precursor.[98] Because both the capping ligands around the cluster and the framework linkers have the same carboxyl coordinating groups, MOF formation can proceed via substitution of the acetates by bridging dicarboxylates. The preformed cluster approach has also shown to be crucial for crystallising Ti^{4+} MOFs, which have proven to be extremely challenging due to the high reactivity of Ti^{4+} and its susceptibility to hydrolysis.[99,100] Typically, these

titanium clusters are not preserved entirely but show enhanced resilience to hydrolysis compared to more simple precursors. When combined with modulation, the preformed cluster approach has also been shown to be highly successful for growing single crystals of Fe-MOFs with the $[Fe_3(\mu_3\text{-}O)(CH_3COO)_6]$ SBU and can prevent the formation of competing phases.[68] It should be noted here that modulation likely also favours the formation of the corresponding modulator-capped SBU prior to synthesis, even when starting from other metal precursors, but is a less controllable method.

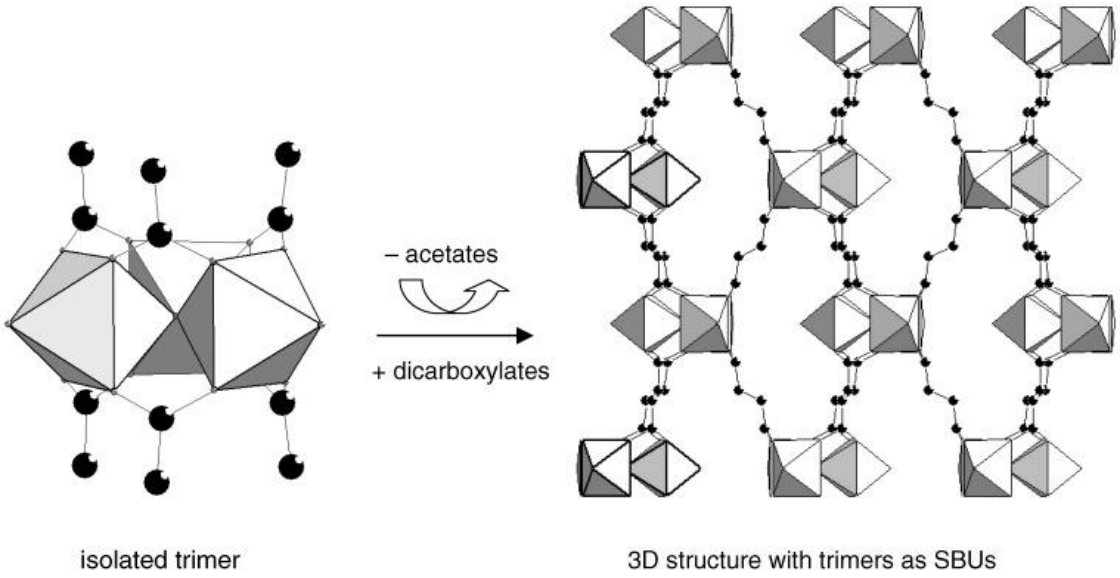

Figure 1.25. Schematic representation of a preformed cluster approach using trimeric SBUs with MIL-88 given as an example.[98]

Another area where this is advantageous is in the design of mixed-metal frameworks, which are desirable due to certain enhanced chemical properties. Conventionally, their synthesis involves the combination of different metal salts, but typically suffers from an inability to control the distribution of the metals to ensure a single phase is formed.[101] To this end the preformed SBU approach is more versatile as a given MOF can be prepared from a robust multimetallic cluster, ensuring the desired topology with perfectly distributed metal sites. This has been used to prepare bimetallic MOFs with $[Fe_2M(\mu_3\text{-}O)(H_2O)_2(CH_3COO)_6]$ clusters (where M = Co^{2+}, Ni^{2+}, Mg^{2+}, Zn^{2+}, or Mn^{2+}).[68,101,102] The introduction of Ni^{2+} sites into MIL-127(Fe) using this approach greatly enhances its CO_2 adsorption capacity relative to the pure Fe material, as the divalent cations are coordinately unsaturated and thus are free to act as strong Lewis acid adsorption sites (Figure 1.26).[102]

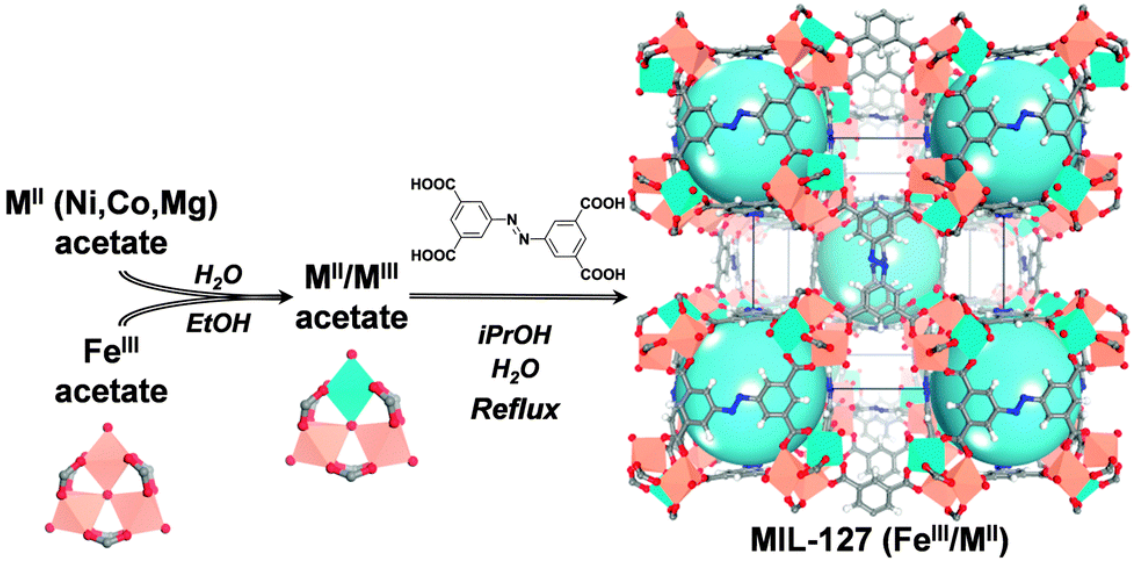

Figure 1.26. Schematic representation of the preparation of mixed-metal oxo-centred clusters and their combination with ABTC to form MIL-127(Fe^{III}/M^{II}).[102]

1.4.5 Summary

As has been discussed, modulators are an exceptionally powerful innovation for MOF synthesis and crucial for the development of high valent MOFs. Their ability to tune crystal size in solvothermal synthesis is especially advantageous for growing large single crystals, which are otherwise much more challenging to obtain, and for enhancing colloidal stability for applications where dispersions are needed. Through modulation, one can influence the kinetics of self-assembly to enhance the crystallinity of products and tune between different phases, providing control over bulk properties. Finally, the use of preformed metal clusters in MOF synthesis can help to direct self-assembly, enabling better topological control as well as allowing the SBU to be modified pre-synthesis, which has been particularly useful for designing mixed-metal MOFs. Aspects of all these synthetic approaches will be explored in the next three chapters in which they are implemented to regulate the crystallisation of Fe^{3+} and Cr^{3+} carboxylate frameworks.

1.5 Biomedical Application of MOFs

There has been considerable interest in utilising MOFs in biomedical applications, typically as nanocarriers in drug delivery but also as imaging agents. The poor solubility of many potent anticancer drugs still prevents their application in cancer therapy, and thus efforts have been made to conjugate or encapsulate these drugs within a nanocarrier to enable intravenous administration. To this end MOFs are good candidates due to their tuneable crystal size and porous nature, which could enable high drug loading and transport to targeted cells.[4,103]

1.5.1 Cytotoxicity

One of the drawbacks associated with MOFs is their toxicity, which varies depending on the nature of both the metal and linker. MOFs based on iron(III) have been found to exhibit relatively low toxicity through both *in vitro* and *in vivo* studies.[59,104] This is unsurprising, as iron(III) is endogenous to mammalian organisms and involved in many biological functions, most saliently transporting oxygen as haemoglobin in red blood cells. A comprehensive *in vitro* study of the cytotoxicity of a range of Fe-MOFs showed that they are on average an order of magnitude less toxic than ZIF-8 (a Zn^{2+} based MOF) and UiO-66 (a Zr^{4+} based MOF),[59] both of which have also been proposed as potential drug carriers. Within these Fe-MOFs, their toxicities were correlated with the hydrophobicity of the constituent linker, with a higher hydrophobicity correlating with a greater cytotoxic effect. To validate the biocompatibility of MOFs, their constituent parts (linker and metal) also need to be tested as they will be released if degradation occurs in the body.

1.5.2 Drug Loading and Release

For effective use in therapy, MOFs need to be loaded with medically relevant drugs. MOFs are unique in that there are many ways in which drugs can be loaded, either within their pores or attached to particle surfaces, via:

1. Coordination to metal sites
2. Covalent attachment to linker or monodentate ligands
3. Intermolecular interactions with framework (van der Waals, hydrogen bonding, etc.)
4. Weak interactions (pore filling, adhesion to external surface)

Depending on how drugs are bound to the framework, the kinetics of loading and release will differ significantly. This has been demonstrated by Férey et al. who have studied the loading and release of ibuprofen in MIL-101(Cr)[105] as well as the Fe and Cr analogues of MIL-53.[106] The loading capacity exhibited by the large pore MIL-101_IBU framework is exceptionally high (138 wt.%) compared to MIL-53_IBU (20 wt.%), but the kinetics of release are much faster during the initial stages with ~40% of weakly bound ibuprofen released in the first 24 hours (Figure 1.27); this is known as 'burst release'. In contrast, the flexible structure of MIL-53 adapts to maximise the interactions with ibuprofen and form hydrogen bonds, which led to a slower release with zero-order kinetics. A controlled drug release such as is shown by MIL-53_IBU is beneficial as it provides more time for nanocarriers to reach tumours or other target tissues, enabling greater delivery to these areas, and also prolongs the therapy time, which in turn reduces the frequency of treatments required.

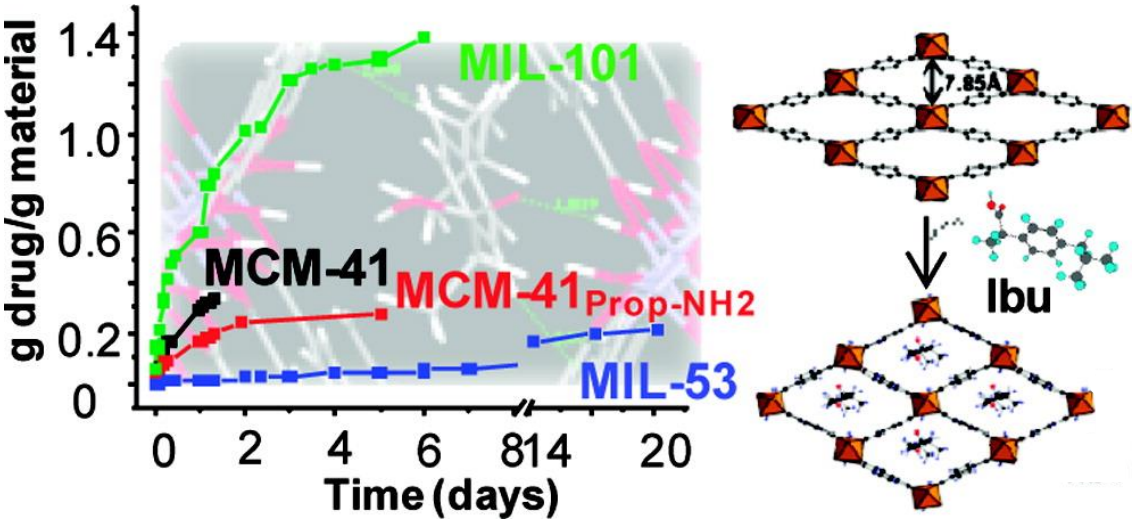

Figure 1.27. (Left) Comparison of ibuprofen release from MIL-53, MIL-101, and MCM-41 (mesoporous silica), (Right) scheme of encapsulation of ibuprofen in MIL-53 and the concomitant structural transformation.[106]

1.5.3 Surface Coating

Another way of addressing the burst release phenomenon and controlling the release from MOFs is to coat the outer surface with an external layer, known as a corona (Figure 1.28a), added to hinder the release of bound drug molecules. In the context of drug delivery, surface coating can also be used to reduce particle aggregation and thus prolong suspension, which helps to prevent build up in blood vessels. The attachment of polymer coatings such as polyethylene glycol (PEG) has proven to enhance the stability of MOFs in suspension in this

way.[88] These types of modification can be achieved using coordination modulation; coatings of PEG could be added to MIL-88A and MIL-89 by addition of PEG chains with an amine terminal group directly to the synthesis mixture as a modulator.[60] A similar result has been also been achieved via click modulation, whereby functionalised modulators are first incorporated during synthesis and then modified post-synthetically, to covalently attach PEG chains to the surface of UiO-66.[88] This slowed the release of the cargo (calcein) and introduced a pH-triggered mechanism which enhances release in acidic media (Figure 1.28b). The diverse range of modification routes is a consequence of the rich surface chemistry of MOFs, which make them ideal cores for complex drug delivery systems which can be tailored for different therapies.

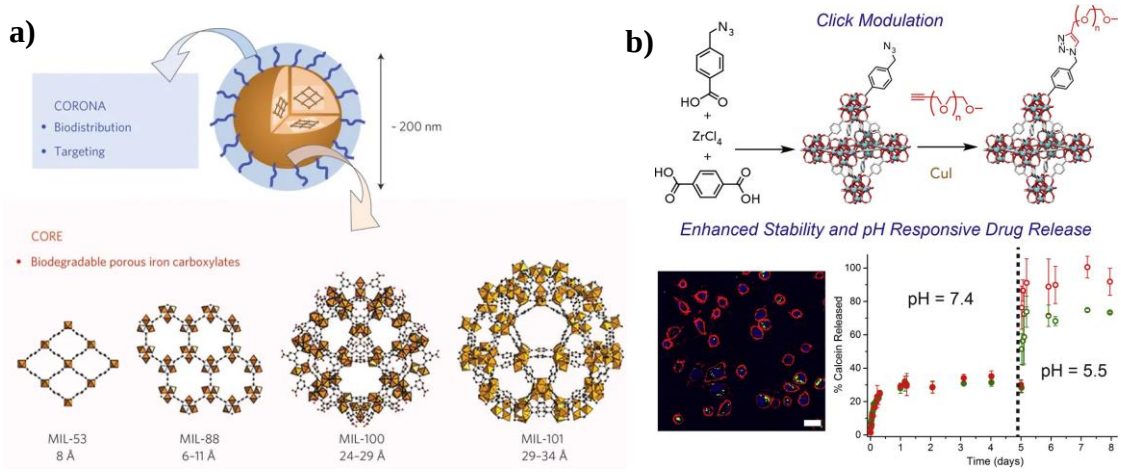

Figure 1.28. a) Scheme of core-corona MOF particles,[60] b) scheme of click modulation to construct PEGylated UiO-66 with enhanced colloidal stability and pH responsive release.[88]

1.5.4 Summary

To summarise, MOFs are promising materials for use in biomedicine and there are several candidates which meet the requirements of biocompatibility as well as demonstrating tunability for enhanced drug release. As we have already mentioned, our focus for synthetic work was originally centred around Fe-MOFs, which appeared to be amongst the most biocompatible frameworks. However, we also identified that Cr-based MOFs, despite the stigma associated and dearth of *in vitro* or *in vivo* studies, may also be viable candidates for use in biomedical applications. This serendipitously tied in with synthetic work we were already carrying out to crystallise new Cr^{3+}-carboxylate MOFs, and thus an in-depth study of their biocompatibility and internalisation is presented in Chapter 5.

1.6 Conclusions and Outlook

In this chapter I have attempted to provide a perspective on the synthesis of trivalent metal-organic frameworks and their potential application in biomedicine. The diversity in structure for M^{3+}-carboxylates has been explored and, while this yields a range of solids with desirable properties, it also poses some specific challenges for synthesis: multiple competing phases can crystallise under relatively similar conditions, resulting in phase impurities. The addition of modulating agents perturbs the kinetics of self-assembly during MOF synthesis, as evidenced by their ability to regulate crystal growth, but this methodology has not been fully explored as a tool for phase-tuning. Hence, I propose that modulation could be a versatile strategy for synergistically enhancing crystallinity and enabling kinetic phase tuning in the synthesis of trivalent MOFs, and I will attempt to prove this part of my thesis in the next three chapters.

1.7 References

(1) Batten, S. R., Champness, N. R., Chen, X.-M., Garcia-Martinez, J., Kitagawa, S., Öhrström, L., O'Keeffe, M., Suh, M. P. and Reedijk, J., *CrystEngComm*, **2012**, *14*, 3001-3004.

(2) Yang, D. and Gates, B. C., *ACS Catalysis*, **2019**, *9*, 1779-1798.

(3) Schoedel, A., Ji, Z. and Yaghi, O. M., *Nature Energy*, **2016**, *1*, 16034.

(4) Horcajada, P., Gref, R., Baati, T., Allan, P. K., Maurin, G., Couvreur, P., Férey, G., Morris, R. E. and Serre, C., *Chem. Rev.*, **2012**, *112*, 1232-1268.

(5) Li, H., Eddaoudi, M., O'Keeffe, M. and Yaghi, O. M., *Nature*, **1999**, *402*, 276-279.

(6) Kaye, S. S., Dailly, A., Yaghi, O. M. and Long, J. R., *J. Am. Chem. Soc.*, **2007**, *129*, 14176-14177.

(7) McKinstry, C., Cathcart, R. J., Cussen, E. J., Fletcher, A. J., Patwardhan, S. V. and Sefcik, J., *Chem. Eng. J.*, **2016**, *285*, 718-725.

(8) Li, M., Li, D., O'Keeffe, M. and Yaghi, O. M., *Chem. Rev.*, **2014**, *114*, 1343-1370.

(9) Chui, S. S.-Y., Lo, S. M.-F., Charmant, J. P. H., Orpen, A. G. and Williams, I. D., *Science*, **1999**, *283*, 1148-1150.

(10) Eddaoudi, M., Kim, J., Rosi, N., Vodak, D., Wachter, J., O'Keeffe, M. and Yaghi, O. M., *Science*, **2002**, *295*, 469-472.

(11) Wang, Z., Tanabe, K. K. and Cohen, S. M., *Chem. Eur. J.*, **2010**, *16*, 212-217.

(12) Tanabe, K. K., Wang, Z. and Cohen, S. M., *J. Am. Chem. Soc.*, **2008**, *130*, 8508-8517.

(13) Haldar, R., Sikdar, N. and Maji, T. K., *Mater. Today*, **2015**, *18*, 97-116.

(14) Yang, S., Lin, X., Lewis, W., Suyetin, M., Bichoutskaia, E., Parker, J. E., Tang, C. C., Allan, D. R., Rizkallah, P. J., Hubberstey, P., Champness, N. R., Mark Thomas, K., Blake, A. J. and Schröder, M., *Nat. Mater.*, **2012**, *11*, 710-716.

(15) Yuan, B., Ma, D., Wang, X., Li, Z., Li, Y., Liu, H. and He, D., *Chem. Commun.*, **2012**, *48*, 1135-1137.

(16) Ugale, B., Dhankhar, S. S. and Nagaraja, C. M., *Inorg. Chem.*, **2016**, *55*, 9757-9766.

(17) Rankine, D., Avellaneda, A., Hill, M. R., Doonan, C. J. and Sumby, C. J., *Chem. Commun.*, **2012**, *48*, 10328-10330.

(18) Ma, S. and Zhou, H.-C., *Chem. Commun.*, **2010**, *46*, 44-53.

(19) Suh, M. P., Park, H. J., Prasad, T. K. and Lim, D.-W., *Chem. Rev.*, **2012**, *112*, 782-835.

(20) Han, S. S., Jung, D.-H. and Heo, J., *J. Phys. Chem. C*, **2013**, *117*, 71-77.

(21) Bara, D. J., Wilson, C., Mörtel, M., Khusniyarov, M. M., Ling, S., Slater, B., Sproules, S. and Forgan, R. S., *J. Am. Chem. Soc.*, **2019**.

(22) Goesten, M. G., Magusin, P. C. M. M., Pidko, E. A., Mezari, B., Hensen, E. J. M., Kapteijn, F. and Gascon, J., *Inorg. Chem.*, **2014**, *53*, 882-887.

(23) Devic, T. and Serre, C., *Chem. Soc. Rev.*, **2014**, *43*, 6097-6115.

(24) Anson, C. E., Bourke, J. P., Cannon, R. D., Jayasooriya, U. A., Molinier, M. and Powell, A. K., *Inorg. Chem.*, **1997**, *36*, 1265-1267.

(25) Senkovska, I., Hoffmann, F., Fröba, M., Getzschmann, J., Böhlmann, W. and Kaskel, S., *Microporous Mesoporous Mater.*, **2009**, *122*, 93-98.

(26) Sudik, A. C., Côté, A. P. and Yaghi, O. M., *Inorg. Chem.*, **2005**, *44*, 2998-3000.

(27) Surble, S., Serre, C., Mellot-Draznieks, C., Millange, F. and Férey, G., *Chem. Commun.*, **2006**, 284-286.

(28) Carson, F., Su, J., Platero-Prats, A. E., Wan, W., Yun, Y., Samain, L. and Zou, X., *Cryst. Growth Des.*, **2013**, *13*, 5036-5044.

(29) Horcajada, P., Salles, F., Wuttke, S., Devic, T., Heurtaux, D., Maurin, G., Vimont, A., Daturi, M., David, O., Magnier, E., Stock, N., Filinchuk, Y., Popov, D., Riekel, C., Férey, G. and Serre, C., *J. Am. Chem. Soc.*, **2011**, *133*, 17839-17847.

(30) Mowat, J. P. S., Miller, S. R., Slawin, A. M. Z., Seymour, V. R., Ashbrook, S. E. and Wright, P. A., *Microporous Mesoporous Mater.*, **2011**, *142*, 322-333.

(31) Guillerm, V., Ragon, F., Dan-Hardi, M., Devic, T., Vishnuvarthan, M., Campo, B., Vimont, A., Clet, G., Yang, Q., Maurin, G., Férey, G., Vittadini, A., Gross, S. and Serre, C., *Angew. Chem. Int. Ed.*, **2012**, *51*, 9267-9271.

(32) Stavitski, E., Goesten, M., Juan-Alcañiz, J., Martinez-Joaristi, A., Serra-Crespo, P., Petukhov, A. V., Gascon, J. and Kapteijn, F., *Angew. Chem. Int. Ed.*, **2011**, *50*, 9624-9628.

(33) Goesten, M. G., Stavitski, E., Juan-Alcañiz, J., Martiñez-Joaristi, A., Petukhov, A. V., Kapteijn, F. and Gascon, J., *Catal. Today*, **2013**, *205*, 120-127.

(34) Serre, C., Mellot-Draznieks, C., Surblé, S., Audebrand, N., Filinchuk, Y. and Férey, G., *Science*, **2007**, *315*, 1828-1831.

(35) Schneemann, A., Bon, V., Schwedler, I., Senkovska, I., Kaskel, S. and Fischer, R. A., *Chem. Soc. Rev.*, **2014**, *43*, 6062-6096.

(36) Millange, F., Serre, C. and Férey, G., *Chem. Commun.*, **2002**, 822-823.

(37) Whitfield, T. R., Wang, X., Liu, L. and Jacobson, A. J., *Solid State Sci.*, **2005**, *7*, 1096-1103.

(38) Barthelet, K., Marrot, J., Riou, D. and Férey, G., *Angew. Chem. Int. Ed.*, **2002**, *41*, 281-284.

(39) Loiseau, T., Serre, C., Huguenard, C., Fink, G., Taulelle, F., Henry, M., Bataille, T. and Férey, G., *Chem. Eur. J.*, **2004**, *10*, 1373-1382.

(40) Volkringer, C., Loiseau, T., Guillou, N., Férey, G., Elkaïm, E. and Vimont, A., *Dalton Trans.*, **2009**, 2241-2249.

(41) Anokhina, E. V., Vougo-Zanda, M., Wang, X. and Jacobson, A. J., *J. Am. Chem. Soc.*, **2005**, *127*, 15000-15001.

(42) Mitchell, L., Gonzalez-Santiago, B., Mowat, J. P. S., Gunn, M. E., Williamson, P., Acerbi, N., Clarke, M. L. and Wright, P. A., *Catal. Sci.*, **2013**, *3*, 606-617.

(43) Fateeva, A., Horcajada, P., Devic, T., Serre, C., Marrot, J., Grenèche, J.-M., Morcrette, M., Tarascon, J.-M., Maurin, G. and Férey, G., *Eur. J. Inorg. Chem.*, **2010**, *2010*, 3789-3794.

(44) Barthelet, K., Marrot, J., Férey, G. and Riou, D., *Chem. Commun.*, **2004**, 520-521.

(45) Yang, Q., Vaesen, S., Vishnuvarthan, M., Ragon, F., Serre, C., Vimont, A., Daturi, M., De Weireld, G. and Maurin, G., *J. Mater. Chem.*, **2012**, *22*, 10210-10220.

(46) Volkringer, C., Meddouri, M., Loiseau, T., Guillou, N., Marrot, J., Férey, G., Haouas, M., Taulelle, F., Audebrand, N. and Latroche, M., *Inorg. Chem.*, **2008**, *47*, 11892-11901.

(47) Alvarez, E., Guillou, N., Martineau, C., Bueken, B., Van de Voorde, B., Le Guillouzer, C., Fabry, P., Nouar, F., Taulelle, F., de Vos, D., Chang, J.-S., Cho, K. H., Ramsahye, N., Devic, T., Daturi, M., Maurin, G. and Serre, C., *Angew. Chem. Int. Ed.*, **2015**, *54*, 3664-3668.

(48) Leung, E., Müller, U., Trukhan, N., Mattenheimer, H., Cox, G. and Blei, S., E. P. Office, **2013**, 11828228.4.

(49) Loiseau, T., Mellot-Draznieks, C., Muguerra, H., Férey, G., Haouas, M. and Taulelle, F., *Comptes Rendus Chimie*, **2005**, *8*, 765-772.

(50) Lo, S.-H., Chien, C.-H., Lai, Y.-L., Yang, C.-C., Lee, J. J., Raja, D. S. and Lin, C.-H., *J. Mater. Chem. A*, **2013**, *1*, 324-329.

(51) Millange, F., Guillou, N., Walton, R. I., Grenèche, J.-M., Margiolaki, I. and Férey, G., *Chem. Commun.*, **2008**, 4732-4734.

(52) Chen, L., Mowat, J. P. S., Fairen-Jimenez, D., Morrison, C. A., Thompson, S. P., Wright, P. A. and Düren, T., *J. Am. Chem. Soc.*, **2013**, *135*, 15763-15773.

(53) Mowat, J. P. S., Seymour, V. R., Griffin, J. M., Thompson, S. P., Slawin, A. M. Z., Fairen-Jimenez, D., Düren, T., Ashbrook, S. E. and Wright, P. A., *Dalton Trans.*, **2012**, *41*, 3937-3941.

(54) Serre, C., Millange, F., Thouvenot, C., Noguès, M., Marsolier, G., Louër, D. and Férey, G., *J. Am. Chem. Soc.*, **2002**, *124*, 13519-13526.

(55) Férey, G., Serre, C., Mellot-Draznieks, C., Millange, F., Surblé, S., Dutour, J. and Margiolaki, I., *Angew. Chem. Int. Ed.*, **2004**, *43*, 6296-6301.

(56) Férey, G., Mellot-Draznieks, C., Serre, C., Millange, F., Dutour, J., Surblé, S. and Margiolaki, I., *Science*, **2005**, *309*, 2040-2042.

(57) Van de Voorde, B., Bueken, B., Denayer, J. and De Vos, D., *Chem. Soc. Rev.*, **2014**, *43*, 5766-5788.

(58) Horcajada, P., Chevreau, H., Heurtaux, D., Benyettou, F., Salles, F., Devic, T., Garcia-Marquez, A., Yu, C., Lavrard, H., Dutson, C. L., Magnier, E., Maurin, G., Elkaïm, E. and Serre, C., *Chem. Commun.*, **2014**, *50*, 6872-6874.

(59) Tamames-Tabar, C., Cunha, D., Imbuluzqueta, E., Ragon, F., Serre, C., Blanco-Prieto, M. J. and Horcajada, P., *J. Mater. Chem. B*, **2014**, *2*, 262-271.

(60) Horcajada, P., Chalati, T., Serre, C., Gillet, B., Sebrie, C., Baati, T., Eubank, J. F., Heurtaux, D., Clayette, P., Kreuz, C., Chang, J.-S., Hwang, Y. K., Marsaud, V., Bories, P.-N., Cynober, L., Gil, S., Férey, G., Couvreur, P. and Gref, R., *Nat. Mater.*, **2010**, *9*, 172-178.

(61) Buragohain, A., Van Der Voort, P. and Biswas, S., *Microporous Mesoporous Mater.*, **2015**, *215*, 91-97.

(62) Lammert, M., Bernt, S., Vermoortele, F., De Vos, D. E. and Stock, N., *Inorg. Chem.*, **2013**, *52*, 8521-8528.

(63) Sonnauer, A., Hoffmann, F., Fröba, M., Kienle, L., Duppel, V., Thommes, M., Serre, C., Férey, G. and Stock, N., *Angew. Chem.*, **2009**, *121*, 3849-3852.

(64) Feng, D., Liu, T.-F., Su, J., Bosch, M., Wei, Z., Wan, W., Yuan, D., Chen, Y.-P., Wang, X., Wang, K., Lian, X., Gu, Z.-Y., Park, J., Zou, X. and Zhou, H.-C., *Nat. Comm.*, **2015**, *6*, 5979.

(65) Belmabkhout, Y., Pillai, R. S., Alezi, D., Shekhah, O., Bhatt, P. M., Chen, Z., Adil, K., Vaesen, S., De Weireld, G., Pang, M., Suetin, M., Cairns, A. J., Solovyeva, V.,

Shkurenko, A., El Tall, O., Maurin, G. and Eddaoudi, M., *J. Mater. Chem. A*, **2017**, *5*, 3293-3303.

(66) Chevreau, H., Permyakova, A., Nouar, F., Fabry, P., Livage, C., Ragon, F., Garcia-Marquez, A., Devic, T., Steunou, N., Serre, C. and Horcajada, P., *CrystEngComm*, **2016**, *18*, 4094-4101.

(67) Dhakshinamoorthy, A., Alvaro, M., Chevreau, H., Horcajada, P., Devic, T., Serre, C. and Garcia, H., *Catal. Sci.*, **2012**, *2*, 324-330.

(68) Feng, D., Wang, K., Wei, Z., Chen, Y.-P., Simon, C. M., Arvapally, R. K., Martin, R. L., Bosch, M., Liu, T.-F., Fordham, S., Yuan, D., Omary, M. A., Haranczyk, M., Smit, B. and Zhou, H.-C., *Nat. Comm.*, **2014**, *5*, 5723.

(69) Alezi, D., Belmabkhout, Y., Suyetin, M., Bhatt, P. M., Weseliński, Ł. J., Solovyeva, V., Adil, K., Spanopoulos, I., Trikalitis, P. N., Emwas, A.-H. and Eddaoudi, M., *J. Am. Chem. Soc.*, **2015**, *137*, 13308-13318.

(70) Towsif Abtab, S. M., Alezi, D., Bhatt, P. M., Shkurenko, A., Belmabkhout, Y., Aggarwal, H., Weseliński, Ł. J., Alsadun, N., Samin, U., Hedhili, M. N. and Eddaoudi, M., *Chem*, **2018**, *4*, 94-105.

(71) Huskić, I., Pekov, I. V., Krivovichev, S. V. and Friščić, T., *Sci. Adv.*, **2016**, *2*, e1600621.

(72) Park, K. S., Ni, Z., Côté, A. P., Choi, J. Y., Huang, R., Uribe-Romo, F. J., Chae, H. K., O'Keeffe, M. and Yaghi, O. M., *Proc. Natl. Acad. Sci. U.S.A.*, **2006**, *103*, 10186-10191.

(73) Pan, Y., Liu, Y., Zeng, G., Zhao, L. and Lai, Z., *Chem. Commun.*, **2011**, *47*, 2071-2073.

(74) Zhao, Y., Song, Z., Li, X., Sun, Q., Cheng, N., Lawes, S. and Sun, X., *Energy Stor. Mater.*, **2016**, *2*, 35-62.

(75) Li, Y., Liu, Y., Gao, W., Zhang, L., Liu, W., Lu, J., Wang, Z. and Deng, Y.-J., *CrystEngComm*, **2014**, *16*, 7037-7042.

(76) Pichon, A., Lazuen-Garay, A. and James, S. L., *CrystEngComm*, **2006**, *8*, 211-214.

(77) Cundy, C. S. and Cox, P. A., *Chem. Rev.*, **2003**, *103*, 663-702.

(78) Caullet, P., Paillaud, J.-L., Simon-Masseron, A., Soulard, M. and Patarin, J., *Comptes Rendus Chimie*, **2005**, *8*, 245-266.

(79) Horcajada, P., Surblé, S., Serre, C., Hong, D.-Y., Seo, Y.-K., Chang, J.-S., Grenèche, J.-M., Margiolaki, I. and Férey, G., *Chem. Commun.*, **2007**, 2820-2822.

(80) Doran, M. B., Cockbain, B. E., Norquist, A. J. and O'Hare, D., *Dalton Trans.*, **2004**, 3810-3814.

(81) McGuire, C. V. and Forgan, R. S., *Chem. Commun.*, **2015**, *51*, 5199-5217.

(82) Guo, Y., Zhang, J., Dong, L.-Z., Xu, Y., Han, W., Fang, M., Liu, H.-K., Wu, Y. and Lan, Y.-Q., *Chem. Eur. J.*, **2017**, *23*, 15518-15528.

(83) Han, Y., Liu, M., Li, K., Zuo, Y., Wei, Y., Xu, S., Zhang, G., Song, C., Zhang, Z. and Guo, X., *CrystEngComm*, **2015**, *17*, 6434-6440.

(84) Surblé, S., Millange, F., Serre, C., Düren, T., Latroche, M., Bourrelly, S., Llewellyn, P. L. and Férey, G., *J. Am. Chem. Soc.*, **2006**, *128*, 14889-14896.

(85) Schaate, A., Roy, P., Godt, A., Lippke, J., Waltz, F., Wiebcke, M. and Behrens, P., *Chem. Eur. J.*, **2011**, *17*, 6643-6651.

(86) Marshall, R. J., Hobday, C. L., Murphie, C. F., Griffin, S. L., Morrison, C. A., Moggach, S. A. and Forgan, R. S., *J. Mater. Chem. A*, **2016**, *4*, 6955-6963.

(87) Morris, W., Wang, S., Cho, D., Auyeung, E., Li, P., Farha, O. K. and Mirkin, C. A., *ACS Appl. Mater. Interfaces*, **2017**, *9*, 33413-33418.

(88) Abánades Lázaro, I., Haddad, S., Sacca, S., Orellana-Tavra, C., Fairen-Jimenez, D. and Forgan, R. S., *Chem*, **2017**, *2*, 561-578.

(89) Shearer, G. C., Chavan, S., Bordiga, S., Svelle, S., Olsbye, U. and Lillerud, K. P., *Chem. Mater.*, **2016**, *28*, 3749-3761.

(90) Cai, G. and Jiang, H.-L., *Angew. Chem. Int. Ed.*, **2017**, *56*, 563-567.

(91) Wu, H., Chua, Y. S., Krungleviciute, V., Tyagi, M., Chen, P., Yildirim, T. and Zhou, W., *J. Am. Chem. Soc.*, **2013**, *135*, 10525-10532.

(92) Gutov, O. V., Hevia, M. G., Escudero-Adán, E. C. and Shafir, A., *Inorg. Chem.*, **2015**, *54*, 8396-8400.

(93) Liu, L., Chen, Z., Wang, J., Zhang, D., Zhu, Y., Ling, S., Huang, K.-W., Belmabkhout, Y., Adil, K., Zhang, Y., Slater, B., Eddaoudi, M. and Han, Y., *Nat. Chem.*, **2019**, *11*, 622-628.

(94) Yang, L., Zhao, T., Boldog, I., Janiak, C., Yang, X.-Y., Li, Q., Zhou, Y.-J., Xia, Y., Lai, D.-W. and Liu, Y.-J., *Dalton Trans.*, **2019**, *48*, 989-996.

(95) Khan, N. A. and Jhung, S. H., *Cryst. Growth Des.*, **2010**, *10*, 1860-1865.

(96) Griffin, S., Briuglia, M., ter Horst, J. and Forgan, R. S., *Chem. Eur. J.*, **2020**, *n/a*.

(97) Surblé, S., Millange, F., Serre, C., Férey, G. and Walton, R. I., *Chem. Commun.*, **2006**, 1518-1520.

(98) Serre, C., Millange, F., Surblé, S. and Férey, G., *Angew. Chem. Int. Ed.*, **2004**, *43*, 6285-6289.

(99) Castells-Gil, J., M. Padial, N., Almora-Barrios, N., da Silva, I., Mateo, D., Albero, J., García, H. and Martí-Gastaldo, C., *Chemical Science*, **2019**, *10*, 4313-4321.

(100) Zou, L., Feng, D., Liu, T.-F., Chen, Y.-P., Yuan, S., Wang, K., Wang, X., Fordham, S. and Zhou, H.-C., *Chemical Science*, **2016**, *7*, 1063-1069.

(101) Peng, L., Asgari, M., Mieville, P., Schouwink, P., Bulut, S., Sun, D. T., Zhou, Z., Pattison, P., van Beek, W. and Queen, W. L., *ACS Appl. Mater. Interfaces*, **2017**, *9*, 23957-23966.

(102) Wongsakulphasatch, S., Nouar, F., Rodriguez, J., Scott, L., Le Guillouzer, C., Devic, T., Horcajada, P., Grenèche, J. M., Llewellyn, P. L., Vimont, A., Clet, G., Daturi, M. and Serre, C., *Chem. Commun.*, **2015**, *51*, 10194-10197.

(103) Sun, C.-Y., Qin, C., Wang, X.-L. and Su, Z.-M., *Expert Opinion on Drug Delivery*, **2013**, *10*, 89-101.

(104) Baati, T., Njim, L., Neffati, F., Kerkeni, A., Bouttemi, M., Gref, R., Najjar, M. F., Zakhama, A., Couvreur, P., Serre, C. and Horcajada, P., *Chemical Science*, **2013**, *4*, 1597-1607.

(105) Horcajada, P., Serre, C., Vallet-Regí, M., Sebban, M., Taulelle, F. and Férey, G., *Angew. Chem. Int. Ed.*, **2006**, *45*, 5974-5978.

(106) Horcajada, P., Serre, C., Maurin, G., Ramsahye, N. A., Balas, F., Vallet-Regí, M., Sebban, M., Taulelle, F. and Férey, G., *J. Am. Chem. Soc.*, **2008**, *130*, 6774-6780.

Chapter 2

Kinetic Control of Interpenetration in Fe-BPDC MOFs

This Chapter is adapted from the following publication:

Kinetic Control of Interpenetration in Fe–Biphenyl-4,4′-dicarboxylate Metal–Organic Frameworks by Coordination and Oxidation Modulation

J. Am. Chem. Soc. **2019**, 14, 120, 8346-8357.

Dominic Bara, Claire Wilson, Max Mörtel, Marat M. Khusniyarov, Sanliang Ling, Ben Slater, Stephen Sproules, Ross S. Forgan

Contributions

All the synthetic work in this chapter was carried out by me. Single-crystal data collection and structure refinement for **3** and **4** were carried out by Claire Wilson (University of Glasgow). DFT studies were carried out jointly by Ben Slater (University College London) and Sanliang Ling (University of Nottingham). Mössbauer spectroscopy was carried out and processed by Stephen Sproules (University of Glasgow), Max Mörtel (University of Erlangen-Nuremberg), and Marat M. Khusniyarov (University of Erlangen-Nuremberg).

Contents

Chapter 2 ..... **41**

2.1 Introduction **44**

2.2 Aims **47**

2.3 Synthesis of Fe-BPDC MOFs (1) **48**

2.4 Modulation of Fe-BPDC MOFs (1) **57**

2.4.1 Acetic Acid (AA) 57

2.4.2 Optimum Modulator Concentrations 60

2.4.3 Formic Acid (FA) 62

2.4.4 Hydrochloric Acid (HCl) 63

2.4.5 Dichloroacetic Acid (DCA) 66

2.4.6 Trifluoroacetic Acid (TFA) 67

2.4.7 Benzoic Acid (BA) 68

2.4.8 Summary 69

2.5 Synthesis of Fe-BPYDC MOFs (2) **70**

2.6 Solvothermal Synthesis of Fe-BPDC MOFs (1′) **78**

2.7 Conclusions **82**

2.8 Experimental **84**

2.8.1 General Experimental Methods 84

2.8.2 Solvothermal Synthesis of 1 85

2.8.3 Microwave Synthesis of 1 85

2.8.4 Synthesis of 2 85

2.8.5 Synthesis of Fe-BPDC MOFs using Fe^{2+} 86

2.8.6 Synthesis of $Fe_3O(OAc)_6$ cluster 86

2.8.7 Synthesis of 3 and 4 87

2.8.8 Crystal data for 3 87

2.8.9 Crystal data for 4 87

2.9 References **88**

2.1 Introduction

Metal-organic frameworks based on iron have attracted attention for bio-applications due to the endogenous nature of iron in the body, which makes them desirable as benign carriers for therapeutic drugs.[1,2] For most applications, size control of crystallites is desirable as it will dictate their colloidal stability, which in a biological context will influence their stability in the bloodstream and prevent agglomeration. Coordination modulation, the addition of monocarboxylates to the synthesis mixture, has proven to be an effective strategy for tuning the crystal size of MOFs and works by competition between the modulator and the bridging linker to slow down the self-assembly process.[3]

MOFs containing iron and linear dicarboxylate linkers tend to form structures in the MIL-88 series of frameworks and exhibit significant flexibility upon the adsorption or evacuation of solvent from the pores (Figure 2.1a). The MOF constructed from iron and biphenyl-4,4′-dicarboxylate (BPDC) adopts an interpenetrated structure (known as MIL-126(Fe)) consisting of two MIL-88D type nets (Figure 2.1b), making it highly rigid due to the inability of either net to significantly contract. MIL-126(Fe) has been identified as a desirable material for heterogenous catalysis, owing to its permanent porosity and accessible Lewis acid sites. Despite the interest in this material, all of the reported syntheses yield material with significantly lower porosity than the theoretical value (SA_{BET} = 2550 m^2g^{-1}).[4] It is also not clear how to control between MIL-126(Fe) and its non-interpenetrated counterpart MIL-88D(Fe) during synthesis, which has only been reported with functionalised BPDC linkers. The lack of a comprehensive study on the synthesis of this MOF was the impetus for us to carry out our own investigation using coordination modulation, among other methods, to perturb the crystallisation process.

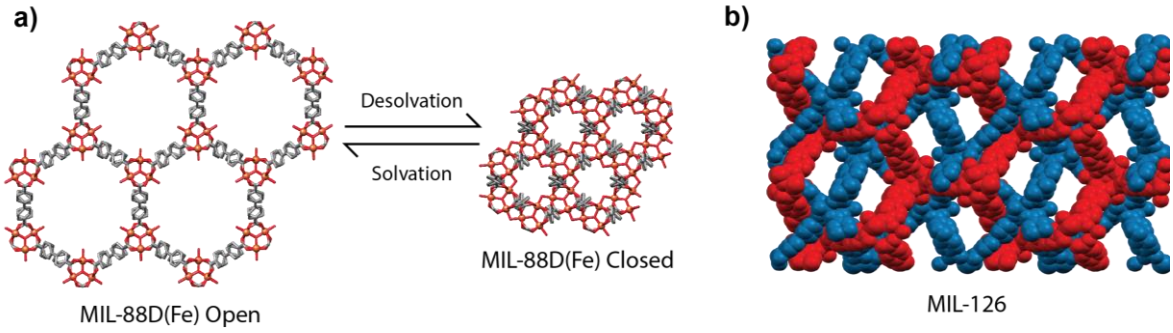

Figure 2.1. a) Packing structure of MIL-88D(Fe) in the ‘open’ and ‘closed’ pore form as viewed down the *c*-axis, b) Packing structure of MIL-126(Fe) as viewed down the *b*-axis.

DFT studies carried out by collaborators at University College London and the University of Nottingham[5] have investigated the thermodynamic relationships between MIL-88D and MIL-126, which is important to discuss in relationship to our experimental study. Because work published by our group had also looked at the scandium analogues of these MOFs[6], both the Fe and Sc frameworks were used for these calculations. The SBU in both frameworks (Figure 2.2) contains three metals with two water molecules and an anion (presumed to be OH) as capping ligands. For MIL-88D, there is no significant difference in the internal energy of frameworks with different configurations of these capping ligands, and they all fall within a ~1 kJ mol^{-1} window, which is comparable to kT at room temperature (2.5 kJ mol^{-1}).

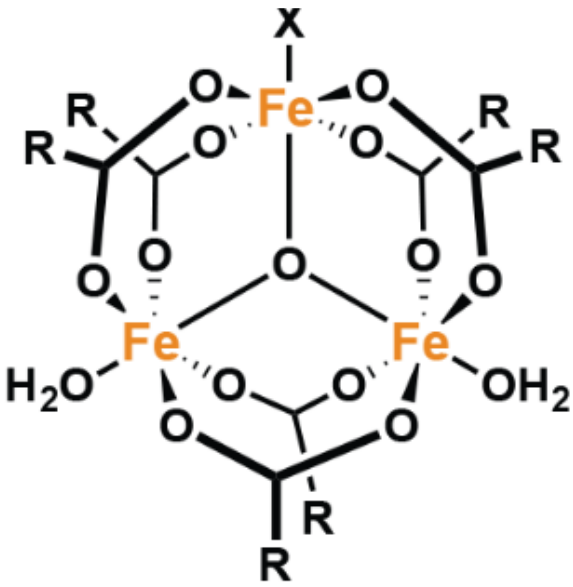

Figure 2.2. Structure of the $[Fe_3O(RCO_2)_6(H_2O)_2X]$ (X = monoanion) SBU.

For MIL-126 the situation is completely different. The two-fold interpenetration results in a close proximity between the two sublattices, and there are 4 points per unit cell where the capping ligands interact with each other (Figure 2.3a). Hydrogen bonding between a hydroxide on one sublattice and a water ligand on the other is strongly preferable by ~33 kJ mol^{-1} relative to the hydroxide-hydroxide case and ~48 kJ mol^{-1} over the water-water case (Figure 2.3b). These values are much greater than the relative energy differences calculated for MIL-88D and suggest that MIL-126 will be formed under thermodynamically controlled conditions (higher temperature, lower pH, etc.). The most stable arrangement of MIL-126 will be the one where these anion-water interactions are maximised, so conditions which favour rearrangement of these clusters in the framework during synthesis should also favour its formation.

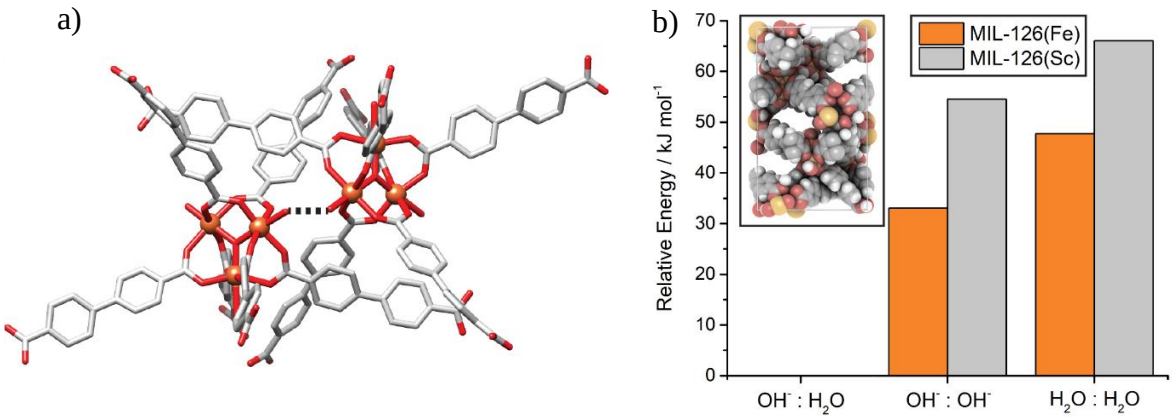

Figure 2.3. a) Image of one of the four close points or "pinch-points" between the sub-lattices of MIL-126(Fe). b) Relative energies of different arrangement of capping species between the sub-lattices in MIL-126 for both Fe and Sc analogues. Inset is a figure of the MIL-126(Fe) unit cell (Fe orange, oxygen red, carbon grey, hydrogen white) showing close interpenetration of the sub-lattices.

2.2 Aims

The main aims of this chapter are:

1. To investigate coordination modulation as a viable strategy for controlling interpenetration in solvothermal and microwave syntheses of Fe- biphenyl-4,4′-dicarboxylate MOFs
2. To evaluate the effects of modulation on the gas uptake, crystallite morphology, and yield of MIL-126(Fe)
3. To explore analogous syntheses using 2,2′-bipyridine-5,5′-dicarboxylate to evaluate the influence that linker rigidity has on interpenetration
4. To investigate the effect that changing the initial oxidation state of the Fe-precursor has on interpenetration and the quality of the obtained products

To control the interpenetration in the Fe-BPDC system, we will explore the effect of adding different modulators (Figure 2.4a) in conventional solvothermal and microwave-assisted synthesis. For the solvothermal route, we will also explore the use of two different Fe-precursors which are in different oxidation states in order to enhance the quality of the obtained products. In addition, we will explore the use of 2,2′-bipyridine-5,5′-dicarboxylate (BPYDC) (Figure 2.4b) in place of BPDC, which has been shown with scandium to favour formation of a non-interpenetrated phase due to its conformation.[6]

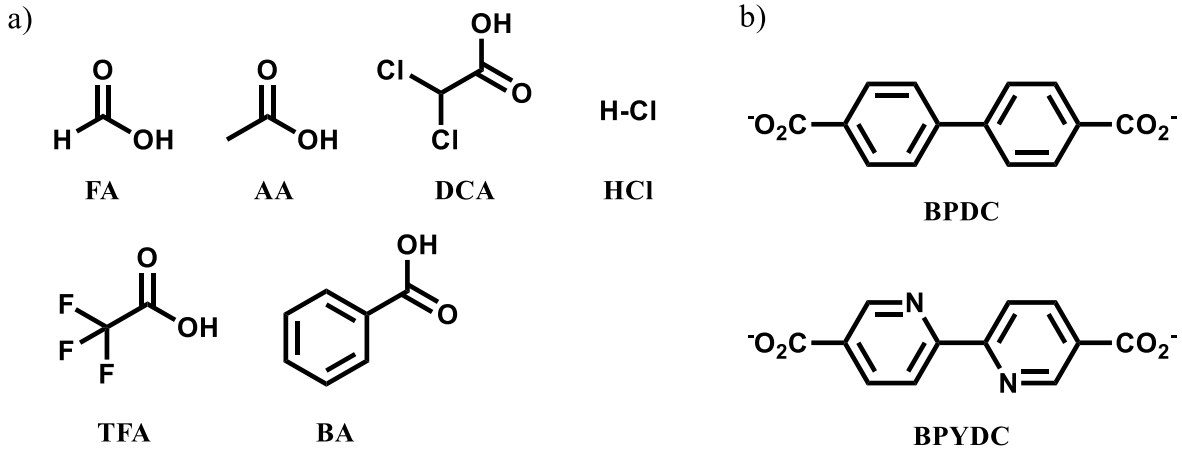

Figure 2.4. Schematic representation of a) coordination modulators, used in this study along with their abbreviations, and b) linkers.

2.3 Synthesis of Fe-BPDC MOFs (1)

Initial solvothermal syntheses were explored using a fixed concentration, temperature, and reaction time, in order to compare the unmodulated and modulated products. A typical synthesis consisted of heating a suspension of H_2BPDC and iron(III) chloride hexahydrate in DMF at 120 °C in an isothermal oven for 48 hours. For the modulated sample, 10 equivalents of acetic acid were added prior to heating and this sample is referred to as **1-AA** for convenience. After allowing to cool to room temperature, the samples were collected by centrifugation and washed with DMF and then DCM before drying under vacuum. Once dry, the samples were analysed using powder X-ray diffraction (PXRD) in order to determine the which crystalline phases are present. Comparison shows that the experimental PXRD pattern (Figure 2.5) for **1-AA** is a close match to the pattern simulated for the crystal structure of MIL-126(Fe), confirming that it is interpenetrated. In contrast, the experimental PXRD pattern for **1** is distinctly different and was found to be a close match to the predicted pattern for MIL-88D(Fe) in a "closed" conformation, which is expected after removing solvent from the pores.

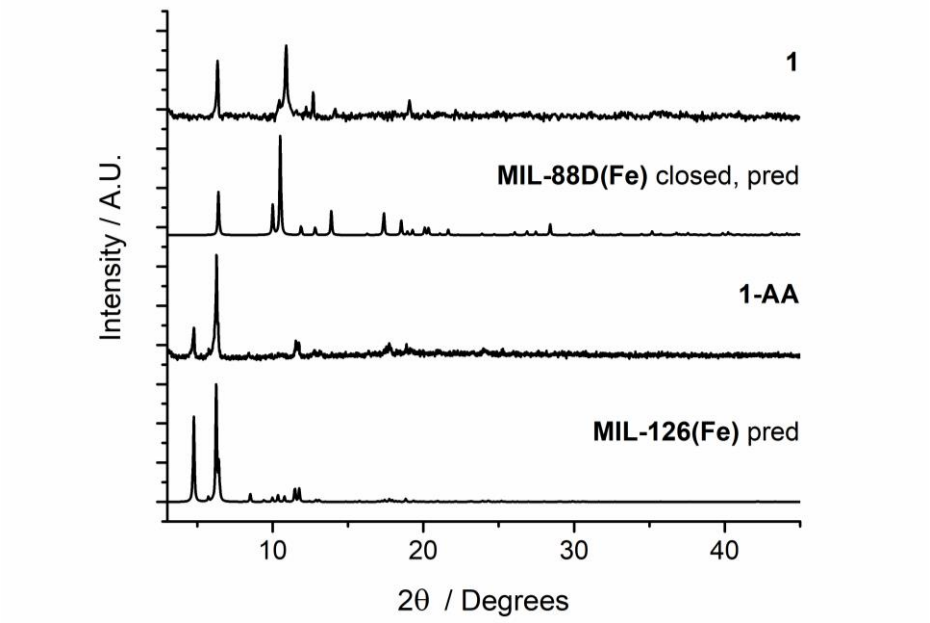

Figure 2.5. Comparison of the predicted PXRD patterns of MIL-126(Fe) (pattern predicted from Cambridge Structural Database (CCDC) Refcode MIBMER[4]) and the closed form of MIL-88D(Fe) (pattern predicted from simulated structure[7]) with the experimental PXRD patterns of **1** and **1-AA**. The background in **1** has been subtracted from its PXRD pattern in order to enable better comparison with the predicted pattern of MIL-88D(Fe) closed.

Due to the low quality of the PXRD pattern of **1**, microwave-assisted heating was explored as an alternative route, as it was expected that rapid nucleation would help to isolate the non-interpenetrated phase. In order to optimise the conditions for microwave heating, the temperature and time were varied accordingly, but otherwise using the same synthetic conditions as with the solvothermal route. Based on the PXRD patterns of the obtained samples (Figure 2.6), it is clear that lower temperature (≤120 °C) favours the formation of MIL-88D(Fe), while higher temperature favours the formation of MIL-126. At 150 °C, MIL-126 forms after 5 minutes but reduces in intensity with time and after 30 minutes new peaks which do not match either MIL-88D(Fe) or MIL-126(Fe) are apparent. As the optimal conditions for synthesising MIL-88D(Fe) were 100 °C for 30 minutes, this sample was used for all further characterisation and is referred to as **1-MW**.

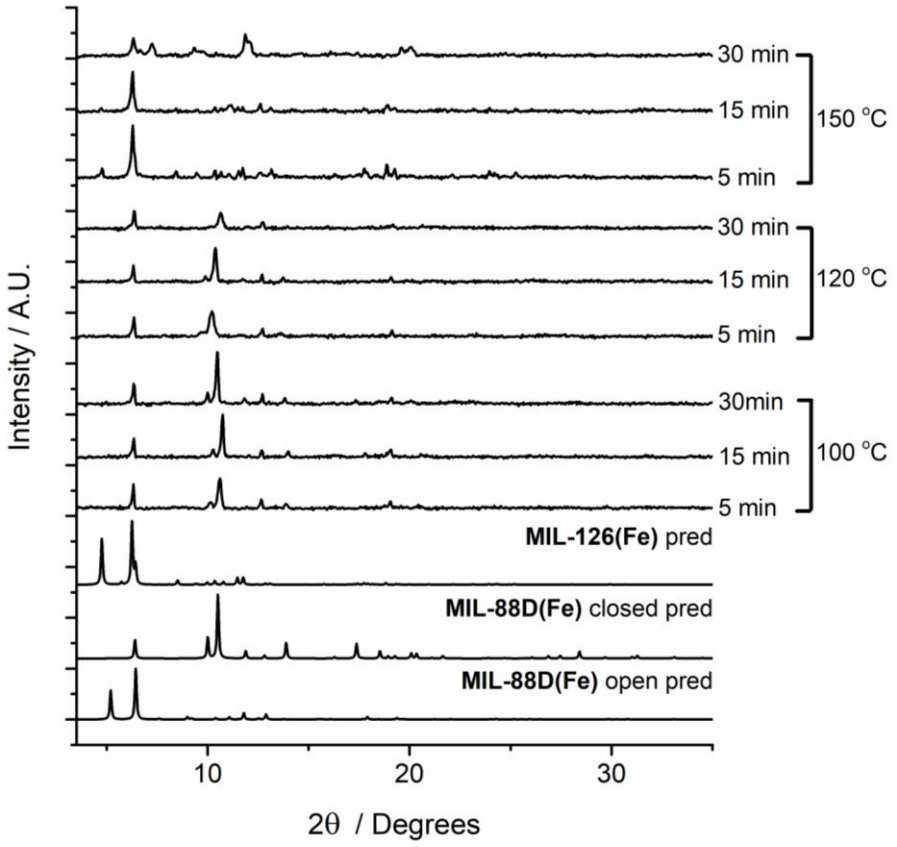

Figure 2.6. Stacked PXRD patterns of **1** synthesised under microwave-assisted heating with different heating parameters. Background subtraction has been performed for each of these experimental patterns for clearer comparison with the predicted patterns of MIL-88D(Fe) 'closed', MIL-88D(Fe) 'open', and MIL-126(Fe).

By comparison of the PXRD patterns (Figure 2.7) the peaks seen in the predicted pattern for MIL-88D(Fe) in a closed conformation. The fact that microwave synthesis appears to favour the non-interpenetrated phase at lower temperatures suggests that it is a kinetic product

relative to MIL-126(Fe). Similar variations of the temperature were attempted for the solvothermal syntheses with a synthesis time of 48 hours (as per the other solvothermal syntheses), but no crystalline product was obtained at 100 °C, while at 150 °C highly crystalline MIL-126(Fe) was obtained, further suggests that MIL-126 is the thermodynamic product relative to MIL-88D. The ability of microwave synthesis to rapidly produce MOFs has been previously reported[8-10] and thus it could be expected that kinetic products such as MIL-88D(Fe) will crystallise faster via a microwave route compared to a solvothermal one.

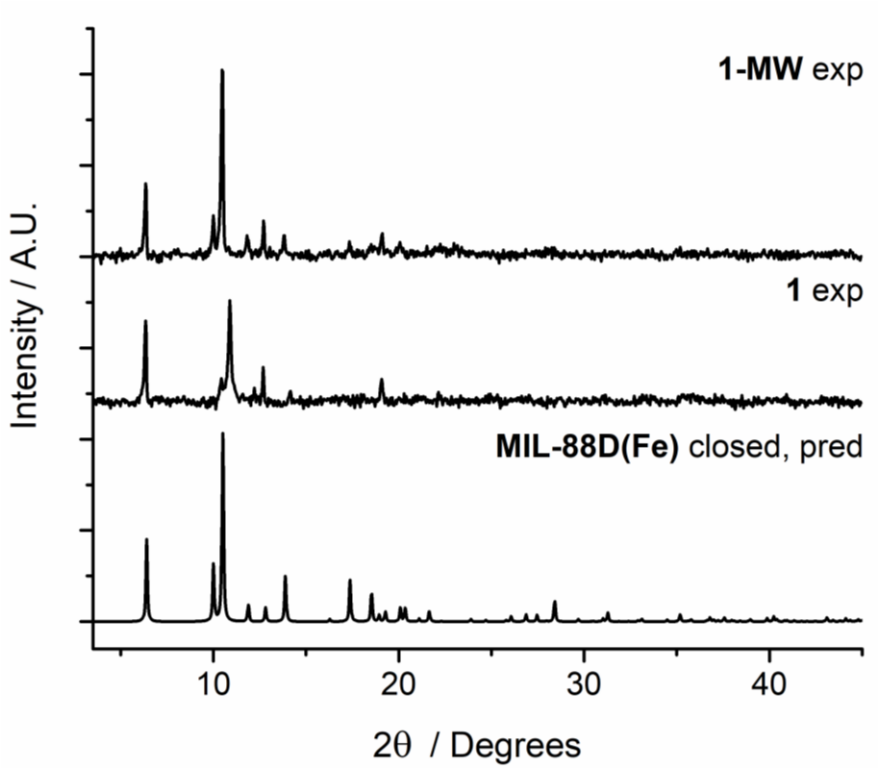

Figure 2.7. Stacked PXRD patterns for **1** and **1-MW** compared to the predicted pattern for MIL-88D(Fe) closed. Background subtraction has been applied to **1** and **1-MW** to enable better comparison with the predicted pattern of MIL-88D(Fe) closed.

To investigate the effect of modulation under microwave-assisted heating, similar syntheses were performed with the addition of 10 equivalents of acetic acid to the reaction mixture. The synthesis time was fixed at 30 minutes and the temperature was varied in a similar manner to the unmodulated synthesis. The addition of 10 equivalents of acetic acid was enough to completely prevent crystallisation at 100 °C, which yielded only a clear solution after 30 minutes of reaction time. This suggests that this concentration of acetic acid is high enough to effectively prevent nucleation, in line with the mechanism of modulation discussion in Chapter 1 (Section 1.4.2). At 120 °C, single crystals of around 30 μm were obtained, with PXRD confirming that this sample corresponds to MIL-126(Fe) (Figure 2.8a),

while synthesis at 150 °C led to poorly crystalline material. This suggests that an optimum temperature is required to balance nucleation with crystal growth, which is exemplified by the case with 120 °C as the synthesis temperature; lower temperature (100 °C) led to no nucleation, while higher temperature (150 °C) led to rapid nucleation but poor crystal growth. As 120 °C was the optimum synthesis temperature, this sample was used for further characterisation and is referred to as **1-AA-MW**. Comparison of the PXRD patterns of the modulated samples **1-AA** and **1-AA-MW** with the predicted patterns of MIL-126(Fe) and MIL-88D(Fe) in the open form confirms that these samples are indeed interpenetrated MIL-126(Fe) and not open MIL-88D(Fe) (Figure 2.8b).

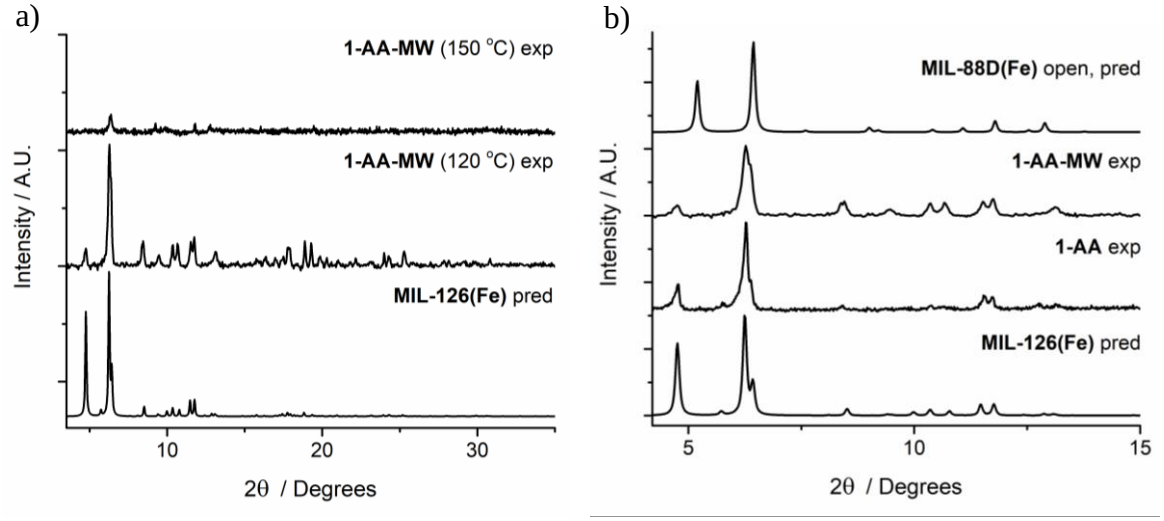

Figure 2.8. a) Stacked PXRD patterns for **1** prepared under microwave-assisted heating with acetic acid as modulator compared to the predicted PXRD pattern for MIL-126(Fe). b) Stacked PXRD patterns of **1-AA** and **1-AA-MW** compared to the predicted PXRD patterns for MIL-126(Fe) and MIL-88D(Fe) closed. Background subtraction has been applied to the PXRD patterns of **1-AA-MW** (120 °C), **1-AA-MW** (150 °C), and **1** to enable better comparison with the predicted patterns of MIL-126(Fe) and MIL-88D(Fe) open.

The PXRD patterns of **1-MW** and **1-AA-MW** were indexed and the unit cell parameters were extracted by Pawley fitting using the program GSAS-II.[11] Pawley fitting of the experimental pattern for **1-AA-MW** gave tetragonal unit cell parameters of $a = b = 21.893(12)$, $c = 36.196(29)$ Å ($R_{wp} = 5.37\%$, Figure 2.9a) which is a close match to the single crystal structure of MIL-126(Fe)[2] which has unit cell parameters of $a = b = 21.800(3)$, $c = 35.407(7)$ Å. The Pawley fit of **1-MW** gave hexagonal unit cell parameters of $a = b = 10.237(6)$, $c = 27.896(26)$ Å ($R_{wp} = 4.12\%$, Figure 2.9b) which is a close match to the predicted closed structure of MIL-88D(Fe)[1] which has unit cell parameters of $a = b = 10.2$, c = 27.6 Å.

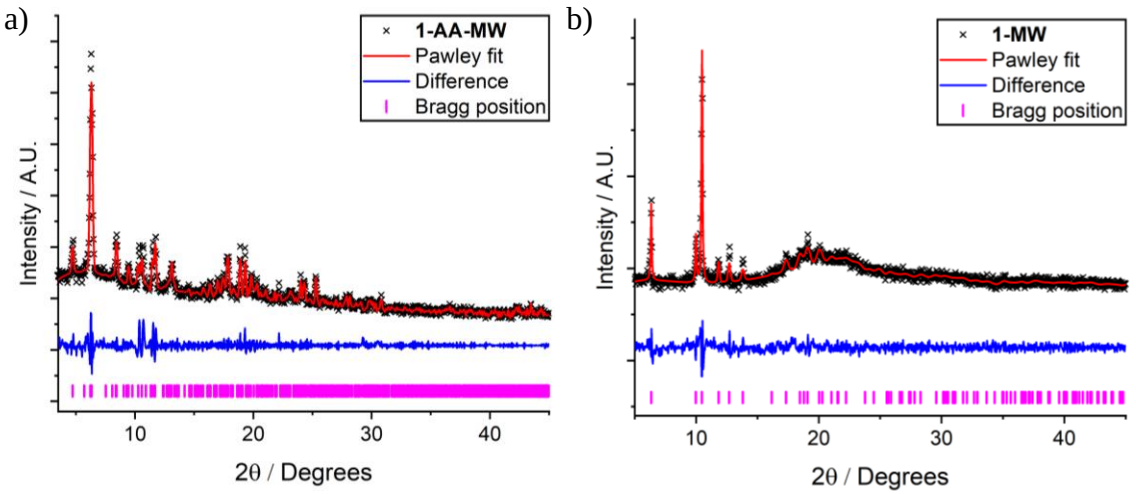

Figure 2.9. Pawley fits for the experimental PXRD patterns of **1-AA-MW** and **1-MW**.

SEM imaging shows that the unmodulated samples **1** and **1-MW** both consist of hexagonal rods (Figure 2.10) which is a reflection of the crystal symmetry and are typical for MOFs with a MIL-88 topology.[12,13] **1** consists of monodisperse crystals of around 5 µm in length whereas **1-MW** appears to be much more polydisperse, with crystals between 2 and 10 µm in length. Both modulated samples contain rod-like crystals which likely correspond to MIL-88D(Fe), however, both consist predominantly of large crystals of MIL-126(Fe). The morphology of these crystals is consistent with those reported for single-crystals of MIL-126(Fe) by Zhou et al.[14]

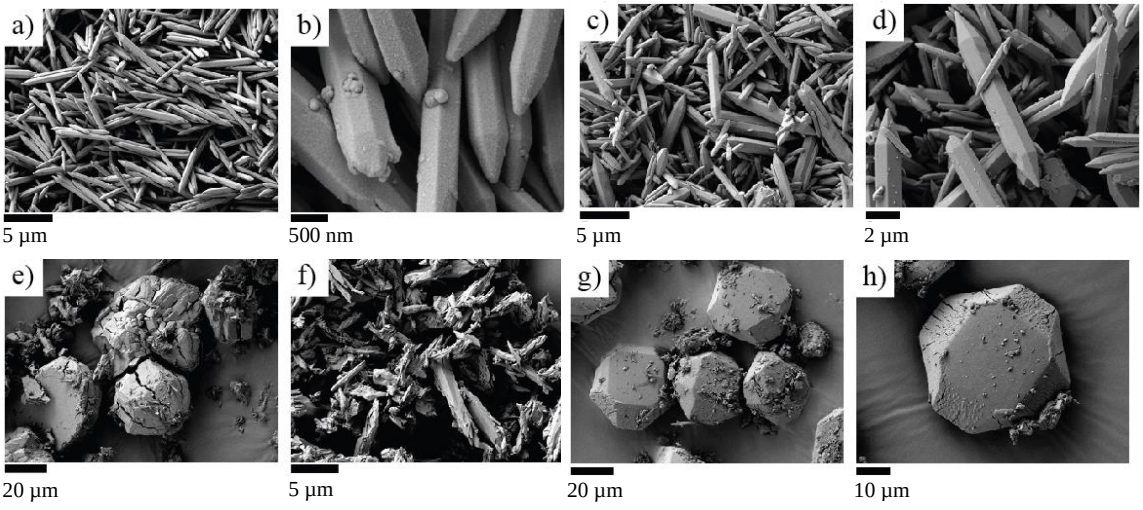

Figure 2.10. SEM images of modulated and unmodulated samples of 1: a-b) **1**, c-d) **1-MW**, e-f) **1-AA**, g-h) **1-AA-MW**.

To confirm that **1** and **1-MW** were the non-interpenetrated materials, N_2 adsorption isotherms were performed at 77 K after activation at 150 °C for 20 hours under vacuum. Upon removal of solvent molecules, MOFs in the MIL-88 series assume a state where their

pores are closed and cannot be probed using gas sorption experiments. In contrast, the rigidity of interpenetrated MIL-126(Fe) allows it to be activated without a significant change in pore size, enabling these materials to adsorb nitrogen gas (reported surface areas of 1690-1750 m^2g^{-1}) [7,15]. As expected, **1** and **1-MW** had much lower nitrogen uptakes than **1-AA** and **1-AA-MW** (Figure 2.11a), indicating that the unmodulated sample adopts the low porosity closed conformation characteristic of non-interpenetrated MIL-88D. Interestingly, the isotherm for **1-AA** exhibits Type IV mesoporosity, suggestive of a defective material, with SA_{BET} = 879 m^2g^{-1}. Despite the structural differences between the interpenetrated and non-interpenetrated MOFs, they have the same overall framework formula $[Fe_3O(BPDC)_3(H_2O)_2X]$ and are expected to exhibit similar thermal properties. Thermogravimetric analysis (TGA) in air was performed on both samples to assess their thermal stabilities and estimate their approximate compositions (Figure 2.11b).

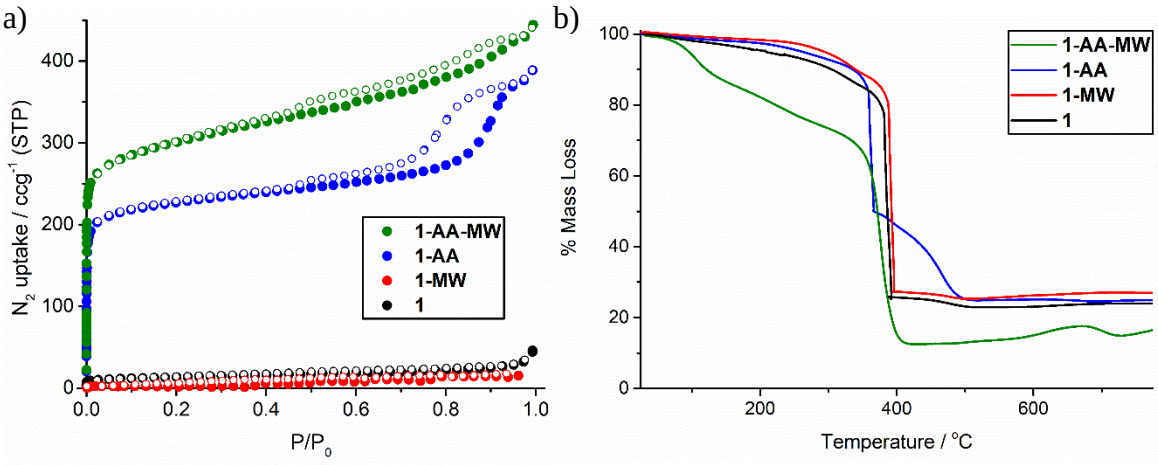

Figure 2.11. a) N_2 gas sorption isotherms for all samples. b) TGA curves for all samples.

Each sample had a steep mass loss at around 350 °C corresponding to framework degradation. The degradation of **1** occurs at a slightly higher (~10 °C) temperature than the modulated sample, again suggesting a different phase. The mass residues are consistent with the expected formula, however, the mass residue for **1-AA** does not indicate significant defectivity, despite its clear mesoporosity. This suggests that this defectivity is in the form of both missing-linkers and missing-clusters, which have opposing influence on the mass of the residue.

To assess the flexibility of **1-MW**, an as-synthesised sample with DMF still in the pores was analysed by PXRD and compared to the dry sample (Figure 2.12a). This shows that the material is obtained first in an open pore form, and then adopts a closed pore form after solvent exchange and drying from DCM. This is confirmation of the flexibility of MIL-

88D(Fe) and is also consistent with its low N_2 uptake post-activation. As the PXRD patterns for MIL-88D(Fe) open and MIL-126(Fe) are slightly similar, both were compared to the obtained pattern for **1-MW** as-synthesised to confirm its identity (Figure 2.12b). The as-synthesised material is a close match to MIL-88D(Fe) open and is not the same as MIL-126(Fe).

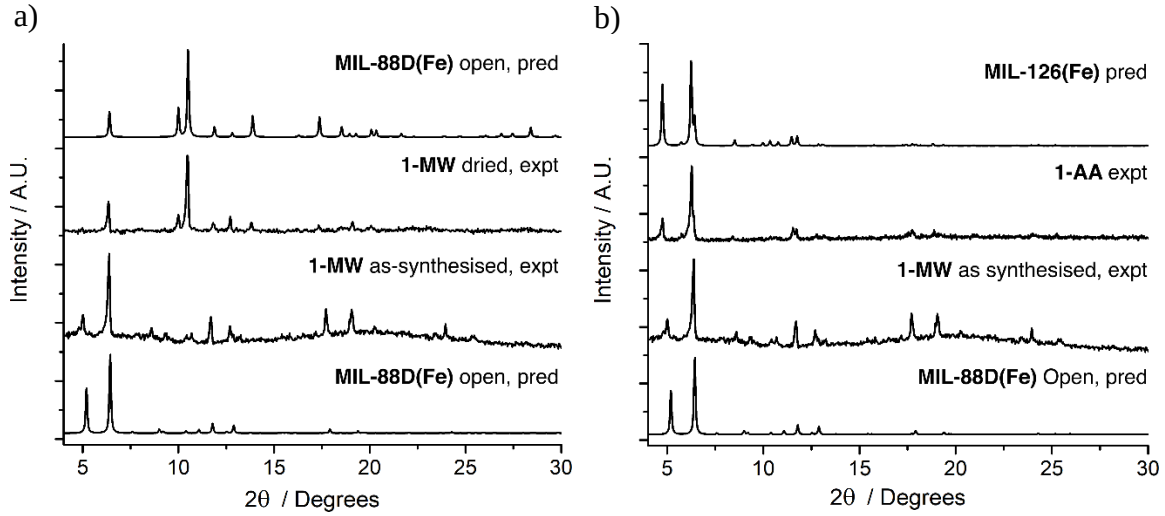

Figure 2.12. Comparison of the predicted PXRD patterns of a) MIL-88D(Fe) in the open and closed forms (patterns predicted from simulated structures[7]) with the experimental PXRD patterns of **1-MW** before and after drying. b) MIL-126(Fe) (pattern predicted from Cambridge Structural Database (CCDC) Refcode MIBMER[4]) and the open form of MIL-88D(Fe) (patterns predicted from simulated structure) with the experimental PXRD patterns of **1-MW** before drying and **1-AA.**

Once MIL-88D(Fe) has been crystallised, it does not appear to interconvert into the interpenetrated framework, as evidenced by the fact that the unmodulated syntheses appear to give phase pure MIL-88D(Fe) when the synthesis temperature is 120 °C or less. This can be rationalised by the fact that the energy penalties for anion-anion and water-water interactions with a newly forming sublattice are quite large (as per the DFT calculations discussed previously), so interpenetration is disfavoured unless the conditions are sufficient to promote rearrangement of the two sublattices in order to maximise the favourable anion-water interactions. The addition of a modulator clearly favours the interpenetrated product, and this can be rationalised by the fact that the modulator competes with the bridging linkers and thus slows down self-assembly, as well as introducing a greater degree of reversibility during crystal growth. This can more readily enable the two nets to grow together while maximising the anion-water interactions via rearrangement, thus making it the preferred product under these conditions.

A similar effect is seen with higher synthesis temperature, with both our microwave syntheses at 150 °C (5-15 minutes) preferring MIL-126(Fe), as well as the reported solvothermal routes for MIL-126(Fe) being at 150 °C.[4,14,15] Further proof of this thermodynamic relationship was observed by heating a small sample of dried MIL-88D(Fe) in a large quantity of DMF at 120 °C. In addition to effectively opening the structure of MIL-88D(Fe), there are PXRD peaks which clearly correspond to the interpenetrated phase (Figure 2.13). This suggests that the transformation has occured via dissolution and recrystallisation, and ultimately favours the formation of the thermodynamic product - which as our DFT calculations predicted is MIL-126(Fe).

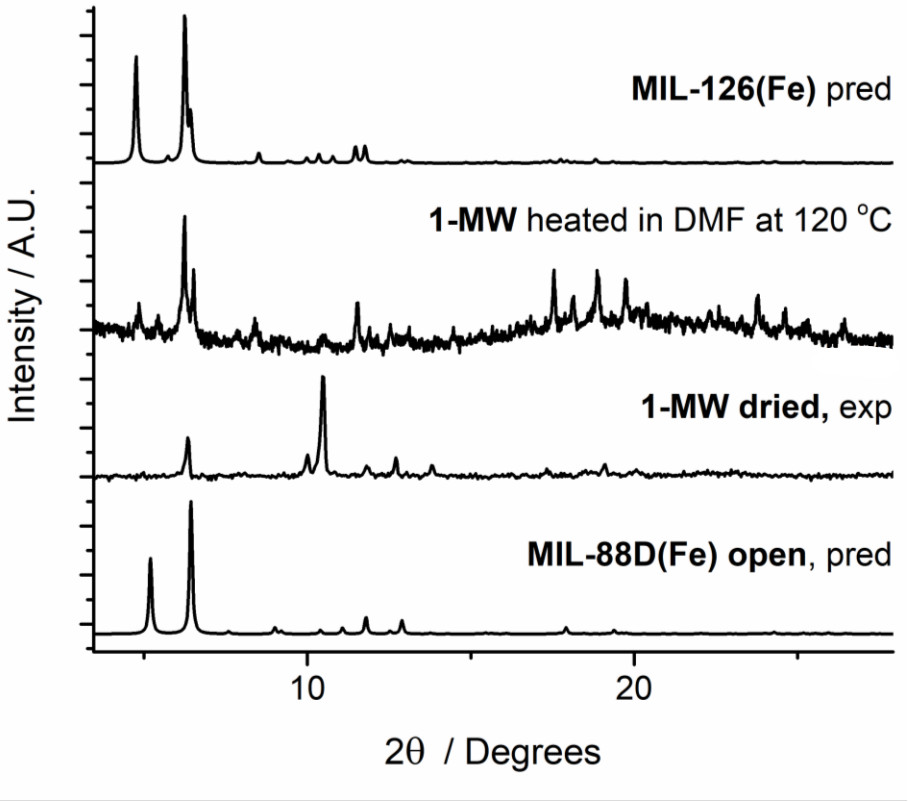

Figure 2.13. Stacked PXRD patterns of **1-MW** before and after heating in DMF.

Our experimental results agree strongly with the results from the DFT study and provide a supportive rationalisation for why MIL-126(Fe) is the thermodynamically preferred product. Having a firm understanding of the thermodynamic relationship between different phases in a given system is important for future research and will be crucial for designing their syntheses on an industrial scale.

In this section we have shown that interpenetration in Fe-BPDC MOFs can be controlled using temperature and modulation in both solvothermal and microwave syntheses, allowing both the interpenetrated and non-interpenetrated matetials to be obtained with high

crystallinity. We propose that modulation slows the self-assembly process by competition with the linker to yield MIL-126(Fe) as the thermodynamic product, while the unmodulated synthesis yields MIL-88D(Fe) as the kinetic product. This would also explain why MIL-88D(Cr) is the predominant product of related syntheses, as Cr(III) is considerably more kinetically inert.[16] Despite the control over interpenetration shown through modulation with acetic acid, these samples still contain a significant amount of MIL-88D(Fe) as a phase impurity, which reduces their nitrogen uptakes. It is clear that PXRD alone is not enough to assess phase purity in this system; MIL-88D(Fe) diffracts weakly and so may be present in samples of MIL-126(Fe) without being seen in powder X-ray diffractograms. In an attempt to optimise the conditions for synthesising MIL-126(Fe), different modulators and their concentrations were evaluated in the next section.

2.4 Modulation of Fe-BPDC MOFs (1)

With modulation control over interpenetration of **1** demonstrated using acetic acid, a range of different modulators, and their effect on the crystallinity, crystal size, and defectivity of **1**, were investigated. Samples were named "**1-mod** (x eq)" where mod is the modulator used and x = the number of equivalents of modulator added to the synthesis with respect to Fe.

2.4.1 Acetic Acid (AA)

Following our initial results, studies were firstly focussed on acetic acid (AA); this example most clearly exemplifies the effects of using monocarboxylates in the synthesis of **1**. Crystalline material was obtained from syntheses containing 1-20 equivalents of AA, above which no solid material formed. Five or more equivalents are required to obtain a highly crystalline material (Figure 2.14), indicating that the modulator plays a vital role in aiding crystallisation of the interpenetrated phase. Between 1 and 5 equivalents of acetic acid, the relative intensity of the MIL-126(Fe) phase increases, as can be seen by PXRD, however this appears to be unchanged at higher concentrations of acetic acid. There is a marked decrease in yield when 20 equivalents of acetic acid are used compared to the other samples, suggesting that here the concentration of acetic acid is sufficient to greatly retard the crystal growth process.

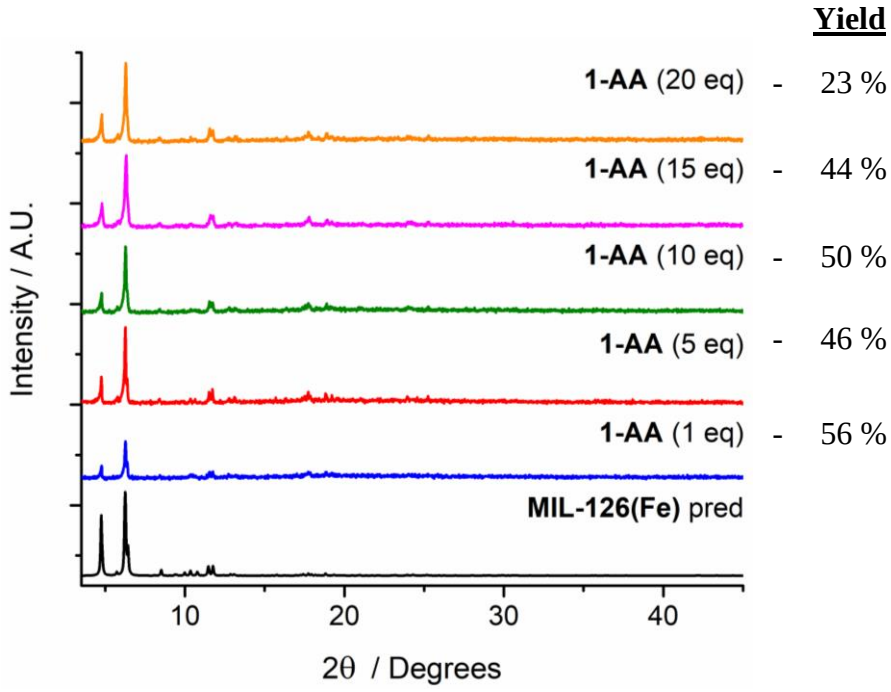

Figure 2.14. Stacked PXRD patterns of **1-AA** prepared using different molar equivalents of AA along with the yields. No background subtraction has been applied to any of these PXRD patterns.

The porosity of the samples increases with increasing AA concentration (Figure 2.15a), although no samples reach the porosity expected of a pure MIL-126(Fe) phase, predicted to be 2550 m^2g^{-1};[4] **1-AA** (20 eq) has the highest BET surface area of 1289 m^2g^{-1} (Figure 2.15c). Hysteresis loops consistent with mesoporosity are present in the N_2 uptake isotherms of samples prepared with 5-20 equivalents of AA. This could be attributed to induced defects from acetates coordinating to the clusters, leading to missing linkers and/or clusters from the framework, thus enhancing porosity without compromising stability. Ordered acetate capping of $[Fe_3O(RCO_2)_6(H_2O)_2X]$ SBUs has previously been observed as a consequence of steric clashes between ligands in PCN-236, forming a monocapped, 5-connected cluster, and because of linker rigidity in PCN-264, forming a bicapped, 4-connected cluster.[14] The pore size distributions show that all **1-AA** samples except **1-AA** (1 eq) have the expected micropore for the ideal MIL-126 structure at around 11 Å, as well as a mesopore at around 40 Å (Figure 2.15b).

a)

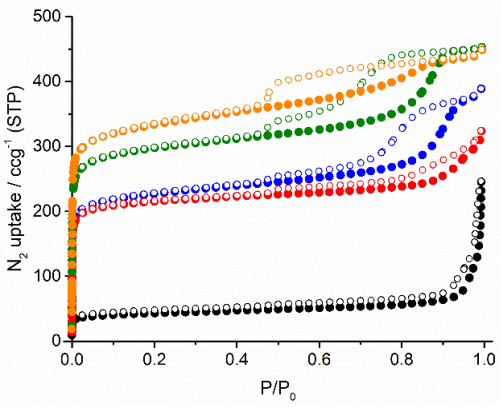

b)

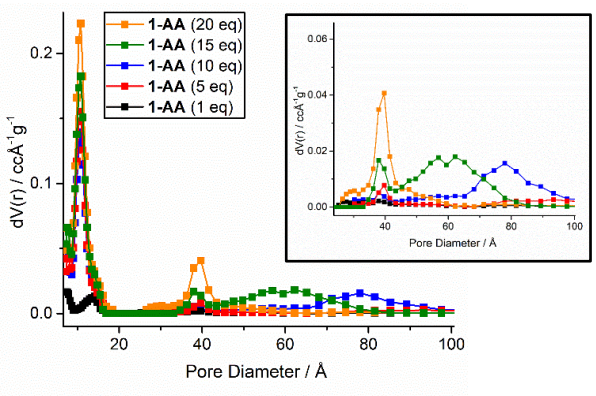

c)

Sample	SA_{BET} / m^2 g^{-1}
1-AA (1 eq)	161
1-AA (5 eq)	847
1-AA (10 eq)	879
1-AA (15 eq)	1158
1-AA (20 eq)	1289

d)

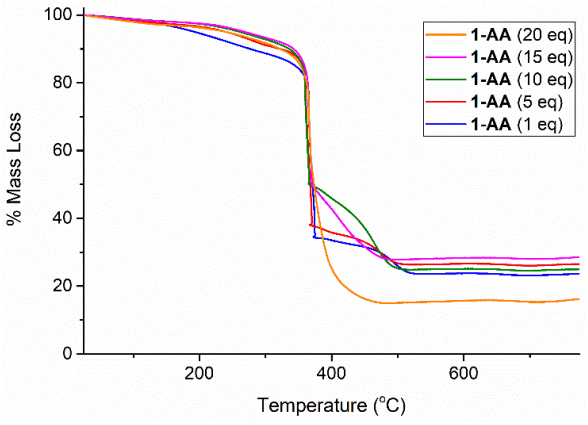

Figure 2.15. Characterisation data for samples of **1-AA** prepared with different quantities of AA: a) N_2 uptake isotherms (77 K, filled symbol adsorption, empty desorption. b) Pore size distributions, with the inset displaying the mesoporous region. c) BET surface areas. d) TGA profiles.

Both the nitrogen uptake and BET surface area increases with increasing acetic acid concentrations (Figure 2.15c). TGA revealed a significantly lower oxide residue for **1-AA** (20 eq) than for the other samples (Figure 2.15d) suggesting that as the quantity of modulator added to synthesis increases, missing cluster defects may become more prevalent compared to missing linker defects.

Multiple phases can be observed from the SEM images of **1-AA** (Figure 2.16), mainly consisting of broken hexagonal rods and larger blocks. It should be noted here that analysis of sample composition via SEM alone is not in any way definitive, but it does give an indication of which phases may be present when compared with the other characterisation data. Presumably, the rods correspond to MIL-88D(Fe), as MIL-88 samples have hexagonal unit cells and tend to adopt similar morphologies,[4,9] while the block crystallites are most likely MIL-126(Fe). In **1-AA** (1 eq) these rods appear to be more numerous than in the other samples, and much larger in size than the block crystallites which presumably correspond to MIL-126(Fe). This is consistent with the low nitrogen uptake as MIL-88D(Fe) does not adsorb a significant amount of nitrogen and is also consistent with the weaker reflections of the MIL-126(Fe) phase seen by PXRD. 15 and 20 equivalents of acetic acid led to sheets of intergrown crystals. In some of the samples, there are clear cracks in the crystallites, particularly for **1-AA** (20 eq), which may suggest that the mesoporosity evident for most of these samples arises from these features, which could be a consequence of the activation protocol, rather than from modulator-induced lattice defects.

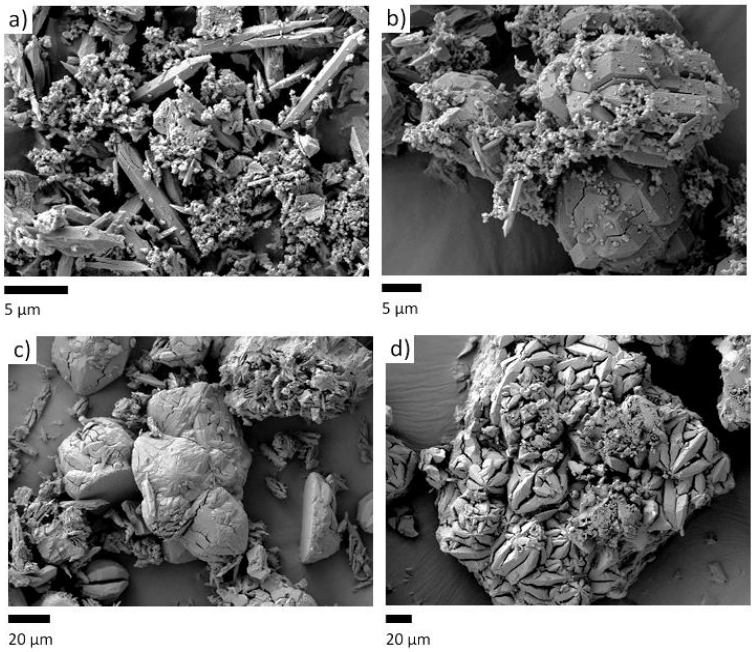

Figure 2.16. SEM images of **1-AA** prepared with different molar equivalents of AA: a) 1 eq, b) 5 eq, c) 15 eq, d) 20 eq.

2.4.2 Optimum Modulator Concentrations

Subsequently, a range of modulators containing carboxylic acid groups, which can compete with the BPDC linker, and differ in their pK_a and steric bulk, was investigated, as they have been successfully used to modulate Zr MOFs.[17-22] The relative pK_a values of the modulators (Figure 2.17) are expected to correlate with their binding strength to the SBUs and therefore potentially tune the degree of defectivity through their incorporation into the framework. Additionally, to independently study the effect of varying the pH of the reaction mixture, hydrochloric acid was also used as a modulator.

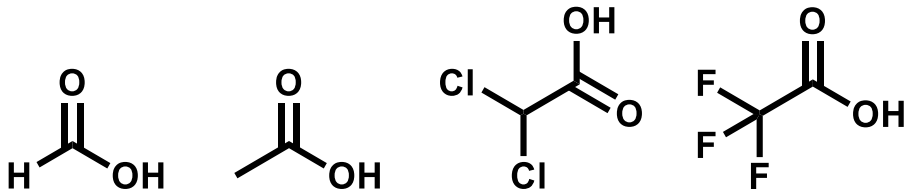

	FA	AA	DCA	TFA
pK_a:	3.77	4.76	1.26	0.23

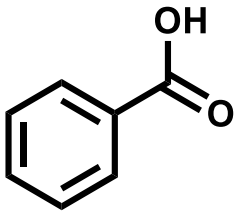

H-Cl

	BA	HCl
pK_a:	4.15	-7

Figure 2.17. Schematic representation of the modulators used in this study along with their abbreviations and pK_a values (determined in water at 298K).

In all cases, an optimum quantity of modulator to be added to the synthesis dictates a balance of crystallinity, yield, and porosity. In general, porosity increases with modulation (Figure 2.18a) but yields drop significantly as the concentration of modulator is increased (Figure 2.18b). Modulation produces predominantly MIL-126(Fe), but at lower modulator concentrations, the presence of MIL-88D(Fe) is evident in the form of rod-shaped crystals in SEM images while not being distinct in PXRD analysis. Modulation also results in a variety of particle morphologies of MIL-126(Fe) (Figure 2.18c). It is important to note that

PXRD alone is not enough to assess phase purity; the presence of quantities of MIL-88D(Fe) in samples can be determined by SEM, and may account for the lower than predicted porosities of MIL-126(Fe) samples reported in the literature to date.[4,15] The optimised quantity for each modulator based primarily on the BET surface areas are presented in Figure 2.18d along with their yields and BET surface areas. A summary of the results from individual modulation scans are discussed in the upcoming sections.

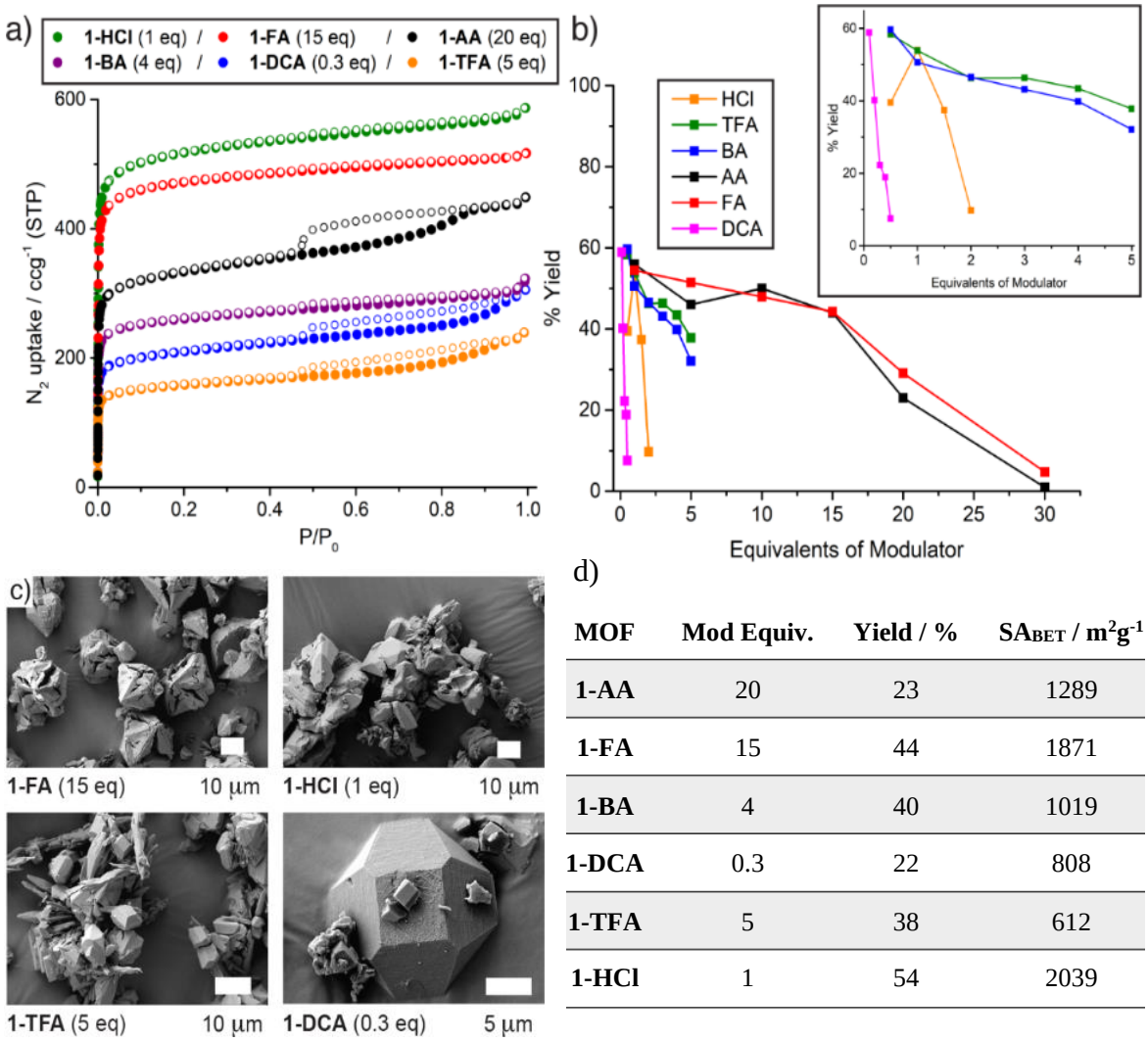

d)

MOF	Mod Equiv.	Yield / %	SA_{BET} / m^2g^{-1}
1-AA	20	23	1289
1-FA	15	44	1871
1-BA	4	40	1019
1-DCA	0.3	22	808
1-TFA	5	38	612
1-HCl	1	54	2039

Figure 2.18. a) N_2 uptake isotherms (77 K, filled symbol adsorption, empty desorption) of optimal samples of **1** prepared with each modulator. b) Plot of reaction yields against modulator equivalents for each synthetic system. c) SEM images showing differing morphologies obtained with different modulators. d) Optimum synthetic conditions (based on porosity) for MIL-126(Fe) with different modulators.

2.4.3 Formic Acid (FA)

Highly crystalline material corresponding to MIL-126(Fe) could be obtained with one or more equivalent of FA, as can be seen by PXRD (Figure 2.19a), with an increasing amount of modulator giving a similar reduction in yield as seen with AA. The N_2 uptake also increases with the addition of more modulator (Figure 2.19b), but in contrast to AA, samples prepared with FA do not exhibit significant mesoporosity, indicating that the degree of defectivity in these samples is lower. Additionally, the approximate linker:cluster ratios based on TGA are generally close to the ideal value, which suggests that these samples contain approximately 3 linkers per cluster (as per the ideal structure) and are not significantly defective. Nitrogen adsorption isotherms show that the highest uptake of the modulated experiments is obtained with **1-FA** (15 eq), with a corresponding SA_{BET} = 1871 $m^2\ g^{-1}$ slightly higher than the previously reported value of 1750 $m^2\ g^{-1}$, but still lower than the value of 2550 $m^2\ g^{-1}$ predicted for an ideal material.[4]

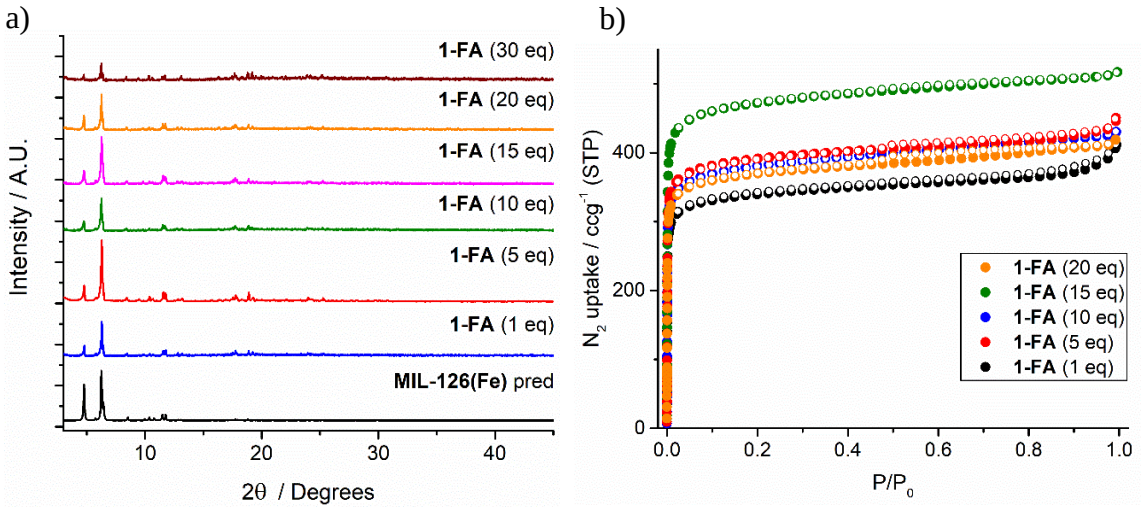

Figure 2.19. a) Stacked PXRD patterns of **1-FA** prepared using different molar equivalents of FA. b) Comparison of nitrogen adsorption (closed circles) and desorption (open circles) isotherms (77 K) of samples of **1-FA** prepared with different equivalents of FA.

SEM imaging shows that **1-FA** (20 eq) has a distinctly different morphology (Figure 2.20) which consists of spherical arrangements of smaller fused sheets rather than the more block-like crystals apparent in the other samples. The lower uptake could be a direct result of this morphology, which may reduce the pore continuity, making some of the pores inaccessible to nitrogen diffusion. Aside from this sample, the rest consist mostly of well-defined and regular single-crystals, which increase in size from around 10 µm to 40 µm as the modulator concentration is increased, with **1-FA** (30 eq) giving perfectly faceted single crystals but in

very low yield. As with AA modulation, some additional rod-like crystals can be seen in the samples prepared with 1-10 equivalents of FA, again suggesting some non-interpenetrated MIL-88D(Fe) is present at lower modulator concentrations. Even though formic acid has a lower pK_a than acetic acid (3.77 vs. 4.76) there does not appear to be a significant reduction in yield in comparison to samples prepared with equivalent molar quantities of acetic acid. This suggests that the timespan required for optimal crystal growth of MIL-126(Fe) when using formic acid is still within the 48-hour synthesis time used in all of these reactions.

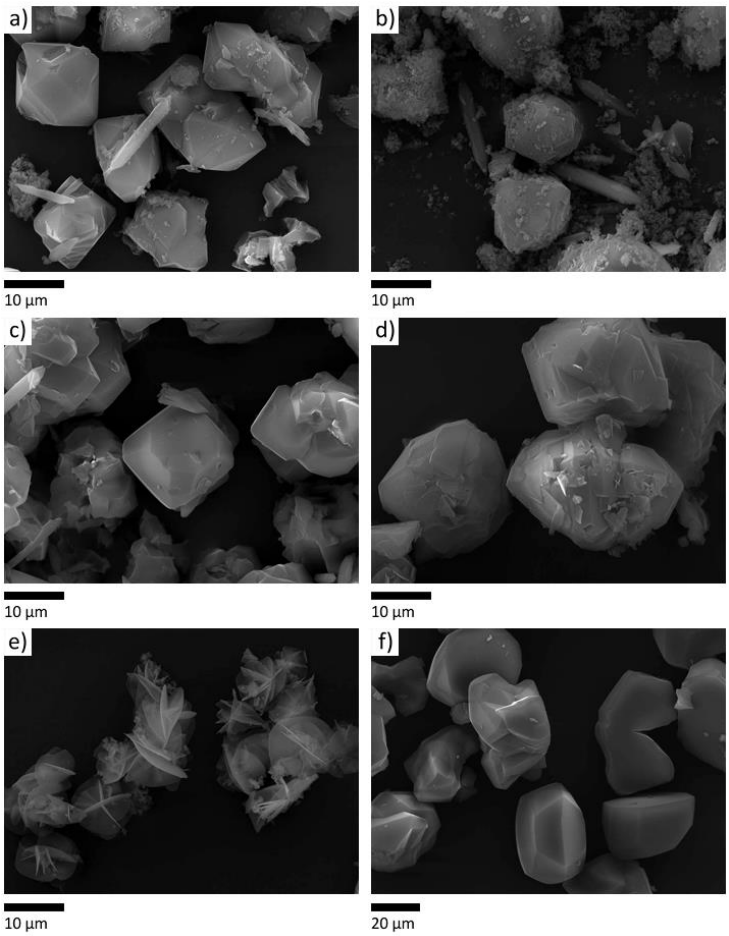

Figure 2.20. SEM images of **1-FA** prepared with different molar equivalents of FA: a) 1 eq, b) 5 eq, c) 10 eq, d) 15 eq, e) 20 eq, f) 30 eq.

2.4.4 Hydrochloric Acid (HCl)

It is assumed that the addition of monocarboxylates to MOF syntheses slows the crystallisation by competition with the linker for coordination sites, potentially pre-forming SBUs, and by lowering the pH.[23] Addition of a strong Brønsted acid should also slow the self-assembly by hindering deprotonation of the linkers; to aid our understanding of this effect, concentrated hydrochloric acid (HCl), which has been shown to successfully enhance the synthesis of UiO-66 series MOFs,[24] was used. A clear increase in both the crystallinity

and porosity of the interpenetrated MIL-126(Fe) phase that is formed can be observed as more HCl is added to the synthesis (Figures 2.21a-b).

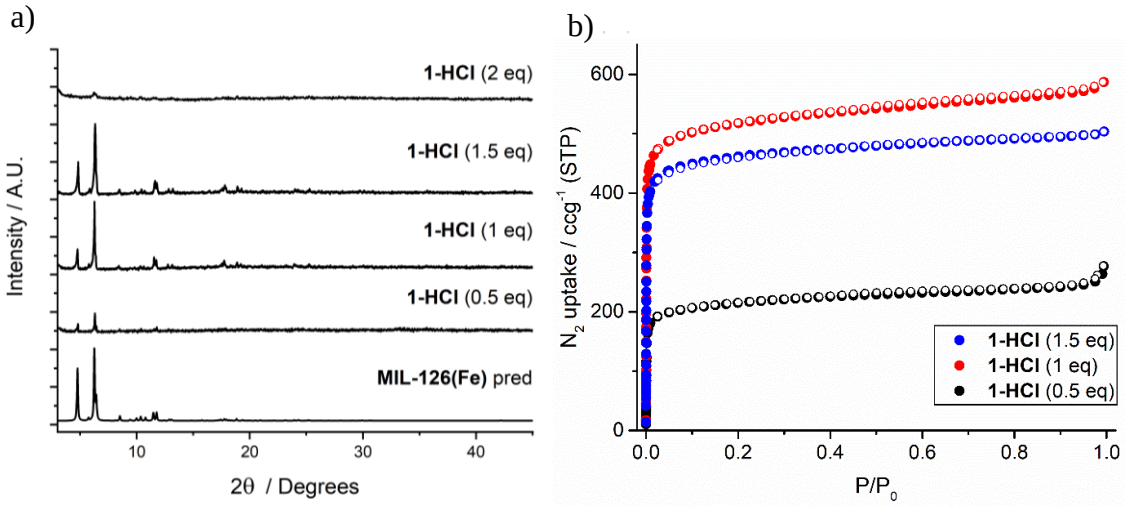

Figure 2.21. a) Stacked PXRD patterns of **1-HCl** prepared using different molar equivalents of HCl. b) Comparison of nitrogen adsorption (closed circles) and desorption (open circles) isotherms (77 K) of samples of **1-HCl** prepared with different equivalents of HCl.

When 2 equivalents of HCl are used, the crystallinity is very low, suggesting that there is an ideal pH range for successful crystallisation of the MOF. The nitrogen adsorption isotherms of the MOFs all display Type I behaviour, typical for microporous materials, and do not display any hysteresis, suggesting minimal defectivity. **1-HCl** (1 eq) possesses the highest BET surface area (Table 2.1) of all the samples presented so far, with SA_{BET} = 2039 m^2g^{-1}.

Table 2.1. BET surface areas for samples of **1-HCl** prepared with different molar equivalents of HCl.

Sample	SA_{BET} / m^2g^{-1}
1-HCl (0.5 eq)	832
1-HCl (1 eq)	2039
1-HCl (1.5 eq)	1829

The TGA trace for **1-HCl** (0.5 eq) shows an abnormally high residue (Figure 2.22a), suggesting that the product is linker deficient. There is no clear evidence in the PXRD pattern of this sample that indicates the presence of crystalline or amorphous oxides/hydroxides (there is neither an amorphous hump nor corresponding Bragg peaks), however, there could be such material present inside the pores of MIL-126(Fe) in this sample which could also

explain the relatively lower nitrogen uptake of this sample and the lower peak intensities compared to the products prepared with 1 and 1.5 equivalents of HCl. However, it should be noted that in the absence of more conclusive data, this is just one possible hypothesis. There is also a large increase in crystal size as the concentration of HCl is increased (Figure 2.22b), going from around 5-10 μm for **1-HCl** (0.5 eq) to around 100 μm for **1-HCl** (1.5 eq), indicating that HCl acts as an effective modulator to increase crystal size.

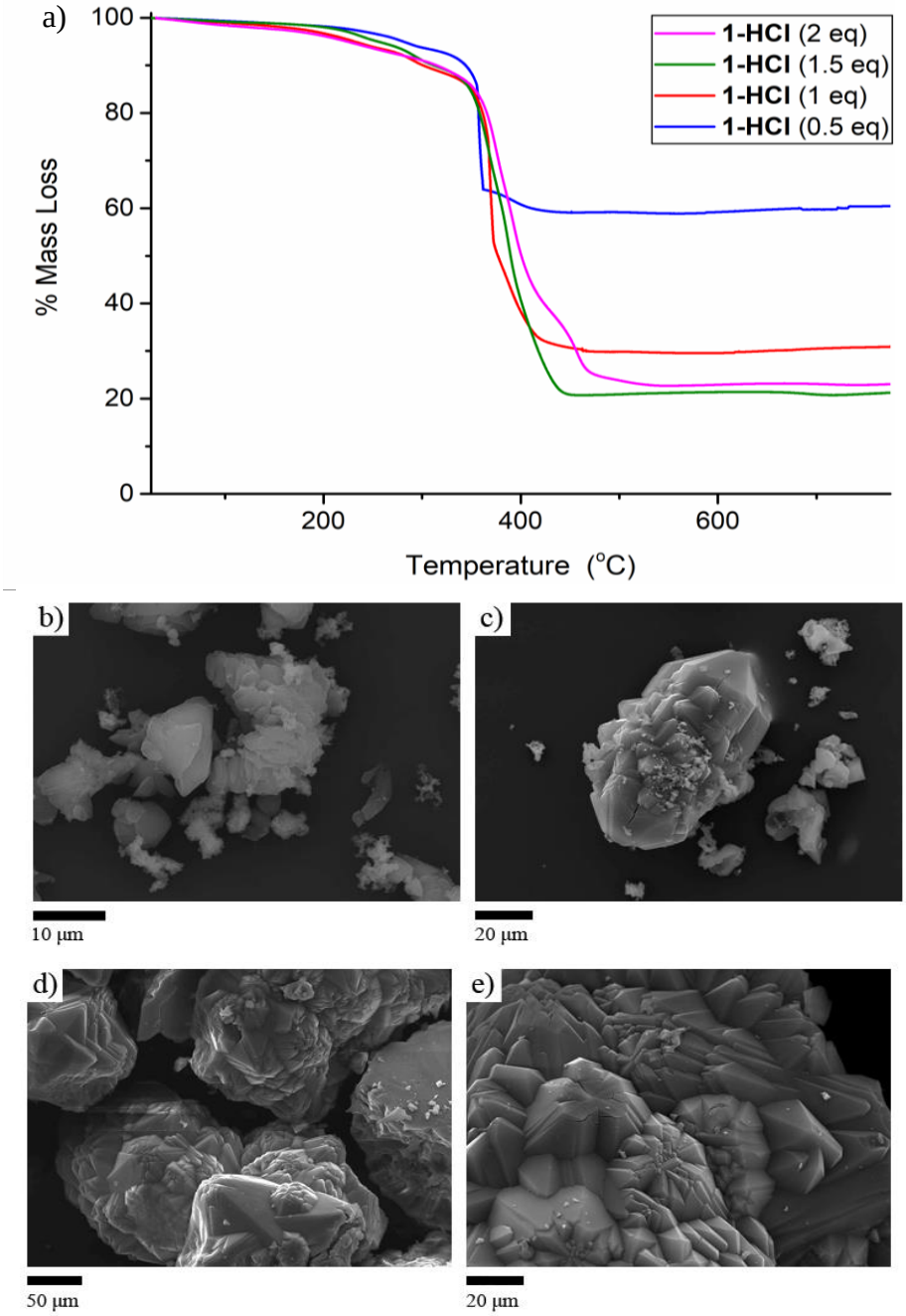

Figure 2.22. Characterisation data for samples of **1-HCl** prepared using different molar equivalents of HCl: a) TGA curves. SEM images for b) 0.5 eq, c) 1 eq, d-e) 1.5 eq.

2.4.5 Dichloroacetic Acid (DCA)

The use of dichloroacetic acid (DCA) as a modulator for Zr MOF syntheses can lead to its significant incorporation at defect sites, allowing it to be used as an effective probe molecule for endocytosis and anticancer drug delivery applications.[25,26] The crystallinity of the Fe materials increases with the quantity of DCA up until 0.5 equivalents, at which point it appears to inhibit MOF formation; addition of one equivalent results in no solids formed - a reflection of the significantly lower pK_a compared to acetic acid. MIL-88D(Fe) appears to be present in **1-DCA** (0.05 eq) when imaged by SEM (Figure 2.23), as it consists mainly of rods. Similar rods are present in samples modulated with up to 0.3 eq, alongside up to 30 µm, well-faceted crystals of MIL-126(Fe). The nitrogen uptake increases as the concentration of modulator increases, and there is also an increase in the hysteresis height, indicating mesoporosity. but the BET surface area is considerably lower than expected, with the highest SA_{BET} = 808 m^2 g^{-1} for **1-DCA** (0.3 eq).

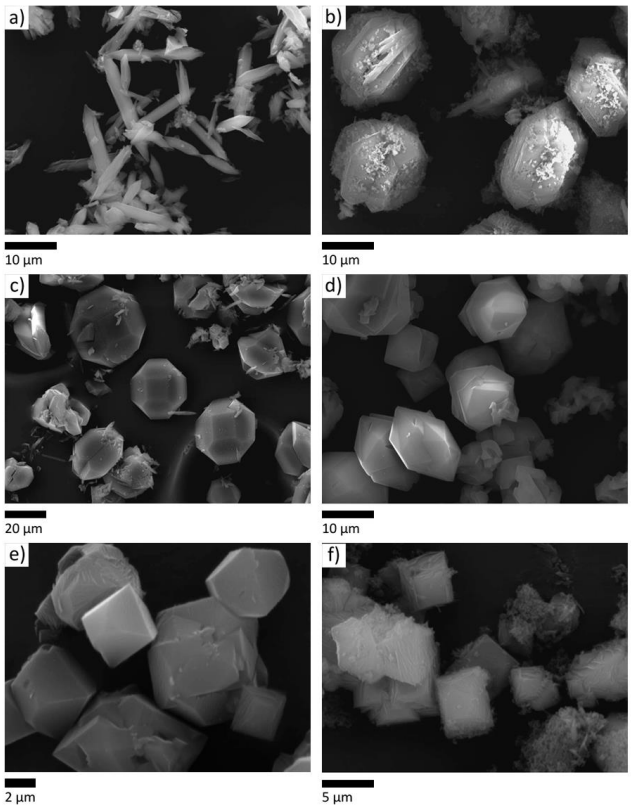

Figure 2.23. SEM images of **1-DCA** prepared with different molar equivalents of DCA: a) 0.05 eq, b) 0.1 eq, c) 0.2 eq, d) 0.3 eq, e) 0.4 eq, f) 0.5 eq.

There are several comparisons which can be made based on these results when considering the pK_a values of the carboxylate modulators. Modulators with low pK_a are expected to bind more strongly to the metal centres, as has been reported for UiO-66,[27] and slow down

nucleation and crystal growth significantly. For DCA this appears to be the case when compared to acetic acid, as the yield drops off significantly at very low concentrations (< 0.5 eq) of DCA while a comparable drop in yield is only seen for 30 equivalents of acetic acid. The crystal size of MIL-126(Fe) decreases from around 20 μm to < 5 μm as the quantity of DCA is increased from 0.2 to 0.5 equivalents, which is in line with a slower crystal growth rate.

2.4.6 Trifluoroacetic Acid (TFA)

The low pK_a of TFA (0.23 compared to 4.76 for AA) was expected to lead to more defective samples, as has been reported for UiO-66.[20] PXRD indicates that the interpenetrated MOF can be prepared with addition of 0.5-5 equivalents of TFA, but SEM revealed a significant proportion of hexagonal rods corresponding to MIL-88D(Fe) in all samples. Furthermore, the BET surface areas are relatively low, with a maximum SA_{BET} = 612 m^2 g^{-1} for **1-TFA** (5 eq), suggesting TFA is a poor modulator for this system. The effect of TFA on the synthesis of MIL-126(Fe) compared to DCA is very unusual as, despite having a much low pK_a than DCA, it can be tolerated at relatively higher concentrations (up to 5 equivalents) and does not appear to have a pronounced detrimental effect on yield: the yields are comparable to those with an equivalent molar quantity of benzoic acid.

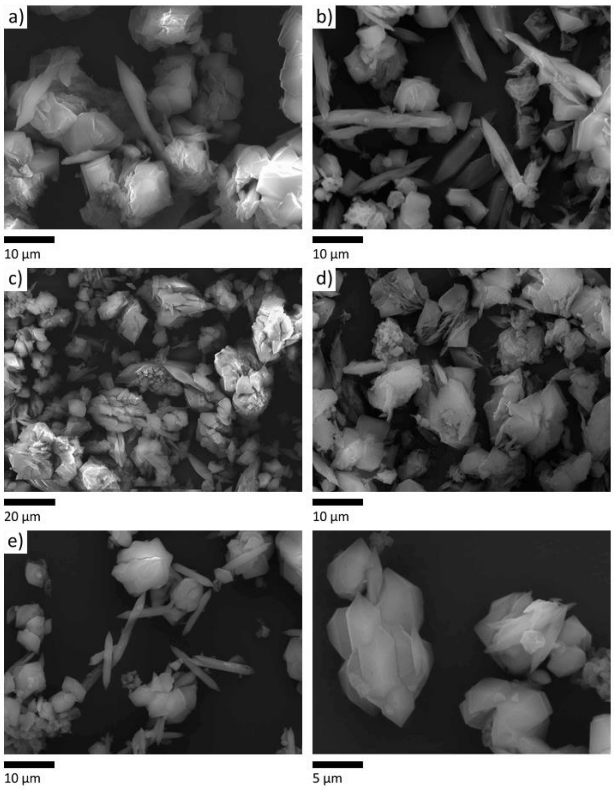

Figure 2.24. SEM images of **1-TFA** prepared with different molar equivalents of TFA: a) 1 eq, b) 2 eq, c) 3 eq, d) 4 eq, e) 5 eq.

2.4.7 Benzoic Acid (BA)

Despite BA having a comparable pK_a to AA, syntheses using 10 or more equivalents yielded clear solutions with no solid product, whereas 30 equivalents of AA could be used and still result in crystallisation. Three equivalents of BA were required to crystallise MIL-126(Fe), with PXRD and SEM (Figure 2.25) showing that fewer equivalents give MIL-88D(Fe). The use of 4 or 5 equivalents gave crystalline sheets, as was seen for higher concentration of AA, and **1-BA** (4 eq) possessed the highest porosity with SA_{BET} = 1019 m^2 g^{-1}. As with TFA, lower concentrations of benzoic acid appear to yield significant quantities of MIL-88D(Fe), which is consistent with our hypothesis that the addition of modulator favours the formation of MIL-126(Fe) as a thermodynamic product via increasing the reversibility during the self-assembly process. The lower tolerance of the synthesis for benzoic acid compared to acetic acid cannot be explained merely by pK_a values: formic acid has a lower pK_a than benzoic acid but could be tolerated at much higher concentrations (30 eq vs. 5 eq). One potential explanation is that the greater steric bulk of benzoate vs. formate has a stronger effect on disfavouring ligand substitution than the electronic effects of ligand-metal binding.

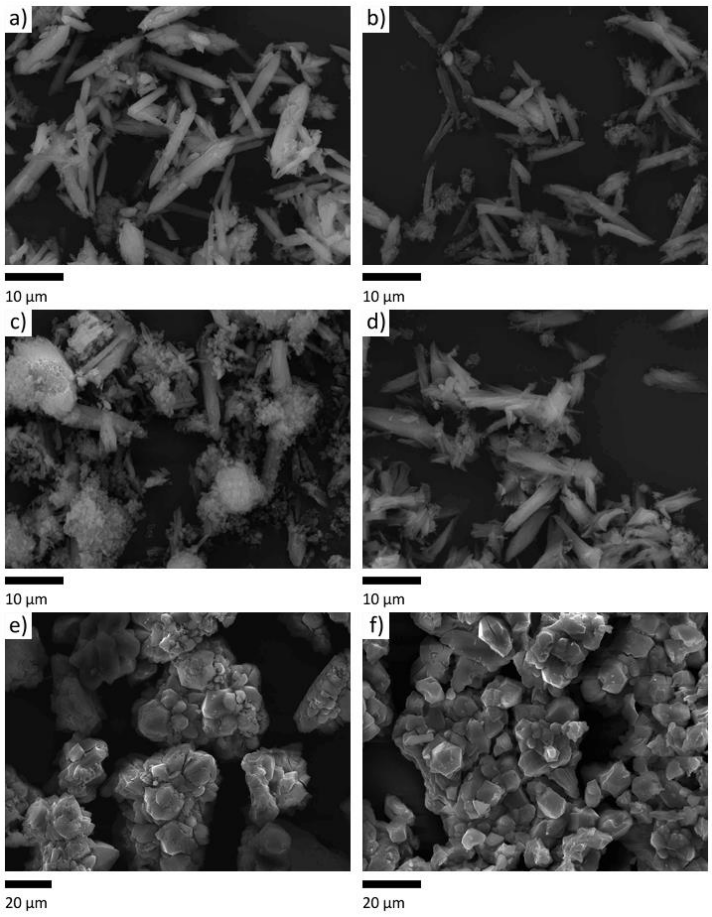

Figure 2.25. SEM images of **1-BA** prepared with different molar equivalents of BA: a) 0.5 eq, b) 1 eq, c) 2 eq, d) 3 eq, e) 4 eq, f) 5 eq.

2.4.8 Summary

In this section we have explored the effects of various modulators on the synthesis of **1** and the resultant properties. Careful optimisation is required in order to maximise the porosity and yield, as well as the phase purity. It is also important to restate here that the use of multiple characterisation techniques is crucial for assessing phase purity and sample quality, as many samples with apparently high crystallinity by PXRD turned out to have less than ideal nitrogen uptakes and other phases could be seen by SEM imaging.

2.5 Synthesis of Fe-BPYDC MOFs (2)

The intermolecular interactions between the individual nets in interpenetrated structures, in this case H-bonding between capping ligands on the SBU, are important structure-directing forces which can drive interpenetration. Within the tightly interpenetrated MIL-126 framework, π-stacking between the BPDC linkers of the individual nets is evident, enabled by the twisted conformation adopted by BPDC to meet the steric constraints of the arrangement (Figure 2.26a). Using Sc^{3+} as the metal, our group have previously shown that replacing BPDC with 2,2′-bipyridine-5,5′-dicarboxylate (BPYDC) (Figure 2.26b) prevents the formation of the interpenetrated MIL-126 phase and yields a non-interpenetrated MIL-88D phase with formula $[Sc_3O(H_2O)_2X(BPYDC)_3]$.[6] In addition to these empirical results, DFT calculations performed on the disodiated BPDC (Na_2-BPDC) and BPYDC (Na_2-BPYDC) linkers revealed that the energy minimised structure of Na_2bpdc has a C–C–C–C torsion angle of 38° (consistent with the torsion angles of 41.3° and 36.7° of the BPDC ligands in the crystal structure of MIL-126(Fe))[4], while for Na_2-BPYDC the energy minimised structure has a N–C–C–N torsion angle of 180°.[6]

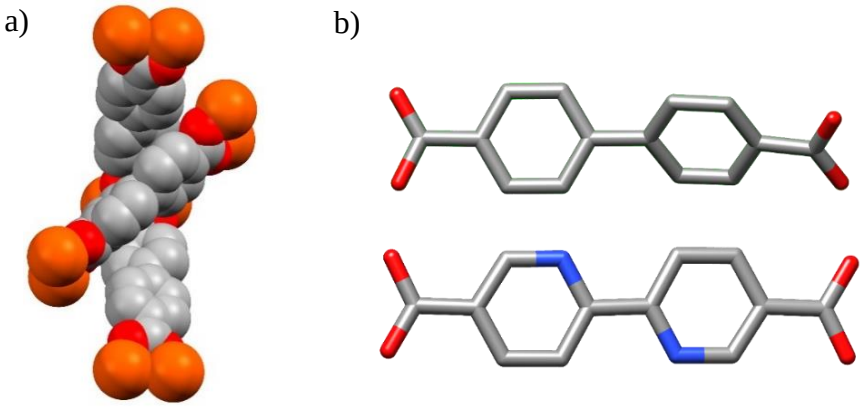

Figure 2.26. Space-fill model of a section of the crystal structure of MIL-126(Fe),[4] b) crystal structures of H_2BPDC[28] and H_2BPYDC.[29]

New DFT calculations carried out by collaborators (see Section **Error! Reference source not found.**) suggest that a hypothetical MIL-126(Fe) form incorporating BPYDC is highly destabilised due to the distortions of the BYPDC linker, such that only 30 kJ mol^{-1} per sub-lattice is gained on interpenetrating two MIL-88D sub-lattices, whilst for BPDC, 92 kJ mol^{-1} per sub-lattice is liberated on interpenetrating two MIL-88D sub-lattices, indicating a much stronger thermodynamic driving force to form the MIL-126(Fe) topology for the more flexible BPDC linker compared to BPYDC. These calculations correlate with our previous crystallographic database mining, which confirmed that BPYDC preferentially adopts a

planar conformation in the solid-state.[6] To examine the analogous Fe-BPYDC system, solvothermal synthesis was performed at 120 °C both with and without use of a modulator. The samples prepared with this linker are hereafter named "**2-mod** (x eq)" where mod is the modulator used and x = the number of equivalents of modulator added to the synthesis with respect to Fe.

Comparison of the PXRD patterns for samples of **2** and the open and closed forms of MIL-88(Fe) (Figure 2.27a) suggests that most of the samples, apart from unmodulated **2**, possess a similar hexagonal unit cell, with varying degrees of "openness". Some of the additional peaks present in **2-TFA** (5 eq) and the other samples could possibly correspond to a previously reported Fe-BPYDC coordination polymer with formula [Fe(H_2O)(BPYDC)],[30] however, the PXRD patterns do not suitably correlate to confirm this (Figure 2.27b). Despite the apparent structural differences between the samples, none of them appear to contain the MIL-126(Fe) phase, suggesting that the difference in conformation between BPYDC and BPDC is significant enough to disfavour interpenetration, as previously observed in Sc analogues.[6]

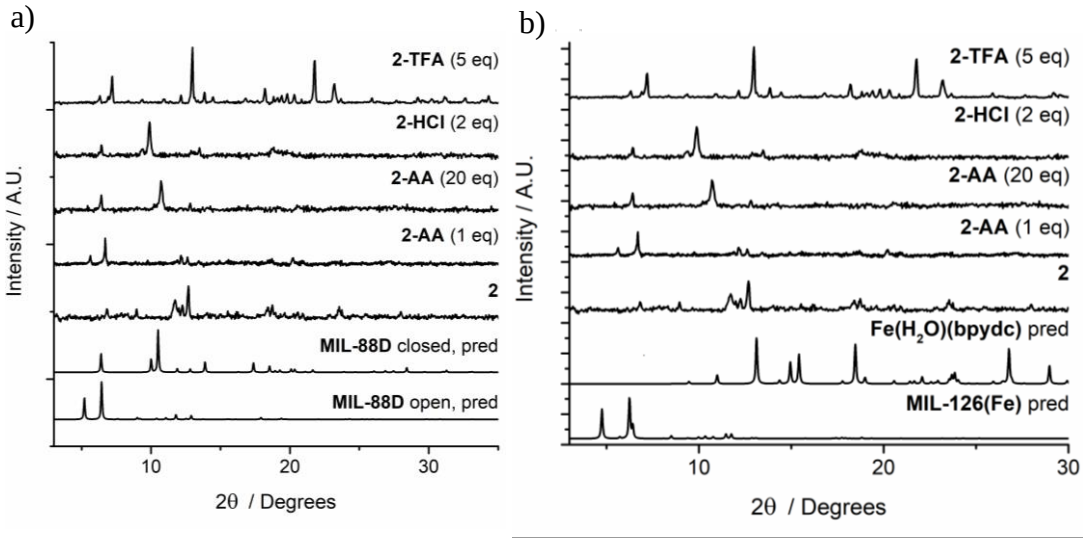

Figure 2.27. Comparison of the predicted PXRD patterns of the open and closed forms of MIL-88D(Fe) (patterns predicted from simulated structures[4,7]) with the experimental PXRD patterns of samples of **2**. b) Comparison of the predicted PXRD patterns of MIL-126(Fe) and [Fe(H_2O)(BPYDC)][30] with the experimental PXRD patterns of samples of **2**.

The TGA profiles for the samples (Figure 2.28) show that the samples degrade at approximately 350 °C, similar to the modulated samples of **1**. An initial mass loss is seen in all of the samples before 100 °C, likely due to the removal of residual solvent from the pores, after which there are slight differences between the samples. **2**, **2-AA** (1 eq), and **2-HCl** (2

eq) have very similar profiles, while in **2-AA** (20 eq) and **2-TFA** (5 eq) the framework degradation steps appear to be significantly broader. **2-TFA** (5 eq) also has an additional mass loss between 250-300 °C, which could be due to the departure of coordinated TFA.

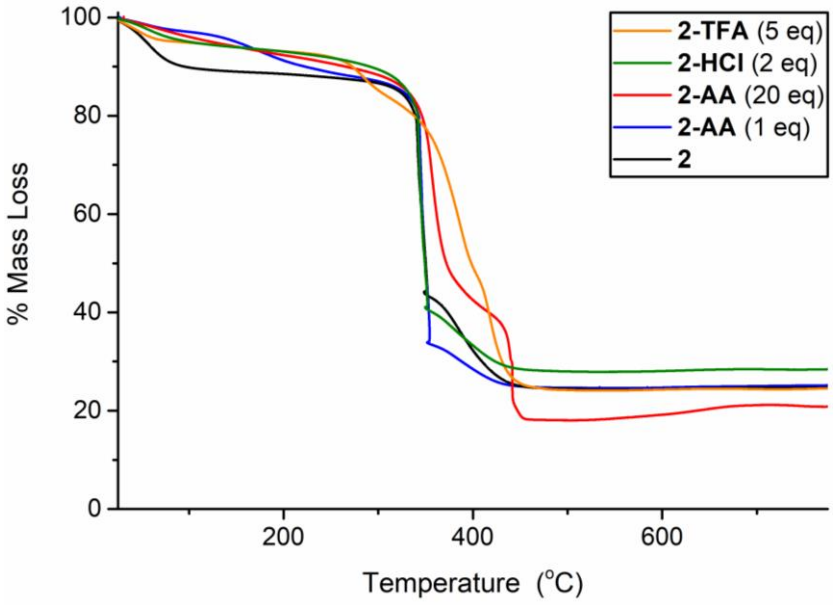

Figure 2.28. TGA curves for samples of **2** prepared using different modulators.

SEM imaging (Figure 2.29) shows that **2-TFA** (5 eq) has a similar morphology to MIL-88D samples prepared from BPDC, which could suggest that it is the BPYDC analogue of MIL-88D(Fe), despite the differences in both the PXRD pattern and TGA profile. Similar shaped crystals are present for **2-AA** (1 eq), **2-AA** (2 eq), and **2-HCl** (2 eq), although there appear to be other phases present in each of these samples. **2** consists of plates, similar to those reported for $[Fe(H_2O)(BPYDC)]$[30] – which was prepared using iron(II) perchlorate in a 50:50 mix of DMF/H_2O – however, **2** is not sufficiently crystalline to confirm this by PXRD.

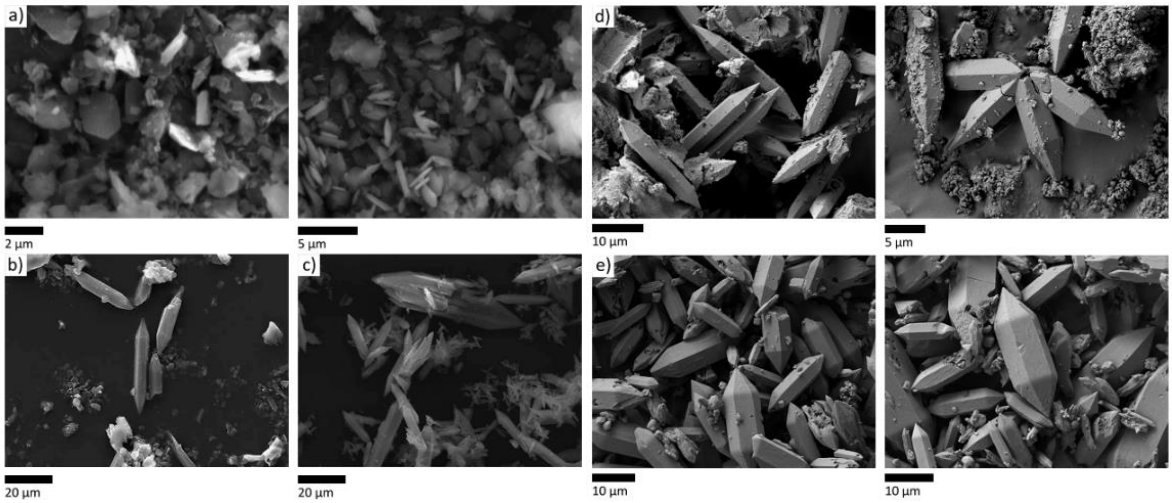

Figure 2.29. SEM images of samples of **2**. a) 1, b) **2-AA** (1 eq), c) **2-AA** (20 eq), d) **2-HCl** (2 eq), e) **2-TFA** (5 eq).

Attempts were made to obtain single crystals of Fe-BPYDC to confirm the MIL-88D structure, following a procedure similar to recent work by Zhou *et al.* which uses pre-formed Fe-oxo-clusters and acetic acid to regulate the crystal growth.[14] The acetate capped Fe^{III}-oxo-cluster was first synthesised according to the literature procedures (Section 2.8.6). The synthesis of the MOFs was conducted in DMF at 150 °C for 18 h with the quantity of AA varied to obtain single crystals suitable for single-crystal X-ray diffraction. Syntheses resulted in two distinct crystal forms which could not be isolated phase pure, named **3** and **4** respectively, and did not correspond to either MIL-126 or MIL-88D topologies. Crystals of each form were analysed by single crystal X-ray diffraction (SCXRD) to elucidate their structures.

3 crystallises as green plates (Figure 2.30a) in the tetragonal $P4_32_12$ space group, with linear trinuclear SBUs (Figure 2.30b) containing two crystallographically independent iron atoms (Fe1 and Fe2) both of which adopt six-coordinated distorted octahedral geometries. The central iron atom (Fe2) is coordinated to four oxygen atoms from four different BPYDC linkers equatorial to the SBU, two each bridging to each Fe1 in the (η_1:η_1:μ_2) motif, with two μ_2-oxo bridges at axial positions also bridging to each Fe1. The second iron atom (Fe1) is therefore coordinated by two oxygens from two different BPYDC linkers, one μ_2-oxo bridge, one oxygen from a disordered monodentate formate/acetate ligand and terminated by two nitrogen donors from a single BPYDC linker. The carboxylate coordination results in a paddlewheel-like square grid which is overlaid by another through the bipyridyl coordination, resulting in a tetragonal net (Figure 2.30c) with potential porosity. **3** is structurally related to two analogues containing five-coordinate Zn^{2+} centres which have bridging carboxylates (one with formate, reported as JLU-Liu4, and one with acetate) in place of the oxo-bridges,[31,32] and a mixed-metal MOF with formula $[Fe^{III}_2Co^{II}(BPYDC)_2(O)_2(H_2O)_2]$ which was prepared in a similar manner using oxo-centred mixed-metal clusters.[15]

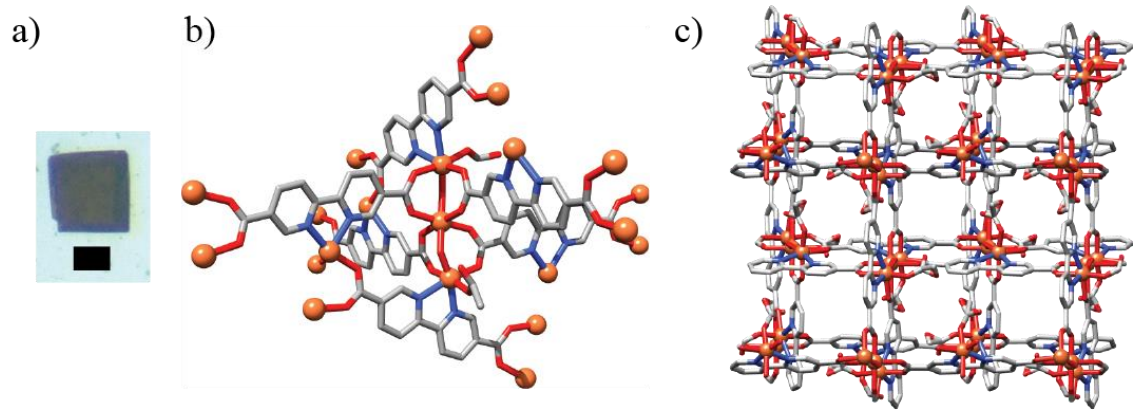

Figure 2.30. a) Image of a single crystal of **3**. b) Trinuclear SBU found in the crystal structure of **3**. c) Packing structure of **3** viewed down the *c* axis. Scale bar: 100 μm. H atoms and disorder removed from crystal structure images for clarity.

4 crystallises as orange rods (Figure 2.31a) in the orthorhombic Fddd space group, and consists of $Fe_2(RCO_2)_4$ paddlewheels (Figure 2.31b) containing one crystallographically independent iron atom (Fe1, related by a two-fold rotation axis) in a distorted octahedral geometry capped at either end by bidentate bipyridyl units. Each SBU is linked by four dicarboxylates to form 2D layers in a diamond array, and these layers are linked together into a 3D network through the bipyridyl linkages to give diamond-shaped channels when viewed down the *a* axis (Figure 2.31c), similar to those in the iron terephthalate MIL-53(Fe). Isostructural variants have previously been reported for Mn^{2+} (reported as JLU-Liu11)[33] and Cd^{2+}.[34]

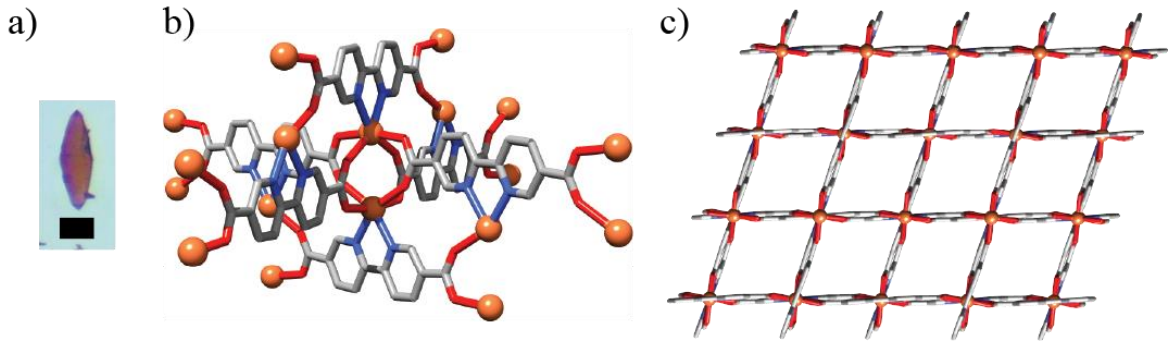

Figure 2.31. a) Image of a single crystal of **4**. b) Dinuclear paddlewheel SBU found in the crystal structure of **4**. c) Packing structure of **4** viewed down the *a* axis. Scale bar: 100 μm.

The BVS calculations for **3** are consistent with a valence of +3 for each of the crystallographically independent Fe atoms, giving V_i values of 3.021 and 3.091 for Fe1 and Fe2, respectively. The formate anion seen in the structure is one of the products from the hydrolysis of DMF, which is known to occur near its boiling point (153 °C). It is therefore assumed that dimethylamine is present within the pores to balance the framework charge,

making the overall formula $[H_2NMe_2][Fe^{III}_3(BPYDC)_2(O)_2(OAc)(HCO_2)]_n$. While dimethylamine could not be modelled crystallographically, this is unsurprising as it would only be half occupied per asymmetric unit and would overlap with electron density from solvent molecules. The BVS for **4** is consistent with a valence of +2, with a V_i value of 2.155, giving an overall formula of $[Fe^{II}(BPYDC)]_n$ which is consistent with what can be seen crystallographically. In both cases, rather than preserving the Fe_3O cluster by simple substitution of the acetates by BPYDC, decomposition allows formation of linear clusters with chelating nitrogen groups capping each end. In the case of **4** there is also a reduction of Fe^{3+} to Fe^{2+} during synthesis.

Variation of the relative ratios of the linker and acetate cluster could be used to tune between these two phases: an approximate 1:1 cluster:linker molar ratio yielded predominantly **3**, **4** was the dominant phase when this was reduced to 0.5:1. To assess the phase-purity of the samples, PXRD patterns were collected by depositing the wet crystals onto a zero background XRD holder made of Si. PXRD analysis (Figure 2.32a) suggested that both samples are phase pure, but each sample visually contained a small proportion of the other crystal form. The PXRD pattern for **4** differs significantly from the predicted pattern due to preferred orientation caused by the rod-shaped nature of the crystallites (Figure 2.32b).

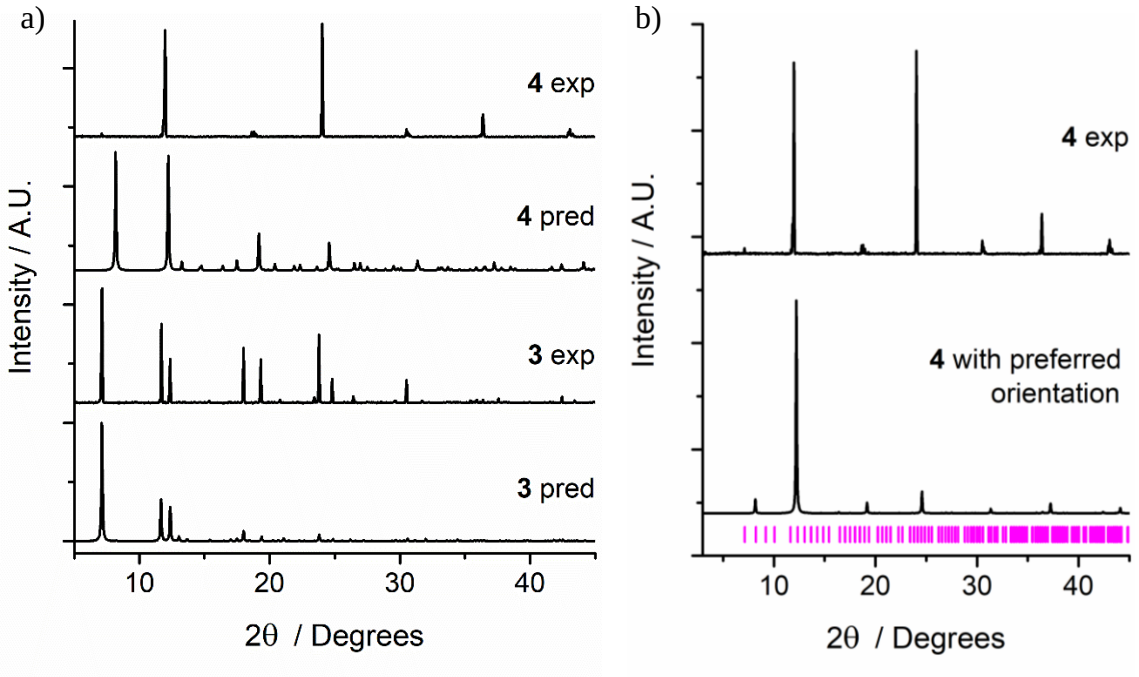

Figure 2.32. Stacked PXRD patterns of: a) **3** and **4** compared to those predicted from their crystal structures. b) **4** compared to the pattern predicted from its crystal structure with preferred orientation modelled.

The interpenetrated MIL-126 phase is not present in any of these samples, regardless of the conditions used, consistent with the results of the DFT study on this system. The tendency for coordination to the metal by the N-donors makes formation of the MIL-88D challenging. Nevertheless, it is seemingly possible to produce a phase-pure sample, despite the possibility of also forming **3** and **4**, with a further reported structure $[Fe^{II}(BPYDC)(H_2O)]\cdot H_2O$ previously isolated from hydrothermal synthesis with $FeCl_2$ adding to the complexity of the system.[30]

Reassessment of the PXRD patterns for the modulated samples of **2** (Figure 2.33) shows that **3** and **4** are not present in any significant quantity, suggesting that they can only be isolated from the iron acetate trimer, despite the trimer decomposing during synthesis.

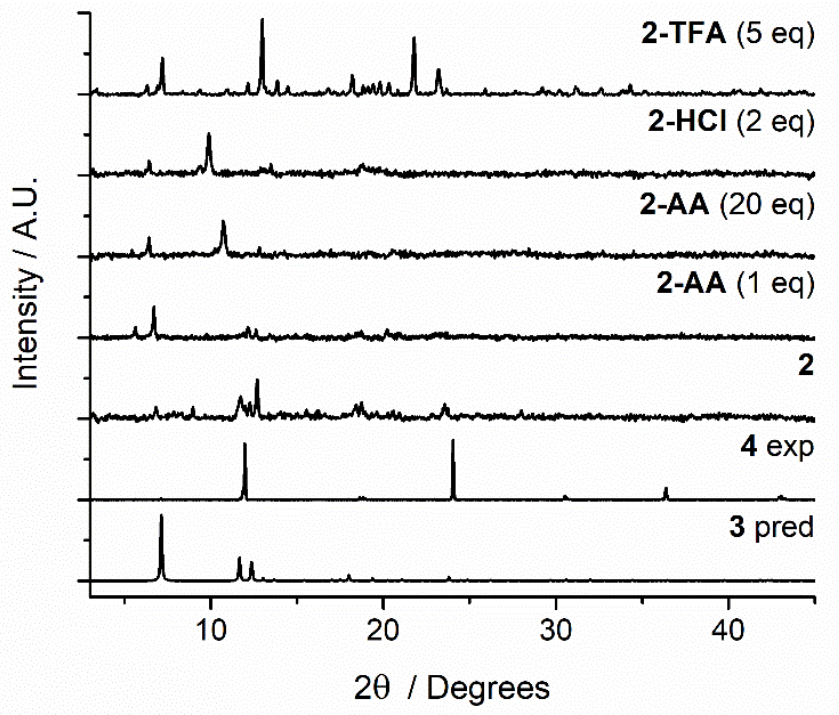

Figure 2.33. Comparison of the predicted PXRD pattern of **3** and experimental pattern of **4** with the experimental PXRD patterns of samples of **2**.

Microwave reactions were also carried out with $FeCl_3\cdot 6H_2O$ and H_2BPYDC in DMF in an analogous way to those performed with BPDC (Section 2.3) in order to see if a MIL-88-type structure could be favoured. The PXRD patterns (Figure 2.34) show peaks corresponding to **4** are present in most of the products, which seems to crystallise best with higher temperature and longer synthesis time, likely due to the in-situ reduction of Fe^{3+} to Fe^{2+} required to form **4**. These results show that even under the conditions which should favour kinetic products (rapid nucleation) the preference for the nitrogen groups in BPYDC to coordinate to metal

centres makes synthesis of phase-pure MIL-88D more challenging than was the case with BPDC.

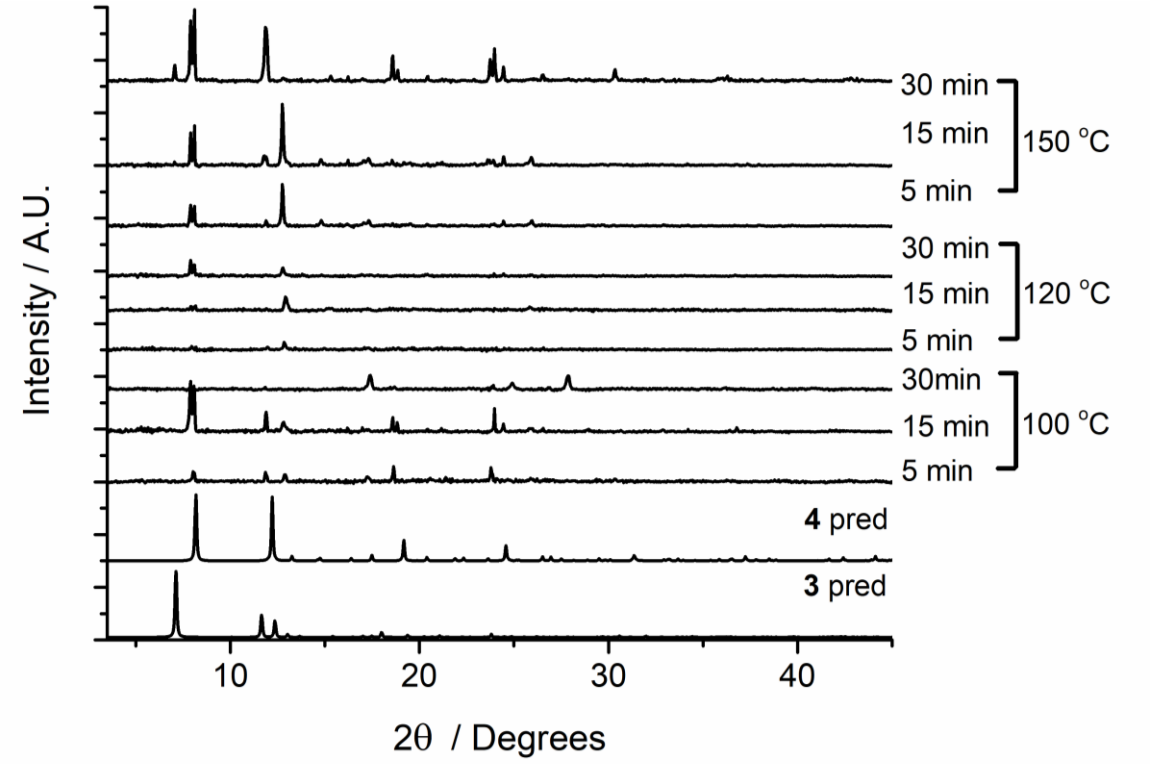

Figure 2.34. Stacked PXRD patterns of **2** synthesised under microwave-assisted heating with different heating parameters.

2.6 Solvothermal Synthesis of Fe-BPDC MOFs (1′)

Despite the improvements in phase-purity and sample quality obtained via modulation of **1**, most of the BET surface areas fell quite short of the theoretical value for MIL-126(Fe) (SA_{BET} = 2550 m^2g^{-1})[4] and in most cases the yields were also quite low (<50 %). We decided to explore alternative iron-precursors as it was expected they would have a crucial influence on the synthesis. While Fe^{3+} salts are generally used to synthesise Fe^{3+} MOFs, there are several examples where Fe^{2+} salts have been used.[35-40] While there are a plethora of inexpensive and commercially available Fe^{2+} salts, $FeCl_2{\cdot}4H_2O$ was selected so that the counterions are kept consistent to avoid potential anion templating affects[41] perturbing self-assembly. Based on the results using $FeCl_3{\cdot}6H_2O$, only acetic acid (1 and 20 eq) and HCl (1 eq) were explored as modulators, as well as performing an unmodulated synthesis (we have termed the samples **1′** to indicate the use of Fe^{2+} starting materials).

It would be expected that the necessary autoxidation of Fe^{2+} to Fe^{3+} in DMF would slow the self-assembly process and therefore lead to the thermodynamic product; in this case with BPDC linkers, the interpenetrated phase. Accordingly, only MIL-126(Fe) is obtained when $FeCl_2$ is used as the Fe source (Figure 2.35a), even without modulator, where $FeCl_3$ gives MIL-88D(Fe) under identical conditions. An alternative possible product MOF-106, $[Fe^{II}(BPDC)(DMF)]_n$, has previously been reported from a sealed solvothermal synthesis using a DMF/propanol mixture at 120 °C,[42] but no corresponding reflections for this phase were evident in the PXRD patterns. TGA analysis (Figure 2.35b) suggests that the samples have the same ideal framework formula as the other MIL-126(Fe) samples of $[Fe_3O(BPDC)_3(H_2O)_2X]$.

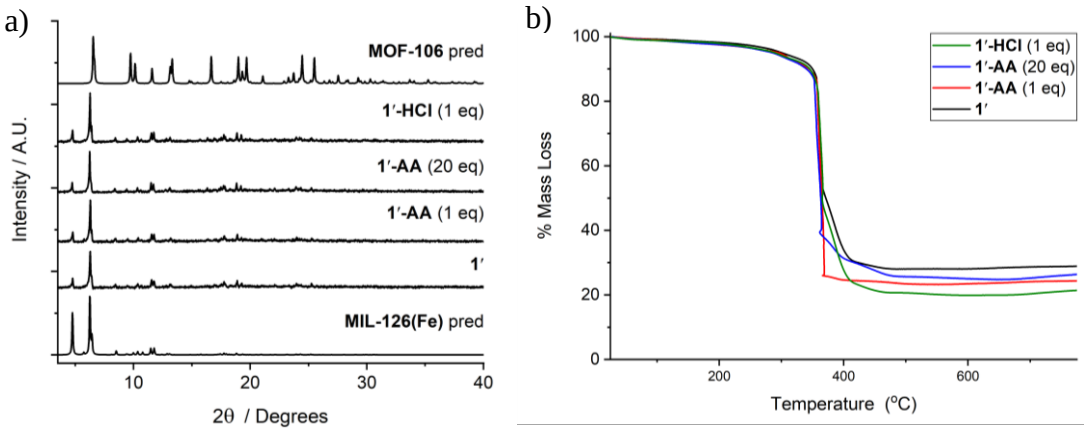

Figure 2.35. Stacked PXRD patterns of samples of **1′** compared to the simulated patterns for MIL-126(Fe) and MOF-106 (CCDC code AGAXIP[42]). b) TGA curves for samples of **1′** prepared using different modulators.

Compared to samples synthesised using $FeCl_3$, the mass loss prior to framework degradation is very little (<5 %), suggesting that they have been more efficiently dried. N_2 isotherms (Figure 2.36a) confirm that all of the modulated samples are highly porous, with corresponding BET surface areas (Figure 2.36b) above 1600 m^2g^{-1}. The unmodulated sample has a reasonable N_2 uptake (SA_{BET} = 637 m^2g^{-1}), which suggests that the use of Fe^{2+} favours the formation of MIL-126(Fe), in line with the PXRD results. Modulation greatly enhances the porosity, and the addition of just 1 molar equivalent of acetic acid to the synthesis was enough to achieve the highest BET surface area reported so far for MIL-126(Fe) (SA_{BET} = 2416 m^2g^{-1}) which is close to the theoretical value for MIL-126(Fe) (SA_{BET} = 2550 m^2g^{-1}).[4] Even where relatively high gas uptake was achieved using $FeCl_3$, the yields were relatively low, whereas for $FeCl_2$ all the samples had yields greater than 80%.

a)

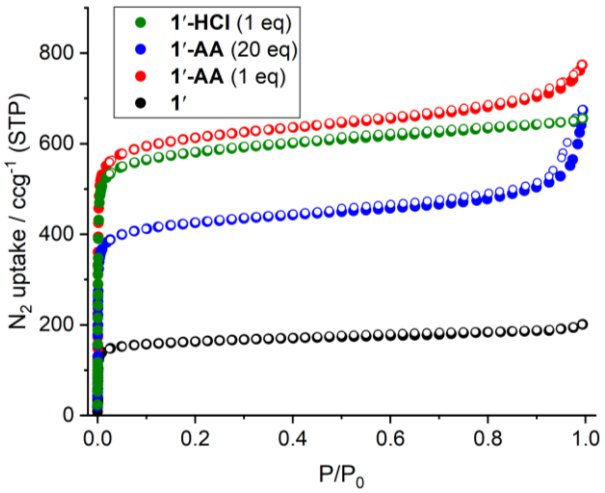

b)

Sample	SA_{BET} / m^2 g^{-1}
1′	637
1′-AA (1 eq)	2416
1′-AA (20 eq)	1670
1′-HCl (1 eq)	2294

Figure 2.36. a) Comparison of nitrogen adsorption (closed circles) and desorption (open circles) isotherms (77 K) of unmodulated and modulated samples of **1′**. b) BET surface areas for unmodulated and modulated samples of **1′**.

SEM imaging (Figure 2.37) reveals that all the samples consist predominantly of MIL-126 crystals, although smaller crystals can also be seen on the surfaces of **1′** and **1′-AA** (20 eq). There are significant number of intergrown crystals present in all the samples, but many single crystals area also visible in **1′-AA** (1 eq) and **1′-HCl** (1 eq).

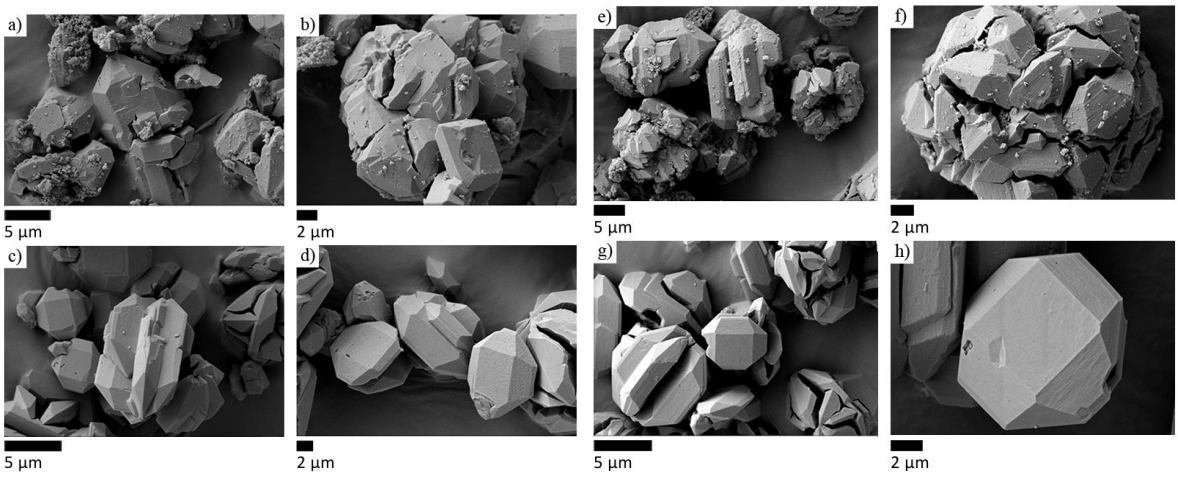

Figure 2.37. SEM images of **1′**. a) **1′**, b) **1′-AA** (1 eq), c) **1′-AA** (20 eq), d) **1′-HCl** (1 eq).

The lack of mesoporous defects and the overall enhancement in sample quality suggest that the crystallisation process occurs differently compared to the equivalents using Fe^{3+} salts. The formation of MIL-126(Fe) indicates oxidation of Fe^{2+} to Fe^{3+}, which is a requirement for the formation of the Fe_3O clusters present in the framework. However, a mixed-valence cluster $[M^{III}_2M^{II}O]$ is also possible; recently this has been exploited[15] to construct MOFs with $[Fe^{III}_2M^{II}O(RCO_2)_6]$ SBUs. ^{57}Fe Mössbauer spectroscopy was used to investigate the Fe oxidation states; two samples were prepared in an identical manner, other than changing the iron source from Fe^{3+} to Fe^{2+}, with 1 eq of HCl as modulator to enhance sample quality while avoiding defect induction. As thermal treatment is reported to reduce Fe^{3+} to Fe^{2+} in MIL-126(Fe),[4] these samples were activated under vacuum only in order to assess the oxidation state of the Fe in the as-synthesised form.

The spectra of **1-HCl** (1 eq), prepared from $FeCl_3$, and **1′-HCl** (1 eq), prepared from $FeCl_2$, have single quadrupolar doublets and show no discernible differences (Figure 2.38). The isomer shifts and quadrupolar splittings are consistent with homovalent $[Fe^{III}_3O(RCO_2)_6]$ SBUs for both samples when compared to data from discrete complexes[43-46] and analogous MOFs,[47] confirming complete oxidation of Fe^{2+} to Fe^{3+} in the synthesis of **1′-HCl** (1 eq).

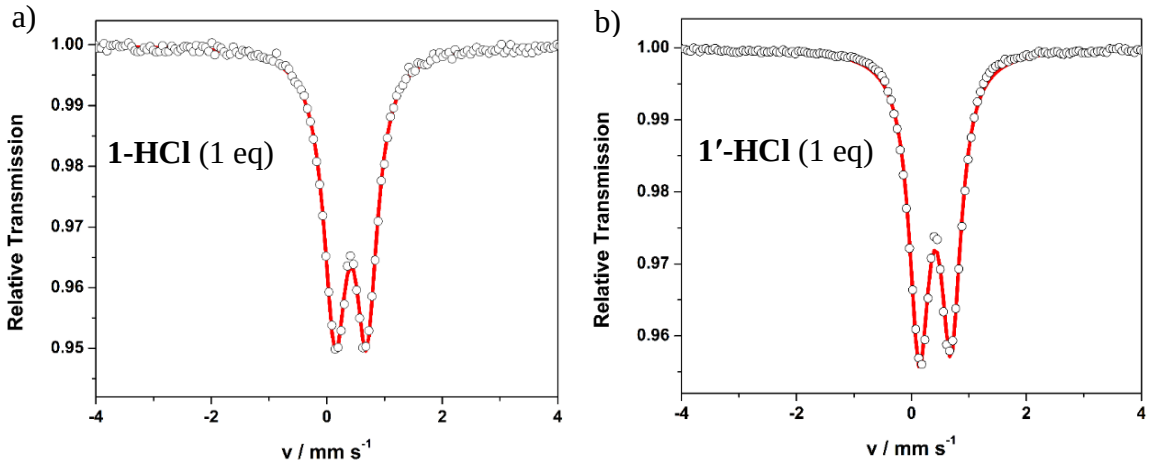

Figure 2.38. Zero-field ^{57}Fe Mössbauer spectra recorded at 290 K of a) **1-HCl** (1 eq). The red solid line represents the fit with a Lorentzian doublet to the experimental values (circles) using the following isomer shift, quadrupole splitting and line width: $\delta = 0.42$ mm s^{-1}, $|\Delta E_Q| = 0.55$ mm s^{-1}, $\Gamma_{FWHM} = 0.45$ mm s^{-1}. b) **1′-HCl** (1 eq). The red solid line represents the fit with a Lorentzian doublet to the experimental values (circles) using the following isomer shift, quadrupole splitting and line width: $\delta = 0.41$ mm s^{-1}, $|\Delta E_Q| = 0.55$ mm s^{-1}, $\Gamma_{FWHM} = 0.42$ mm s^{-1}.

There are multiple potential mechanisms to be considered such as oxidation first in solution and then self-assembly, self-assembly of clusters and/or framework and then oxidation, or even dynamic redox and self-assembly. The presence of Fe^{2+} during synthesis, which is a softer Lewis acid, may increase ligand lability, coordinative reversibility, and "error-checking", thus reducing defectivity and enhancing crystallinity in the resulting MOFs. This could explain the success of this synthetic approach and why only a relatively small amount of modulator (1 equiv of AA) is required to induce dramatic enhancements to the porosity of **1′**. A similar observation has been reported elsewhere for the iron(III) trimesate MIL-100(Fe) when synthesised using an Fe^{2+} salt, with higher crystallinity and porosity achieved from room temperature syntheses without requiring HF.[40] These results show that tuning of the initial oxidation state of the metal – a process we term oxidation modulation – is also a potential strategy for controlling the phase purity, as well as physical properties of the resulting MOFs, by providing additional kinetic barriers during the self-assembly process.[48]

To summarise, we have shown that oxidation modulation is a potent strategy for controlling interpenetration and achieving phase pure MIL-126(Fe). The ability to obtain high-quality MIL-126(Fe) without the apparent admixture of MIL-88D(Fe) or any significant defectivity is valuable and makes this material much more viable for future applications, particularly as ferrous chloride tetrahydrate is also relatively inexpensive.

2.7 Conclusions

To conclude, the synthesis of MIL-126/MIL-88D type MOFs based on Fe^{3+} and BPDC and BPYDC has been investigated, and controllable synthetic routes to both interpenetrated and non-interpenetrated materials have been established. When using BPDC as the linker, coordination modulation has been demonstrated to slow the self-assembly process to favour the interpenetrated MIL-126(Fe) framework as the thermodynamic product, while the non-interpenetrated framework MIL-88D(Fe) appears to be a kinetic product that can only be obtained through unmodulated synthesis at relatively low temperatures (≤120 °C). DFT simulations show a strong preference for the arrangement of capping species in MIL-126 that is not evident for MIL-88D, for both Fe^{3+} and Sc^{3+} analogues, indicating that the thermodynamics of correlated anion disorder influence the formation of MIL-126(Fe). By varying the quantity and identity of the modulator added during synthesis, it is possible to tune between these two crystal phases and also control the size, morphology, and defectivity of the interpenetrated MOF. Significantly, PXRD analysis alone is not able to determine phase purity of MIL-126(Fe); SEM images show appreciable quantities of MIL-88D(Fe) in many samples which do not diffract strongly and detract from the porosity of the bulk material.

The use of BPYDC in place of BPDC inhibits the formation of the interpenetrated MIL-126(Fe) phase as a consequence of the prohibitively distorted linker conformation required, as previously demonstrated for Sc^{3+} analogues, and confirmed by new DFT calculations and modulated experiments. In contrast to Sc^{3+}, Fe^{3+} can coordinate to the bipyridyl N-donors and form MOFs with different topologies to MIL-88D, which can also be isolated under specific modulation conditions. Interestingly, one of the frameworks (**4**) contains Fe^{2+}, despite the synthesis utilising an Fe^{3+} precursor, which indicates that in-situ reduction has occurred, and this could be used as a strategy to access other Fe^{2+} MOFs. Both new structures are non-interpenetrated and possess significant potential void space, however, phase-pure samples of either MOF could not be obtained on a large enough scale for further investigation.

Finally, the use of an Fe^{2+} salt as starting material effectively slows the synthesis to favour interpenetration and, when combined with modulation, greatly enhances the porosity of the resulting MOF without inducing defectivity. Our results with the Fe-BPDC system suggest that oxidation modulation - the deliberate use of metal precursors in different oxidation states to that found in the resulting MOF - could be used in other MOF systems to favour

thermodynamic products (Figure 2.39). In addition, the overall greater sample quality suggests that oxidation modulation could also be a simple and effective synthetic tool for preparing high quality MOFs with improved physical properties crystallinity and porosity.

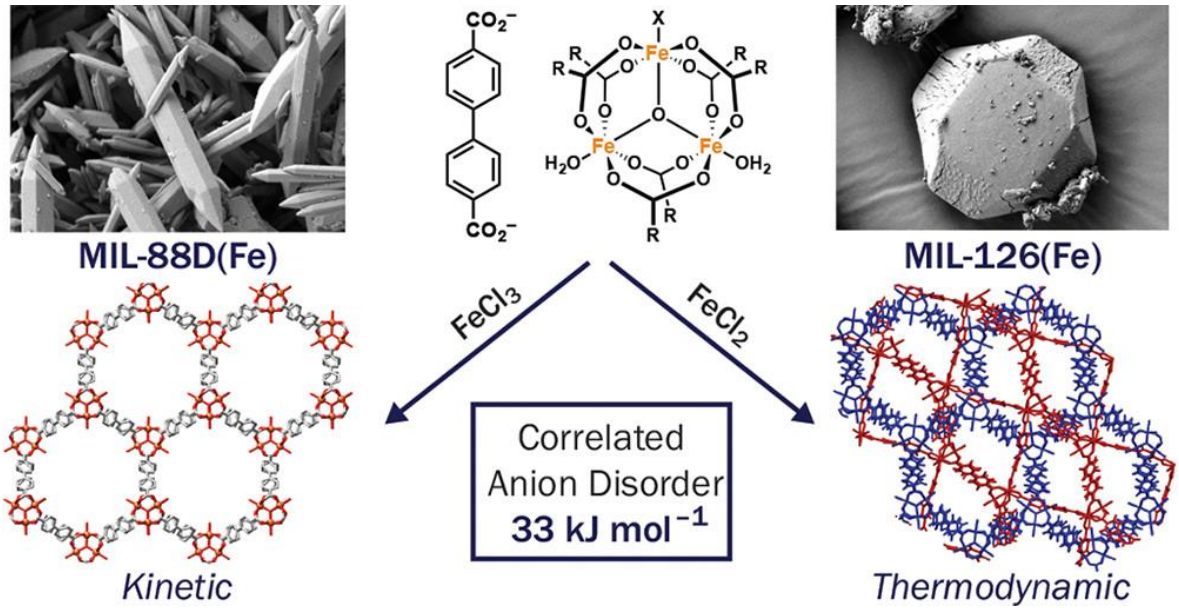

Figure 2.39. Schematic view of oxidation modulation as a tool to control between the kinetic phase MIL-88D(Fe) and the thermodynamic phase MIL-126(Fe).[5]

There is a lot of potential scope to use these techniques with other Fe-MOF systems, some of which will be explored in the next chapter which focuses on the Fe-terephthalate system.

2.8 Experimental

2.8.1 General Experimental Methods

All starting materials were purchased from commercial sources and used without further purification.

Powder X-Ray Diffraction (PXRD): PXRD measurements were carried out at 298 K using a PANalytical X'Pert PRO diffractometer (λ (CuKα) = 1.5405 Å) on a mounted bracket sample stage. The data was collected over the range 3-45 ° and the pulse height discrimination (PHD) lower level was raised to 45% to filter out some of the low-energy X-rays caused by fluorescence from iron. Where background subtraction was performed, the program HighScore Plus was used to process the data and remove the background. Every instance of this is indicated in the relevant figure caption.

Microwave Synthesis: Microwave reactions were performed in 35 ml pressure vials using a CEM Discover SP microwave, equipped with an Explorer 12 Hybrid autosampler. The power was allowed to fluctuate to maintain a constant temperature throughout the reaction.

Single Crystal X-Ray Diffraction (SCXRD): Data for **3** and **4** were collected using a Bruker D8 VENTURE diffractometer (MoK_α = 0.71073 Å).

Scanning Electron Microscopy (SEM): Powders were deposited onto carbon tabs mounted on aluminium stubs, these were subsequently coated with Pd for 150 seconds using a Polaron SC7640 sputter coater. Samples of **1-DCA, 1-TFA,** and **1-BA** were imaged using a Philips XL30 ESEM. All other samples were imaged using a Carl Zeiss Sigma variable Pressure Analytical SEM with Oxford Microanalysis.

Thermogravimetric Analysis (TGA): Measurements were carried out using a TA Instruments Q500 Thermogravimetric Analyser. Measurements were collected from room temperature to 800 °C with a heating rate of 10 °C min^{-1} under an air atmosphere.

Gas Uptake: N_2 adsorption and desorption isotherms were carried out at 77 K on a Quantachrome Autosorb iQ gas sorption analyser. Samples were degassed under vacuum at 150 °C for 20 hours using the internal turbo pump. BET surface areas were calculated from the isotherms using the Micropore BET Assistant in the Quantachrome ASiQwin operating software.

^{57}Fe Mössbauer Spectroscopy: Mössbauer data were recorded on a spectrometer with alternating constant acceleration. The minimum experimental line width was 0.24 mm s^{-1}

(full width at half-height). The field at the sample is perpendicular to the γ-beam. Isomer shifts are quoted relative to iron metal at 300 K.

2.8.2 Solvothermal Synthesis of 1

Biphenyl-4,4′-dicarboxylic acid (121 mg, 0.5 mmol) was added to a 50 mL Pyrex jar, *N*,*N*-dimethylformamide (DMF) (30 mL) was added and the mixture was sonicated to achieve a homogeneous suspension. Iron(III) chloride hexahydrate (270 mg, 1 mmol) was then added and the resulting mixture was heated in an isothermal oven at 120 °C for 48 hours. After allowing to cool naturally to room temperature, the solid was collected by centrifugation (4500 rpm, 15 minutes) and subsequently washed with DMF (3 x 30 mL) and then dichloromethane (DCM) (3 x 30 mL) before drying overnight in a vacuum desiccator at room temperature. Prior to thermal analysis, the samples were dried at 80 °C in an oven overnight. The modulated syntheses follow the same procedure except that the modulator was added prior to sonication.

2.8.3 Microwave Synthesis of 1

Biphenyl-4,4′-dicarboxylic acid (81 mg, 0.33 mmol) was added to a 35 mL microwave vial, then DMF (20 mL) was added and sonicated to achieve a homogeneous suspension. Iron(III) chloride hexahydrate (180 mg, 0.66 mmol) was added and the vial was sealed and heated in a microwave (250 watts) for either 5, 15, or 30 minutes without stirring. After allowing to cool to room temperature, the solid was collected by centrifugation (4500 rpm, 15 minutes) and subsequently washed with DMF (3 x 30 mL) and then DCM (3 x 30 mL) before drying overnight in a vacuum desiccator at room temperature. The synthesis time and temperature were varied in order to optimise the conditions for obtaining pure-phase MIL-88D (Fe). The modulated syntheses follow the same procedure except that acetic acid (0.572 mL, 10 mmol) was added prior to sonication.

2.8.4 Synthesis of 2

2,2′-Bipyridine-5,5′-dicarboxylic acid (122 mg, 0.5 mmol) was added to a 50 mL Pyrex jar, DMF (30 mL) was added and sonicated to achieve a homogeneous suspension. Iron(III) chloride hexahydrate (270 mg, 1 mmol) was added and the resulting mixture was heated in an isothermal oven at 120 °C for 48 hours. After removing from the oven and allowing to cool naturally to room temperature, the solid was collected by centrifugation (4500 rpm, 15 minutes) and subsequently washed with DMF (3 x 30 mL) and then DCM (3 x 30 mL) before drying overnight in a vacuum desiccator at room temperature.

2.8.5 Synthesis of Fe-BPDC MOFs using Fe^{2+}

Biphenyl-4,4′-dicarboxylic acid (121 mg, 0.5 mmol) was added to a 50 mL Pyrex jar, DMF (30 mL) was added and sonicated to achieve a homogeneous suspension. Iron(II) chloride tetrahydrate (199 mg, 1 mmol) was added and the resulting mixture was heated in an isothermal oven at 120 °C for 48 hours. After removing from the oven and allowing to cool naturally to room temperature, the solid was collected by centrifugation (4500 rpm, 15 minutes) and subsequently washed with DMF (3 x 30 mL) and then DCM (3 x 30 mL) before drying overnight in a vacuum desiccator at room temperature. Prior to thermal analysis, the samples were dried at 80 °C in an oven overnight. Modulated syntheses were prepared in an identical manner except that the modulator was added prior to sonication.

2.8.6 Synthesis of $Fe_3O(OAc)_6$ cluster

$[Fe_3O(CH_3COO)_6(H_2O)_3]Cl{\cdot}6H_2O$ clusters were prepared by dissolving $FeCl_3{\cdot}6H_2O$ (8.11 g, 30 mmol) in H_2O (10 mL) at 50 °C. Separately, sodium acetate trihydrate (8.16 g, 60 mmol) was dissolved in H_2O (10 mL) at 50 °C. These solutions were then combined and stirred at 50 °C for 10 minutes before leaving to cool down to room temperature. Large dark red cubic crystals formed within 2 weeks and were collected by filtration followed by washing with diethyl ether multiple times. The product was dried under vacuum at room temperature overnight and the crystals were ground down to a fine powder for PXRD analysis. Yield: 2.867 g, 39%. Comparison of the PXRD pattern with the reported structure confirms its identity.

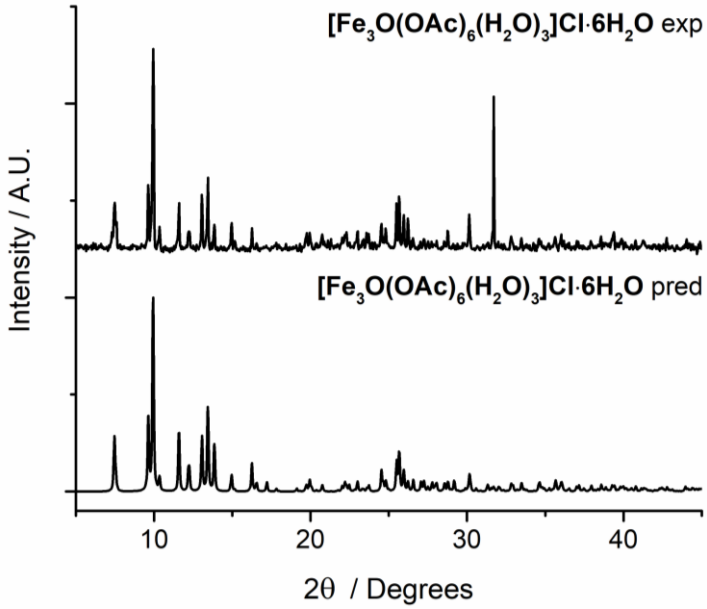

Figure 2.40. PXRD pattern of synthesised $Fe_3O(OAc)_6$ clusters compared to the simulated PXRD pattern from the reported crystal structure (CCDC Refcode RIPLEH[49]).

2.8.7 Synthesis of 3 and 4

2,2′-Bipyridine-5,5′-dicarboxylic acid and $[Fe_3O(CH_3COO)_6(H_2O)_3]Cl{\cdot}6H_2O$ were added to a 25 mL Pyrex jar. DMF (2 mL) and acetic acid (0.6 mL) were added and the mixture were sonicated until a homogeneous suspension was achieved. Once tightly capped, the jar was placed in an isothermal oven at 150 °C for approximately 18 hours. After allowing to cool to room temperature, the solvent was replaced multiple times with fresh DMF before the solid was characterised by powder and single-crystal X-ray diffraction. For powder-X-ray diffraction, solid was transferred with solvent via pipette onto a silicon zero background holder and then excess solvent was removed before collecting the data. The quantities of H_2BPYDC and $Fe_3O(OAc)_6$ used to prepare **3** and **4** are given in Table 2.2.

Table 2.2. Molar quantities of salt and ligand used in the synthesis of **3** and **4**.

Sample name	**Quantity of H_2BPYDC / mg**	**mmols**	**Quantity of $Fe_3O(OAc)_6$ / mg**	**mmols**
3	5	0.02	10	0.014
4	5	0.02	5	0.007

2.8.8 Crystal data for 3

$Fe_3(O)_2(C_{12}H_6N_2O_4)(COO)(CH_3COO)$, M_r = 787.99, crystal dimensions 0.18 × 0.13 × 0.02 mm, Tetragonal, $a = b$ = 15.1681 (11) Å, c = 21.4872 (18) Å, V = 4943.59 Å^3, T = 150 K, space group $P4_32_12$ (No. 96), Z = 4, 32912 measured reflections, 6119 independent reflections (R_{int} = 0.047), which were used in all calculations. The final R_1 = 0.030 for 6119 observed data $R[F^2 > 2\sigma(F^2)]$ and $wR(F^2)$ = 0.079 (all data).

2.8.9 Crystal data for 4

$Fe_2(C_{12}H_6N_2O_4)_2$, M_r = 596.08, crystal dimensions 0.28 × 0.07 × 0.06 mm, Orthorhombic, a = 16.224 (2) Å, b = 18.154 (3), c = 18.154 (3) Å, V = 7064.31 Å^3, T = 150 K, space group *Fddd*, (No. 70), Z = 8, 2046 measured reflections, 2046 independent reflections (R_{int} = 0.045), which were used in all calculations. The final R_1 = 0.046 for 2046 observed data $R[F^2 > 2\sigma(F^2)]$ and $wR(F^2)$ = 0.111 (all data).

2.9 References

(1) Horcajada, P., Chalati, T., Serre, C., Gillet, B., Sebrie, C., Baati, T., Eubank, J. F., Heurtaux, D., Clayette, P., Kreuz, C., Chang, J.-S., Hwang, Y. K., Marsaud, V., Bories, P.-N., Cynober, L., Gil, S., Férey, G., Couvreur, P. and Gref, R., *Nat. Mater.*, **2010**, *9*, 172-178.

(2) Tamames-Tabar, C., Cunha, D., Imbuluzqueta, E., Ragon, F., Serre, C., Blanco-Prieto, M. J. and Horcajada, P., *J. Mater. Chem. B*, **2014**, *2*, 262-271.

(3) McGuire, C. V. and Forgan, R. S., *Chem. Commun.*, **2015**, *51*, 5199-5217.

(4) Dan-Hardi, M., Chevreau, H., Devic, T., Horcajada, P., Maurin, G., Férey, G., Popov, D., Riekel, C., Wuttke, S., Lavalley, J.-C., Vimont, A., Boudewijns, T., de Vos, D. and Serre, C., *Chem. Mater.*, **2012**, *24*, 2486-2492.

(5) Bara, D. J., Wilson, C., Mörtel, M., Khusniyarov, M. M., Ling, S., Slater, B., Sproules, S. and Forgan, R. S., *J. Am. Chem. Soc.*, **2019**.

(6) Marshall, R. J., Lennon, C. T., Tao, A., Senn, H. M., Wilson, C., Fairen-Jimenez, D. and Forgan, R. S., *J. Mater. Chem. A*, **2018**, *6*, 1181-1187.

(7) Horcajada, P., Salles, F., Wuttke, S., Devic, T., Heurtaux, D., Maurin, G., Vimont, A., Daturi, M., David, O., Magnier, E., Stock, N., Filinchuk, Y., Popov, D., Riekel, C., Férey, G. and Serre, C., *J. Am. Chem. Soc.*, **2011**, *133*, 17839-17847.

(8) Li, Y., Liu, Y., Gao, W., Zhang, L., Liu, W., Lu, J., Wang, Z. and Deng, Y.-J., *CrystEngComm*, **2014**, *16*, 7037-7042.

(9) Jhung, S. H., Lee, J.-H., Yoon, J. W., Serre, C., Férey, G. and Chang, J.-S., *Adv. Mater.*, **2007**, *19*, 121-124.

(10) Marshall, R. J., Hobday, C. L., Murphie, C. F., Griffin, S. L., Morrison, C. A., Moggach, S. A. and Forgan, R. S., *J. Mater. Chem. A*, **2016**, *4*, 6955-6963.

(11) Toby, B. H. and Von Dreele, R. B., *J. Appl. Crystallogr., 46(2)*, 544-549.

(12) Mejia-Ariza, R. and Huskens, J., *J. Mater. Chem. B*, **2016**, *4*, 1108-1115.

(13) Pham, M.-H., Vuong, G.-T., Vu, A.-T. and Do, T.-O., *Langmuir*, **2011**, *27*, 15261-15267.

(14) Feng, D., Wang, K., Wei, Z., Chen, Y.-P., Simon, C. M., Arvapally, R. K., Martin, R. L., Bosch, M., Liu, T.-F., Fordham, S., Yuan, D., Omary, M. A., Haranczyk, M., Smit, B. and Zhou, H.-C., *Nat. Comm.*, **2014**, *5*, 5723.

(15) Peng, L., Asgari, M., Mieville, P., Schouwink, P., Bulut, S., Sun, D. T., Zhou, Z., Pattison, P., van Beek, W. and Queen, W. L., *ACS Appl. Mater. Interfaces*, **2017**, *9*, 23957-23966.

(16) Helm, L. and Merbach, A. E., *Chem. Rev.*, **2005**, *105*, 1923-1960.

(17) Schaate, A., Roy, P., Godt, A., Lippke, J., Waltz, F., Wiebcke, M. and Behrens, P., *Chem. Eur. J.*, **2011**, *17*, 6643-6651.

(18) Morris, W., Wang, S., Cho, D., Auyeung, E., Li, P., Farha, O. K. and Mirkin, C. A., *ACS Appl. Mater. Interfaces*, **2017**, *9*, 33413-33418.

(19) Sawano, T., Thacker, N. C., Lin, Z., McIsaac, A. R. and Lin, W., *J. Am. Chem. Soc.*, **2015**, *137*, 12241-12248.

(20) Shearer, G. C., Chavan, S., Bordiga, S., Svelle, S., Olsbye, U. and Lillerud, K. P., *Chem. Mater.*, **2016**, *28*, 3749-3761.

(21) Xu, R., Wang, Y., Duan, X., Lu, K., Micheroni, D., Hu, A. and Lin, W., *J. Am. Chem. Soc.*, **2016**, *138*, 2158-2161.

(22) Yuan, S., Zou, L., Li, H., Chen, Y.-P., Qin, J., Zhang, Q., Lu, W., Hall, M. B. and Zhou, H.-C., *Angew. Chem. Int. Ed.*, **2016**, *55*, 10776-10780.

(23) Bosch, M., Yuan, S., Rutledge, W. and Zhou, H.-C., *Acc. Chem. Res.*, **2017**, *50*, 857-865.

(24) Katz, M. J., Brown, Z. J., Colón, Y. J., Siu, P. W., Scheidt, K. A., Snurr, R. Q., Hupp, J. T. and Farha, O. K., *Chem. Commun.*, **2013**, *49*, 9449-9451.

(25) Abánades Lázaro, I., Abánades Lázaro, S. and Forgan, R. S., *Chem. Commun.*, **2018**, *54*, 2792-2795.

(26) Abánades Lázaro, I., Haddad, S., Sacca, S., Orellana-Tavra, C., Fairen-Jimenez, D. and Forgan, R. S., *Chem*, **2017**, *2*, 561-578.

(27) Van de Voorde, B., Stassen, I., Bueken, B., Vermoortele, F., De Vos, D., Ameloot, R., Tan, J.-C. and Bennett, T. D., *J. Mater. Chem. A*, **2015**, *3*, 1737-1742.

(28) Øien-Ødegaard, S., Bouchevreau, B., Hylland, K., Wu, L., Blom, R., Grande, C., Olsbye, U., Tilset, M. and Lillerud, K. P., *Inorg. Chem.*, **2016**, *55*, 1986-1991.

(29) Wang, C., *Acta Cryst. E.*, **2009**, *65*, o2081.

(30) Finn, R. C. and Zubieta, J., *Solid State Sci.*, **2002**, *4*, 83-86.

(31) Wang, J., Luo, J., Zhao, J., Li, D.-S., Li, G., Huo, Q. and Liu, Y., *Cryst. Growth Des.*, **2014**, *14*, 2375-2380.

(32) Bon, V., Kavoosi, N., Senkovska, I., Müller, P., Schaber, J., Wallacher, D., Többens, D. M., Mueller, U. and Kaskel, S., *Dalton Trans.*, **2016**, *45*, 4407-4415.

(33) Wang, J., Jing, X., Cao, Y., Li, G., Huo, Q. and Liu, Y., *CrystEngComm*, **2015**, *17*, 604-611.

(34) Liu, Y., *CSD Private Communication*, **2016**, YADGIW.

(35) Choi, S. B., Seo, M. J., Cho, M., Kim, Y., Jin, M. K., Jung, D.-Y., Choi, J.-S., Ahn, W.-S., Rowsell, J. L. C. and Kim, J., *Cryst. Growth Des.*, **2007**, *7*, 2290-2293.

(36) Cairns, A. J., Eckert, J., Wojtas, L., Thommes, M., Wallacher, D., Georgiev, P. A., Forster, P. M., Belmabkhout, Y., Ollivier, J. and Eddaoudi, M., *Chem. Mater.*, **2016**, *28*, 7353-7361.

(37) Yoon, J. H., Choi, S. B., Oh, Y. J., Seo, M. J., Jhon, Y. H., Lee, T.-B., Kim, D., Choi, S. H. and Kim, J., *Catal. Today*, **2007**, *120*, 324-329.

(38) Sanselme, M., Grenèche, J.-M., Riou-Cavellec, M. and Férey, G., *Solid State Sci.*, **2004**, *6*, 853-858.

(39) Sudik, A. C., Côté, A. P. and Yaghi, O. M., *Inorg. Chem.*, **2005**, *44*, 2998-3000.

(40) Guesh, K., Caiuby, C. A. D., Mayoral, Á., Díaz-García, M., Díaz, I. and Sanchez-Sanchez, M., *Cryst. Growth Des.*, **2017**, *17*, 1806-1813.

(41) Vuong, G.-T., Pham, M.-H. and Do, T.-O., *CrystEngComm*, **2013**, *15*, 9694-9703.

(42) Eddaoudi, M., Kim, J., Vodak, D., Sudik, A., Wachter, J., O'Keeffe, M. and Yaghi, O. M., *Proc. Natl. Acad. Sci. U.S.A.*, **2002**, *99*, 4900-4904.

(43) Dziobkowski, C. T., Wrobleski, J. T. and Brown, D. B., *Inorg. Chem.*, **1981**, *20*, 671-678.

(44) Oh, S. M., Kambara, T., Hendrickson, D. N., Sorai, M., Kaji, K., Woehler, S. E. and Wittebort, R. J., *J. Am. Chem. Soc.*, **1985**, *107*, 5540-5541.

(45) Sato, T., Ambe, F., Endo, K., Katada, M., Maeda, H., Nakamoto, T. and Sano, H., *J. Am. Chem. Soc.*, **1996**, *118*, 3450-3458.

(46) Fernandes, C., Stadler, E., Drago, V., Jorge da Cunha, C. and Hiroko Kuwabara, I., *Spectrochim. Acta A*, **1996**, *52*, 1815-1821.

(47) Ma, M., Noei, H., Mienert, B., Niesel, J., Bill, E., Muhler, M., Fischer, R. A., Wang, Y., Schatzschneider, U. and Metzler-Nolte, N., *Chem. Eur. J.*, **2013**, *19*, 6785-6790.

(48) Bosch, M., Sun, X., Yuan, S., Chen, Y.-P., Wang, Q., Wang, X. and Zhou, H.-C., *Eur. J. Inorg. Chem.*, **2016**, *2016*, 4368-4372.

(49) Anson, C. E., Bourke, J. P., Cannon, R. D., Jayasooriya, U. A., Molinier, M. and Powell, A. K., *Inorg. Chem.*, **1997**, *36*, 1265-1267.

Chapter 3

Synthesis and Flexibility of Fe-terephthalate Frameworks

Contributions

A significant proportion of the synthetic work in this chapter was carried out by Emily Meekel (University of Glasgow) under my direct supervision. Single-crystal data collection and structure refinement were carried out by Claire Wilson (University of Glasgow). All other synthetic work, data collections, and data analysis was performed solely by me.

Contents

Chapter 3 ..... **91**

3.1 Introduction **94**

3.2 Aims **96**

3.3 Synthesis of Fe-terephthalate MOFs **97**

3.3.1 Initial Modulation Scans 97

3.3.2 Assessing the Kinetic and Thermodynamic Relationships Between Phases 100

3.3.3 Summary 106

3.4 Variation of the Fe-precursor **109**

3.4.1 Summary 113

3.5 Flexibility of MIL-53(Fe) **114**

3.5.1 Solvent exchanges in MIL-53(Fe) 114

3.5.2 Summary 118

3.6 Conclusions and Future Work **119**

3.7 Experimental **121**

3.7.1 General Experimental Methods 121

3.7.2 General Conditions for Fe-terephthalate MOF Synthesis 121

3.7.3 Single-Crystal Synthesis of MIL-53(Fe)_DMF 122

3.7.4 MIL-53(Fe)_DMSO 122

3.7.5 Single-Crystal Synthesis of $[Fe_3O(DMF)_3(BDC)_3][BF_4]$ 122

3.7.6 Single-Crystal Synthesis of [Fe(DMF)(BDC)] 123

3.7.7 Crystal data for MIL-53(Fe)_DMF 123

3.7.8 Crystal data for of $[Fe_3O(DMF)_3(BDC)_3][BF_4]$ 123

3.7.9 Crystal data for [Fe(DMF)(BDC)] 123

3.8 References **124**

3.1 Introduction

As discussed previously, metal-organic frameworks based on iron have attracted particular attention for bio-applications due to the endogenous nature of iron, which makes them desirable as benign carriers for therapeutic drugs.[1] Fe-MOFs also comprise a larger subgroup of robust frameworks, compared to most MOFs containing M^{2+} cations, and thus are desirable for applications where both their low toxicity and relative stability can be utilised.

There has been significant interest in the Fe-terephthalate framework MIL-88B(Fe) due to its flexible nature whereby it displays a breathing amplitude of 136% between the closed and open pore forms of the material.[2] Despite the clear interest expressed by the volume of publications aiming to study its properties,[2-8] we have identified several examples where other phases have been incorrectly assigned as MIL-88B(Fe).[4,6-9] The main challenge encountered is that there is another framework known as MOF-235(Fe) with formula $[Fe_3O(BDC)_3(DMF)_3][FeCl_4]$[10] (Section 1.3.2) which is topologically identical to MIL-88B(Fe), making it particularly challenging to distinguish between the two phases. Furthermore, despite their similarities, the two frameworks behave completely differently: MIL-88B(Fe) has a highly flexible structure while MOF-235(Fe) is practically rigid. Therefore, it is crucial to determine how the synthetic conditions can be manipulated to selectively synthesise these solids.

Synthetic protocols are frequently modified by researchers based on their requirements and/or available equipment, and this is particularly the case with MOFs. For example, there are countless synthetic procedures for the widely studied Zr-terephthalate framework UiO-66, where the parameters can vary wildly while all yielding the same phase. However, there are cases where these changes in the synthetic conditions, however small, make it impossible to accurately predict the product of a given reaction mixture, particularly when multiple competing structures can crystallise in the same phase space. In Chapter 2 we looked at the Fe-4,4′-biphenyl dicarboxylate system and explored how the addition of a modulator and changing the initial oxidation state of the metal precursor could be used to tune between two polymorphic phases: non-interpenetrated MIL-88D(Fe) and interpenetrated MIL-126(Fe). For Fe-terephthalates the phase space appears to be far more complex, as depending on the synthesis conditions, at least 8 distinct MOFs can be obtained.[2,10-15] Most of these solids have been reported to form with DMF as a solvent at temperatures in the range of 100-150 $^{\circ}$C, therefore the synthetic conditions need to be carefully controlled to achieve the desired phase in a pure form.

Knowledge of the influence synthetic parameters have on the obtained phase is crucial to find the most appropriate conditions for each MOF and also to gain an insight into the kinetic and thermodynamic relationship between them, which have implications for their stability and transformations in solvent media both during and post-synthesis. An *ex situ* high-throughput study was conducted by Stock et al.[16] which investigated the reaction products between $FeCl_3 \cdot 6H_2O$ and 2-aminoterephthalic acid, focusing on the effects of temperature, solvent, and pH on the resultant phase. It was found that, when using DMF as solvent, increasing the temperature favoured the formation of MIL-88B(Fe)_NH_2 over MIL-101(Fe)_NH_2, which confirmed that MIL-88B(Fe)_NH_2 was the thermodynamically favoured phase under these conditions. Under aqueous conditions, MIL-53(Fe)_NH_2 was the thermodynamic product relative to MIL-88B(Fe)_NH_2, while in DMF MIL-53(Fe)_NH_2 did not form under any of the conditions tested. These results are very similar to those seen with the vanadium analogues of these frameworks when using terephthalic acid as linker, where it was found that the thermodynamic stability of the phases obtained were in the order MIL-53(V)>MIL-88B(V)>MIL-101(V).[17] As for MOF-235, there has been an *in situ* study using energy-dispersive X-ray diffraction (EDXRD) which revealed that MOF-235(Fe) forms early in the synthesis (DMF, 150 $^{\circ}$C) but eventually transforms into MIL-53(Fe)[18] which provides evidence that MOF-235(Fe) is the kinetic product relative to MIL-53(Fe). A similar study on the aluminium amino-terephthalates has also found that MOF-235(Al)_NH_2 forms prior to the crystallisation of MIL-101(Al)_NH_2 when using DMF as solvent, with MIL-101(Al)_NH_2 in turn transforming into MIL-53(Al)_NH_2.[19]

Considering all of these prior studies, we can deduce that MIL-53(Fe) is a thermodynamic product relative to the other phases, but the relationship between MIL-88B(Fe) and MOF-235(Fe) is still unclear as none of these studies show their sequential formation or uncover the phase boundary between them. Therefore, we decided to conduct our own study to investigate the Fe-terephthalate phase space and address these questions.

3.2 Aims

The main aims of this chapter are:

1. Investigate the effects of varying the initial oxidation state of the metal salt, modulator concentration, temperature, and time on the crystallisation of Fe-terephthalate frameworks.
2. Explore the use of other commonly available Fe-salts in similar syntheses.
3. Conduct preliminary assessment of the flexibility of MIL-53(Fe) using single-crystal and powder X-ray diffraction techniques.

In the previous chapter we have shown that, by tuning some of the synthetic parameters that impact on the kinetics of crystallisation, namely the quantity of modulator and initial oxidation state of the metal precursor, we can reliably control between the formation of MIL-88D(Fe) and MIL-126(Fe) in MOFs containing 4,4′-biphenyl dicarboxylate linkers.[20] In this chapter we will investigate the synthesis of Fe-terephthalates and explore variation of the oxidation state of the metal-precursor, concentration of modulator, synthesis time and temperature, as well as the counterion of the metal precursor. In this study we have isolated conditions that yield high quality single crystals of MIL-53(Fe), a highly flexible framework previously only studied using PXRD, and thus we will also attempt to characterise its flexibility using single-crystal X-ray diffraction.

3.3 Synthesis of Fe-terephthalate MOFs

3.3.1 Initial Modulation Scans

To investigate the phase space, initial reactions were carried out with either $FeCl_3 \cdot 6H_2O$ (1 mmol) or $FeCl_2 \cdot 4H_2O$ (1 mmol) and terephthalic acid (1 mmol) in DMF (10 mL) at 120 °C for 24 hours. After allowing to cool naturally to room temperature, the samples were collected by centrifugation and washed with DMF (x3) and then DCM (x3) before drying under vacuum. Subsequently, the samples were analysed using PXRD in order to assess the crystalline phases present. These reactions were carried out unmodulated and with the addition of varying amounts of acetic acid to evaluate the effect of modulation on the synthesis. The naming system for these samples is **$FeCl_2$-AA**x and **$FeCl_3$-AA**x where 'x' equals the number of molar equivalents of acetic acid (**AA**) added.

The results of these initial modulation scans show that for $FeCl_3 \cdot 6H_2O$ (Figure 3.1a) without the presence of modulator, peaks corresponding to MOF-235(Fe) are present (Figure 3.1b). The addition of modulator appears to hinder its formation, and at 20 eq no corresponding peaks are evident by PXRD.

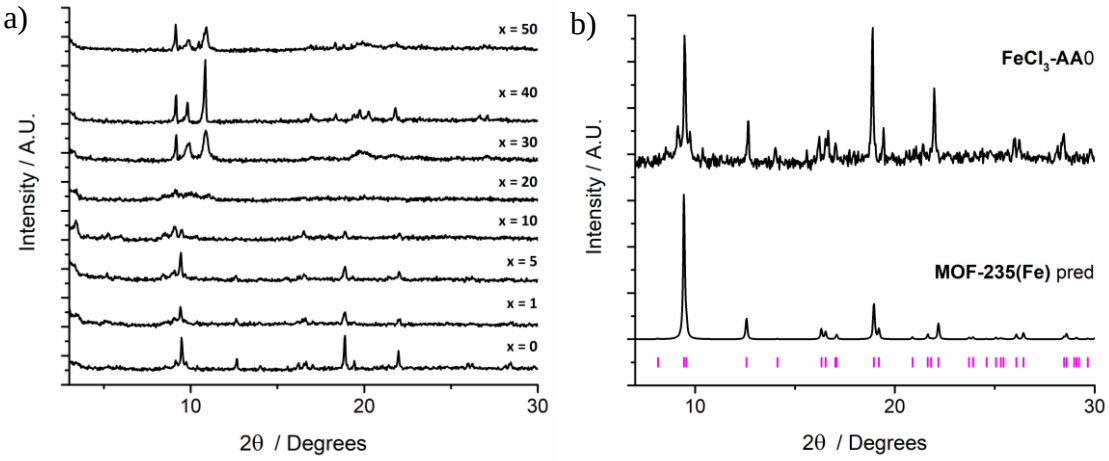

Figure 3.1. Stacked PXRD patterns of **$FeCl_3$-AA**x where 'x' is the number of molar equivalents of acetic acid (**AA**) used in the synthesis, b) comparison of the PXRD pattern of **$FeCl_3$-AA**0 with the predicted pattern of MOF-235(Fe).[10]

When 30 eq or more is used, a distinctly different phase is obtained, which resembles MIL-88B(Fe) in its "closed" state. Hexagonal rods typical of MIL-88-type frameworks could be observed by SEM imaging (Figure 3.2a). To confirm this, the procedure was repeated and the solid was washed and kept in DMF for PXRD, which enabled the pattern to be compared with the predicted pattern reported for the DMF-solvated form of MIL-88B(Fe) (Figure

3.2b). The close match of these PXRD patterns and similar unit cell obtained via a Pawley fit of the data confirmed that they possess the same structure (Figure 3.2c). The DCM-dried form of our material is not as closed as the "closed" form previously reported by Serre et al.[2] The difference in unit cell parameters between the DCM-dried sample and the reported MIL-88B(Fe) closed structure can be understood by considering the fact that the SBU in MIL-88B can have coordinated solvent molecules (up to 2 per cluster) which can prevent full closing of the framework. When heated, these coordinated solvents are removed, enabling a closer packing of the network. In fact, the reported 'as-synthesised' form of MIL-88B(Cr) has both coordinated and strongly interacting pyridine and thus a larger unit cell than the 'closed' form.[21,22] The larger size of pyridine relative to DMF may explain why the unit cell of MIL-88B(Cr) as-synthesised is larger than **FeCl$_3$-AA**40 dry (Figure 3.2c).

a)

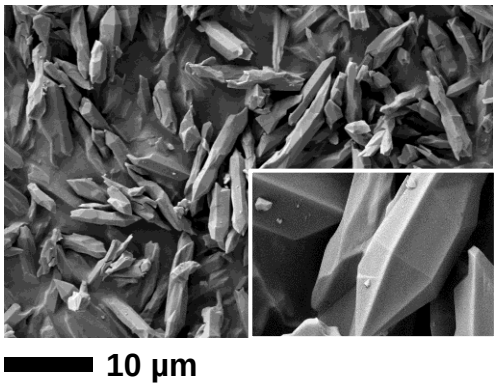

b)

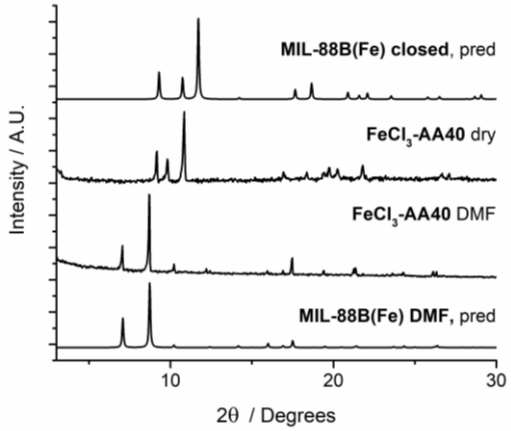

c)

Sample	FeCl$_3$-AA40 DMF	MIL-88B(Fe)_DMF	FeCl$_3$-AA40 dry	MIL-88B(Fe) closed	MIL-88B(Cr) as synthesised
a **(Å)**	14.539	14.4162	10.3926	9.500	11.028
c **(Å)**	17.244	17.3040	19.2981	19.000	18.972
V **(Å)**	3156.81	3114.43	1805.08	1485.02	1998.2

d)

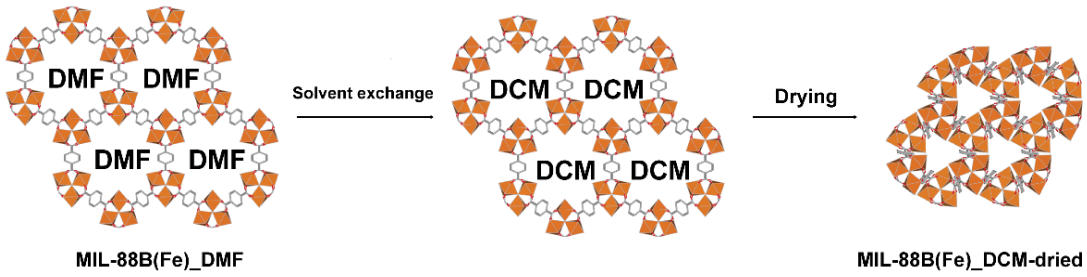

Figure 3.2. a) SEM image of **FeCl$_3$-AA**40, b) stacked PXRD patterns of **FeCl$_3$-AA**40 taken wet in DMF and after drying from DCM, compared to the predicted patterns for MIL-88B(Fe) in DMF and the closed form of MIL-88B(Fe), c) unit cell parameters from crystal structures and those extracted from Pawley refinements. d) schematic of solvent exchange and drying.

For $FeCl_2 \cdot 4H_2O$, the unmodulated synthesis displays peaks which correspond to MIL-101(Fe) (Figure 3.3a), which drop in intensity when 1 eq of acetic acid is used and then show no XRD peaks when 5-20 eq of acetic acid are used (Figure 3.3b). The samples obtained with 40 and 50 eq display peaks corresponding to MIL-88B(Fe). The preference for MIL-101(Fe) over MOF-235(Fe) when using $FeCl_2$ rather than $FeCl_3$ in unmodulated syntheses could also be due to the lower Cl^- content.

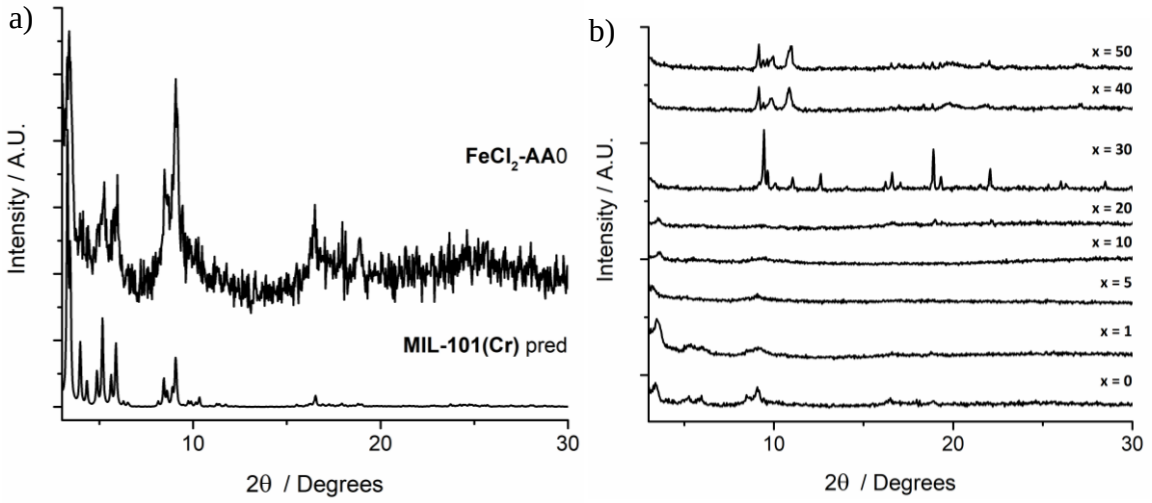

Figure 3.3. a) Comparison of the PXRD pattern of **$FeCl_2$-AA**0 with the predicted pattern for MIL-101(Cr),[23] b) stacked PXRD patterns of **$FeCl_2$-AA**x where 'x' is the number of molar equivalents of acetic acid (**AA**) used in the synthesis.

When 30 equivalents were used, a highly crystalline phase corresponding to MOF-235(Fe) was obtained, along with additional peaks corresponding to MIL-88B(Fe) (Figure 3.4a). SEM imaging revealed that the sample contains a mixture of three discernible crystal morphologies (Figure 3.4b). The bulk of the sample consists of hexagonal plates of around 3-5 μm in diameter (Figure 3.4c), which likely correspond to MOF-235(Fe). The reported morphology for MOF-235(Fe) is octahedral,[10] but this is likely due to differences in the synthesis conditions: MOF-235 was originally synthesised in a DMF/EtOH solvent mix whereas our procedure only uses DMF and acetic acid.[10] Also present are hexagonal rods typical of MIL-88B(Fe) (Figure 3.4d) of various sizes (2-10 μm in length), and much smaller (100-200 nm) octahedral crystals (Figure 3.4e) which resemble MIL-101(Fe). The presence of these three phases suggests that these conditions lie on a phase boundary, as ten or more equivalents of acetic acid led to the predominant phase being MIL-88B(Fe), and using fewer equivalents led to poorly crystalline MIL-101(Fe).

Already we have seen three of the common Fe-BDC phases, and so it is worth stating how to discriminate between them using only PXRD. MIL-88B(Fe) is flexible, and thus there are

large differences in the peak positions depending on whether the framework is solvated or dried, whereas the PXRD peaks of MOF-235(Fe) remain invariant to these processes. It should be noted that this is more difficult to determine from PXRD alone for phase-impure samples: no peaks for MIL-101(Fe) were observed in the PXRD pattern of **$FeCl_2$-AA**30, despite its presence being detected by SEM imaging. MIL-101(Fe) is a much less dense phase than either MOF-235(Fe) or MIL-88B(Fe), resulting in relatively weaker diffraction for MIL-101(Fe) compared to these two phases. This makes it harder to detect in these samples by PXRD alone and explains why no corresponding Bragg peaks for MIL-101(Fe) can be identified by PXRD.

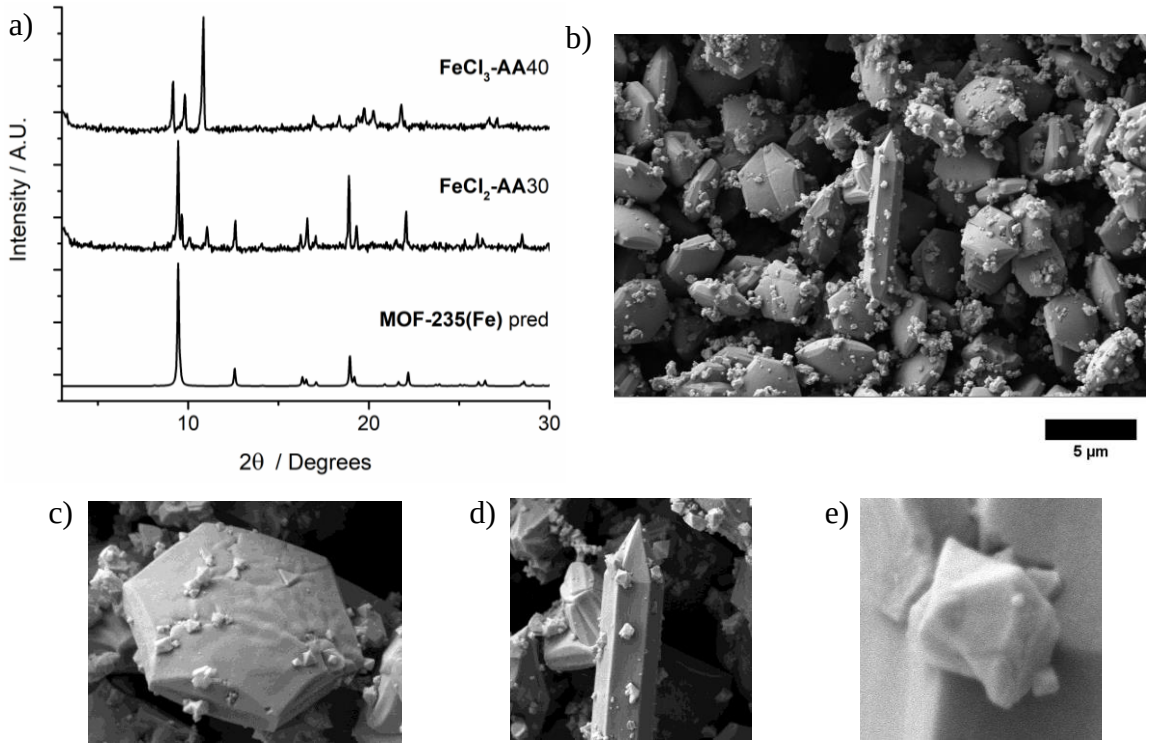

Figure 3.4. a) Comparison of the PXRD pattern of **$FeCl_2$-AA**30 with the predicted pattern for MOF-235(Fe) and the experimental pattern of **$FeCl_3$-AA**40, b) SEM image of **$FeCl_2$-AA**30, along with SEM images of c) MOF-235, d) MIL-88B(Fe), and e) MIL-101(Fe).

3.3.2 Assessing the Kinetic and Thermodynamic Relationships Between Phases

To aid in understanding the kinetic and thermodynamic relationship between the formation of these phases, identical reactions were carried out for 72 hours instead of 24 hours to further enable the mixtures to reach an equilibrium. The results of these experiments are summarised in a crystallisation diagram (Figure 3.5a-b) which gives a qualitative assessment of the phases determined by PXRD. The naming system for these samples is **$FeCl_2$-AA**x(T,t)

and **$FeCl_3$-AA**x(T,t) where 'x' equals the number of molar equivalents of acetic acid (**AA**) added, 'T' is the synthesis temperature, and 't' is the synthesis time. For both $FeCl_2 \cdot 4H_2O$ and $FeCl_3 \cdot 6H_2O$, the crystallinity of the products increases as the concentration of acetic acid is increased (Figure 3.5c-d), demonstrating the effective role of acetic acid as a modulator in these systems. Higher acetic acid concentrations also tend to favour the formation of MIL-88B(Fe) at 24 hours, but at 72 hours MOF-235(Fe) is the predominant phase under almost all conditions. These results suggest strongly that MOF-235(Fe) is the thermodynamic product relative to MIL-88B(Fe).

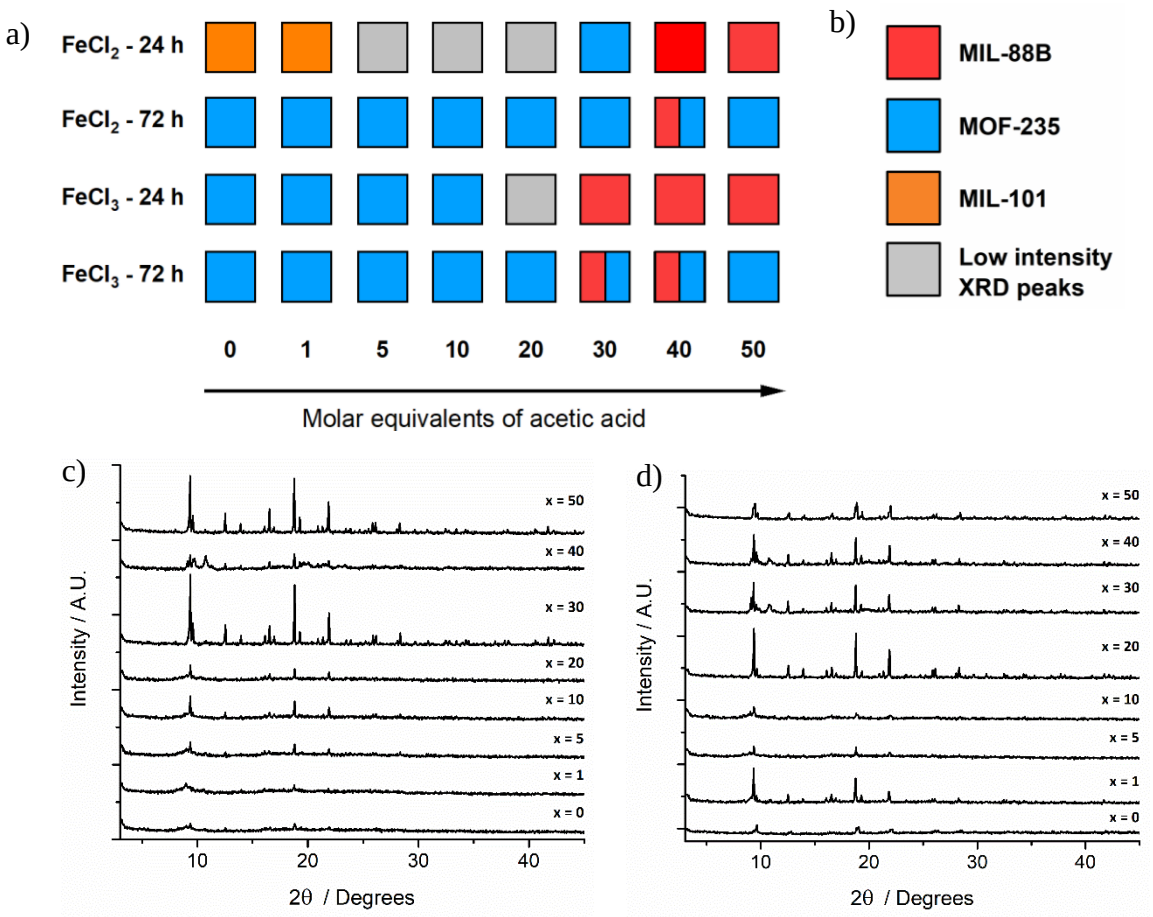

Figure 3.5. a) Crystallisation diagrams for syntheses with $FeCl_3 \cdot 6H_2O$ and $FeCl_2 \cdot 4H_2O$ for both 24 and 72 hours at each modulator concentration, b) key. Stacked PXRD patterns of c) **$FeCl_2$-AA**x(120°C,72h), and d) **$FeCl_3$-AA**x(120°C,72h), where 'x' is the number of molar equivalents of acetic acid (**AA**) used in the synthesis.

Once we had established the relationships between time, modulator concentration, and the crystallisation kinetics, we looked at exploring this over more time points. Thus, additional reactions were carried out with fixed reaction times between 2 hours and 3 days (in some cases, even longer reaction times were used), both unmodulated and with the addition of 30 eq of acetic acid – as this concentration yielded either MOF-235(Fe) or MIL-88B(Fe) during

24 and 72 hour reactions. These reactions were carried out at both 120 and 150 °C to also investigate the role of temperature in this system.

At 150 °C without a modulator, large yellow rod-shaped crystals appear after 48 hours (Figure 3.6a). After a 72-hour synthesis with $FeCl_2 \cdot 4H_2O$, a suitable crystal was characterised by single-crystal X-ray diffraction (SCXRD) and found to possess the already well-known MIL-53 structure. The structure consists of infinite chains of Fe(OH) linked together by terephthalates to give diamond-shaped channels that run down the *a*-axis. This structure contains disordered DMF inside the pores, and will be referred to as MIL-53(Fe)_DMF, while the previously reported single-crystal structure[12] contained pyridine.

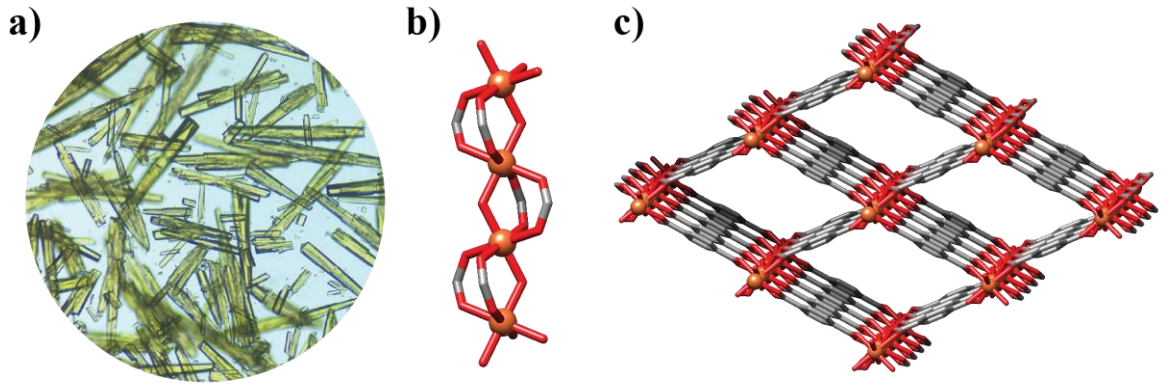

Figure 3.6 a) Image of crystals of MIL-53(Fe)_DMF, b) chain SBU present in MIL-53(Fe)_DMF, c) projection of the crystal structure of MIL-53(Fe)_DMF at a slight angle from the *a*-axis.

PXRD revealed that after drying from DCM, the hydrated phase of MIL-53(Fe) known as MIL-53(Fe)_lt is obtained,[24] and this is the sole phase present after 48 hours (Figure 3.7a-b). Since only crystals of MIL-53 are present after 48 hours, and any powder formed previously has dissolved, it can be assumed that the phase transformation from MOF-235(Fe) to MIL-53(Fe) is dissolution and recrystallisation – this has been previously hypothesised based on time-resolved energy-dispersive X-ray diffraction studies of their formation.[18] MIL-53(Fe)_lt has a peak at 12.67° which overlaps with the [102] reflection in MOF-235(Fe), thus this phase is challenging to identify in phase-impure samples of MOF-235(Fe). Despite this, it can be assumed that the greater peak intensity at this position for the 24-hour synthesis is indicative of the presence of MIL-53(Fe), and similar rod-shaped crystals were also observed by brightfield microscopy.

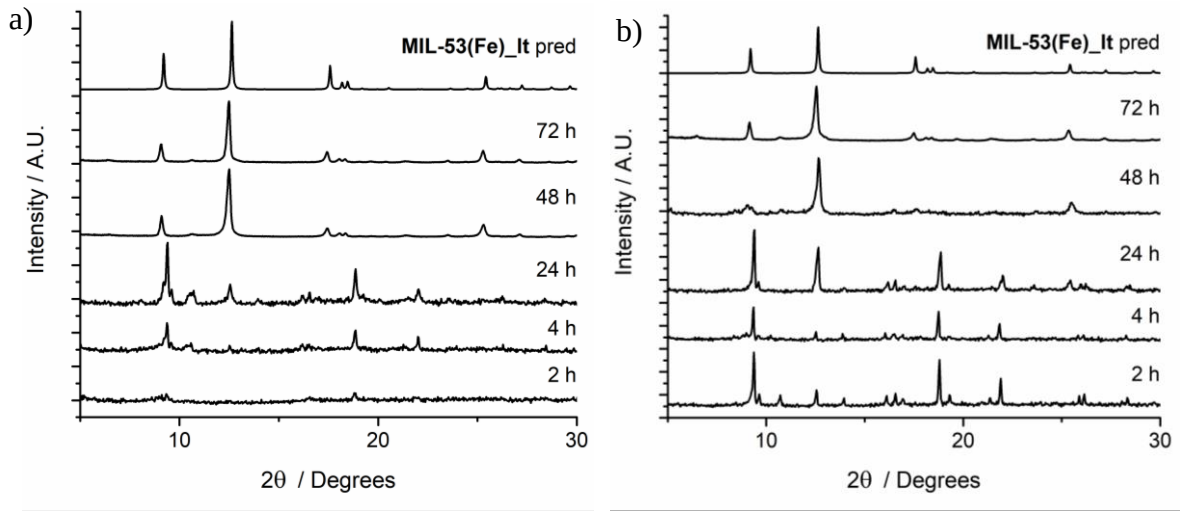

Figure 3.7. Stacked PXRD patterns of a) **$FeCl_2$**(150˚C,t), and b) **$FeCl_3$**(150˚C,t), where 't' is the synthesis time in hours, the predicted pattern of MIL-53(Fe)_lt is included for comparison.

When acetic acid is added, there is a distinctly different behaviour between the two salts. For $FeCl_3 \cdot 6H_2O$, some MIL-88B(Fe) forms within 2 hours but is absent after 4 hours, after which only highly crystalline MOF-235(Fe) is evident by PXRD (Figure 3.8a). For $FeCl_2 \cdot 4H_2O$, MOF-235(Fe) forms more rapidly, within 2 hours, along with additional peaks corresponding to MIL-88B(Fe), but unlike $FeCl_3 \cdot 6H_2O$, a complete dissolution occurs after 48 hours (Figure 3.8b). On extended reaction times (168 hours), solid Fe_2O_3 is obtained, as confirmed by PXRD. One possible explanation might be that with a lower concentration of chloride ions in solution, the long-term stability of MOF-235(Fe) is lower for $FeCl_2 \cdot 4H_2O$ and thus it eventually breaks down.

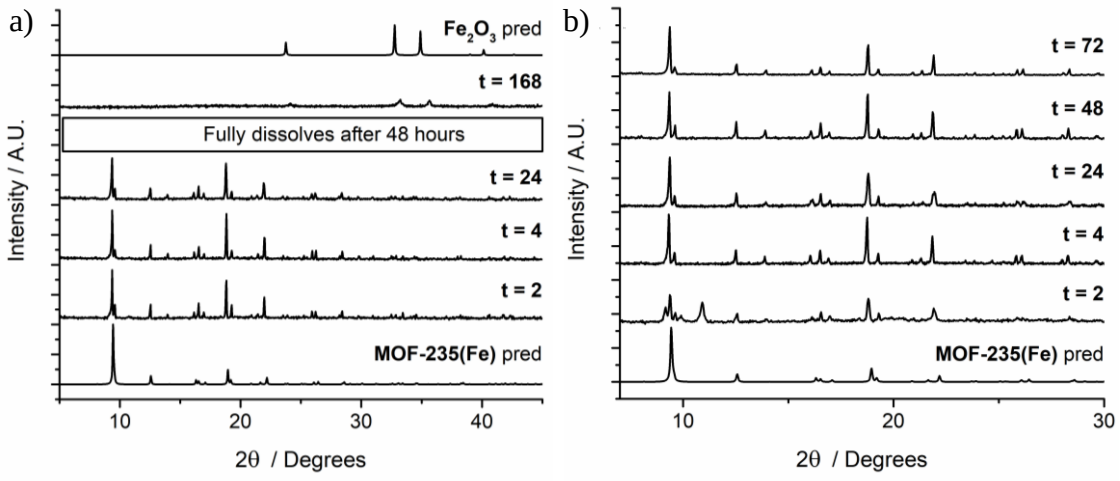

Figure 3.8. Stacked PXRD patterns of a) **$FeCl_2$-AA**30(150˚C,t), and b) **$FeCl_3$-AA**30(150˚C,t), where 't' is the synthesis time in hours and the predicted patterns of MOF-235(Fe) and Fe_2O_3 are included for comparison.

The samples of MOF-235(Fe) prepared from $FeCl_3 \cdot 6H_2O$ appear to be phase pure, as determined by PXRD and SEM (Figure 3.9a-c). Indexing the PXRD peaks yielded a hexagonal cell with approximately the same unit cell parameters as MOF-235(Fe), thus confirming its identity (Figure 3.9d). Compared to the MOF-235(Fe) crystallites seen in **$FeCl_2$-AA**30, these crystals are more elongated along the [001] direction (Figure 3.9c) and look more like MIL-88B(Fe), demonstrating that temperature and synthesis time can have a profound effect on crystallite morphology.

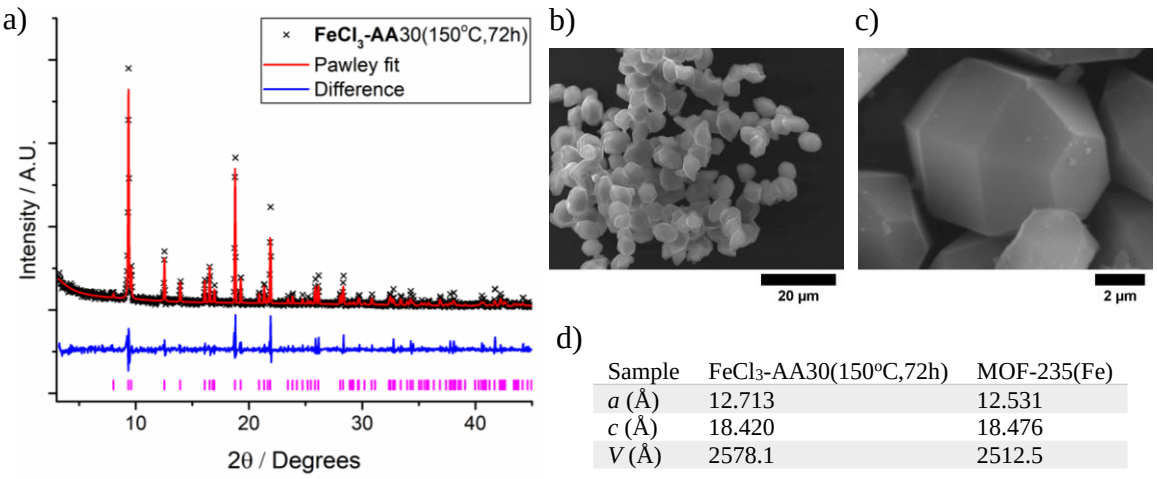

Sample	$FeCl_3$-AA30(150°C,72h)	MOF-235(Fe)
a (Å)	12.713	12.531
c (Å)	18.420	18.476
V (Å)	2578.1	2512.5

Figure 3.9. a) Pawley fit of **$FeCl_3$-AA**30(150°C,72h), b-c) SEM images of **$FeCl_3$-AA**30(150°C,72h), d) extracted unit cell parameters from the Pawley refinement of **$FeCl_3$-AA**30(150°C,72h) compared to those from the crystal structure of MOF-235(Fe).[10]

At 120 °C, $FeCl_2 \cdot 4H_2O$ did not yield a highly crystalline product until 168 hours, at which point MIL-68(Fe) forms, as evidenced by PXRD (Figure 3.10a). MIL-68 possesses a Kagomé topology and is a kinetically favoured intermediate product relative to MIL-53.[25] The sample contained large needle-like crystals which presumably correspond to this phase, as well as some orange powder. The PXRD pattern shows that this sample contains a phase impurity which has XRD peaks very similar to those seen for MIL-88B(Fe) (Figure 3.10b). This is also consistent with the morphology as can be seen by optical microscopy. An attempt to isolate the crystals in phase-pure form was conducted by slightly increasing the reaction time (192 hours) and recovering the crystals by removing the suspension and replacing with fresh DMF. PXRD of this sample shows that there is a mixture of MIL-68(Fe) and MIL-53(Fe). As both samples contain the same Fe(OH) infinite chain SBU, it is likely that MIL-68(Fe) converts over time to the denser MIL-53 structure. For acetic acid modulated samples, highly crystalline MOF-235(Fe) is obtained up to 72 hours (Figure 3.10c), but an

additional phase can be seen by PXRD after 4 hours, which is persistent and could correspond potentially to either MIL-53(Fe) or MIL-88B(Fe).

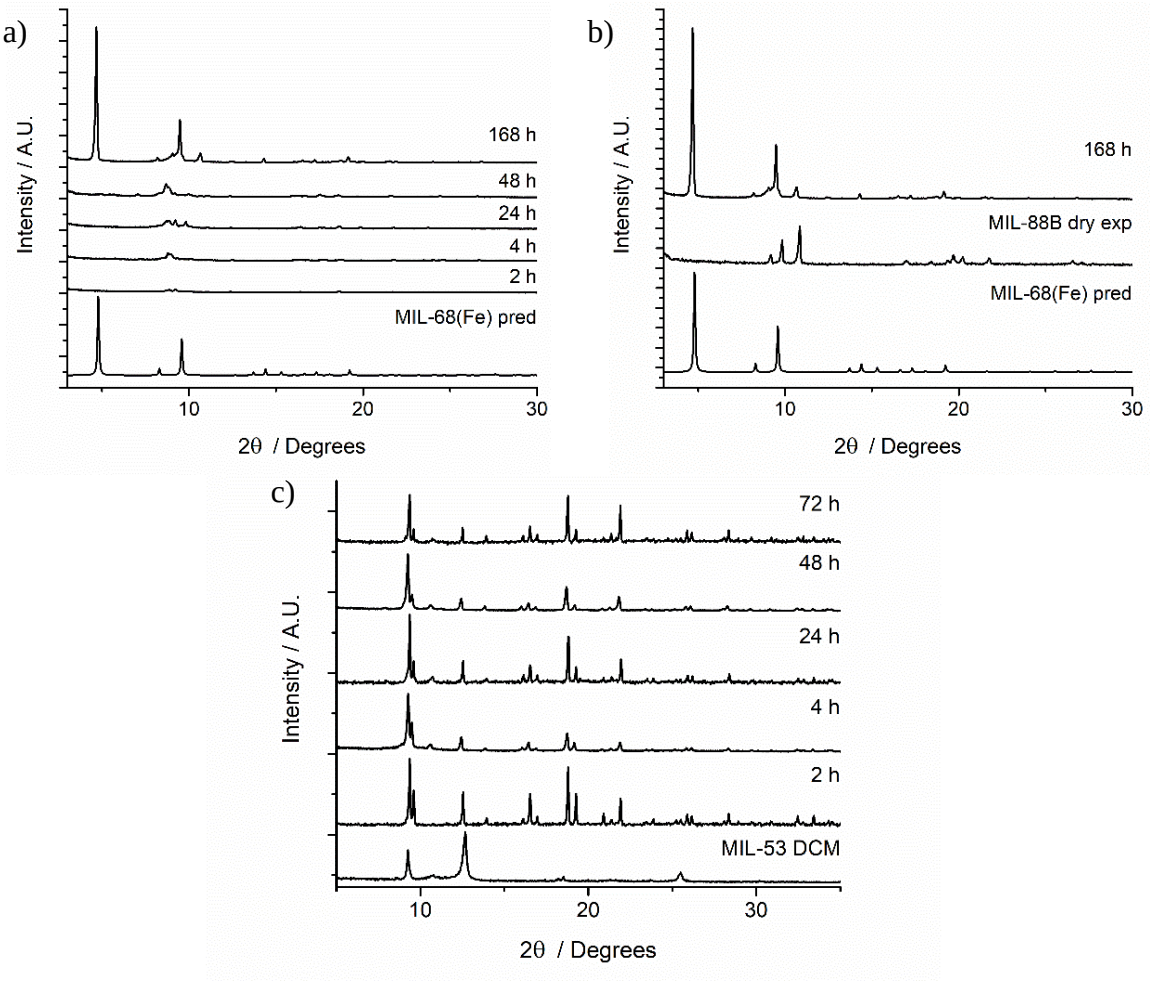

Figure 3.10. Stacked PXRD patterns of a) **$FeCl_2$-AA**0(120°C,t), b) **$FeCl_2$-AA**0(120°C,168) compared to the experimental pattern of MIL-88B dry and the predicted pattern for MIL-68(Fe), c) **$FeCl_3$-AA**30(120°C,t), where 't' is the synthesis time in hours.

When using $FeCl_3 \cdot 6H_2O$ and no modulator, MOF-235(Fe) begins to form after 2 hours and peaks in crystallinity after 4 hours (Figure 3.11a). After 24 hours the crystallinity drops and continues to drop with extended heating. The addition of acetic acid prevents any solid formation after 4 hours, and then leads to the formation of MIL-88B(Fe) by 24 hours (Figure 3.11b). By 72 hours, highly crystalline MOF-235(Fe) is obtained, which remains after 120 hours and appears to be phase pure.

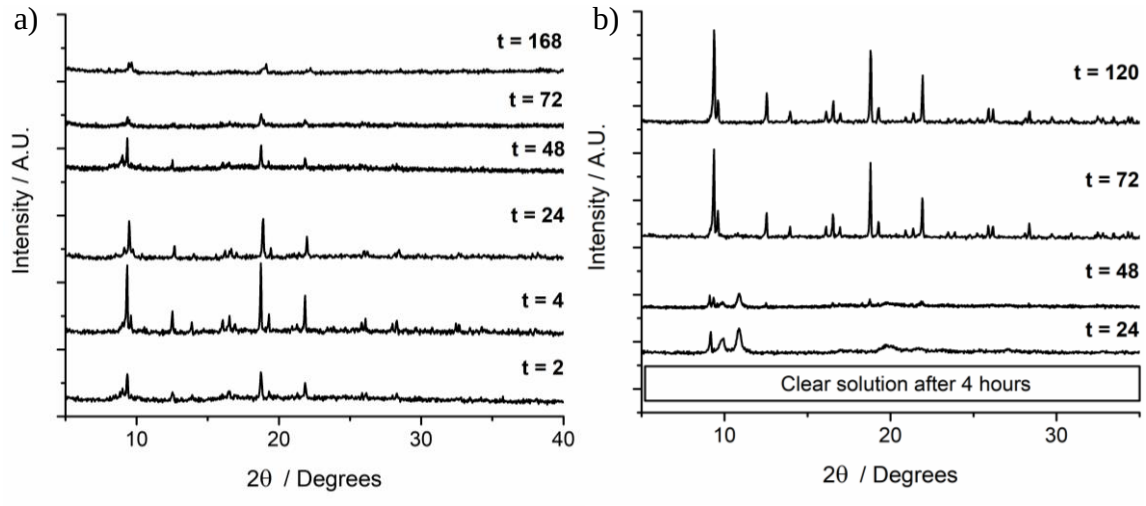

Figure 3.11. Stacked PXRD patterns of a) **$FeCl_3$-AA**0(120˚C,t), and b) **$FeCl_3$-AA**30(120˚C,t), where 't' is the synthesis time in hours.

3.3.3 Summary

The results are summarised in Figure 3.12a-c and show that MOF-235(Fe) will eventually convert to MIL-53(Fe) given a sufficient amount of time at T > 120 ºC, and thus MIL-53(Fe) can be assumed to be the thermodynamically favoured product relative to MOF-235(Fe). The presence of acetic acid clearly impedes the formation of MIL-53(Fe), likely by favouring the formation and stabilisation of the $[Fe_3O(RCO_2)_6]$ cluster. This is supported by the fact that MIL-53(Fe) is favoured with long synthesis times (> 1 week) at 120 ˚C or relatively short times at 150 ˚C (2 days), but only ever observed as a phase impurity when acetic acid is used as a modulator. Subsequent reactions using HCl as a modulator instead of acetic acid showed that it can give MIL-53(Fe) as the sole product regardless of the salt used or the temperature. This is consistent with previous studies on the synthesis of the iron amino-terephthalate analogues[16] and also suggests that acetic acid plays a greater phase-directing role, i.e. acting as a coordination modulator, than merely modulating the pH and slowing down the kinetics of crystallisation by inhibiting linker deprotonation.

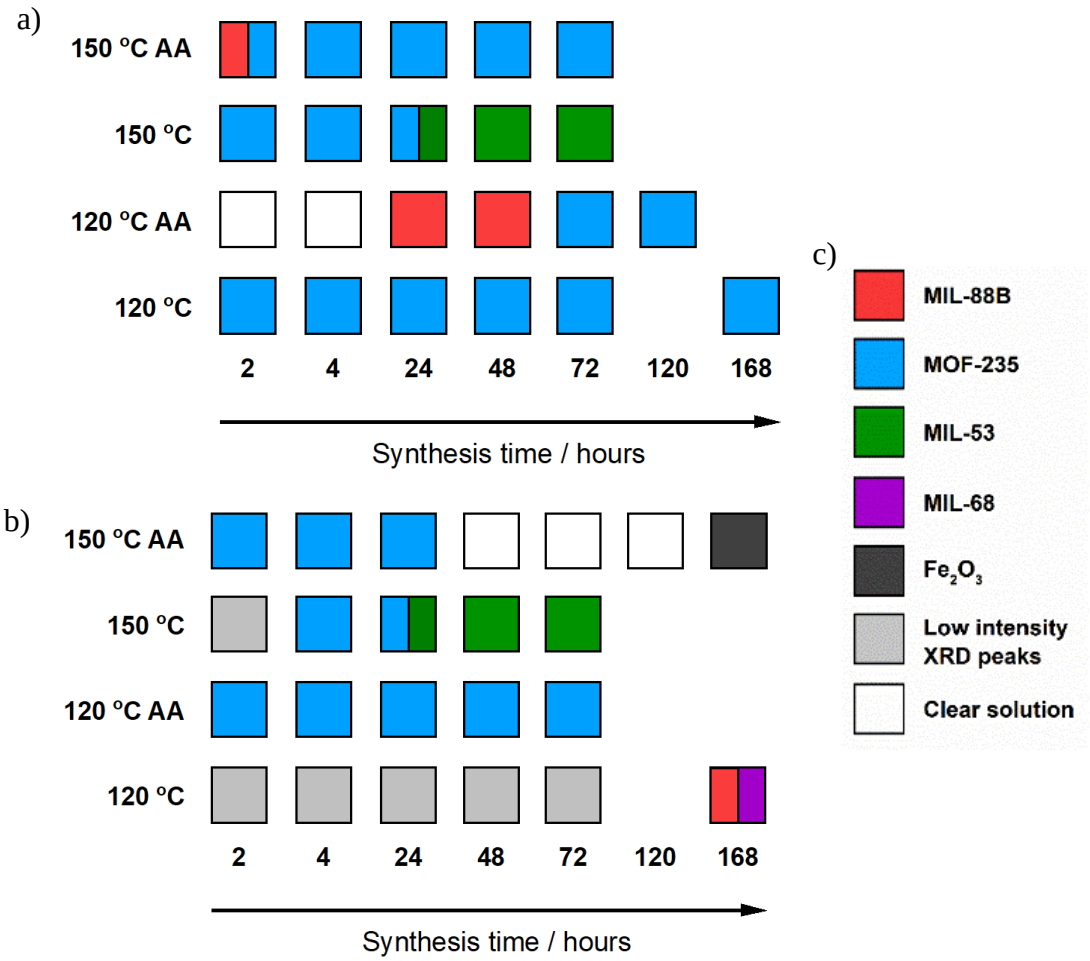

Figure 3.12. Crystallisation diagrams for syntheses with a) $FeCl_3 \cdot 6H_2O$ and b) $FeCl_2 \cdot 4H_2O$ for both 24 and 72 hours with and without acetic acid, c) key.

MOF-235(Fe) forms under nearly all conditions save for **$FeCl_2$-AA**0(120°C, t) (Figure 3.12) and is often the final product formed over time, suggesting that it is the thermodynamically preferred product. When considering that $[FeCl_4]^-$ is required to form MOF-235(Fe), it is unsurprising that it forms more readily when using $FeCl_3 \cdot 6H_2O$ than $FeCl_2 \cdot 4H_2O$, as this increases the Cl^- concentration and starts with Fe^{3+}.

These results contradict a previous study that investigated the formation of MOF-235(Fe) vs. MIL-88B(Fe) using single metal and mixed-metal approaches.[5] It was found that mixed-metal MIL-88B(Fe_2Ni) forms preferentially over MOF-235(Fe), which is unsurprising as the Fe_2NiO cluster should form preferentially over Fe_3O and a MOF-235(Fe_2Ni) cannot form due to the charge imbalance, as Ni is in the 2+ oxidation state. Therefore, over time MIL-88B(Fe_2Ni) should dominate. They also show that MIL-88B(Fe) forms after MOF-235(Fe) in single metal syntheses, however, their synthesis includes the use of NaOH (0.8 eq) which has already been reported to favour the formation of MIL-88B(Fe)[16]. Since it is unclear

exactly what effect NaOH has on the synthesis other than to favour deprotonation of the terephthalic acid, our results give a much clearer indication of the preference for either phase. When using $FeCl_3 \cdot 6H_2O$, both the unmodulated and acetic-acid modulated syntheses show that MIL-88B(Fe) forms first and then transforms into MOF-235(Fe), and at 120 °C without a modulator there is no formation of MIL-88B(Fe) at all. Reducing the oxidation state of the metal starting material from +3 to +2 also appears to prevent the formation of MIL-88B(Fe) completely, suggesting again that MOF-235(Fe) is the thermodynamically preferred product as was the case with MIL-126(Fe) vs. MIL-88D(Fe) (Chapter 2). The thermodyanmic relationships we have discerned are illustrated in Figure 3.13.

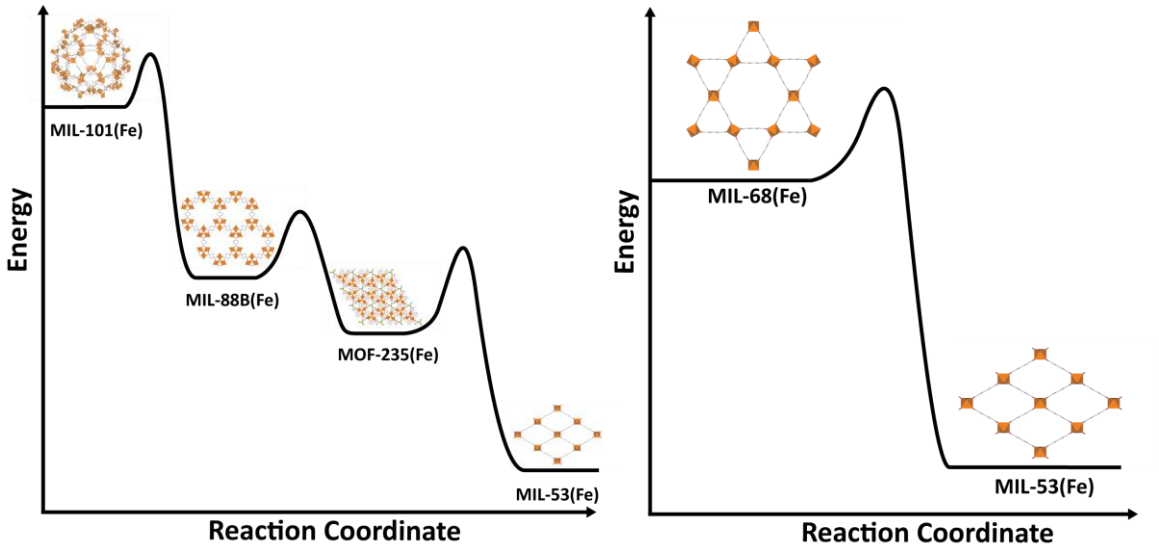

Figure 3.13. Reaction coordinate graphs for Fe-terephthalate MOFs.

3.4 Variation of the Fe-precursor

All of the experiments performed in the previous section used chloride salts, and in both cases MOF-235(Fe) appears to be the predominant phase when acetic acid is used as a modulator. To remove the possibility of forming MOF-235(Fe), we must use chloride-free Fe-sources. While chlorides are typically the most commonly used, there are a plethora of other common and inexpensive iron complexes which can also be used to synthesise Fe-MOFs. In an attempt to map out the landscape of the other Fe-BDC phases which can be formed, iron(II) acetate, iron(III) nitrate nonahydrate, and iron(II) tetrafluoroborate hexahydrate were all employed in similar syntheses. As with the chloride salts, initial acetic acid modulation scans were conducted at 120 °C for 24 hours. Additionally, reactions were carried out at 150 °C for 72 hours without a modulator, as these were the ideal conditions for obtaining MIL-53(Fe). The naming system used is **Fe(counterion) -AA**x(T,t) where 'x' equals the number of molar equivalents of acetic acid (**AA**) added, 'T' is the synthesis temperature, and 't' is the synthesis time.

For the nitrate salt, at a synthesis temperature of 120 °C crystalline materials could only be obtained with 20 eq or more of acetic acid (Figure 3.14a); these correspond to MIL-88B(Fe). Increasing the reaction times to 72 hours for nitrate did not yield a significant improvement for most of the modulator concentrations, and for 20 eq of acetic acid the crystallinity drops significantly (Figure 3.14b). The 150 °C synthesis without modulator yielded only amorphous material, similar to those at 120 °C.

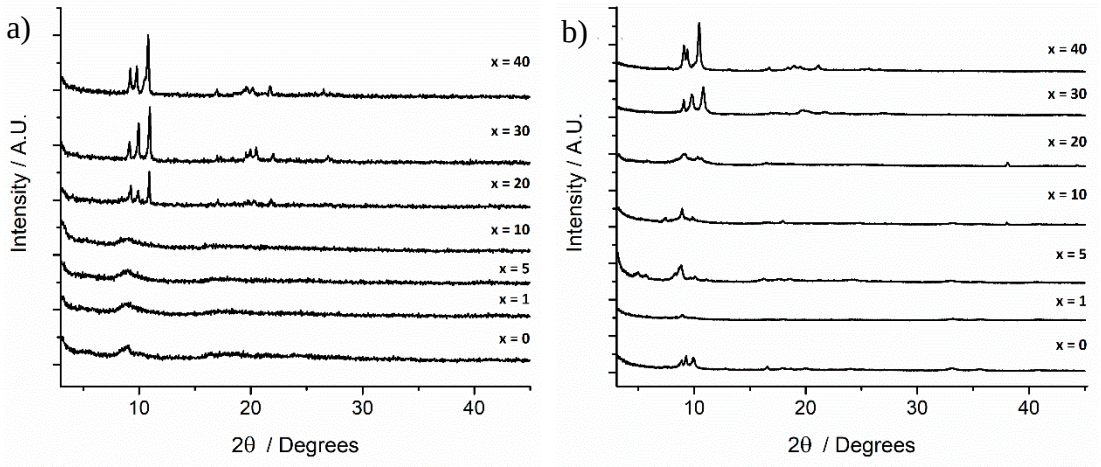

Figure 3.14. Stacked PXRD patterns of a) **Fe(NO$_3$)$_3$-AA**x(120°C,24h), and b) **Fe(NO$_3$)$_3$-AA**x(120°C,72h), where 'x' is the number of molar equivalents of acetic acid (**AA**) used in the synthesis.

Synthesis with $Fe(BF_4)_2 \cdot 6H_2O$ at 120 °C with 40 eq of acetic acid yielded large hexagonal plate crystals (Figure 3.15a), which were suitable for SCXRD. The structure consists of $Fe_3O(DMF)_3(RCO_2)_6$ SBUs (Figure 3.15b) bridged by terephthalates into a MIL-88-type topology with hexagonal channels that run down the *c*-axis (Figure 3.15c). These channels are occupied by $[BF_4]^-$ anions that are present in a 1:3 ratio relative to Fe, giving an overall framework formula of $[Fe_3O(DMF)_3(BDC)_3][BF_4]$. The structure is very similar to MOF-235(Fe), except with a $[BF_4]^-$ anion in place of $[FeCl_4]^-$. The carbonyl carbon in the coordinated DMF molecule is disordered between 2 positions, and the F atoms are disordered in multiple orientations around the B atom. Bond valance sum calculations give a value of 3.070 for the Fe atom, confirming that it is in the +3-valence state. Comparison between the predicted and experimental PXRD patterns confirm that the bulk of the sample corresponds to $[Fe_3O(DMF)_3(BDC)_3][BF_4]$ (Figure 3.15d).

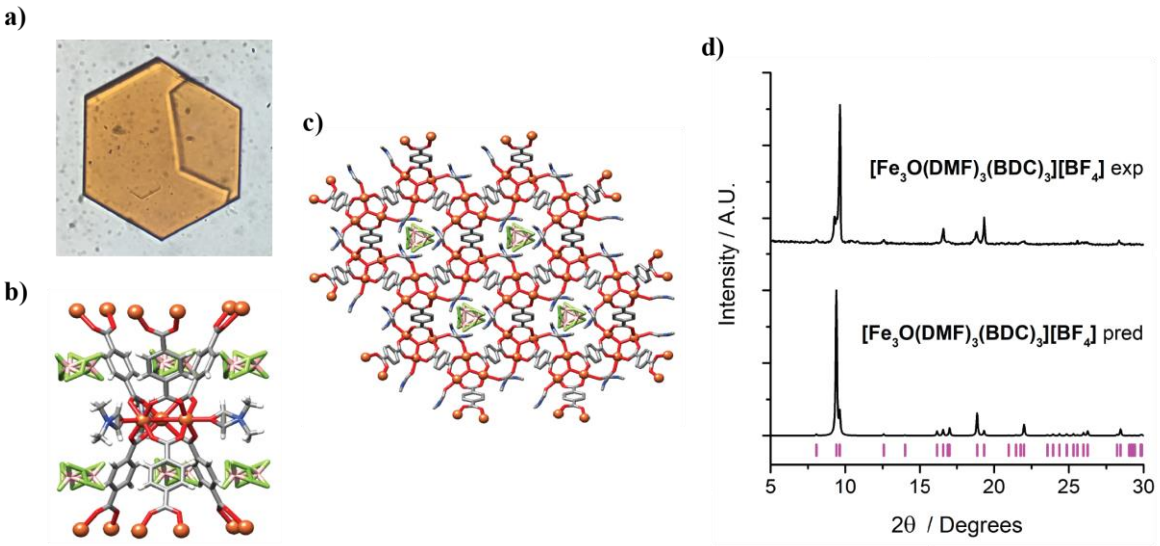

Figure 3.15. Characterisation data for $[Fe_3O(DMF)_3(BDC)_3][BF_4]$: a) optical image of a crystal, b) SBU present in the crystal structure, c) crystal packing as viewed down the *c*-axis, d) experimental and simulated PXRD patterns.

At 150 °C without a modulator, large yellow crystals (Figure 3.16a) suitable for SCXRD were obtained after 3 days. The structure is identical to the already-reported [Fe(DMF)(BDC)] structure (YAXBUV in the CCDC)[12] which is similar to MIL-53(Fe) but in this case the bridging hydroxides are replaced by DMF molecules (Figure 3.16b-c). Interestingly, we found that the PXRD pattern changes upon drying from DCM, suggesting either decomposition or flexibility (Figure 3.16d).

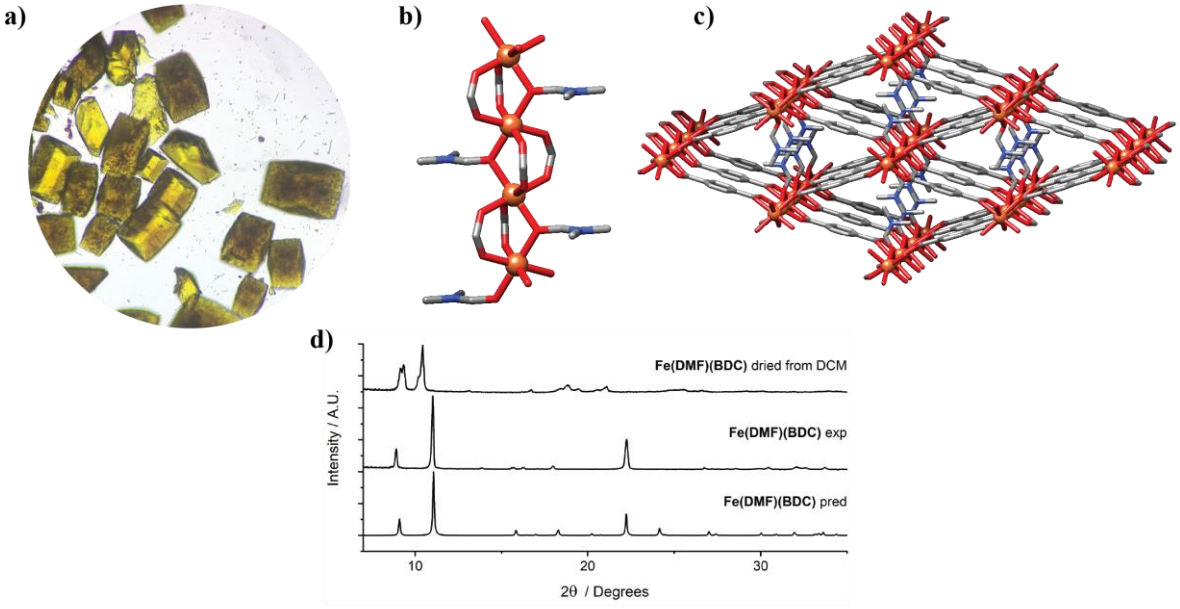

Figure 3.16. a) Crystals of [Fe(DMF)(BDC)], b) Chain SBU in [Fe(DMF)(BDC)], c) crystal packing in [Fe(DMF)(BDC)] at a slight angle from the *b*-axis, d) comparison of the predicted and experimental PXRD patterns of [Fe(DMF)(BDC)] along with the pattern of the DCM-dried sample.

When the reaction time at 120 °C was extended to 3 days, [Fe(DMF)(BDC)] is obtained up to 10 eq of acetic acid, while 20 eq or more gives $[Fe_3O(DMF)_3(BDC)_3][BF_4]$. From a formula perspective, both contain coordinated DMF molecules and differ primarily in their oxidation states and the presence of $[BF_4]^-$. As far as oxidation state goes, [Fe(DMF)(BDC)] contains Fe^{2+} and $[Fe_3O(DMF)_3(BDC)_3][BF_4]$ contains Fe^{3+}; there are a number of examples where Fe^{3+} can be reduced to Fe^{2+} and vice versa during solvothermal synthesis (see Chapter 2). The kinetic and thermodynamic relationship between these two structures is much harder to establish from these experiments, as there is no case where both phases are crystallised from an identical synthesis mixture at different temperatures or over different synthesis times. The effect of acetic acid clearly favours $[Fe_3O(DMF)_3(BDC)_3][BF_4]$, but this could be a cluster templating effect rather than modulating the kinetics, particularly as [Fe(DMF)(BDC)] is obtained at both 120 °C and 150 °C in the absence of acetic acid. This is supported by the fact that an identical reaction at 150 °C with 30 equivalents of acetic acid also yields $[Fe_3O(DMF)_3(BDC)_3][BF_4]$.

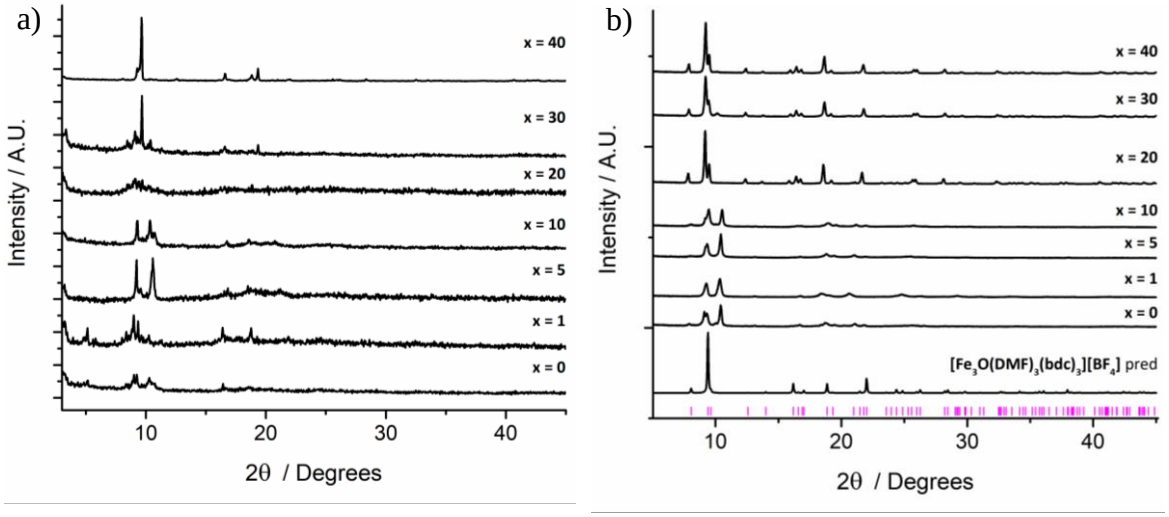

Figure 3.17. Stacked PXRD patterns of a**) Fe(BF$_4$)$_2$-AA**x(120˚C,24h), and b) **Fe(BF$_4$)$_2$-AA**x(120˚C,72h), where 'x' is the number of molar equivalents of acetic acid (**AA**) used in the synthesis and the predicted pattern of [Fe$_3$O(DMF)$_3$(BDC)$_3$][BF$_4$] is included for comparison.

When using Fe(OAc)$_2$ as starting material, two phases can be seen by PXRD (Figure 3.18a). Peaks corresponding to the dried sample of [Fe(DMF)(BDC)] (Figure 3.18b) are seen with 0-10 eq of AA, and then MIL-88B(Fe) is present as a highly-crystalline phase from 20-50 eq. SEM revealed that these samples contain large hexagonal rods typical of MIL-88B(Fe) (Figure 3.18c). Fe(OAc)$_2$ being an Fe^{2+} salt likely favours the formation of [Fe(DMF)(BDC)] at low modulator concentrations, similar to what was seen with Fe(BF$_4$)$_2$·6H$_2$O, whereas at higher concentrations the equilibrium shifts towards favouring Fe$_3$O(RCO$_2$)$_6$ clusters, as seen in MIL-88B(Fe), as we have rationalised for modulation scans with the other salts.

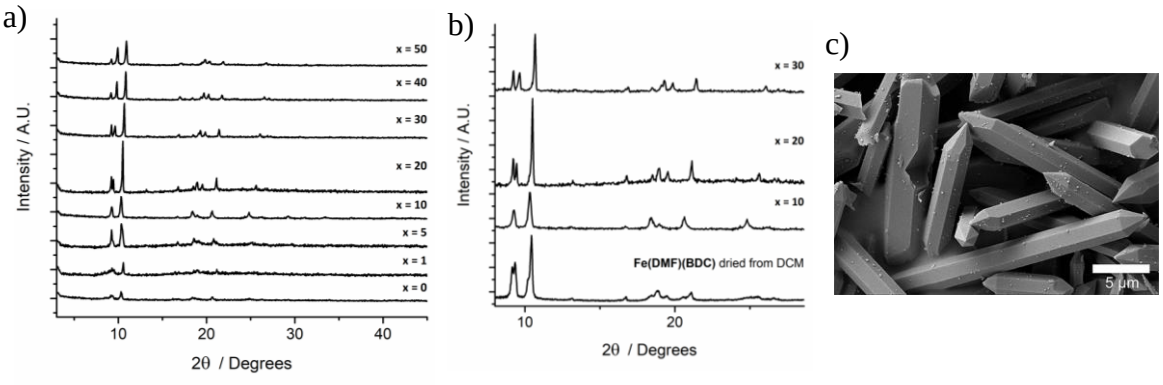

Figure 3.18. Stacked PXRD patterns of a) **Fe(OAc)$_2$-AA**x(120˚C,24h), and b) stacked PXRD patterns of samples of **Fe(OAc)$_2$-AA**x(120˚C,24h) where x = 10-30 are compared the experimental pattern of [Fe(DMF)(BDC)] after drying from DCM, c) SEM image of **Fe(OAc)$_2$-AA**40.

3.4.1 Summary

The choice of metal precursor has a profound effect on which phase crystallises (Figure 3.19), and in some cases greatly enhances the speed of synthesis, crystallinity, and phase purity of the resulting materials. MIL-88B(Fe) is the product from reactions with $Fe(NO_3)_3$, $FeCl_3$, or $Fe(OAc)_2$ and BDC after heating for 24 hours at 120 °C when a sufficient quantity of acetic acid (> 30 eq) is added to the synthesis. $Fe(BF_4)_2$ is the only Fe-source that does not ever yield MIL-88B(Fe), regardless of modulator concentration or time, which proves that the MOF-235(Fe)/$[Fe_3O(DMF)_3(BDC)_3][BF_4]$ structures are formed preferentially over MIL-88B(Fe) when there is a suitable anion to enable their formation. For both $Fe(OAc)_2$ and $Fe(BF_4)_2$, it seems that the use of a carboxylate modulator favours the formation of the Fe_3O cluster, while at lower concentrations the [Fe(DMF)(BDC)] phase is predominant.

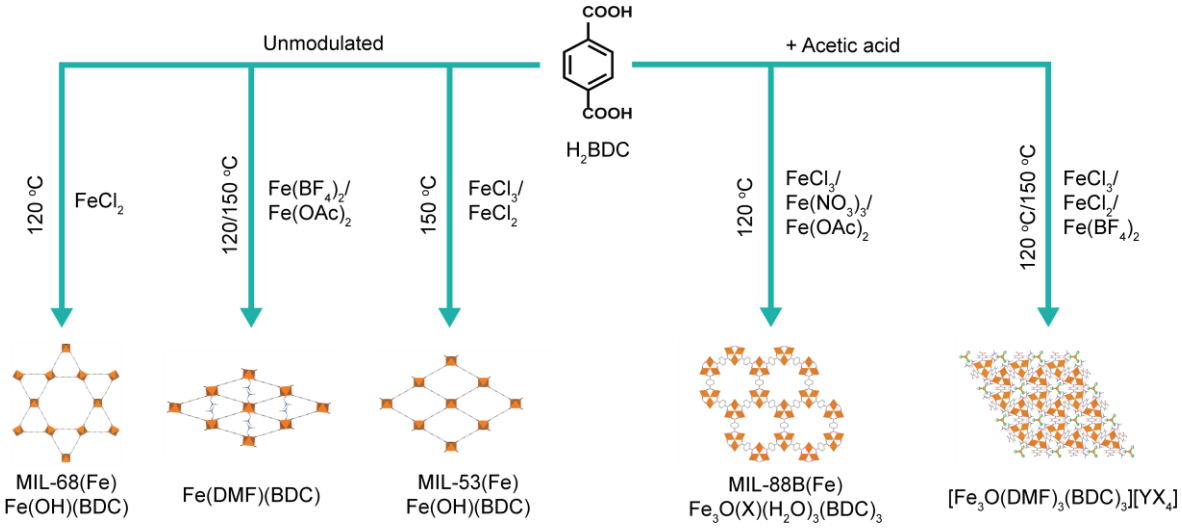

Figure 3.19. Scheme showing the main phases which can be obtained from each metal precursor, both unmodulated and with the addition of acetic acid.

3.5 Flexibility of MIL-53(Fe)

3.5.1 Solvent exchanges in MIL-53(Fe)

The flexibility of MIL-53(Fe) has previously only been studied by PXRD, due to the lack of synthetic procedures to obtain high-quality crystals of a suitable size for SCXRD. Direct immersion of the hydrated powder into various solvents has been reported and was characterised by *in situ* PXRD, showing that in all cases there is a change in symmetry and/or pore size.[26] Once we managed to obtain the single-crystal structure of MIL-53(Fe)_DMF, we began to conduct solvent exchanges with many available solvents to assess how well DMF could be exchanged. This work was part of a preliminary assessment of the material for potential SCXRD studies of the flexibility of MIL-53(Fe) which could be conducted in the future. Initial solvent exchanges were attempted by gradually adding the new solvent to the crystals while still in DMF, and then fully exchanging the solvent every day for 3 days. Afterwards all crystals were visually inspected to see if they remained intact for SCXRD - these results are summarised in Table 3.1.

Table 3.1. Unit cell data for solvent exchanged samples.

Solvent	S.G.	*a* / Å	*b* / Å	*c* / Å	V / Å^3	α / °	β / °	γ / °	Z	V/Z (Å^3)
DMF	P-1	6.8403(12)	10.7142(18)	10.7928(18)	670	117.3	94.2	103.3	2	335
Et_2O	C2/c	19.095(7)	10.906(3)	6.8511(19)	1360	90	107.6	90	4	340
Petroluem ether	P-1	6.837(4)	10.724(9)	10.803(10)	670	117.4	93.9	103.5	2	335
Acetone	C2/c	19.423(5)	10.042(2)	6.8779(16)	1279	90	107.6	90	4	319.75
Hexane	P-1	6.8329(13)	10.721(4)	10.791(3)	668	117.4	94.0	103.4	2	334
Propan-2-ol	C2/c	19.547(4)	9.714(2)	6.8846(17)	1252	90	106.8	90	4	313
Isopropyl ether	P-1	6.816(3)	10.726(9)	10.863(9)	667	118.1	93.3	103.6	2	333.5
DMSO	C2/c	19.367(12)	10.093(5)	6.856(4)	1280	90	107.3	90	4	320

S.G. = Space Group, Z = number of formula units Fe(OH)(BDC) per unit cell

Interestingly, more than half of the solvents tried caused the crystals to break apart, either immediately or upon repeated exchanges, and thus their structures could not be collected: chloroform, tetrahydrofuran, ethanol, methanol, acetonitrile, dichloromethane, ethyl acetate, and water. This may arise due to mechanical stress, and it is currently unclear what factors

determine this. This is only an issue for single crystal analysis, as it does not appear to correspond to chemical instability and is not a problem for PXRD; DCM-exchanged samples retained their crystallinity as demonstrated in Section 3.3.2. Out of the crystals which were suitable for SCXRD, three had the same unit cell as the parent material, while the remaining four caused a change in pore size as well as a change in symmetry from P-1 to C2/c, indicating that successful solvent exchange had occurred. Because of this change in symmetry, we have included the volume per formula unit (*V*/*Z*) to allow better comparison of the relative changes in volume between different samples, which are also given in Table 3.1.

When comparing the pore dimensions 'd' (short dimension) and 'D' (long dimension), they typically have an inverse relationship when looking across the various solvates, with the 'd/D' ratio decreasing as the pore volume decreases (Figure 3.20). Comparison of the unit cell volumes previously reported for hydrated powder samples treated in various solvents with our data shows that we observe the same trend between the solvents (DMF>DMSO>propan2-ol) (Figure 3.20). The differences between the volumes of our solvates and the literature are likely due to the differences in the temperature during data collection, with our SCXRD data collected at 150 K and the PXRD data likely collected at 298 K.

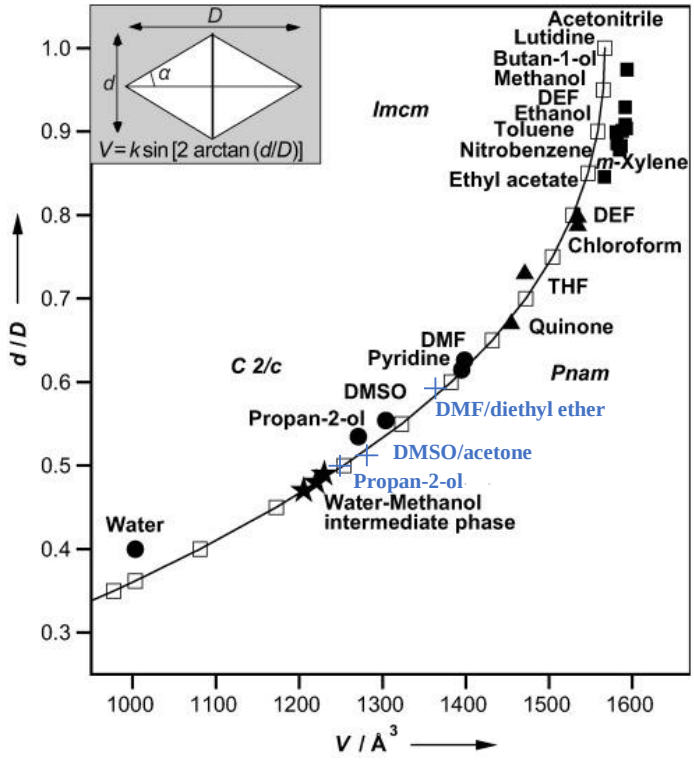

Figure 3.20. Pore aspect ratio (d/D) of MIL-53(Fe) in various solvents with our values added in approximate positions (blue).[26]

MIL-53(Fe)_DMF is completely stable to drying and displays the same patterns even after removing the crystals from their mother solvent and drying in a desiccator (Figure 3.21a) – this was the case for three separate samples. To first establish the composition of the DMF-solvate, elemental analysis and TGA (Figure 3.21b) were used to determine the solvent content and approximate formula of the material, which was found to be [Fe(OH)(BDC)(DMF)].

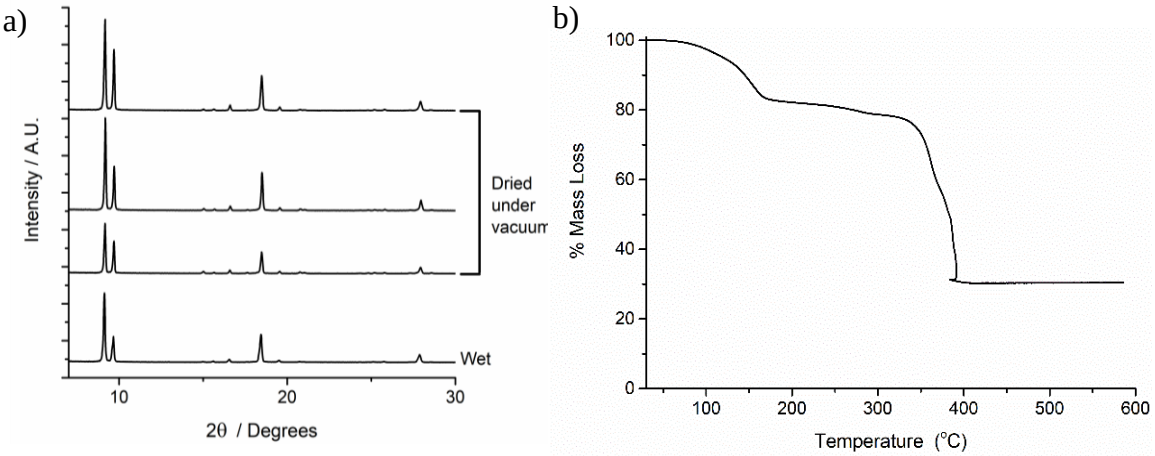

Figure 3.21. a) Stacked PXRD patterns of MIL-53(Fe)_DMF taken wet and after drying under vacuum at RT (3 different samples), b) TGA profile of MIL-53(Fe)_DMF.

For MIL-53(Fe)_DMSO, there are slight shifts between the experimental PXRD pattern and the one predicted from the crystal structure of MIL-53(Fe)_DMSO (Figure 3.22a) which can be attributed to differences in unit cell size between room temperature PXRD data and SXRD data collected at low temperature (150 K). The presence of DMF is indicated by elemental analysis (1.71 %) and suggests that it has not been fully exchanged by DMSO. As the samples were soaked in solvent and replaced multiple times, it can be assumed that the structure has a high affinity towards DMF, and it cannot be removed easily via solvent exchange at room temperature. The ability of DMF to interact with the hydroxide chain in MIL-53 has been reported elsewhere[27] and likely accounts for our results. From elemental analysis we can estimate an approximate formula of $[Fe(OH)(BDC)(DMF)_{0.4}(DMSO)_{0.8}]$, however, the solvent loss by TGA (Figure 3.22b) is lower than predicted (18.7% compared to 27.9% theoretical). It is likely that the differences in solvent content between these two techniques is due to evaporation of solvent between the two measurements.

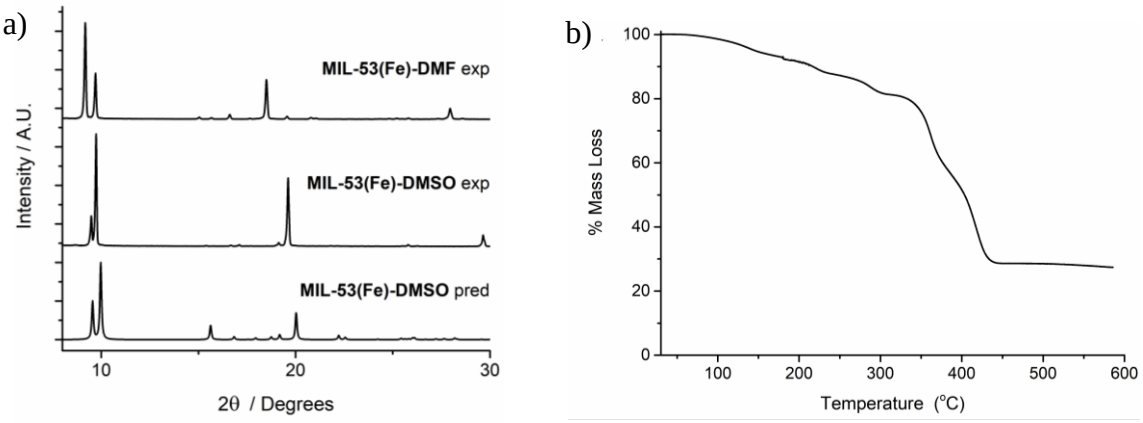

Figure 3.22. a) Stacked PXRD patterns of MIL-53(Fe)_DMSO predicted and experimental with the experimental pattern for MIL-53(Fe)_DMF, b) TGA profile for MIL-53(Fe)_DMSO.

For MIL-53(Fe)_acetone, when allowed to dry at room temperature it converts to the hydrated phase (MIL-53-Fe_lt) similar to what was observed previously with samples dried from DCM. Variable time PXRD reveals that this phase transition occurs very quickly when the crystals are isolated from their mother solvent and is complete within 10 minutes (Figure 3.23a). The reported Cr-analogue MIL-53(Cr) shows similar behaviour and rapidly adsorbs water from the air when its terephthalic acid guests are removed from the pores.[27] As only the two phases, MIL-53(Fe)_acetone and MIL-53(Fe)-lt, are observed in these experiments, it can be assumed that this phase transformation occurs stepwise and not via a continuous change in unit cell size, as is consistent with previous literature.[24,27-29] Because of this rapid phase transition, it was also not possible to accurately determine the solvent content via thermal gravimetric or elemental analyses. The TGA shows very little solvent loss prior to framework degradation (Figure 3.23b), even less than predicted for a formula of [Fe(OH)(BDC)(H_2O)]. Elemental analysis reveals that there is still some nitrogen content, suggesting that DMF (1.32%) is still present within the MOF. Because of the low solvent loss observed by TGA, it is not possible to estimate the solvent content. All attempts to collect the single-crystal structure of MIL-53(Fe)_lt have been unsuccessful as the crystals break apart upon drying.

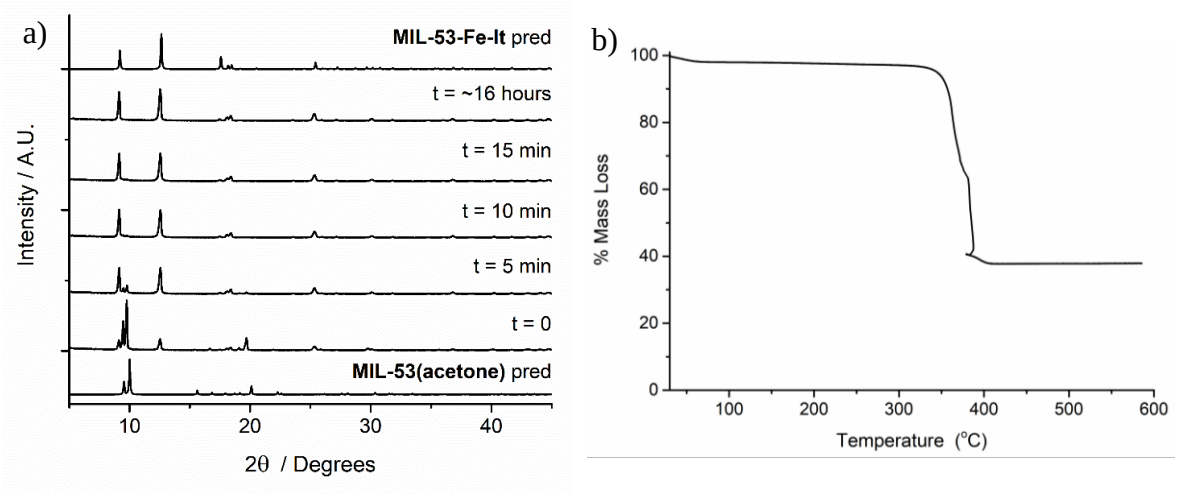

Figure 3.23. a) Time-dependent PXRD patterns of MIL-53(Fe)_acetone compared to the predicted patterns of MIL-53(Fe)_acetone and MIL-53(Fe)_lt, b) TGA profile of MIL-53(Fe)_acetone.

3.5.2 Summary

To build upon the reported PXRD studies on MIL-53(Fe), in our study we have tried to obtain single-crystal structures of various solvates, and thus there is a requirement for the crystals to remain intact, which has proven challenging. However, this preliminary work does show that its feasible for MIL-53(Fe) to undergo phase transformations while maintaining crystal integrity, and future work could be focused towards characterising these transformations *in situ* using SCXRD.

3.6 Conclusions and Future Work

We have explored the phase space of Fe-terephthalate MOFs and found routes to various MOFs containing the chain and trigonal SBUs, as well as gaining some insight into the kinetic/thermodynamic relationships between them. Compared to the previous chapter, the kinetic role of varying the oxidation state of the metal precursor is a lot more complex as the counterion dictates the nature of the phases which can form as well as preferentially favouring one over another. We have demonstrated that MOFs with the trigonal SBU can be best stabilised by the addition of a monocarboxylate modulator, such as acetic acid, while MOFs with the chain SBU can best be obtained without modulator or by use of a mineral acid such as HCl. Time is a crucial factor in these syntheses, as for a given reaction mixture, some phases are transient and can dissolve or even lose their crystallinity over time.

Despite their similar symmetry and composition, we have been able to clearly differentiate between MOF-235(Fe) and MIL-88B(Fe) using multiple characterisation methods. It seems that MOF-235(Fe) is the thermodynamically preferred product that forms in DMF, while MIL-88B(Fe) can be obtained when both the synthesis time is relatively short and acetic acid is used as modulator. MIL-53(Fe) appears to be thermodynamically more stable than both MOF-235(Fe) and MIL-88B(Fe), but its formation can be wholly prevented by addition of acetic acid to the synthesis mixture. This suggests that the modulator has a guiding role in preforming and stabilising the SBU in the framework.

A similar effect can be seen when using $Fe(BF_4)_2$, with higher acetic acid concentrations preferring the formation of the novel MOF-235(Fe) analogue $[Fe_3O(DMF)_3(BDC)_3][BF_4]$, while [Fe(DMF)(BDC)] forms at lower concentrations of acetic acid. The formation of these $[Fe_3O(DMF)_3(BDC)_3][YX_4]$ frameworks can be entirely avoided by use of Fe-precursors which cannot provide the necessary YX_4 anions for their formation, and thus MIL-88B(Fe) can be more easily obtained. MIL-53(Fe) has only been obtained when using the chloride salts, suggesting that the halogen also plays a role in directing the synthesis. To confirm this, it would be necessary to determine the Cl^- content of the materials, as it may be present to some extent in place of OH in the Fe(OH) chain SBU.

These results can guide future *in situ* studies into this phase-space, which will enable the thermodynamic and kinetic relationships to be more accurately probed and will also answer fundamental questions about the synthesis mechanism. These could be conducted using a synchrotron source, as has been reported for other MOF based systems.[18,30,31]

The flexibility of MIL-53(Fe) has been investigated using SCXRD and PXRD techniques and helps to confirm and build upon the reported literature. MIL-53(Fe) undergoes stepwise framework transformations when the guest is exchanged, however, single crystal structures of most of the solvates cannot be obtained due to break up of crystals upon solvent exchange. Despite this, we now have the crystal structures of 5 distinct MIL-53(Fe) solvates which possess different unit cell parameters to one another. While non-volatile solvents such as DMSO and DMF will remain in the pores even after removal from their mother liquor, volatile solvents such as acetone and DCM rapidly evaporate to yield the hydrated form of MIL-53(Fe) (MIL-53(Fe)_lt) when exposed to air. Understanding these transitions will aid in further study of the structural transformations that take place during adsorption/desorption processes, which we aim to conduct in the future.

The work in the next chapter was conducted concurrently with this chapter and is aimed at applying the phase-tuning techniques we developed in Chapter 2 with Cr^{3+} MOFs.

3.7 Experimental

3.7.1 General Experimental Methods

All starting materials were purchased from commercial sources and used without further purification.

Powder X-Ray Diffraction (PXRD): PXRD measurements were carried out at 298 K using primarily a PANalytical X'Pert PRO diffractometer (λ (CuKα) = 1.5405 Å) on a mounted bracket sample stage, and the pulse height discrimination (PHD) lower level was raised to 55% to filter out some of the low-energy X-rays caused by fluorescence from iron. All other measurements were carried out using a Rigaku MiniFlex diffractometer (λ (CuKα1) = 1.54056 Å, (CuKα2) = 1.54439 Å) on a spinning zero-background holder All indexing and Pawley fitting was carried out using GSAS-II.[32]

Single Crystal X-Ray Diffraction (SCXRD): Data was collected using a Bruker D8 VENTURE diffractometer (MoKα = 0.71073 Å).

Scanning Electron Microscopy (SEM): Powders were deposited onto carbon tabs mounted on aluminium stubs, these were subsequently coated with Pd for 150 seconds using a Polaron SC7640 sputter coater. Samples of **x** were imaged using a Philips XL30 ESEM. All other samples were imaged using a Carl Zeiss Sigma variable Pressure Analytical SEM with Oxford Microanalysis.

Thermogravimetric Analysis (TGA): Measurements were carried out using a TA Instruments Q500 Thermogravimetric Analyser. Measurements were collected from room temperature to 600 °C with a heating rate of 10 °C min^{-1} under an air atmosphere.

3.7.2 General Conditions for Fe-terephthalate MOF Synthesis

The iron precursor (1 mmol) and terephthalic acid (1 mmol) were added to a 50 mL Pyrex reagent jar and DMF (10 mL) was added along with any modulator. The jar was capped and sonicated until the solids dissolved before heating in an isothermal oven. After allowing to cool to room temperature, the suspension was separated by centrifuging. The supernatant was decanted and fresh DMF (20 mL) was added before centrifuging again. This was repeated three times, before repeating the procedure another three times with DCM (20 mL). The sample was then dried overnight in a desiccator under vacuum. All the specific conditions (temperature, time, metal precursor, molar equivalents of modulator, etc.) for individual samples are provided in relevant naming schemes and figures in the main section.

3.7.3 Single-Crystal Synthesis of MIL-53(Fe)_DMF

$FeCl_2 \cdot 4H_2O$ (1 mmol) and terephthalic acid (1 mmol) were added to a 50 mL Pyrex reagent jar and DMF (10 mL) was added. The jar was capped and sonicated until the solids dissolved, before heating at 150 °C in an isothermal oven. After 3 days, the jar was removed and allowed to cool to room temperature. Yellow needle-shaped crystals were evident and the DMF was decanted and replaced several times with fresh DMF, in which the crystals were kept for further analysis. A formula of [Fe(OH)(BDC)(DMF)] was determined by elemental analysis and TGA. EA: Expected C, 42.60; H, 3.87; N, 4.52. Found C, 42.36; H, 3.83; N, 4.83. Two mass losses can be seen by TGA: one up to 200 °C due to solvent loss, and another which starts around 300 °C corresponding to framework degradation. 1st mass loss = 21.4% (DMF, theoretical = 23.6%), 2nd mass loss = 48.2% (BDC, theoretical = 50.7%).

3.7.4 MIL-53(Fe)_DMSO

Single crystals of MIL-53(Fe)_DMF were kept immersed in the mother solvent and DMSO was added gradually, followed by removing a portion of the mother solvent. This was repeated multiple times, eventually replacing the mother solvent entirely. The DMSO was replaced once every day for three days. Quantitative exchange of DMF for DMSO was initially considered, but the elemental analysis gives a poor fit for a formula of [Fe(OH)(BDC)(DMSO)]: Theoretical C, 38.11; H, 3.49; N, 0. Found C, 39.33; H, 3.28; N, 1.71. A much better fit is obtained for a formula of $[Fe(OH)(BDC)(DMF)_{0.4}(DMSO)_{0.8}]$: Theoretical C, 40.27; H, 3.11; N, 1.69. Found C, 39.33; H, 3.38; N, 1.71.

3.7.5 Single-Crystal Synthesis of $[Fe_3O(DMF)_3(BDC)_3][BF_4]$

$Fe(BF_4)_2 \cdot 6H_2O$ (1 mmol) and terephthalic acid (1 mmol) were added to a 50 mL Pyrex reagent jar and DMF (10 mL) was added along with acetic acid (40 mmol). The jar was capped and sonicated until the solids dissolved before heating at 120 °C in an isothermal oven. After 24 hours, the jar was removed and allowed to cool to room temperature. Orange hexagonal-shaped crystals were evident and the DMF was decanted and replaced several times with fresh DMF, in which the crystals were kept for further analysis. Elemental analysis suggests the formula $[Fe_3O(DMF)_3(BDC)_3][BF_4] \cdot 1.8H_2O \cdot 0.2DMF$: Expected C, 39.21; H, 3.70; N, 4.36. Found C, 39.21; H, 3.82; N, 4.38.

3.7.6 Single-Crystal Synthesis of [Fe(DMF)(BDC)]

$Fe(BF_4)_2 \cdot 6H_2O$ (1 mmol) and terephthalic acid (1 mmol) were added to a 50 mL Pyrex reagent jar and DMF (10 mL) was added. The jar was capped and sonicated until the solids dissolved before heating at 150 °C in an isothermal oven. After 3 days, the jar was removed and allowed to cool to room temperature. Yellow polyhedral crystals were evident and the DMF was decanted and replaced several times with fresh DMF, in which the crystals were kept for further analysis.

3.7.7 Crystal data for MIL-53(Fe)_DMF

$C_{16}H_{10}Fe_2O_{10}$, M_r = 473.94, crystal dimensions 0.16 × 0.04 × 0.03 mm, Triclinic, a = 6.8403 (12) Å, b = 10.7142 (18) Å, c = 10.7928 (18) Å, V = 669.5 (2) Å^3, T = 150 K, space group , $P\bar{1}$, (No. 2), Z = 1, 3285 measured reflections, 3285 independent reflections (R_{int} = 0.054), which were used in all calculations. The final R_1 = 0.060 for 2479 observed data $R[F^2 > 2\sigma(F^2)]$ and $wR(F^2)$ = 0.137 (all data).

3.7.8 Crystal data for of $[Fe_3O(DMF)_3(BDC)_3][BF_4]$

$0.5(C_{66}H_{48}Fe_6N_6O_{32}) \cdot BF_4$, M_r = 981.98, crystal dimensions 0.12 × 0.1 × 0.01 mm, Hexagonal, a = 12.6391 (8), Å, b = 12.6391 (8), Å, c = 18.3551 (14) Å, V = 2539.3 (4) Å^3, T = 150 K, space group $P\bar{6}2c$, (No. 74), Z = 2, 16518 measured reflections, 2161 independent reflections (R_{int} = 0.038), which were used in all calculations. The final R_1 = 0.055 for 2120 observed data $R[F^2 > 2\sigma(F^2)]$ and $wR(F^2)$ = 0.139 (all data).

3.7.9 Crystal data for [Fe(DMF)(BDC)]

$C_{11}H_{11}FeNO_5$, M_r = 293.06, crystal dimensions 0.08 × 0.07 × 0.03 mm, Orthorhombic, a = 19.4334 (19) Å, b = 7.2431 (7) Å, c = 8.7675 (9) Å, V = 1234.1 (2) Å^3, T = 150 K, space group *Pnma*, (No. 62), Z = 4, 9927 measured reflections, 1654 independent reflections (R_{int} = 0.033), which were used in all calculations. The final R_1 = 0.032 for 1654 observed data $R[F^2 > 2\sigma(F^2)]$ and $wR(F^2)$ = 0.097 (all data).

3.8 References

(1) Horcajada, P., Chalati, T., Serre, C., Gillet, B., Sebrie, C., Baati, T., Eubank, J. F., Heurtaux, D., Clayette, P., Kreuz, C., Chang, J.-S., Hwang, Y. K., Marsaud, V., Bories, P.-N., Cynober, L., Gil, S., Férey, G., Couvreur, P. and Gref, R., *Nat. Mater.*, **2010**, *9*, 172-178.

(2) Horcajada, P., Salles, F., Wuttke, S., Devic, T., Heurtaux, D., Maurin, G., Vimont, A., Daturi, M., David, O., Magnier, E., Stock, N., Filinchuk, Y., Popov, D., Riekel, C., Férey, G. and Serre, C., *J. Am. Chem. Soc.*, **2011**, *133*, 17839-17847.

(3) Pham, M.-H., Vuong, G.-T., Vu, A.-T. and Do, T.-O., *Langmuir*, **2011**, *27*, 15261-15267.

(4) Ma, M., Noei, H., Mienert, B., Niesel, J., Bill, E., Muhler, M., Fischer, R. A., Wang, Y., Schatzschneider, U. and Metzler-Nolte, N., *Chem. Eur. J.*, **2013**, *19*, 6785-6790.

(5) Vuong, G.-T., Pham, M.-H. and Do, T.-O., *CrystEngComm*, **2013**, *15*, 9694-9703.

(6) Ma, M., Bétard, A., Weber, I., Al-Hokbany, N. S., Fischer, R. A. and Metzler-Nolte, N., *Cryst. Growth Des.*, **2013**, *13*, 2286-2291.

(7) Cai, X., Lin, J. and Pang, M., *Cryst. Growth Des.*, **2016**, *16*, 3565-3568.

(8) Choi, S., Cha, W., Ji, H., Kim, D., Lee, H. J. and Oh, M., *Nanoscale*, **2016**, *8*, 16743-16751.

(9) Gao, X., Zhai, M., Guan, W., Liu, J., Liu, Z. and Damirin, A., *ACS Appl. Mater. Interfaces*, **2017**, *9*, 3455-3462.

(10) Sudik, A. C., Côté, A. P. and Yaghi, O. M., *Inorg. Chem.*, **2005**, *44*, 2998-3000.

(11) Fateeva, A., Horcajada, P., Devic, T., Serre, C., Marrot, J., Grenèche, J.-M., Morcrette, M., Tarascon, J.-M., Maurin, G. and Férey, G., *Eur. J. Inorg. Chem.*, **2010**, *2010*, 3789-3794.

(12) Whitfield, T. R., Wang, X., Liu, L. and Jacobson, A. J., *Solid State Sci.*, **2005**, *7*, 1096-1103.

(13) Sanselme, M., Grenèche, J.-M., Riou-Cavellec, M. and Férey, G., *Solid State Sci.*, **2004**, *6*, 853-858.

(14) Taylor-Pashow, K. M. L., Della Rocca, J., Xie, Z., Tran, S. and Lin, W., *J. Am. Chem. Soc.*, **2009**, *131*, 14261-14263.

(15) Férey, G., Millange, F., Morcrette, M., Serre, C., Doublet, M.-L., Grenèche, J.-M. and Tarascon, J.-M., *Angew. Chem. Int. Ed.*, **2007**, *46*, 3259-3263.

(16) Bauer, S., Serre, C., Devic, T., Horcajada, P., Marrot, J., Férey, G. and Stock, N., *Inorg. Chem.*, **2008**, *47*, 7568-7576.

(17) Carson, F., Su, J., Platero-Prats, A. E., Wan, W., Yun, Y., Samain, L. and Zou, X., *Cryst. Growth Des.*, **2013**, *13*, 5036-5044.

(18) Millange, F., Medina, M. I., Guillou, N., Férey, G., Golden, K. M. and Walton, R. I., *Angew. Chem. Int. Ed.*, **2010**, *49*, 763-766.

(19) Stavitski, E., Goesten, M., Juan-Alcañiz, J., Martinez-Joaristi, A., Serra-Crespo, P., Petukhov, A. V., Gascon, J. and Kapteijn, F., *Angew. Chem. Int. Ed.*, **2011**, *50*, 9624-9628.

(20) Bara, D. J., Wilson, C., Mörtel, M., Khusniyarov, M. M., Ling, S., Slater, B., Sproules, S. and Forgan, R. S., *J. Am. Chem. Soc.*, **2019**.

(21) Surble, S., Serre, C., Mellot-Draznieks, C., Millange, F. and Férey, G., *Chem. Commun.*, **2006**, 284-286.

(22) Serre, C., Mellot-Draznieks, C., Surblé, S., Audebrand, N., Filinchuk, Y. and Férey, G., *Science*, **2007**, *315*, 1828-1831.

(23) Férey, G., Mellot-Draznieks, C., Serre, C., Millange, F., Dutour, J., Surblé, S. and Margiolaki, I., *Science*, **2005**, *309*, 2040-2042.

(24) Millange, F., Guillou, N., Walton, R. I., Grenèche, J.-M., Margiolaki, I. and Férey, G., *Chem. Commun.*, **2008**, 4732-4734.

(25) Embrechts, H., Kriesten, M., Ermer, M., Peukert, W., Hartmann, M. and Distaso, M., *RSC Advances*, **2020**, *10*, 7336-7348.

(26) Millange, F., Serre, C., Guillou, N., Férey, G. and Walton, R. I., *Angew. Chem. Int. Ed.*, **2008**, *47*, 4100-4105.

(27) Serre, C., Millange, F., Thouvenot, C., Noguès, M., Marsolier, G., Louër, D. and Férey, G., *J. Am. Chem. Soc.*, **2002**, *124*, 13519-13526.

(28) Loiseau, T., Serre, C., Huguenard, C., Fink, G., Taulelle, F., Henry, M., Bataille, T. and Férey, G., *Chem. Eur. J.*, **2004**, *10*, 1373-1382.

(29) Chen, L., Mowat, J. P. S., Fairen-Jimenez, D., Morrison, C. A., Thompson, S. P., Wright, P. A. and Düren, T., *J. Am. Chem. Soc.*, **2013**, *135*, 15763-15773.

(30) Ragon, F., Horcajada, P., Chevreau, H., Hwang, Y. K., Lee, U. H., Miller, S. R., Devic, T., Chang, J.-S. and Serre, C., *Inorg. Chem.*, **2014**, *53*, 2491-2500.

(31) Zahn, G., Zerner, P., Lippke, J., Kempf, F. L., Lilienthal, S., Schröder, C. A., Schneider, A. M. and Behrens, P., *CrystEngComm*, **2014**, *16*, 9198-9207.

(32) Toby, B. H. and Von Dreele, R. B., *J. Appl. Crystallogr., 46(2)*, 544-549.

Chapter 4

Modulated Synthesis of Chromium Metal-Organic Frameworks

Contributions

Single-crystal data collection and structure refinement were carried out by Claire Wilson (University of Glasgow). Gas sorption simulations of MIL-53(Cr)_Br were carried out by Ignas Pakamore (University of Glasgow). All other synthetic work, data collections, and data analysis was performed solely by me.

Contents

Chapter 4 126

4.1 Introduction 130

4.2 Aims 132

4.3 Synthesis of Cr-biphenyl-4,4′-dicarboxylate Frameworks 133

4.3.1 Summary 139

4.4 Synthesis of Isoreticular MIL-88 Frameworks 140

4.4.1 Single Crystal Synthesis of MIL-88B(Cr)_1,4-NDC 142

4.4.2 Summary 144

4.5 Flexibility of MIL-88 and MIL-88-int Frameworks 146

4.5.1 MIL-88B(Cr)_1,4-NDC 147

4.5.2 MIL-88C(Cr) 148

4.5.3 MIL-88D(Cr) 150

4.5.4 Cr-SDC 151

4.5.5 Summary 153

4.6 Synthesis of Cr(OH)-dicarboxylate Frameworks 155

4.6.1 Summary 164

4.7 Synthesis with Higher Connectivity Linkers 165

4.7.1 Synthesis of Cr-soc-MOF 165

4.7.2 Summary 169

4.7.3 Mixed and Single Linker Frameworks Containing BTB 170

4.7.4 Summary 177

4.8 Conclusions 178

4.9 Experimental 180

4.9.1 General Experimental Methods 180

4.9.2 General Synthesis of Cr-BPDC MOFs 181

4.9.3 Synthesis of $[Cr_3O(CH_3COO)_6(H_2O)_3]NO_3 \cdot 6H_2O$ clusters 181

4.9.4 General Synthesis of Isoreticular MIL-88 Series 182

4.9.5 Single-Crystal Synthesis of MIL-88B(Cr)_1,4-NDC 183

4.9.6 Crystal data for MIL-88B(Cr)_1,4-NDC.....183
4.9.7 Synthesis of MIL-53(Cr).....183
4.9.8 Crystal data for MIL-53(Cr).....183
4.9.9 Synthesis of MIL-53_Br(Cr).....184
4.9.10 Crystal data for MIL-53(Cr)_Br.....184
4.9.11 Synthesis of Cr(OH)(1,4-NDC).....184
4.9.12 Synthesis of Cr(OH)(2,6-NDC).....184
4.9.13 General Synthesis of Cr-soc-MOF.....185
4.9.14 Synthesis of Mixed Linker MOFs.....185
4.9.15 Synthesis of MIL-100(Cr)_BTB.....185
4.10 References.....187

4.1 Introduction

Despite the large interest in MOFs, stability continues to present a barrier to many applications. MOFs constructed from divalent cations are typically susceptible to attack by water molecules, which can easily substitute the metal-ligand bonds and cause framework degradation.[1] This has directed a significant proportion of MOF research towards synthesising frameworks which contain higher valent metals such as Fe^{3+} and Zr^{4+}, and hard Lewis bases, such as carboxylates, which tend to form stronger bonds.[1-5]

Cr-MOFs were one of the first of such framework types to be investigated synthetically, with the Cr-terephthalate based MOF MIL-53(Cr) first reported in 2002.[6,7] Its highly flexible nature, expressed by changes in the pore size upon the adsorption of different guest molecules, makes it a promising material for gas and liquid phase separations; along with its many M^{3+} analogues, it is one of the most widely studied MOFs to date.[8-11] The slow kinetics of reactions involving Cr^{3+} enable easier access to frameworks which possess large pores, which are thermodynamically unfavourable but are stabilised by the slow ligand exchange rate of Cr^{3+}. A notable example is the Cr-terephthalate MIL-101(Cr), which possesses exceptionally large pores and exceptional stability, and has thus become one of the most widely studied MOFs[12] since it was first reported in 2005.[13] The combination of high-chemical stability and high-porosity, exemplified by both MIL-53(Cr) and MIL-101(Cr), make Cr-MOFs some of the most desirable materials for commercialisation, and that alone warrants further investigation into their synthesis.

Compared to MOFs containing other metals, there are still relatively few Cr-MOFs in the literature. This is in part a consequence of the slower kinetics of reactions involving Cr^{3+} and the frequent use of HF, which is extremely hazardous, to enhance crystallinity, both of which make synthesising Cr-MOFs challenging and unattractive. Another likely reason is that there is no direct synthetic route to grow large single crystals of Cr-MOFs, and the vast majority have only ever been obtained as microcrystalline powders. This presents another challenge when studying Cr-MOFs, as solving MOF structures from powder diffraction data is much more time-consuming and technically challenging than using modern single-crystal diffraction techniques.

In addition to the directly synthesised Cr-MOFs, there are also several Cr-MOFs obtained from their Fe-analogues via metathesis,[14-16] which is enabled by their similar ionic radii. There are clear advantages to this technique, particularly when large and poorly soluble linkers are employed, as it enables the synthesis to be conducted at relatively low

temperatures in DMF rather than the aqueous conditions often required in Cr-MOF synthesis. This also means that large single crystals can be obtained, thus far unheard of for Cr-MOFs, which greatly facilitates structural analysis. The main drawback is that, when these metathesis reactions are attempted, careful characterisation of the degree of exchange is required and must be accompanied by further optimisation to ensure that the exchange has been complete and successful.

In order to develop synthetic protocols for Cr-MOFs, it is important to have an appreciation of what has been shown to be successful in the past and then to apply this to new systems. As has been alluded to, the most common synthetic method is hydrothermal synthesis at relatively high temperature (180-220 $^{\circ}$C) using suitable pressure vessels (usually acid digestion bombs). HF (typically 1-2 molar equivalents) is added to the synthetic mixture in most cases, but in a few cases has been replaced for more benign additives such as acetic acid or nitric acid. Mixtures of water and pyridine have also been used to synthesise MIL-88B(Cr) and its isoreticular analogue MIL-88D(Cr).[17] In the case of MIL-88D(Cr) this is likely necessary to enable dissolution of the water-insoluble BPDC linker as the pyridinium salt. DMF is used much less commonly than water but has been shown to yield MIL-88-type frameworks such as MIL-88B(Cr),[18] MIL-88B(Cr)_NH_2,[18] and BUT-8(Cr)[19] when used in combination with HF. In addition to the nitrate and chloride salts, which are more commonly used as the source of Cr^{3+} ions, metallic chromium has also been used to synthesise MIL-100(Cr),[20] MIL-96, and MIL-102,[21] which could be referred to as a form of 'oxidation modulation' as they require the oxidation of Cr(0) to Cr(III).

4.2 Aims

The main aims of this chapter are:

1. To develop a reliable and HF-free synthetic protocol for obtaining MIL-88D(Cr)
2. To extend this method to isoreticular analogues through variation of the linker length
3. To characterise the flexibility of MIL-88 and MIL-88-int frameworks
4. To synthesise MIL-53(Cr) and some of its isoreticular analogues
5. To synthesise rigid Cr-MOFs by using higher connectivity linkers and characterise their porosity

To establish a reliable synthetic route for Cr-MOFs, I have explored the use of additives which could replace HF as a crystallising agent first in syntheses with biphenyl dicarboxylate as a linker. I have then attempted to extend this method to synthesise a range of isoreticular Cr-MOFs by varying the linker length and then characterise their flexibility using PXRD techniques. In an effort to obtain frameworks that possess high permanent porosity, I have explored synthesis with higher connectivity linkers, which are expected to impart rigidity and enhance gas uptake.

4.3 Synthesis of Cr-biphenyl-4,4′-dicarboxylate Frameworks

MIL-88D(Cr) has been synthesised previously from H_2BPDC and $Cr(NO_3)_3 \cdot 9H_2O$ in a water/pyridine mixture (2 mL of water and 3 mL of pyridine) with HF as a mineraliser, heating at 220 ˚C for 16 hours.[22] Once washed and dried, this yielded MIL-88D(Cr) in what will be henceforth referred to as the 'as-synthesised' form[23] which adopts an intermediate unit cell volume between the 'open' and 'closed' forms. This study was started by utilising this same procedure but replacing HF with other mineral acids: nitric and hydrochloric acid. After synthesis, the solids were collected by centrifuging and washed multiple times with DMF to remove unreacted starting materials, and then with DCM to help dry the material. Surprisingly, the unmodulated synthesis appeared to yield MIL-88D(Cr) as-synthesised with low crystallinity, as evidenced by PXRD (Figure 4.1a). Similar reflections were evidenced when 1 equivalent of nitric acid was added to the synthesis, but in general neither of the two mineral acids seemed to yield a more crystalline product, and thus were not investigated further. To avoid the use of pyridine, it was replaced with DMF and the water:DMF ratio was varied to see if there was an optimum ratio for obtaining crystalline material. There is at least one literature example where MIL-101(Cr) has successfully been synthesised in a DMF:water mix[24] and two examples where DMF has been used as a single solvent to synthesise MIL-88-type frameworks with chromium(III) and HF.[18,19] The products were very poorly crystalline, as can be seen by PXRD (Figure 4.1b), which suggests that DMF is not a suitable solvent. Further attempts to replace pyridine with other weak organic bases, including 3-methylpyridine and 2,6-lutidine, amongst others, also failed to yield a crystalline product.

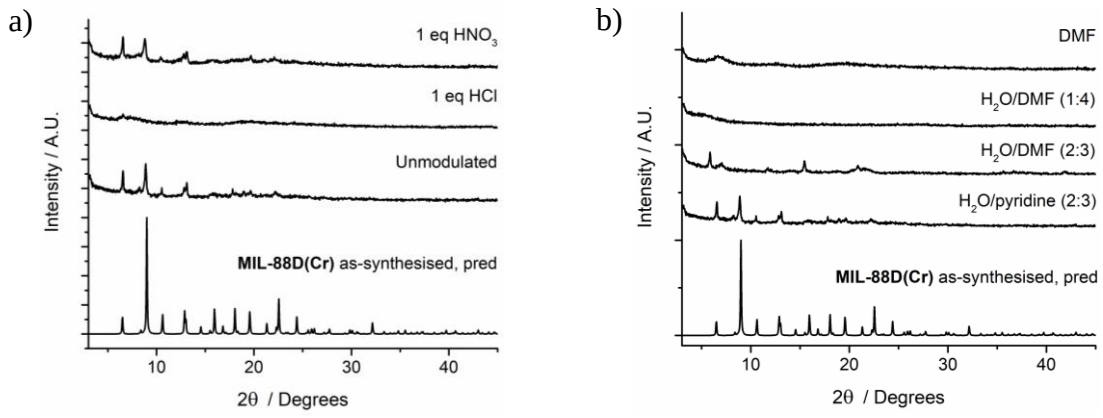

Figure 4.1. Stacked PXRD patterns of a) Cr-BPDC prepared with different modulators compared to the predicted pattern for MIL-88D(Cr) as-synthesised, and b) Cr-BPDC prepared with different solvent mixtures compared to the predicted pattern for MIL-88D(Cr) as-synthesised.[17]

The role of HF is essentially to behave as a modulator, however, neither of the mineral acids used appeared to improve the crystallinity. Carboxylate modulators should be more effective at crystallising frameworks which contain the $M_3O(RCO_2)_6$ cluster than mineral acids (as was demonstrated in Chapter 3), and thus acetic acid (AA), formic acid (FA), and trifluoroacetic acid (TFA) were all used, keeping the other synthetic conditions identical (2:3 ratio of water:pyridine and heating at 220 °C for 16 hours). Based on the PXRD patterns (Figure 4.2a), acetic acid appeared to be the best modulator, but a significant amount of unreacted linker was evident in the PXRD pattern (Figure 4.2b), even after further DMF washes.

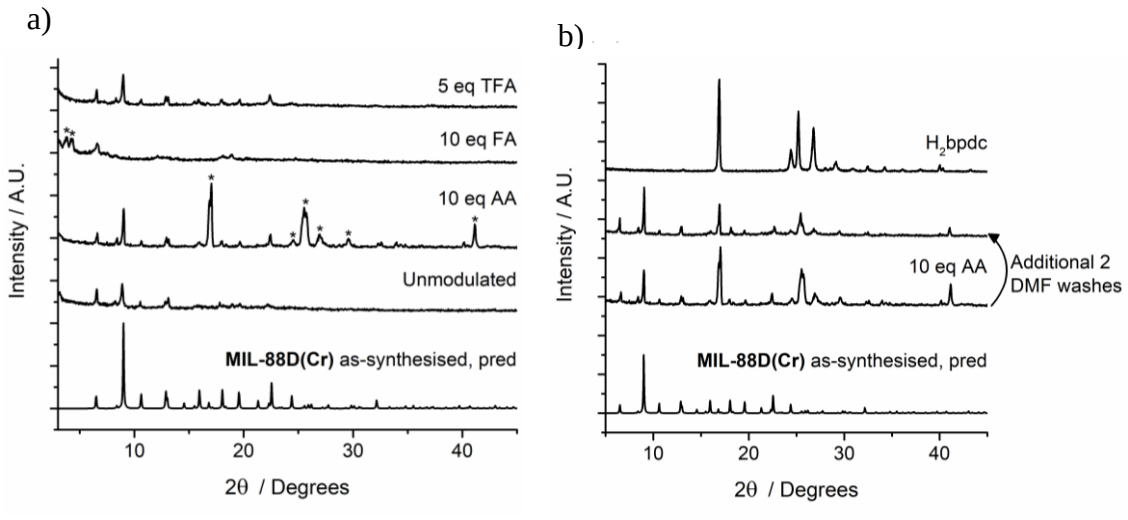

Figure 4.2. Stacked PXRD patterns of a) Cr-BPDC prepared with different modulators using a mixed solvent (2 mL of water and 3 mL of pyridine) compared to the predicted pattern for MIL-88D(Cr) as-synthesised,[17] and b) Cr-BPDC prepared with 10 eq of AA before and after additional DMF washes, with the experimental pattern for H_2BPDC for comparison.

To help to prevent this, the concentration of the reagents was reduced by half by doubling the solvent volume, so that more of the linker would remain in solution during synthesis, keeping the synthesis time constant (16 hours). The obtained PXRD patterns show that doing this both prevented unreacted linker from remaining in the final product, and also enhanced the crystallinity of the obtained solid significantly. There is a close match between the obtained PXRD patterns and the reported structure of MIL-88D(Cr) (Figure 4.3a), thus confirming its identity. SEM imaging was used to investigate the crystal size and morphology, and shows that both samples contain hexagonal rods (Figure 4.3b), which bear a close resemblance to the Fe-analogue discussed in Chapter 2 and appear to be phase pure.

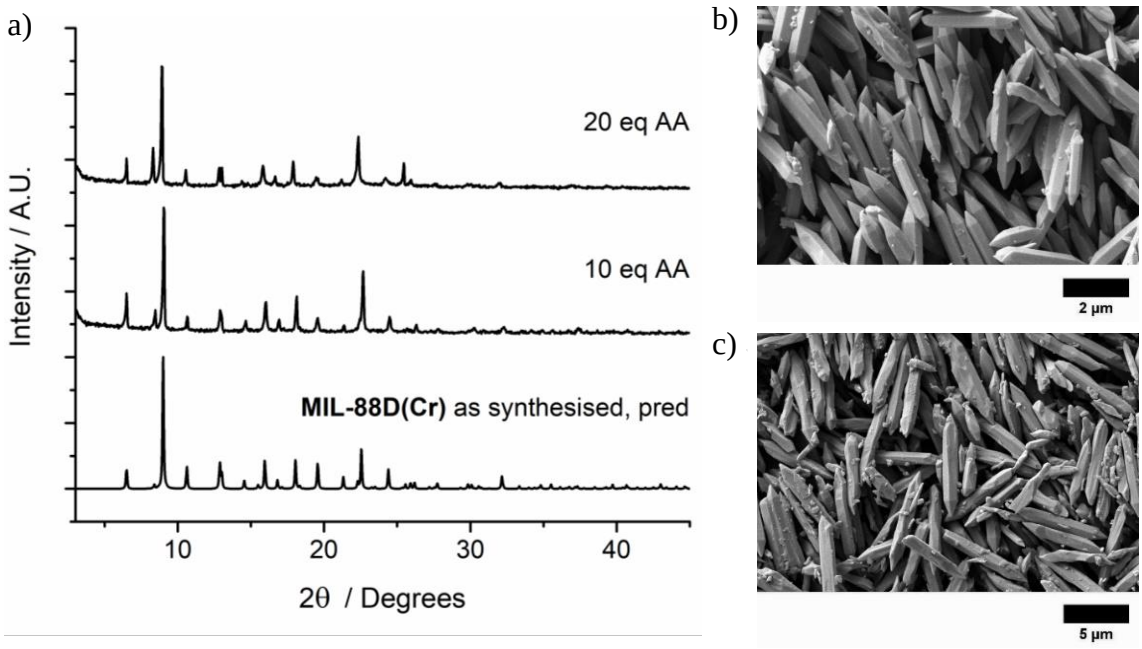

Figure 4.3. a) Stacked PXRD patterns of Cr-BPDC synthesised at lower concentration (4 mL of water and 6 mL of pyridine) with different quantities of AA compared to the predicted pattern for MIL-88D(Cr) as-synthesised, and b) SEM image of Cr-BPDC prepared with 10 eq of AA, c) SEM image of Cr-BPDC prepared with 20 eq of AA.

It is worth discussing here that, unlike in the case of Fe-biphenyl-4,4′-dicarboxylates (discussed in Chapter 2), modulation in this case does not appear to favour the formation of the two-fold interpenetrated MIL-126(Cr) and both PXRD and SEM suggest phase-pure MIL-88D(Cr) is obtained in all cases. This is unsurprising, as Cr^{3+} is much more inert than Fe^{3+} and thus kinetic products are stabilised. The PXRD pattern obtained with 10 eq of AA was of sufficient quality to allow indexing of the peaks to extract a unit cell, which was further refined by the Pawley method and compared to the already reported MIL-88D(Cr) in its as-synthesised form. The as-synthesised material in the literature is a sample which has only been washed with water and acetone following synthesis.[22] The first twenty peaks were indexed to give a hexagonal unit cell with, the Pawley fit given in Figure 4.4a, and it is clear from the Pawley fit that all of the experimental peaks can be attributed to MIL-88D(Cr). As expected, there is a close match between the obtained unit cell parameters and those reported for MIL-88D(Cr) in the as-synthesised form (Figure 4.4b).

a)

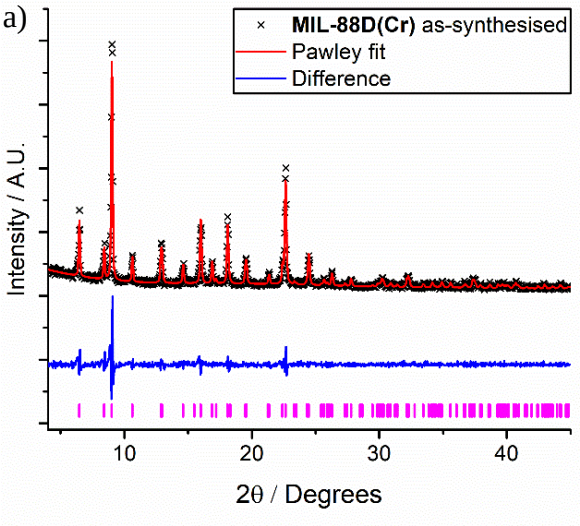

b)

Parameters	Experimental fit	Literature reference
a **(Å)**	12.115	12.165
c (Å)	27.296	27.191
V **(Å^3)**	3469.7	3485

Figure 4.4. a) Pawley fit of MIL-88D(Cr) as-synthesised, b) comparison of the obtained unit cell parameters from Pawley fitting with the literature reference.[17]

In an attempt to aid in deprotonation of the linker during synthesis, sodium acetate was explored as an alternative modulator due to its basic nature and similar coordinating ability. Compared to acetic acid, only relatively small amounts of sodium acetate could be used, with 5 equivalents yielding only recrystallised linker. Synthesis was thus conducted with one and two equivalents of modulator, both giving different PXRD patterns to those of MIL-88D(Cr) (Figure 4.5a). A search for known MOFs containing M^{3+} metals and biphenyl-4,4′-dicarboxylate linkers enabled the phase to be identified as DUT-5, an aluminium framework with the formula Al(OH)(BPDC), which is an isoreticular analogue of MIL-53 with an orthorhombic crystal structure (Figure 4.5a-b). There is a strong resemblance between the low angle peaks in the reported PXRD pattern for DUT-5 and the samples obtained here (Figure 4.5c). However, there are clearly some broader peaks at higher angle (at around 20 and 25° 2θ) which do not correspond to either MIL-88D(Cr) or DUT-5 – they also do not correspond to peaks for NaOAc or H_2BPDC. It is reasonable to assume that these peaks likely correspond to some insoluble inorganic compound (such as a hydroxide or oxide) as further treatment with DMF had no effect on their intensity, but there appears to be no match for this phase in the available databases. SEM imaging shows that the samples consist of rectangular blocks (Figure 4.5d-e), but a significant number of rods corresponding to MIL-88D(Cr) are also evident. More of these rods are present with 1 equivalent of NaOAc compared to the sample with 2 equivalents; this is consistent with their PXRD patterns. Other acetate salts were explored, such as ammonium acetate and tetrabutylammonium acetate, as alternative reagents, with the hope that they would be less basic and thus prevent the formation of oxide/hydroxide by-products, but none of these attempts produced a crystalline

material. Regardless, the ability to tune between the two phases merely by tuning the nature of the modulator is interesting and could potentially be investigated further to obtain the phase-pure DUT-5(Cr) material.

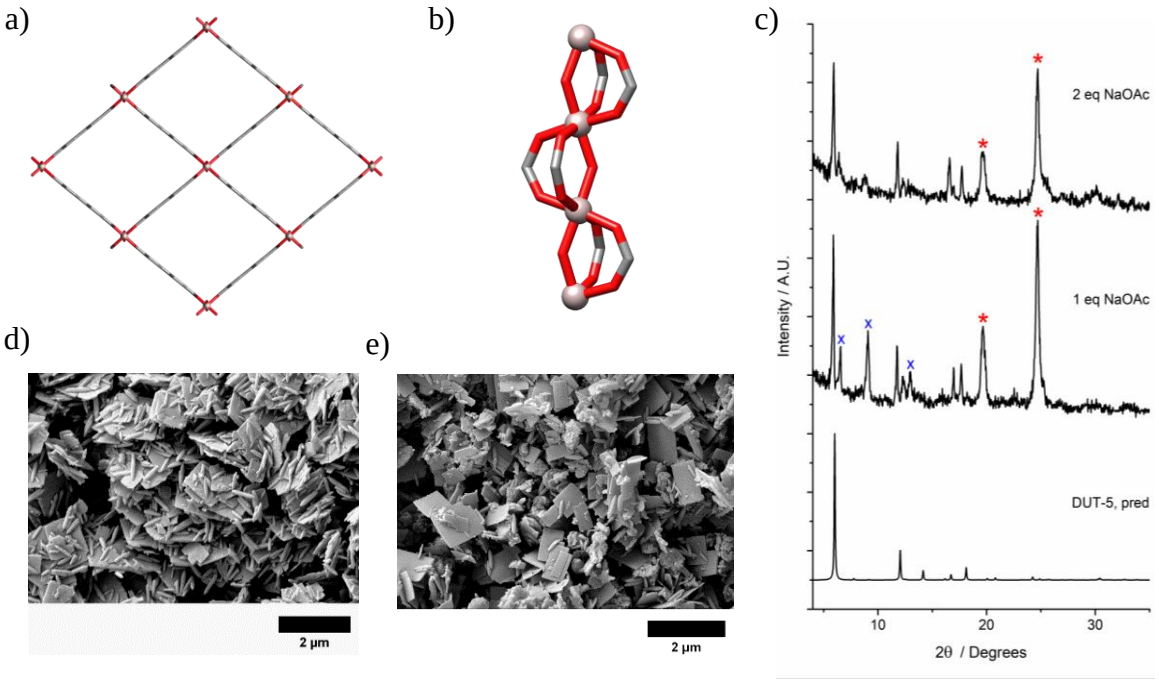

Figure 4.5. a) Packing structure of DUT-5, b) Al(OH) chain SBU in DUT-5, c) stacked PXRD patterns of Cr-BPDC prepared with different quantities of sodium acetate compared to the predicted pattern for DUT-5 (* = peaks from unknown phase, x = peaks from MIL-88D(Cr) as-synthesised), and d) SEM image of Cr-BPDC prepared with 1 eq of sodium acetate, e) SEM image of Cr-BPDC prepared with 2 eq of sodium acetate.

Another variable which was exploited in the previous chapter is the nature of the metal-containing salt, which was shown to have an important effect on the obtained phase in the synthesis of Fe-dicarboxylates. Both chromium (III) sulfate hydrate and chromium (III) chloride hexahydrate were investigated for synthesis using the ideal conditions found for MIL-88D(Cr) with the nitrate (2:3 ratio of water: pyridine, 10 eq of acetic acid, 220 $^{\circ}$C, 16 hours). It is immediately evident from the PXRD patterns (Figure 4.6a) that both samples contain, in addition to MIL-88D(Cr), an additional phase which has its major peaks at low angle. Because of its similarity to MIL-101(Fe)_BPDC,[25] an extended analogue of MIL-101 with BPDC as linker, which is expected to be a kinetic product, an identical reaction was performed for 4 hours using the $CrCl_3$ salt as precursor. As expected, the shorter reaction time favoured the formation of only the low-angle phase, as evidenced by PXRD (Figure 4.6b), and SEM imaging revealed that this sample consists of small intergrown crystallites

(Figure 4.6c). The sample could then be identified as MIL-101(Cr)_BPDC by comparison of the PXRD pattern to the reported Fe-analogue (Figure 4.6d).[25]

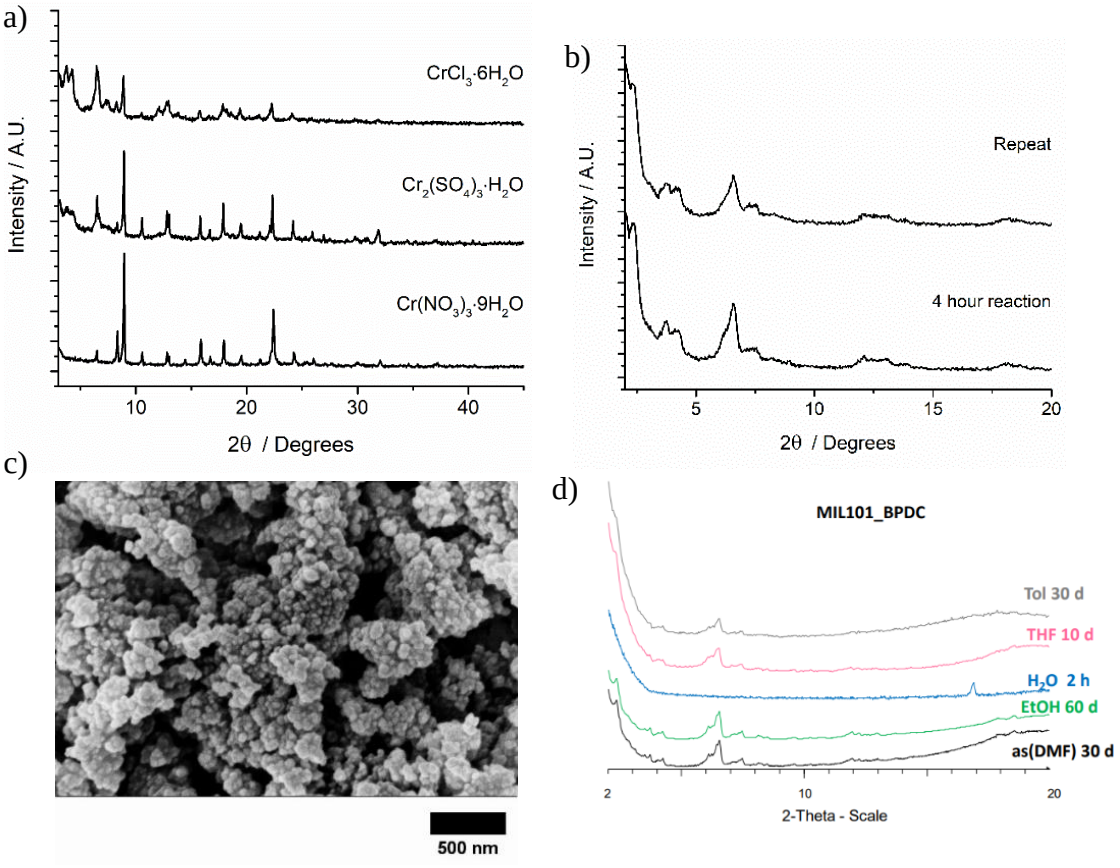

Figure 4.6. a) Stacked PXRD patterns of Cr-BPDC prepared from different chromium salts, and b) PXRD patterns of Cr-BPDC prepared with $CrCl_3$ synthesised for 4 hours, c) SEM image of Cr-BPDC prepared with $CrCl_3$ synthesised for 4 hours, d) stacked PXRDs of MIL-101(BPDC) from the literature.[25]

The interest in this material is due to the already well-known high-porosity of the terephthalate analogue MIL-101, which has a BET surface area of >3000 m^2g^{-1}. While the Fe-analogue, MIL-101(Fe)_BPDC has been reported previously, it was found to rapidly decompose in water and the activated material had a very low porosity (210 m^2g^{-1}).[25] As the Cr-analogue of MIL-101 has excellent stability in water, and MIL-101(Cr)_BPDC was in fact synthesised in water, I expected that this MOF would display very high porosity and improved stability over the Fe-analogue. In an attempt to activate the material, the sample was soaked in DMF for 1 day at RT followed by the same procedure with methanol. Finally, the sample was heated at 150 °C for 20 hours under vacuum before analysis. N_2 adsorption/desorption isotherms were conducted at 77 K to assess the porosity of the material. The nitrogen uptake is significantly lower than expected (Figure 4.7a), however,

the BET surface area SA_{BET} = 500 m^2g^{-1} is still higher than the Fe-analogue SA_{BET} = 210 m^2g^{-1}.[25] The PXRD pattern of the material after activation (Figure 4.7b) suggests that there is a loss of crystallinity, indicating that the framework has collapsed somewhat during evacuation. This is not uncommon for large pore MOFs, which often require milder activation conditions such as activation using supercritical CO_2 which has a much lower surface tension. Nevertheless, further efforts to synthesise and activate this material are essential to gain further insight into its behaviour.

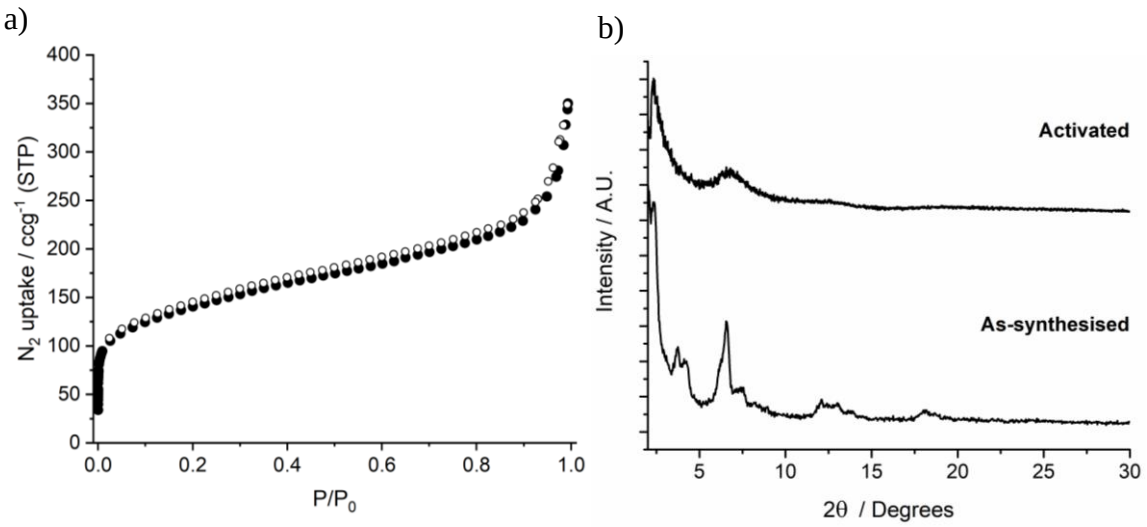

Figure 4.7. a) Nitrogen adsorption (closed circles) and desorption (open circles) isotherms (77 K) of MIL-101(Cr)_BPDC, b) PXRD patterns of MIL-101(Cr)_BPDC before and after gas-sorption analysis.

4.3.1 Summary

In this section a successful HF-free route to the synthesis of Cr-MOFs has been established, enabling high-quality MIL-88D(Cr) to be obtained for the first time without the need for HF. Acetic acid is evidently highly effective at enhancing crystallinity in this system, and the resulting materials appear to be phase-pure as determined by PXRD and SEM. Through variation of the synthesis conditions and reagents, we have also observed two novel phases, DUT-5(Cr) and MIL-101(Cr)_BPDC, which also contain the BPDC linker that MIL-88D(Cr) is constructed from. The boundaries between these three framework topologies are clearly quite narrow in terms of synthetic conditions, which further highlights how challenging this type of synthesis can be. In the next section I will extend the successful acetic acid modulation route to other linkers in order to find out how general the method is.

4.4 Synthesis of Isoreticular MIL-88 Frameworks

Once suitable conditions had been established for the synthesis of MIL-88D(Cr), other linkers were employed in a similar manner. These were initially targeted towards similar dicarboxylate linkers, 1,4-NDC and 2,6-NDC (Figure 4.8a), which have been reported to form frameworks with MIL-88 topology (Figure 4.8b)[26] but have not been produced with Cr(III), and which will be referred to as MIL-88B(Cr)_1,4-NDC for the 1,4-NDC containing framework and MIL-88C(Cr) for the 2,6-NDC containing framework. The 4,4′-stilbenedicarboxylic (SDC) containing framework Cr-SDC is expected to adopt a two-fold interpenetrated topology (which will be referred to as MIL-88-int.), which is shown in Figure 4.8c and is based on the Fe- and Sc-SDC frameworks synthesised within our own group (currently unpublished). This type of interpenetration is different to MIL-126 (Chapter 2): in MIL-126 the two nets are orthogonal to one another (Figure 4.8d), while in MIL-88-int. the nets are parallel (Figure 4.8e).

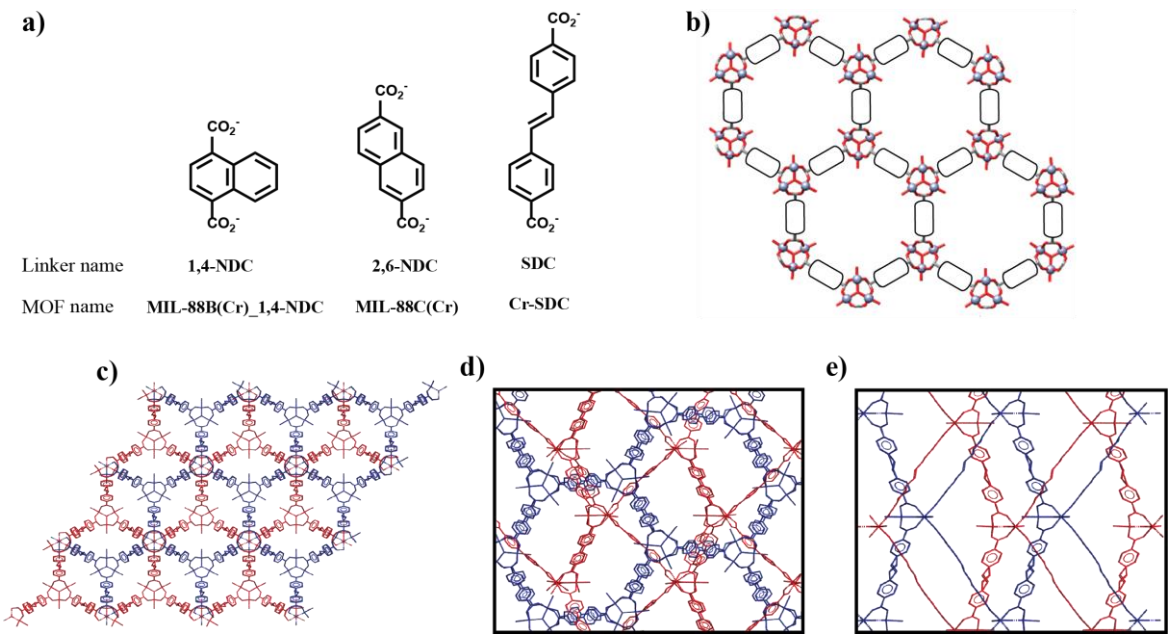

Figure 4.8. a) Scheme of the linkers used in this section and naming system, b) topology of MIL-88 frameworks as viewed down the *c*-axis, c) packing of MIL-88-int. as viewed down the *c*-axis, d) packing of MIL-126 as viewed down the *a* or *b* axes, e) view of MIL-88-int. as viewed down the *a* or *b* axes.

After scanning a range of conditions, including varying the time, starting reagent, and modulator concentration, the optimal conditions for each framework were obtained. The optimal samples were all obtained using preformed $Cr_3O(OAc)_6$ clusters,[27] similar to the preformed cluster approach that has been used for other trivalent MOFs (Section 1.4.4), with

a heating time of 16 hours for MOF formation and an optimised quantity of acetic acid used as modulator. As with MIL-88D(Cr), each sample was washed with DMF and DCM before drying at room temperature. The MIL-88 frameworks are particularly difficult to characterise because their flexibility is continuous and thus they can exist in any state between fully open and closed; I have therefore compared our PXRD patterns with those predicted from both the open and closed structures where available.

For the as-synthesised forms of MIL-88B(Cr)_1,4-NDC and MIL-88C(Cr), the main low angle peaks in the PXRD patterns lie between those for the "open" and "closed" forms of the related Fe-analogues (Figure 4.9a-b), consistent with what has been reported for MIL-88B(Cr) and MIL-88D(Cr).[23] MIL-88B(Cr)_1,4-NDC is much closer to the open form of MIL-88B(Fe) than the reported as-synthesised form of MIL-88B(Cr)[17], as can be seen by PXRD (Figure 4.9a), which is likely due to the greater steric bulk of the 1,4-NDC linker compared to BDC. The as-synthesised form of Cr-SDC has almost identical peak positions to the simulated Fe-SDC analogue (Figure 4.9c), confirming that it adopts the same MIL-88-int topology. SEM imaging was also used to assess the morphology and phase purity of the samples, and in each case hexagonal rods with the expected MIL-88 morphology were present as the predominant phase (Figure 4.9d-f), further confirming their identities.

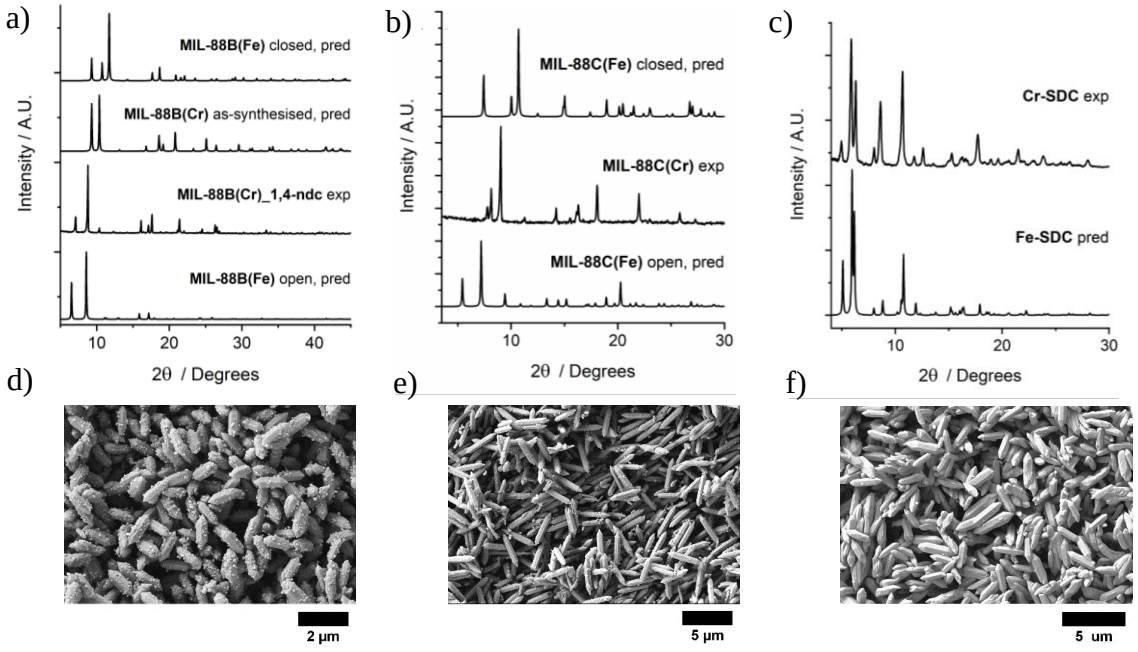

Figure 4.9. Stacked PXRD patterns of MIL-88B(Cr)_1,4-NDC compared the open and closed forms of MIL-88B(Fe),[22] b) stacked PXRD patterns of MIL-88C(Cr) compared the open and closed forms of MIL-88C(Fe),[23] c) stacked PXRD patterns of Cr-SDC compared to the predicted pattern for Fe-SDC. SEM images of d) MIL-88B(Cr)_1,4-NDC, e) MIL-88C(Cr), f) Cr-SDC.

Each of the samples was sufficiently crystalline to enable their PXRD patterns to be indexed and refined using the Pawley method in order to extract unit cell parameters (Figure 4.10a-d). The size of unit cells for the as-synthesised forms are also consistent with the length of linker, and are in the order Cr-SDC > MIL-88D(Cr) (Section 4.3) > MIL-88C(Cr) > MIL-88B(Cr)_1,4-NDC.

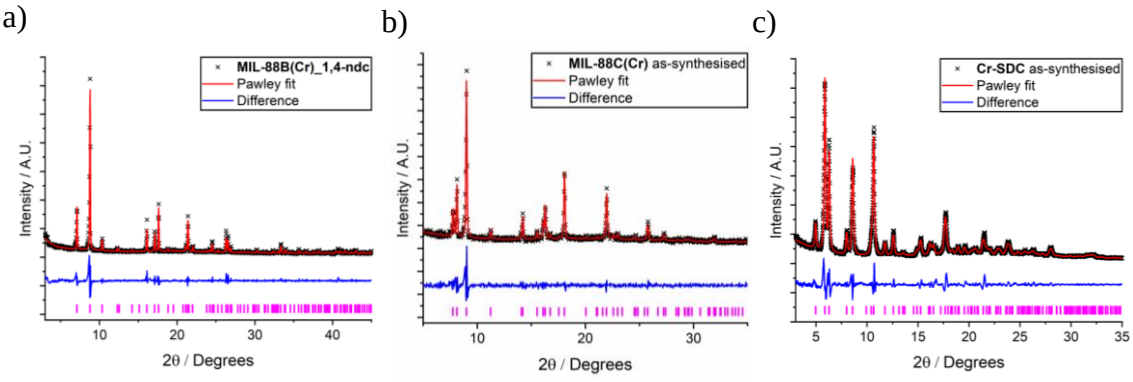

d)

Sample	MIL-88B(Cr)_1,4-NDC	MIL-88C(Cr)	Cr-SDC
a **(Å)**	14.398	12.557	20.586
c (Å)	17.103	22.792	28.182
V **(Å^3)**	3070.2	3112.4	10343.0

Figure 4.10. Pawley fits for the as-synthesised forms of a) MIL-88B(Cr)_1,4-NDC, b) MIL-88C(Cr), c) Cr-SDC, d) extracted unit cell parameters.

The synthesis of Cr-SDC proved to be quite challenging compared to the other MOFs and, despite the initial success, it could not be reliably synthesised using $Cr(NO_3)_3{\cdot}9H_2O$ or $CrCl_3{\cdot}6H_2O$. In many cases the stilbene linker was oxidised into terephthalate, as evidenced by the formation of MIL-101(Cr), a chromium terephthalate MOF, and further confirmed by ^{1}H NMR spectroscopy performed on the base-digested product. When the synthesis time was extended beyond 24 hours, this occurred under all conditions regardless of the Cr-source or the concentration of acetic acid. Shorter reaction times often failed to produce a highly crystalline material, and synthesis with the nitrate salt appeared to have less of a tolerance for acetic acid than for the other linkers (>5 eq usually led to clear solution). The most effective and reliable conditions were 16-24 hours with $Cr_3O(OAc)_6$ as starting material and 7 eq of acetic acid.

4.4.1 Single Crystal Synthesis of MIL-88B(Cr)_1,4-NDC

One of the major challenges for research into Cr-MOFs is the fact that Cr^{3+} is very inert, and thus the growth of large crystals of MOFs synthesised directly with Cr is unheard of and widely accepted as unfeasible.[14,15,28] This makes the discovery of new Cr-MOFs quite

challenging as it usually requires the use of computational modelling aided by PXRD analysis, which is both expensive and highly time-consuming. In order to obtain a structure using traditional direct methods, the crystals need to be of a sufficient size and therefore the synthesis conditions need to be carefully controlled. Even though the inertness of Cr^{3+} appears to be an impassable synthetic barrier to this end, very few of the reported Cr-MOFs have been prepared using modulation, which is well-known to be a powerful technique for growing single crystals of MOFs.

The most promising candidate out of the novel Cr-MOFs synthesised was MIL-88B(Cr)_1,4-NDC, due to the high solubility of the linker in the water/pyridine solvent mix. By increasing the synthesis time from 16 hours to 72 hours, the crystal size increased over 10 times in all dimensions, going from approximately 1.3 x 0.5 μm to 15 x 5.5 μm (Figure 4.11). This is not wholly unsurprising as crystal growth typically occurs over a longer timespan than nucleation,[29] and the crystal growth rate for MOFs constructed from Cr^{3+} is expected to be relatively slow.

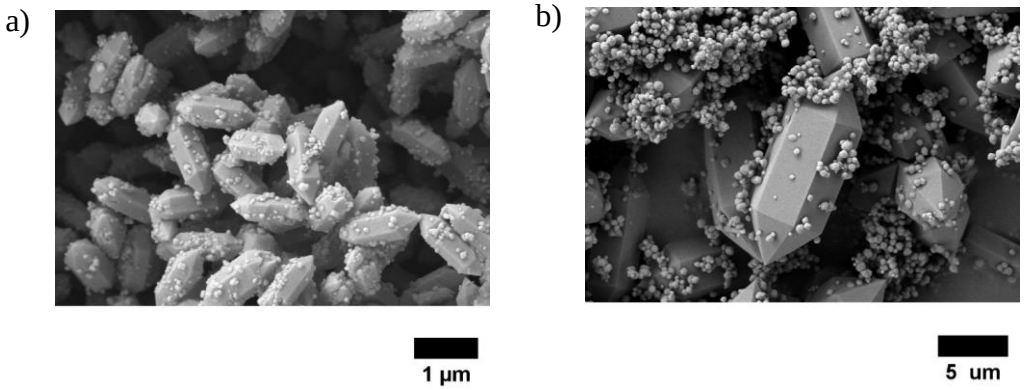

Figure 4.11. SEM images of MIL-88B(Cr)_1,4-NDC synthesised for a) 16 hours, b) 72 hours.

The next step was to increase the quantity of acetic acid, which should result in a further increase in crystal size by slowing down the nucleation rate. As expected, the crystal size increased even further, although the crystals were still relatively quite small (~ 20 x 10 μm). A reasonable data set was collected at the National Crystallography Service (NCS) from a dark green crystal with dimensions 0.02 × 0.01 × 0.01 mm (Figure 4.12a). As expected, based on the previous PXRD refinements, the structure has space group *P*63/*mmc* with unit cell parameters of a = 14.2017 Å, c = 17.189 Å and V = 3002.35 Å^3. The structure is topologically identical to the other MIL-88x frameworks previously reported, with Cr_3O oxo-centred clusters connected by 6 linkers each to form a 3-dimensional hexagonal network with **acs** topology (Figure 4.12b). The linker is twisted by ~45 ° relative to the terephthalate

in MIL-88B and is disordered over 2 possible positions, while the side-ring of the naphthalene is disordered over 4 positions (Figure 4.12c). There is a close match between the PXRD pattern predicted from the obtained crystal structure and the experimental pattern, with only minor differences seen at higher angle (Figure 4.12d). This represents the first single crystal structure obtained for a directly synthesised Cr-MOF.

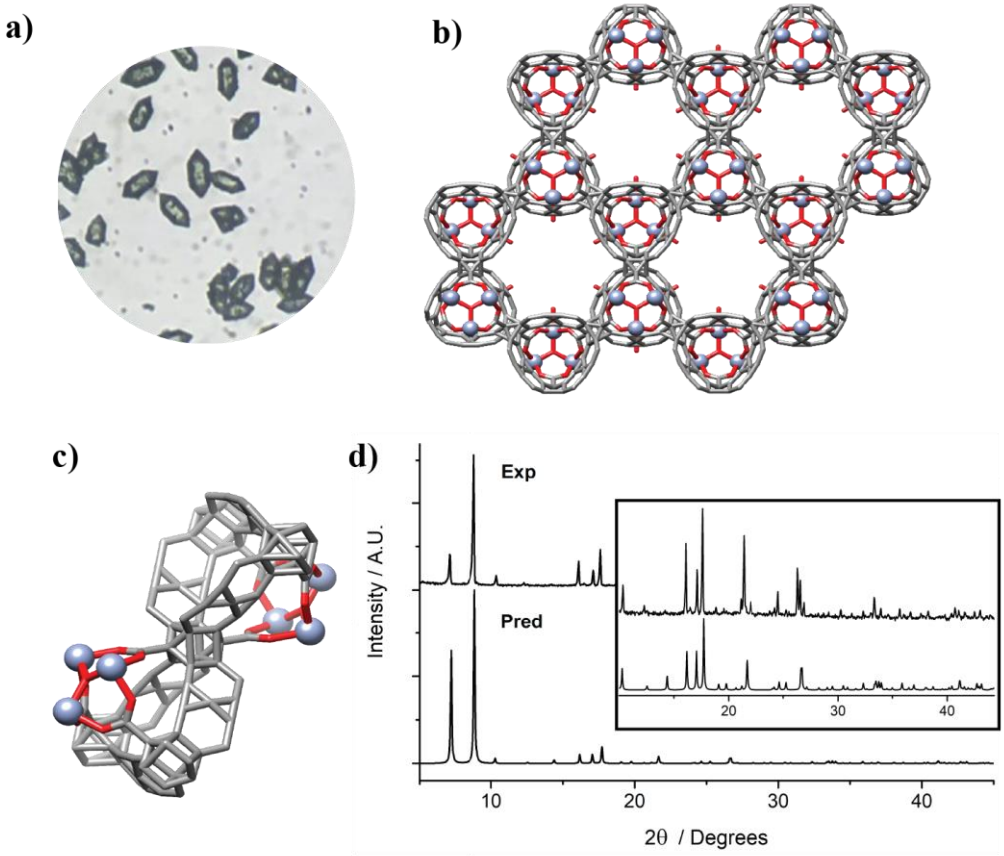

Figure 4.12. a) Image of crystals of MIL-88B(Cr)_1,4-NDC, b) packing structure of the framework viewed down the *c*-axis, c) linker disorder in MIL-88B(Cr)_1,4-NDC, d) comparison of the PXRD patterns of the experimental pattern with the pattern predicted from the crystal structure, with an inset showing the high angle region.

4.4.2 Summary

In this section I have explored the use of reticular synthesis in the synthesis of MIL-88-type Cr-MOFs, demonstrating that our synthetic method is a successful general method for obtaining highly crystalline Cr-MOFs. These frameworks all possess either MIL-88 or MIL-88-int topologies, and thus this synthetic method is clearly selective for these types of frameworks when ditopic linkers are used. The remarkable crystallinity and phase-purity of these samples enables investigation of their flexibility using standard lab-based PXRD

techniques rather than requiring a synchrotron source as has been the case previously. In the next section the flexible nature of these frameworks will be explored in more detail.

4.5 Flexibility of MIL-88 and MIL-88-int Frameworks

The MIL-88 series of MOFs are well-known to be highly flexible, a phenomenon which is induced by the nature and quantity of solvent molecules absorbed in the pores,[23] with the desolvated structures adopting a closed-pore conformation. The mechanism of flexibility in MIL-88 has been found to be due to a hinge-like motion of the carboxylates around the $[M_3O(RCO_2)_6]$ cluster, which allows continuous motion of the network from an open solvated form and an activated closed form.[23] MOFs that undergo continuous flexibility are rare compared to those that exhibit step-wise transitions, of which MIL-53 is the best-known example.[30,31]

To investigate the flexibility of each of the four MOFs: MIL-88B(Cr)_1,4-NDC, MIL-88C(Cr), MIL-88D(Cr), and Cr-SDC, the samples were subjected to a variety of treatments and their powder patterns compared. Where possible, the PXRD patterns were indexed and then refined using the Pawley method in order to extract unit cell parameters. The different forms of the materials are described below:

1. **Open** – Wet sample taken after synthesis and washing with DMF
2. **As-synthesised** – Sample washed with DMF, then DCM, then allowed to dry at room temperature. Although this is not technically 'as-synthesised' in a literal sense, this terminology is consistent with the relevant literature discussing the flexibility of MIL-88 materials.[23]
3. **DMF dry** – Sample soaked in DMF at room temperature for a few days, then washed with DCM and allowed to dry at room temperature
4. **Heated** – As-synthesised sample heated in air at 120 °C overnight
5. **MeOH** – As-synthesised sample refluxed overnight in methanol, then allowed to dry at room temperature

To further investigate the flexibility *in situ*, the DMF-solvated (**Open**) samples were packed into zero background holders which were open to the air and PXRD patterns were recorded every 5 minutes overnight, similar to what was done with MIL-88B(Fe) in Chapter 3. Care was taken to keep the samples wet prior to the first measurement. The shorthand naming scheme is t_χ where χ is equal to the time t in minutes that the PXRD pattern was collected relative to the first measurement (where $\chi = 0$). Each of the MOFs investigated will first be discussed individually.

4.5.1 MIL-88B(Cr)_1,4-NDC

The DMF-solvated form of MIL-88B(Cr)_1,4-NDC (open) is similar in terms of unit cell volume to the reported open form of MIL-88B[23] (Figure 4.13a). Interestingly, both the open and as-synthesised forms of MIL-88B(Cr)_1,4-NDC are more 'open' than the reported $Fe_2CoO(DMF)_3(1,4\text{-NDC})_3$ framework (PCN-241), which is the only reported crystal structure containing 1,4-NDC that possesses the MIL-88 topology. Upon treatment with DMF or methanol, the unit cell decreases somewhat compared to the as-synthesised form, but decreases much more when heated overnight. Compared to the closed form of MIL-88B, the unit cell of the heated sample is still significantly (+65%) larger (Figure 4.13b), which is likely due to the increased steric bulk of the 1,4-NDC linker compared to terephthalic acid. This is comparable to the reported closed form of MIL-88B(Fe)_$2CF_3$ (where the linker is 2,5-bis(trifluoromethyl)terephthalic acid),[22] which gives an indication of where the 1,4-NDC linker sits in comparison to the other modified MIL-88B frameworks discussed in Chapter 1.

a)

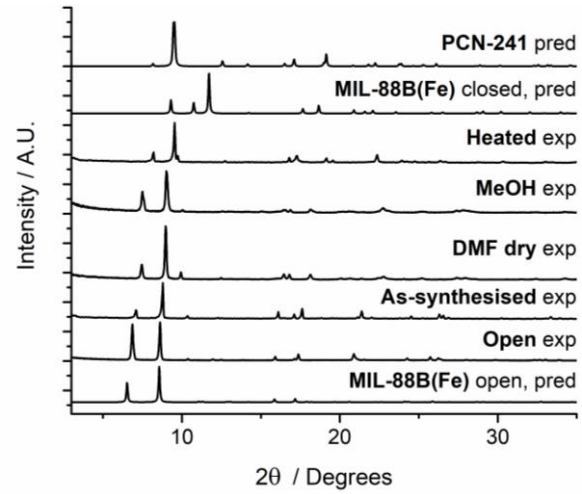

b)

Sample	*a* (Å)	c (Å)	*V* (Å^3)
Open	14.880	16.956	3251.3
As-synthesised	14.398	17.103	3070.2
Heated	12.467	18.157	2443.9
MeOH	13.583	17.635	2817.5
DMF dry	13.841	17.317	2872.9
MIL-88B open	15.626	15.960	3375.0
MIL-88B closed	9.600	19.100	1524.4
MIL-88B as-synthesised	11.028	18.972	1998.2
PCN-241	12.493	18.533	2505.0

Figure 4.13. a) Stacked PXRDs of MIL-88B(Cr)_1,4-NDC subjected to different treatments, compared to the simulated patterns of MIL-88B(Fe) open and closed,[23] as well as PCN-241.[26] b) Extracted unit cell parameters.

In situ PXRD during drying in air from DMF reveals that the framework spontaneously closes without any external stimuli (Figure 4.14a) which to the best of our knowledge has never previously been studied for the MIL-88-type frameworks. While the ability of the dried and as-synthesised forms of the MIL-88 series to swell upon guest adsorption is already well-known, the tendency of these materials to close has not been reported before. It is

unsurprising that relatively volatile solvents such as DCM and MeOH would evaporate and leave the pores of the MOF, as this was how we obtained the closed form of MIL-88D(Fe) (Chapter 2), but it was surprising that this occurs from a relatively non-volatile solvent such as DMF – which ordinarily remains inside the pores of other MOFs even when heat and/or vacuum is applied. Inspections of the (100) and (101) reflections during the first 8 hours (Figure 4.14b) shows that both shift to higher 2θ values over time, consistent with a contraction of the unit cell in the *a* and *b* axes, respectively.

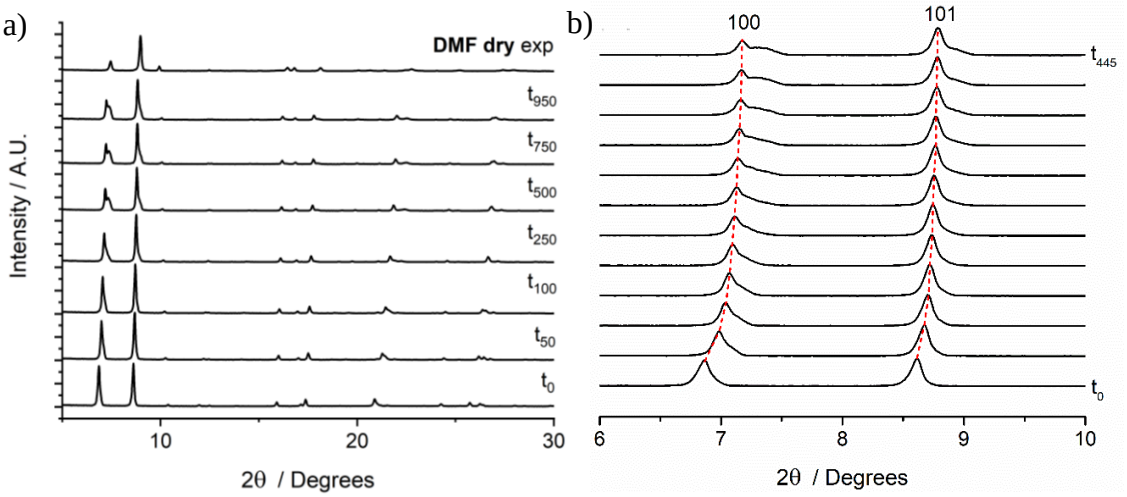

Figure 4.14. a) PXRD patterns recorded over time χ under an air atmosphere, with the DMF dry sample given for comparison, b) evolution of the PXRD pattern during the first 445 minutes, shown every 40 minutes, with shifts in the (100) and (101) reflections indicated.

4.5.2 MIL-88C(Cr)

The DMF-solvate of MIL-88C(Cr) (**open**) is comparable in terms of its unit cell volume to the reported open form of MIL-88C(Fe) (Figure 4.15a), which was solvated with pyridine,[23] which suggests that it is close to "fully open". Interestingly, the reported DMF-solvate of MIL-88C(Fe) has a much smaller unit cell than this (3415 vs. 5695 $Å^3$). The origin of this difference lies in the fact that the reported DMF-solvate of MIL-88C(Fe) was obtained from soaking a calcined (150 °C, overnight)[23] sample in DMF whereas here I have merely exchanged the pyridine for DMF and thus retained the original open form. This retention of unit cell volume may occur regardless of the nature of the solvent, but this could not be investigated with volatile solvents due to their rapid evaporation. Heating our **as-synthesised** MIL-88C(Cr) material at 120 °C causes the structure to close somewhat, but it still does not reach the reported closed form of MIL-88C(Fe). The most closed form is obtained after treatment in methanol. Since none of these treatments leads to a form as closed as has been reported for MIL-88C(Fe), it is unclear if our material can adopt the same closed form.

a)

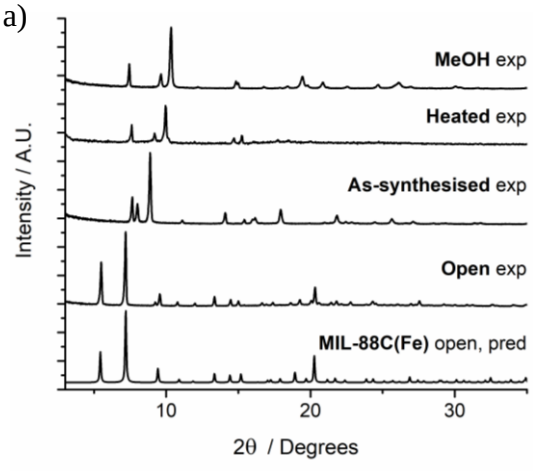

b)

Sample	*a* (Å)	c (Å)	*V* (Å³)
Open	18.699	19.028	5761.5
As-synthesised	12.557	22.792	3112.4
Heated	11.104	23.280	2485.7
MeOH	10.599	23.773	2312.8
MIL-88C open	18.753	18.743	5708.2
MIL-88C closed	9.900	23.800	2020.1
MIL-88C as-synthesised	10.175	23.772	2131.5

Figure 4.15. a) Stacked PXRD pattern of DMF-solvated MIL-88C(Cr) compared to MIL-88C(Fe) open,[23] b) extracted unit cell parameters.

Allowing the sample to gradually dry in air revealed that the framework spontaneously closes over time, similar to MIL-88B(Cr)_1,4-NDC (Figure 4.16a). Initially there is a uniform shift in the peaks of the powder pattern (Figure 4.16b), but eventually the peaks become very broad and it seems as if there are multiple unit cells superimposed over each other. This is likely due to non-uniform drying within the sample and perhaps even within individual crystallites, which displays as if the sample is becoming amorphous. After ~9 hours, the pattern becomes much more well-defined again and has clearly reached a more stable state of solvation. Compared to the previously obtained as-synthesised form, the unit cell is slightly smaller and the peaks themselves are broader. It can be assumed that this is due to the pyridine being displaced by DMF, which is expected to interact strongly with the framework.

a)

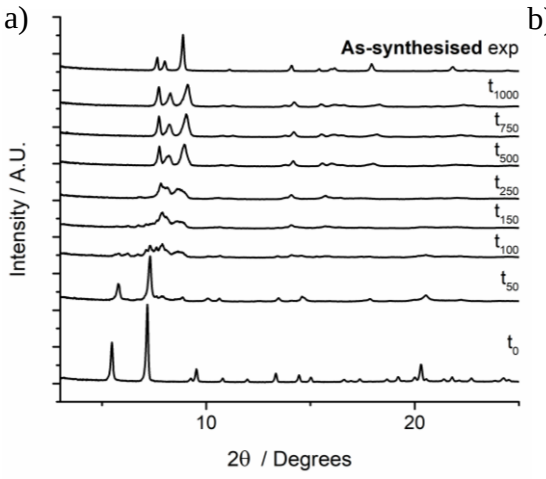

b)

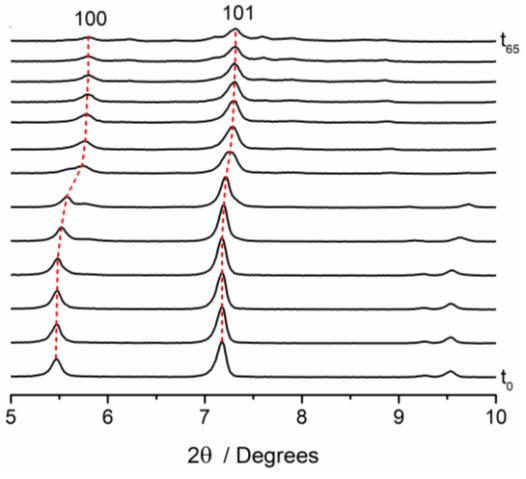

Figure 4.16. a) PXRD patterns recorded over time χ under an air atmosphere, with MIL-88C(Cr) as-synthesised for comparison, b) evolution of the PXRD pattern during the first 65 minutes, shown every 5 minutes, with shifts in the (100) and (101) reflections indicated.

4.5.3 MIL-88D(Cr)

The PXRD pattern I obtained for the DMF-solvated sample of MIL-88D(Cr) reveals that it is more open than the reported open form of MIL-88D(Cr) (Figure 4.17a), which was solvated with 2,6-lutidine.[23] When the as-synthesised form of MIL-88D(Cr) is treated with methanol and then left to dry at room temperature, it gives a smaller unit cell than the previously-reported closed form of MIL-88D(Fe).[22] Both of these results suggest that MIL-88D(Cr) has a greater swelling amplitude (defined as $(V_{open}-V_{closed})/V_{closed}$ in %) than has previously been reported: 282% from our study compared to the 237% which was reported by Ferey et al. in 2011.[22] This is quite significant, as I have only scratched the surface of possible conditions (soaking the DMF-solvate in other solvents, collecting PXRD patterns in sealed capillaries, heating the methanol-treated sample, etc.) which could reveal an even greater swelling amplitude.

a)

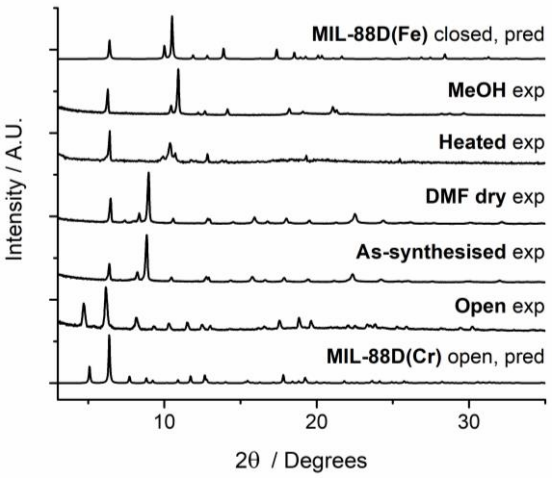

b)

Sample	*a* (Å)	c (Å)	*V* (Å^3)
Open	21.615	22.008	8904.4
As-synthesised	12.115	27.296	3469.7
Heated	10.181	28.077	2520.3
MeOH	9.783	28.155	2333.7
DMF dry	12.213	27.350	3532.8
MIL-88D open	20.041	22.911	7968.7
MIL-88D closed	10.100	27.800	2455.9
MIL-88D as-synthesised	2.165	27.197	3485.4

Figure 4.17. Stacked PXRD pattern of DMF-solvated MIL-88D(Cr) compared to MIL-88D(Cr) open[23] and MIL-88D(Fe) closed,[22] b) extracted unit cell parameters.

When air-dried from DMF, the PXRD pattern shifts very rapidly (Figure 4.18a-b), likely due to the huge pore volume of the DMF-solvate (>8000 Å^3). It is clear from the PXRD patterns that there are multiple solvated phases with different degrees of openness, similar to what was seen with MIL-88C(Cr), which suggests that again there is non-uniform drying. This effect is more pronounced than in MIL-88C(Cr), occurring within the first 10 minutes (Figure 4.18b), which suggests that it is due to the larger pore size compared to MIL-88C. In this case it is harder to assign a unit cell to the patterns during the first 100 minutes, and afterwards the peaks are still fairly broad, which again indicates a distribution of unit cells.

Despite this broadening, the average peak positions are very similar to those of the 'DMF dry' sample

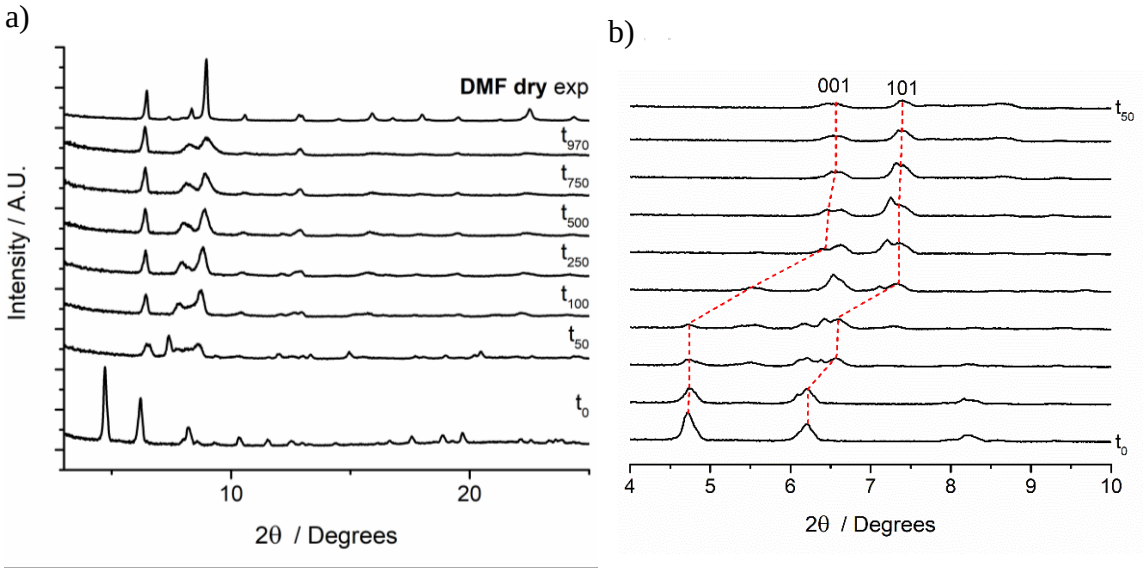

Figure 4.18. a) PXRD patterns recorded over time χ under an air atmosphere, with the as-synthesised pattern given for comparison, b) evolution of the PXRD pattern during the first 50 minutes, shown every 5 minutes, with shifts in the (100) and (101) reflections indicated.

4.5.4 Cr-SDC

The unit cell of the as-synthesised form of Cr-SDC is close to that obtained for the DMF-solvated Fe-SDC, which possesses the same MIL-88-int structure (determined by SCXRD), (Figure 4.19a-b). The DMF-solvated (Open) sample of Cr-SDC displays an even more open form of the structure (113% of the unit cell volume of the as-synthesised form). Subsequent treatments reduce the unit cell significantly, with the greatest contraction being seen for the methanol-treated sample (MeOH). This gives a swelling amplitude of 100% between the Open and MeOH forms of the material. This is quite impressive considering the two-fold interpenetrated topology of the material and highlights that the orientation of interpenetrated nets can have a huge influence on framework properties; MIL-88-int is highly flexible while MIL-126 is rigid.

There is a striking difference between the unit cell volume of the as-synthesised form of Cr-SDC compared to those of the MIL-88 frameworks. While the as-synthesised forms of MIL-88C and D are only ~1000 $Å^3$ larger than their closed form, the equivalent unit cell of Cr-SDC as-synthesised is more than 4000 $Å^3$ larger than the most closed form I have obtained. It has already been reported that pyridine strongly interacts with MIL-88 frameworks, by coordination to the metal clusters and/or interaction with the linkers via π-π stacking.[23] It is

likely that these interactions are amplified by the close proximity between the two nets of the interpenetrated structure, and thus hold the structure open to a much greater degree than in MIL-88.

a)

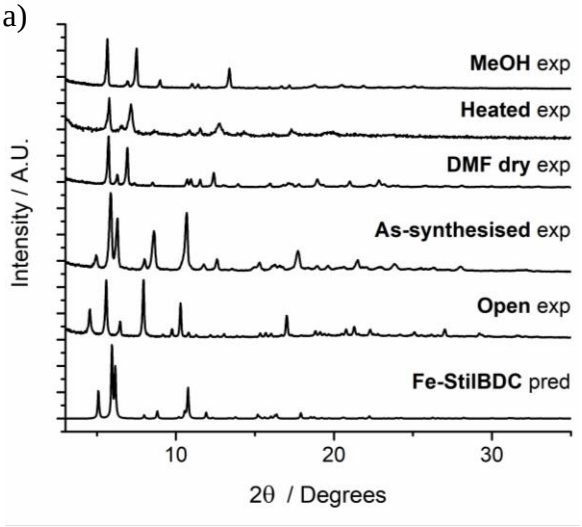

b)

Sample	*a* (Å)	c (Å)	*V* (Å^3)
Open	22.384	27.043	11735
As-synthesised	20.526	28.182	10343
Heated	15.610	30.736	6486.2
MeOH	14.708	31.269	5858.3
DMF dry	16.207	30.877	7023.9
Fe-SDC	20.039	28.698	9980.4

Figure 4.19. a) Stacked PXRDs of Cr-SDC subjected to different treatments, compared to the simulated pattern of MIL-88B(Fe) closed, b) extracted unit cell parameters.

As with MIL-88B(Cr)_1,4-NDC, allowing the sample to dry at room temperature in air leads to a gradual contraction of the unit cell (Figure 4.20a). This is expressed by a shifting of the (100) and (101) reflections towards higher angle and a shift of the (002) reflection towards lower angle (Figure 4.20a). These shifts indicate that the *a* and *b* parameters are becoming smaller while *c* increases. The fact that the reflections in the PXRD pattern can be seen to gradually shift, rather than one pattern disappearing and a new phase appearing, is proof that this transformation is continuous just like with MIL-88B(Cr)_1,4-NDC.

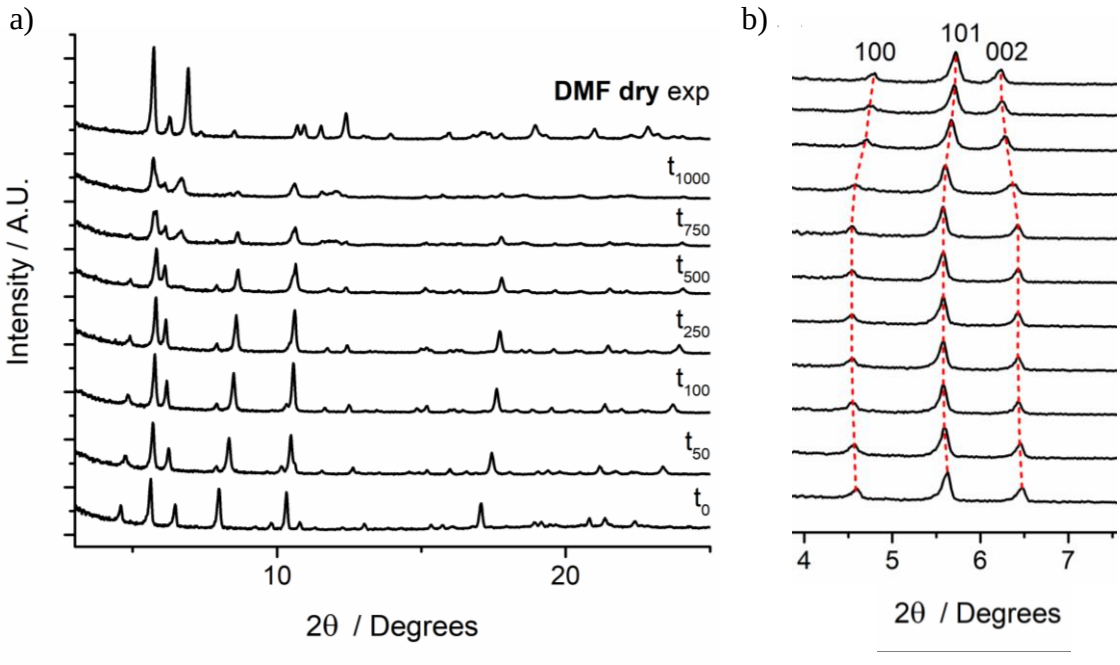

Figure 4.20. a) PXRD patterns recorded over time χ under an air atmosphere, with the DMF treated sample dried from DCM given for comparison, b) evolution of the PXRD pattern during the first 55 minutes, shown every 5 minutes, with shifts in the (100) and (101) reflections indicated.

4.5.5 Summary

A wide range of unit cells can be obtained depending on the exact treatments applied to each sample and, while this study is in no way exhaustive in this regard, it does serve as a useful reassessment of some of the archetypal MIL-88 frameworks, as well as exploring the flexibility of the MIL-88-int topology for the first time. The unit cell parameters *V* and *a* are plotted for each framework in Figure 4.21, the swelling amplitudes are also provided for comparison.

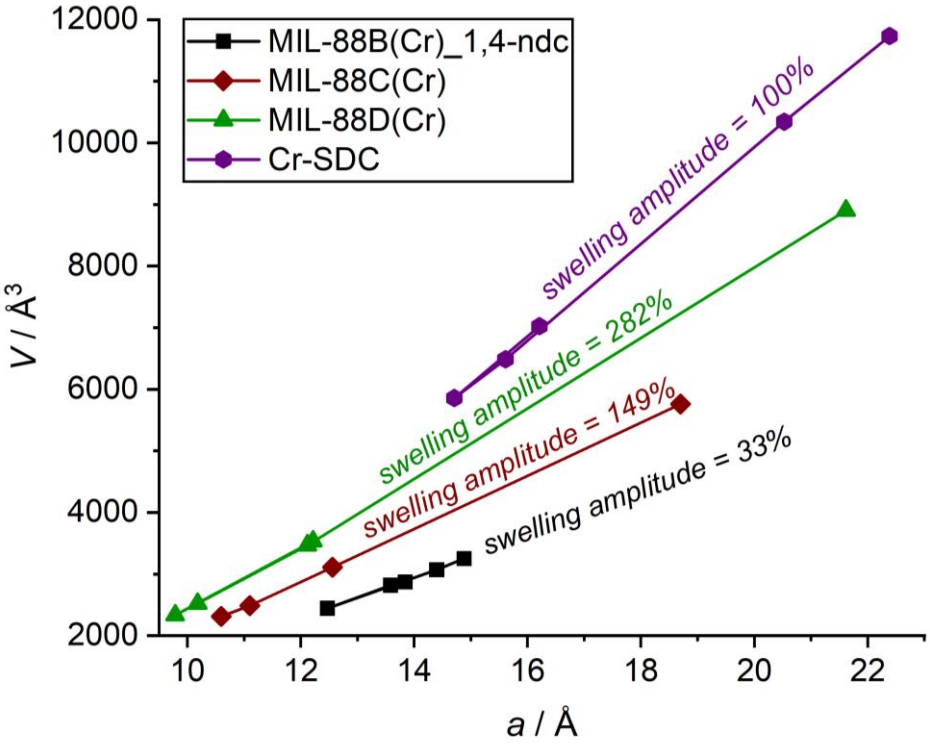

Figure 4.21. Unit cell volume *V* plotted against the *a* parameter for each of the frameworks, with individual points for each of their experimentally-obtained forms. The swelling amplitude is included and defined as $(V_{max}-V_{min})/V_{min}$ in %.

All of the MOFs with MIL-88 topology have similar unit cell volumes in their "closed" forms, but differ significantly in their swelling amplitudes, which increase in the order MIL-88B(Cr)_1,4-NDC < MIL-88C(Cr) < MIL-88D(Cr). When considering Cr-SDC, the open form has a larger unit cell than MIL-88D(Cr), as would be expected for the longer framework linker, but the most closed form is much larger than for the non-interpenetrated materials. The presence of the two interpenetrated nets within the unit cell decreases the solvent accessible volume significantly and thus limits the degree of closing which can occur. In theory, the most closed form of Cr-SDC should be at least double the size of the closed form of a non-interpenetrated framework. It is worth restating that, since the swelling amplitude is determined from the upper and lower unit cell volumes, they are subject to change depending on the available data, as I have already demonstrated a significantly larger swelling amplitude for MIL-88D(Cr) than has been previously reported. In addition, the *in situ* drying studies I have conducted help to demonstrate the continuous nature of framework contraction, which has not been explored previously in any depth. An understanding of both the swelling amplitude and subsequent contract could be useful for applications such as drug delivery, as they provide important parameters that can be used to predict the loading of drug molecules.

4.6 Synthesis of Cr(OH)-dicarboxylate Frameworks

While the Cr-MOFs synthesised and studied in the previous sections all contain the $Cr_3O(RCO_2)_6$ cluster, I focused attention to the MIL-53-type frameworks – which consist of Cr(OH) chains bridged by dicarboxylates. Despite MIL-53(Cr) being the first nanoporous Cr^{3+} framework, and also one of the most well-known for its impressive flexibility, there is still no HF-free synthesis. Our attempts to synthesise MIL-88B(Cr) or MIL-53(Cr) using the same water/pyridine solvent mixture that was used to obtain the other Cr-MOFs. However, no crystalline product could be obtained, and only amorphous gels and monoliths were produced. It is not clear why this was the case; however, it is worth restating that the 1,4-NDC analogue of MIL-88B was also surprisingly difficult to synthesise and required the use of preformed $Cr_3O(OAc)_6$ clusters for its self-assembly. The use of pyridine and acetic acid seems in every case to favour the formation or stabilisation of the $Cr_3O(RCO_2)_6$ cluster, likely forming before the MOF assembles, and thus a different approach was used to target MIL-53(Cr). In Chapter 3, we saw that MIL-53(Fe) could be synthesised successfully from the chloride salts, and HCl appeared to be the only suitable modulator, with carboxylate modulators inducing the formation of MIL-88B. Thus, $CrCl_3{\cdot}6H_2O$ was used as Cr-source and the solvent used was exclusively water. The heating conditions used were the same as those reported previously for the synthesis of MIL-53(Cr) of 220 $^{\circ}$C for 72 hours.[7] The synthesis was performed both unmodulated and with the addition of HCl as a modulator.

The unmodulated synthesis yielded highly crystalline material corresponding to MIL-53(Cr) (Figure 4.22a). Interestingly, the addition of 1 eq of HCl induces the formation of MIL-101(Cr), a kinetic product relative to MIL-53(Cr); when 2 eq or more are added, MIL-53(Cr) is the sole product. SEM revealed that both MIL-53(Cr) samples consist of block-like crystallites, many of which are intergrown (Figure 4.22b-c), and there is not a large difference in the crystallite size, but there are thinner blocks in the unmodulated sample. The peak seen at $2\theta = 9.2^{\circ}$ for the unmodulated sample is due to washing with DMF, which was reported to absorb into the pores and form a new phase.[6] As such, the samples modulated with HCl were heated with ethanol in an attempt to prevent any phase transformation, but unreacted terephthalic acid persists in most cases (Figure 4.22a) because of its poor solubility.

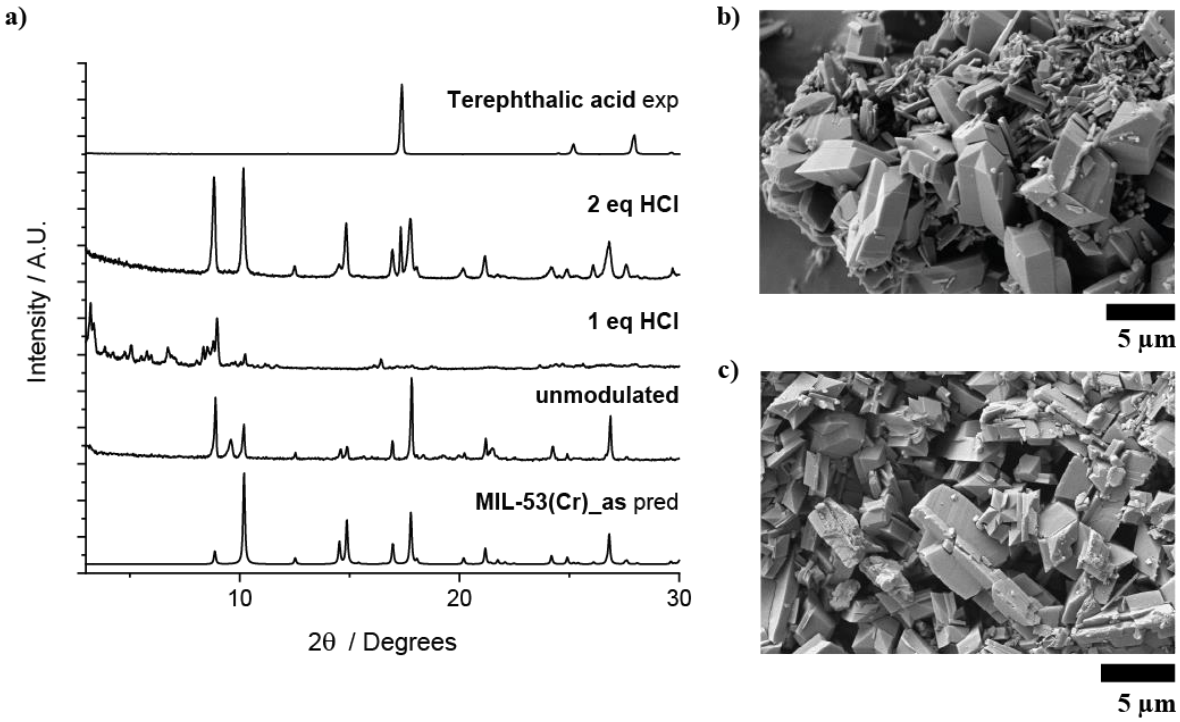

Figure 4.22. a) Stacked PXRD patterns of Cr-BDC synthesised with and without HCl as a modulator, compared to the predicted pattern of MIL-53(Cr)_as and the experimental pattern for terephthalic acid, b) SEM image of MIL-53(Cr) unmodulated, c) SEM image of MIL-53(Cr) modulated with 2 eq of HCl.

A further increase of the HCl concentration to 3 equivalents resulted in large crystals suitable for SCXRD, which were washed multiple times with DMF and then retained in solvent. A grey block-crystal with dimensions 0.06 × 0.04 × 0.04 mm (Figure 4.23a) was selected to collect a full dataset and was processed and refined as a two-component twin. The refined structure is very similar to the one previously reported for MIL-53(Cr) which was solved by Rietveld refinement.[6] The space group is *Pnma* and has unit cell parameters of a = 17.5739, b = 6.8259 Å, c = 11.8443 Å, and V = 1420.81 Å^3. The structure itself consists of chains of $Cr^{III}O_4(OH)_2$ octahedra (Figure 4.23b), linked together by terephthalates to form a 3D network with diamond-shaped channels running down the b axis (Figure 4.23c). These channels are occupied by highly disordered terephthalic acid, as has been previously reported, but they have been omitted from the structure here for clarity. Comparison of the predicted pattern with the experimental pattern (Figure 4.23d) helped to confirm that the structure was correct and that the sample is phase-pure; only small differences in peak intensity and position are evident between the two patterns.

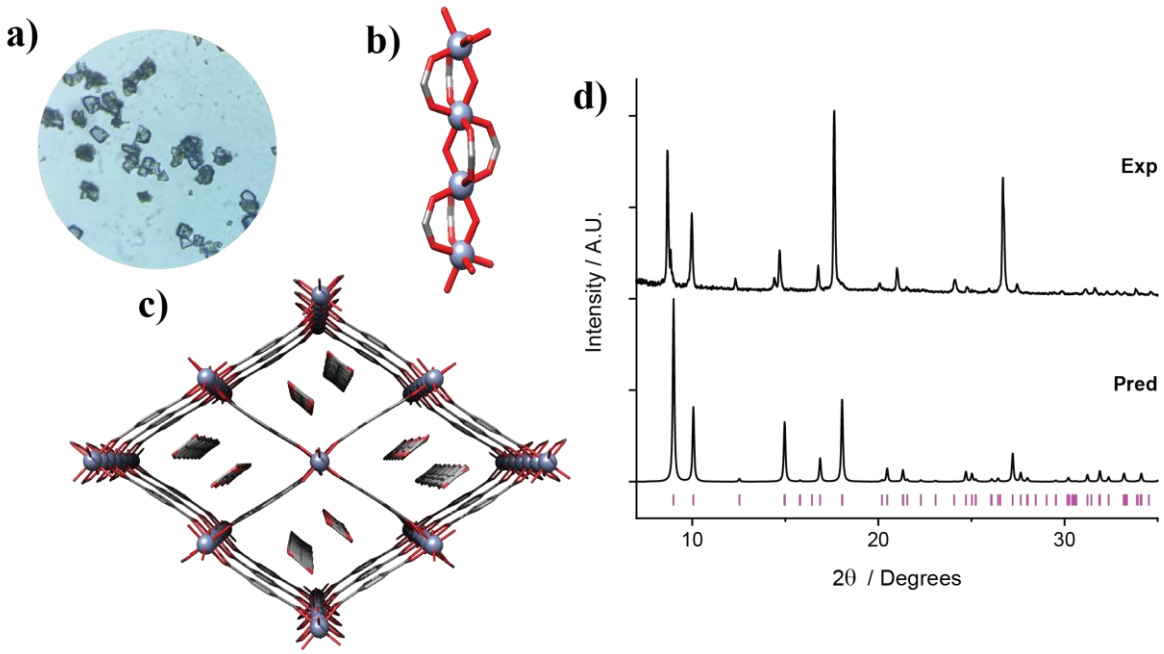

Figure 4.23. a) Image of crystals of MIL-53(Cr), b) chain SBU found in MIL-53(Cr), c) packing structure as viewed down the *b* axis, d) comparison of the experimental PXRD pattern of MIL-53(Cr) (**exp**) with the pattern predicted from the obtained crystal structure (**pred**).

Considering the dearth of single-crystal structures of Cr-MOFs, and the clear advantage in structural determination by SCXRD as opposed to PXRD, I attempted synthesis with functionalised terephthalate ligands. Similar work has been carried out previously in the literature for the Fe-analogues of MIL-53,[32] although the synthesis conditions are sometimes quite disparate. Synthesis at temperatures as high as 220 °C can be problematic because of the tendency for some of the functional groups to br cleaved or converted to other moieties, as was found for the functionalised MIL-101(Cr) series.[33] Nevertheless, it was possible to successfully synthesise the BDC-Br derivative (MIL-53(Cr)_Br) as large single-crystals, enabling its structure to be investigated. A suitable crystal with dimensions 0.07 × 0.04 × 0.03 mm was mounted and a full dataset was collected overnight. The framework crystallises in the orthorhombic *Imma* space group and has cell dimensions of a = 16.861 Å, b = 6.8523 Å, c = 13.003 Å, and V = 1502.3 Å^3. The structure is similar to MIL-53(Cr), particularly in terms of its underlying topology, but the linker is tilted and sits in one of two positions equally, and the bromo group is also disordered over 4 positions (Figure 4.24b). The structure itself consists of infinite chains of Cr(OH) (Figure 4.24d) linked together by the terephthalate to give diamondoid channels along the *b* axis (Figure 4.24e). The experimental powder pattern for this sample is a close match to that predicted from the crystal structure (Figure 4.24c), confirming that the bulk of the sample consists of this phase.

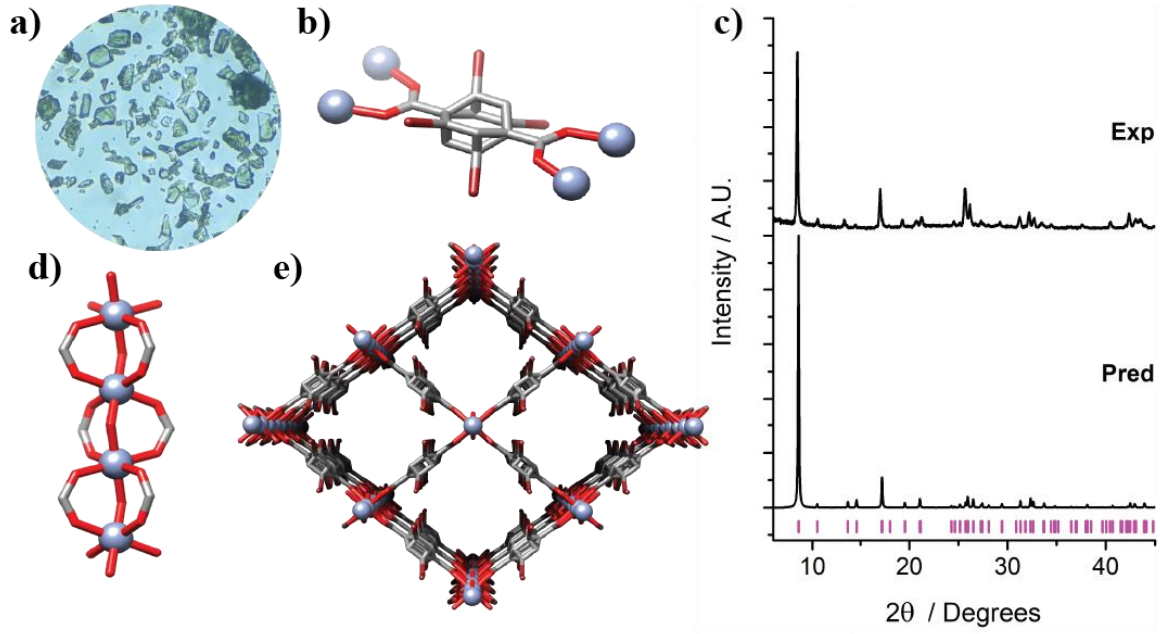

Figure 4.24. a) Image of crystals of MIL-53(Cr)_Br, b) Linker disorder in MIL-53(Cr)_Br, c) PXRD patterns of the experimental pattern of MIL-53(Cr)_Br compared to the pattern predicted from the obtained crystal structure, with an inset showing the higher angle region, d) Infinite chain SBU found in MIL-53(Cr)_Br, e) Packing structure of MIL-53(Cr)_Br as viewed down the *b*-axis.

To investigate the bulk properties of the material, the synthesis was successfully scaled up by a factor of 10. After washing with DMF and then water, the sample was activated at 150 °C overnight under vacuum prior to gas sorption analysis. N_2 adsorption isotherms revealed that the sample only adsorbs a small amount of nitrogen and has a very low surface area with SA_{BET} = 24 m^2g^{-1}. The simulated isotherm, calculated using a Grand Canonical Monte Carlo (GCMC) approach,[34] for an ideal sample has a much higher uptake (Figure 4.25a) and the predicted SA_{BET} = 989 m^2g^{-1}. Variable temperature powder X-Ray diffraction (VT-PXRD) shows that no significant change in unit cell occurs during heating (Figure 4.25b), even at temperatures which should remove bound solvent. In fact, amorphisation occurs before any transition, suggesting that the structure is not flexible. For the pores to simultaneously be open *and* inaccessible to N_2 suggests that the activation protocol was insufficient to remove all the bound solvent and/or residual bromoterephthalic acid from the pores. Elemental analysis before and after the activation protocol suggests that DMF is not fully removed (N found = 0.67%), suggesting 0.15 DMF molecules per unit formula. More crucially, there is a greater carbon content, even after accounting for this residual DMF: Expected C, 31.41; H, 1.56; N, 0.65. Found C, 32.99; H, 1.44; N, 0.67. The most likely explanation is that there is bound bromoterephthalic acid (0.1-0.3 per formula unit) which can effectively block the

pore channels similar to what has been reported for many of the other MIL-53 materials.[6,7,35,36] Assuming a formula of [Cr(OH)(BDC-Br)]·0.15DMF·0.3BDC-Br gives a closer match to the elemental analysis results: Expected C, 32.85; H, 1.65; N, 0.53. Found C, 32.99; H, 1.44; N, 0.67. Further study into the activation of this material is currently ongoing and will help to answer these questions. As the first functionalised Cr-analogue of MIL-53, developing a general activation protocol will be essential for unlocking the potential of these materials.

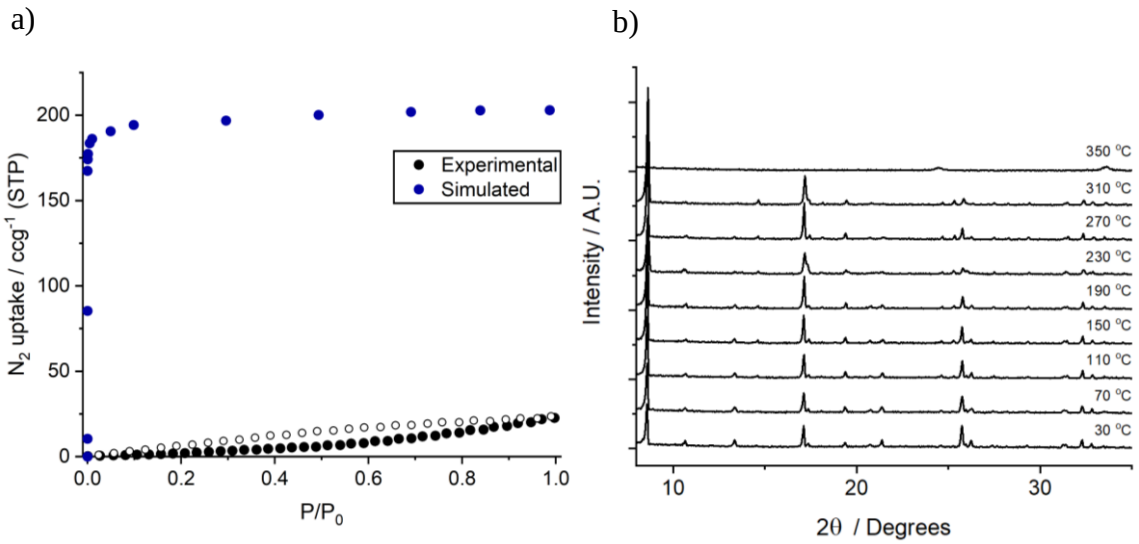

Figure 4.25. a) Simulated and experimental N_2 adsorption isotherms (77 K) of MIL-53(Cr)_Br, filled circles adsorption, empty circles desorption, b) VT-PXRD performed over the temperature range 30-350 °C. The heating rate was 2 °C/min and the furnace was held at the target temperature for 10 minutes prior to each measurement. Each measurement took 30 minutes and were collected at every 20 °C interval. λ = 1.5419 Å (Cu, Kα).

A MIL-53-type framework containing Cr^{3+} and 1,4-NDC has previously been reported,[37] and was identified to be isostructural to an aluminium framework Al(OH)(1,4-NDC)[38] based on its powder pattern. The synthetic procedure used is virtually identical to the one employed by us to synthesise MIL-53(Cr) and MIL-53(Cr)_Br, except with a 1:2 ratio of linker:salt. I followed this procedure, both unmodulated and with the addition of 3 equivalents of hydrochloric acid, in order to assess whether a similar increase in crystal size could be achieved as was the case for MIL-53(Cr), and the subsequent products were characterised by PXRD and SEM. PXRD confirmed the successful synthesis of the target product (Figure 4.26a) for the unmodulated synthesis, giving a PXRD pattern very similar to the one predicted for Al(OH)(1,4-NDC)[38], and will be referred to as Cr(OH)(1,4-NDC). Our attempts to modulate this synthesis with HCl show that the same phase can be obtained

(Figure 4.26a), and a large increase in crystal size and quality can be achieved when 3 equivalents of HCl are added to the synthesis (Figure 4.26c-b). Despite the relatively large crystallite size of our material, the crystallites are all intergrown, and our attempts to obtain large single crystals have thus far not been successful, with increases in the HCl concentration either giving similar results or clear solutions.

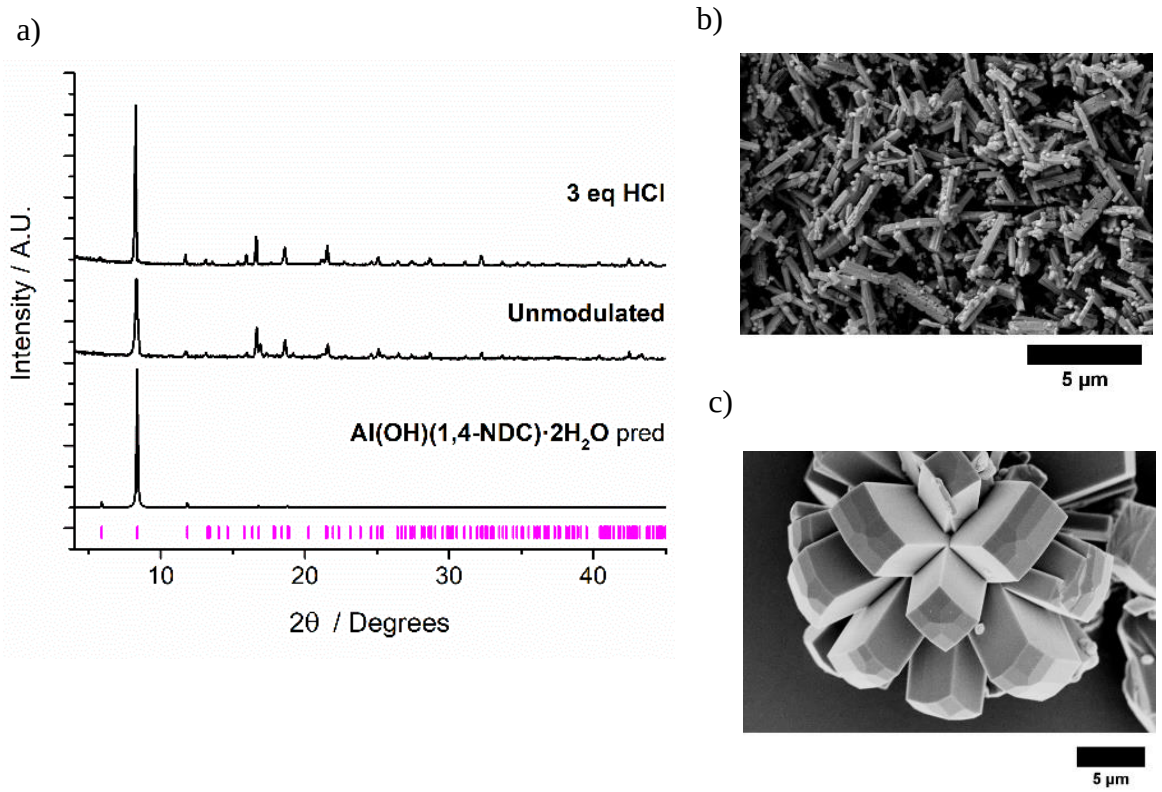

Figure 4.26. a) Stacked PXRD patterns of Cr(OH)(1,4-NDC) prepared with and without modulator, compared to the predicted pattern for Al(OH)(1,4-NDC), b) SEM image of Cr(OH)(1,4-NDC) unmodulated, c) SEM image of Cr(OH)(1,4-NDC) with 3 eq HCl.

Even though large single-crystals of Cr(OH)(1,4-NDC) were not obtained, the synthetic protocol with HCl as modulator appears to yield high-quality material, and thus I attempted to extend this to the other isomer of the linker: 2,6-NDC. Trivalent MOFs containing 2,6-NDC and chains of $M^{III}(OH)$ are relatively sparse, however there are two aluminium MOFs (DUT-4[39] and MIL-69[40]) which have thus far been reported. MIL-69 and DUT-4 are topologically identical, both possessing the Al(OH) chain SBU bridged by 2,6-NDC linkers, but MIL-69 adopts a narrow pore structure containing water while DUT-4 adopts a large pore form which is invariant to solvent removal.[39] When I applied the same synthetic method used to obtain Cr(OH)(1,4-NDC), modulated with 3 equivalents of HCl, a highly crystalline material was obtained (Figure 4.27a) which will be referred to as Cr(OH)(2,6-NDC). There is a close match between the PXRD patterns of our material and DUT-4, confirming that

Cr(OH)(2,6-NDC) adopts the large pore form. SEM (Figure 4.27b) revealed that our sample consists of block-like crystallites typical of frameworks with MIL-53 topology.

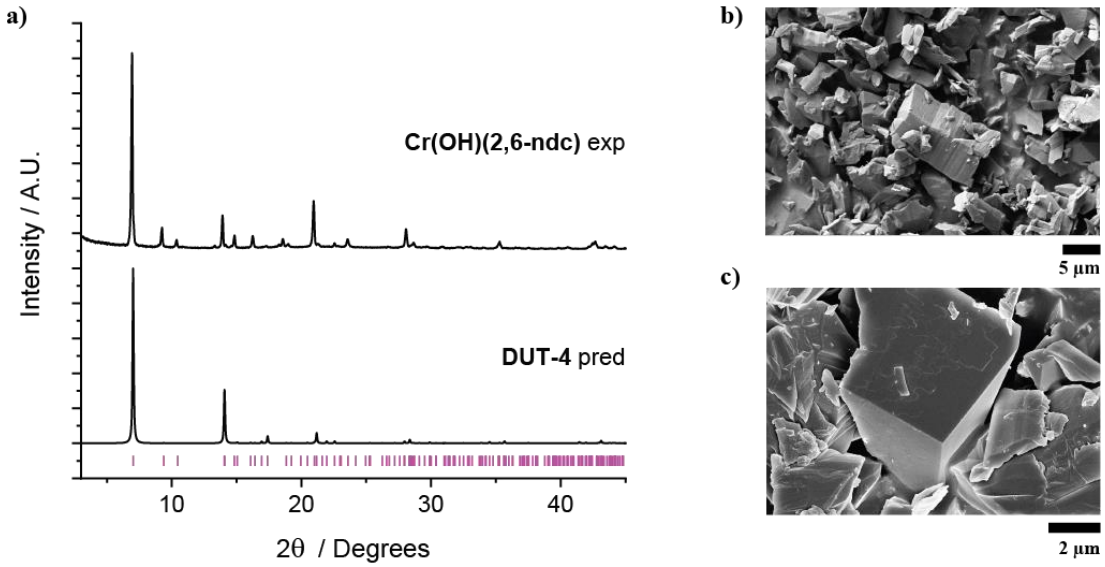

Figure 4.27. a) Stacked PXRD patterns of Cr(OH)(2,6-NDC) and DUT-4.[39] b-c) SEM images of Cr(OH)(2,6-NDC).

DUT-4 was used as a reference point when determining the unit cell of Cr(OH)(2,6-NDC) by Pawley refinement of the PXRD pattern. DUT-4 crystallises in the orthorhombic *Pnna* space group and an adequate fit was obtained for this cell with Cr(OH)(2,6-NDC) (Figure 4.28), giving parameters of a = 6.7816(10) Å, b = 17.1996(19) Å, c = 19.4369(26) Å and V = 2267.14(38) Å^3.

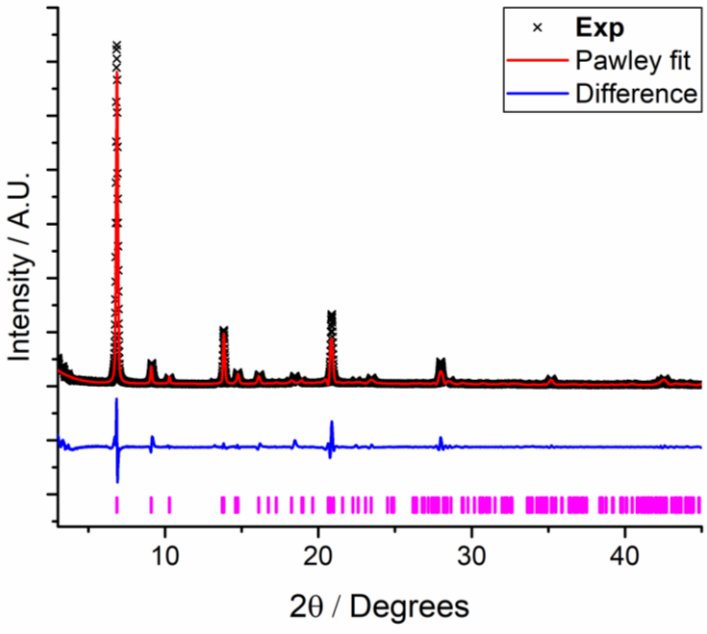

Figure 4.28. a) Pawley fit for Cr(OH)(2,6-NDC) .

The solvent content of the DMF-washed sample was determined by TGA (Figure 4.29a) and elemental analysis and is consistent with a formula of Cr(OH)(2,6-NDC)·2DMF. To characterise the desolvated phase of the material, DMF was removed by heating at 220 ˚C in air and then analysed by PXRD (Figure 4.29b). The obtained pattern is very different to the solvated form and appears to adopt a narrow pore structure similar to MIL-69 which has formula Al(OH)(2,6-NDC)·H_2O.[40] Elemental analysis is consistent with partial removal of DMF and adsorption of water to give Cr(OH)(2,6-NDC)·H_2O: Expected C, 47.84; H, 2.99; N, 0.00. Found C, 48.67; H, 2.76; N, 0.18. Such adsorption of water after thermal solvent removal is common for MIL-53-type frameworks as water can form hydrogen bonds to the hydroxides.[6,7]

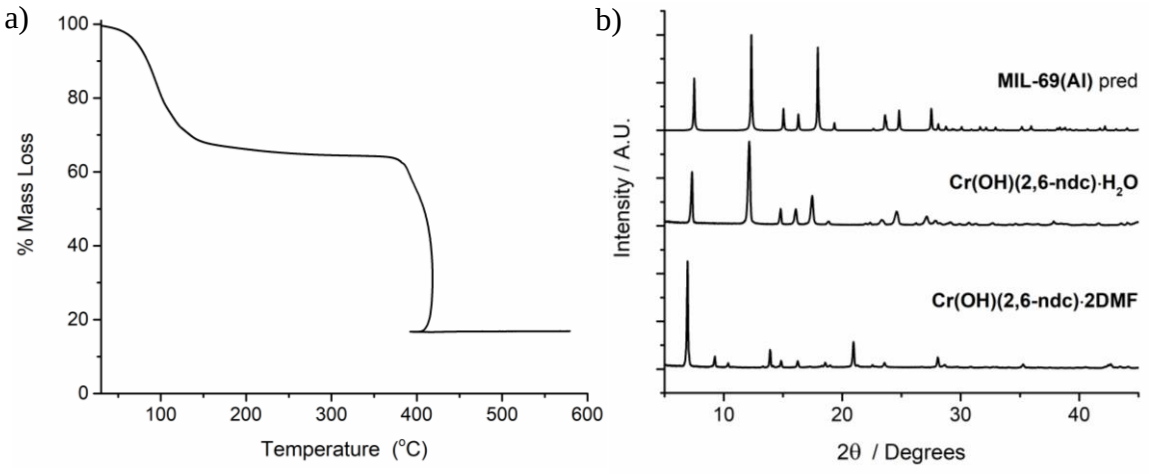

Figure 4.29. a) TGA curve of Cr(OH)(2,6-NDC)·2DMF, b) stacked PXRD patterns of Cr(OH)(2,6-NDC)·2DMF and Cr(OH)(2,6-NDC)·H_2O compared to MIL-69(Al).[40]

Nitrogen adsorption/desorption isotherms show that the material adsorbs very little N_2 after activating under vacuum (150 ˚C, overnight) (Figure 4.30a) and the surface area calculated by the BET method is very low SA_{BET} = 22 m^2g^{-1}. During activation the material lost ~37% of its weight and PXRD of the material post-activation, collected in air, matches the hydrated phase (Figure 4.30b), which confirms that the activation conditions remove DMF effectively. It is possible that the material adsorbs water from the air while reweighing the sample cell prior to starting the measurement, which would cause the material to adopt the narrow pore hydrated form. Retreatment of the activated sample in DMF at 120 ˚C overnight effectively reopens the pores, as confirmed by the PXRD pattern collected in air (Figure 4.29d).

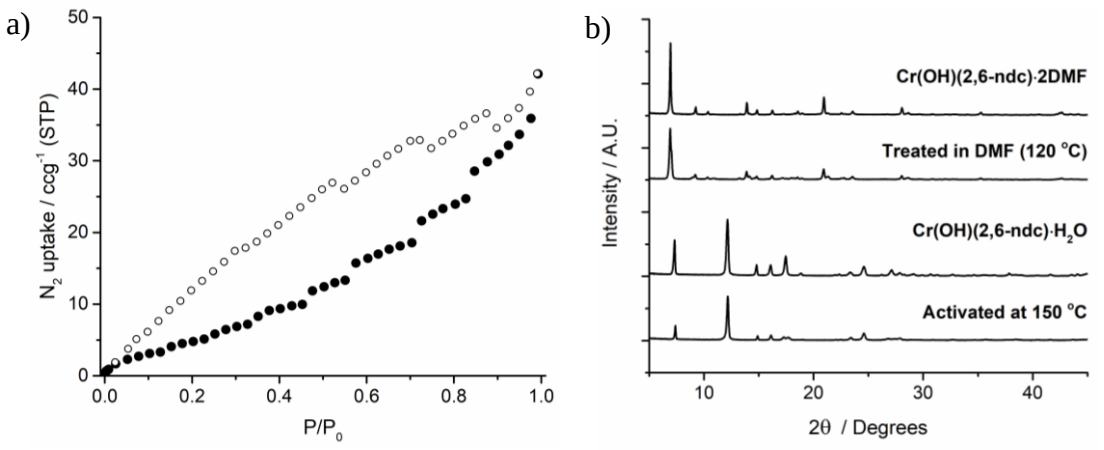

Figure 4.30. a) N_2 adsorption isotherms (77 K) of Cr(OH)(2,6-NDC)·2DMF after activation, b) stacked PXRD patterns after activation and treatment in DMF.

To investigate the flexibility in more depth, variable temperature PXRD measurements on Cr(OH)(2,6-NDC)·2DMF were collected in the range 30-250 °C (Figure 4.31). The framework appears to undergo multiple transformations at low temperature 30-150 °C, after which it adopts a narrow pore form when fully dehydrated, displaying peak positions very similar to those of the hydrated phase Cr(OH)(2,6-NDC)·H_2O. When the sample is cooled back to room temperature, the unit cell expands, as indicated by the peak positions shifting to lower angle, which is consistent with the adsorption of water to form Cr(OH)(2,6-NDC)·H_2O. The initial transformations suggest intermediate phases which are thus far unidentified and will require more investigation to discern.

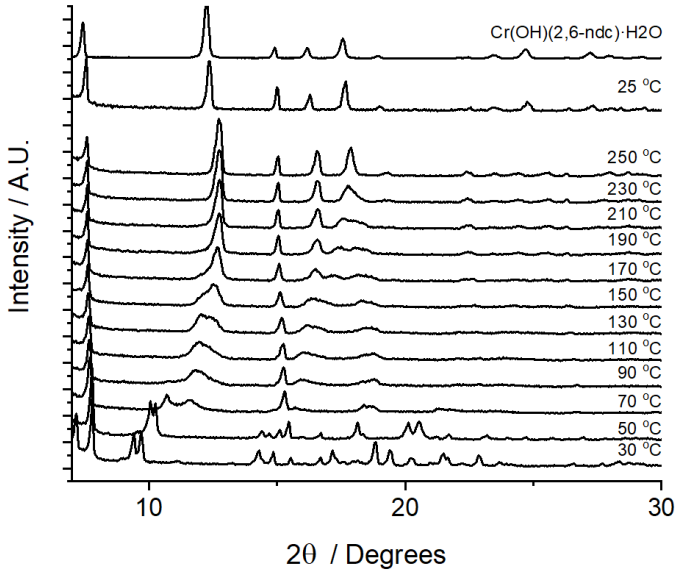

Figure 4.31. VT-PXRD performed over the temperature range 30-250 °C. The heating rate was 2 °C/min and the furnace was held at the target temperature for 10 minutes prior to each measurement. Each measurement took 26 minutes and were collected at every 20 °C interval. λ = 1.5419 Å (Cu, Kα).

From these results the transformations which occur during heating/cooling can be suggested (Figure 4.32): Cr(OH)(2,6-NDC)·DMF starts in a wide pore form; it then adopts several intermediate forms which are presumably due to partial desolvation; it adopts a narrow pore form when heated above 150 °C to form the fully dehydrated phase Cr(OH)(2,6-NDC); finally the framework adsorbs water when cooled back to room temperature, forming Cr(OH)(2,6-NDC)·H_2O. This is consistent with the low uptake of N_2 after activation, as the pores are closed and thus inaccessible to nitrogen. This behaviour is similar to MIL-53(Fe)[9] and is surprising considering that MIL-53(Cr) adopts a wide pore form upon dehydration[6] and the Al(OH)(2,6-NDC) frameworks (DUT-4 and MIL-69) are completely rigid,[39,40] suggesting a further layer of complexity to the landscape of flexible MIL-53-type framework than has been seen before.

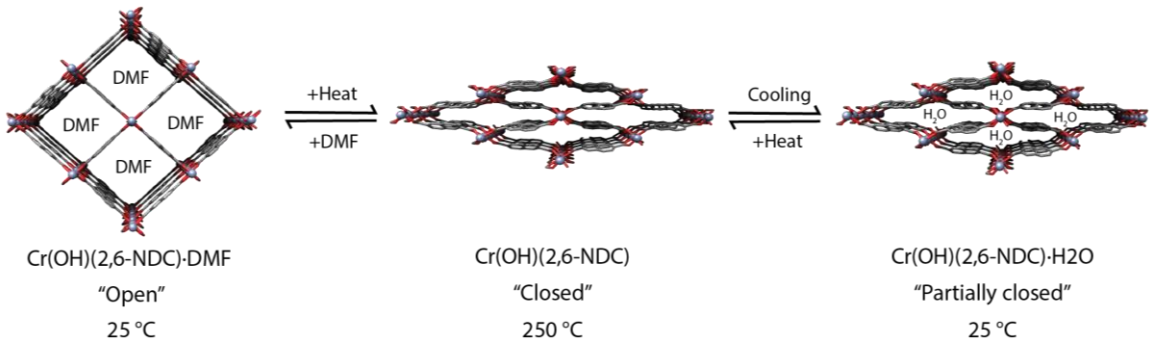

Figure 4.32. Schematic representation of the phase transformations of Cr(OH)(2,6-NDC).

4.6.1 Summary

In this section I have demonstrated that HCl is an effective modulator for growing single crystals of MIL-53-type MOFs containing Cr^{3+}. This has enabled us to obtain a single crystal structure of MIL-53(Cr) for the first time, having previously only being solved from PXRD data, as well as a new framework MIL-53(Cr)_Br, which has to the best of our knowledge never been synthesised. Other isoreticular frameworks such as Cr(OH)(1,4-NDC) and Cr(OH)(2,6-NDC) can be obtained as highly crystalline powders, the latter of which is a novel framework. The wider impact of this work is that it paves the way to study the flexibility of these frameworks using *in situ* SCXRD experiments, which would otherwise be impossible. This work is still ongoing as it will require more time and effort to grow crystals of the other isoreticular frameworks, however this is a priority for future work. The gas sorption properties of these materials also deserves attention, but the activation conditions need to be optimised beforehand to ensure removal of the bound terephthalic acid guests from MIL-53(Cr) and MIL-53(Cr)_Br. Additionally, the flexibility of these frameworks can now be investigated by both PXRD and SCXRD methods.

4.7 Synthesis with Higher Connectivity Linkers

4.7.1 Synthesis of Cr-soc-MOF

Having successfully established a synthetic route towards the synthesis of Cr-MOFs containing ditopic linkers, an obvious next step was to explore synthesis with linkers that have higher connectivity. The 3,3′,5,5′-azobenzenetetracarboxylate (ABTC) linker was selected, as the corresponding tetraacid can be synthesised relatively easily from commercially available 5-nitroisophthalic acid.[41] ABTC is known to form rigid and highly porous networks when combined with M^{3+} metals; these are known colloquially as soc-MOFs due to their square-octahedron (**soc**) topology (Figure 4.33).[42] Because our synthesis route with water, pyridine, and acetic acid appears to selectively yield Cr-MOFs containing the $Cr_3O(RCO_2)_6$ SBU, I expected that similar conditions would yield the abovementioned soc-MOF when using the ABTC linker.

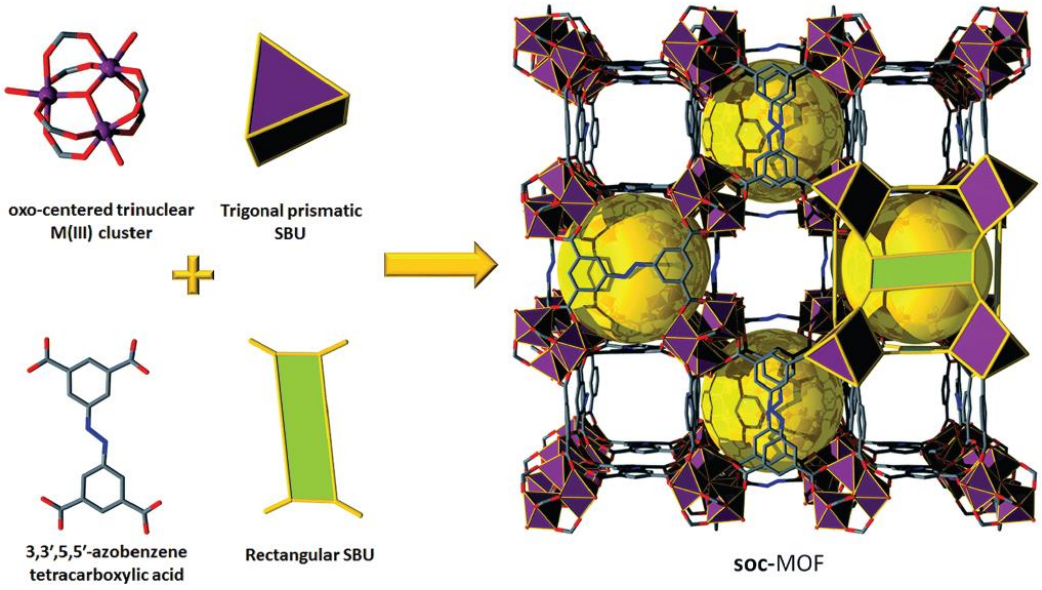

Figure 4.33. Topological representation of soc-MOF.[42]

Synthesis with this linker and chromium(III) nitrate using the water/pyridine/acetic acid approach developed in Section 4.3 yielded a highly crystalline solid when 40 or more equivalents of acetic acid were added to the synthesis (Figure 4.34a). Compared to synthesis with the ditopic linkers, the amount of acetic acid required is much higher (~4 times) which can be explained by the higher connectivity of the linker (4 carboxylates per linker). SEM revealed that these samples contain well-faceted crystallites between 200-500 nm in size (Figure 4.34b-c). The optimal conditions seem to be synthesis with 60 eq of acetic acid, with both the PXRD reflections being stronger in intensity for a similar quantity of analysed material and the SEM showing that the crystallites have sharper edges and are more uniform.

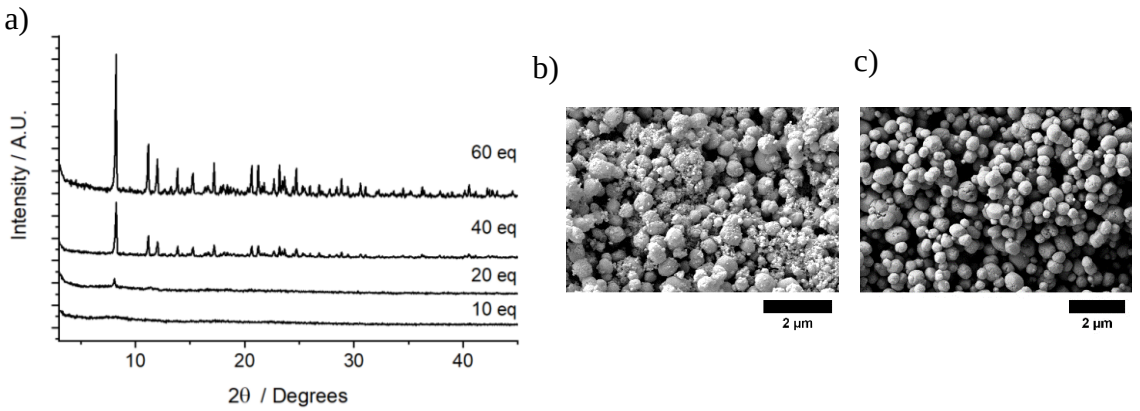

Figure 4.34. a) Stacked PXRD patterns of Cr-ABTC prepared with different molar quantities of AA, b) SEM image of Cr-ABTC prepared with 40 eq of AA, c) SEM image of Cr-ABTC prepared with 60 eq of AA.

In order to identify the obtained phase, the PXRD pattern of the activated material was compared to all of the reported frameworks containing the ABTC linker and trivalent metals. These frameworks are already well-known and have multiple names: soc-MOF,[43] MIL-127,[44] and PCN-250[26], but all possess the same underlying **soc** topology. Interestingly, the obtained pattern matched that of PCN-250″, a polymorph of the Fe-containing PCN-250, which was reported to form when the parent framework was placed under high pressure.[45] The transformation of PCN-250 to PCN-250″ is an interesting case of pressure-induced single-crystal to single-crystal transformation, where N=N bond flipping and distortion of the Fe-O bonds leads to a contraction of the unit cell and a change of symmetry from a cubic to a rhombohedral lattice while conserving the topology of the framework. The close match between the PXRD patterns can be seen in Figure 4.35, and confirms its identity.

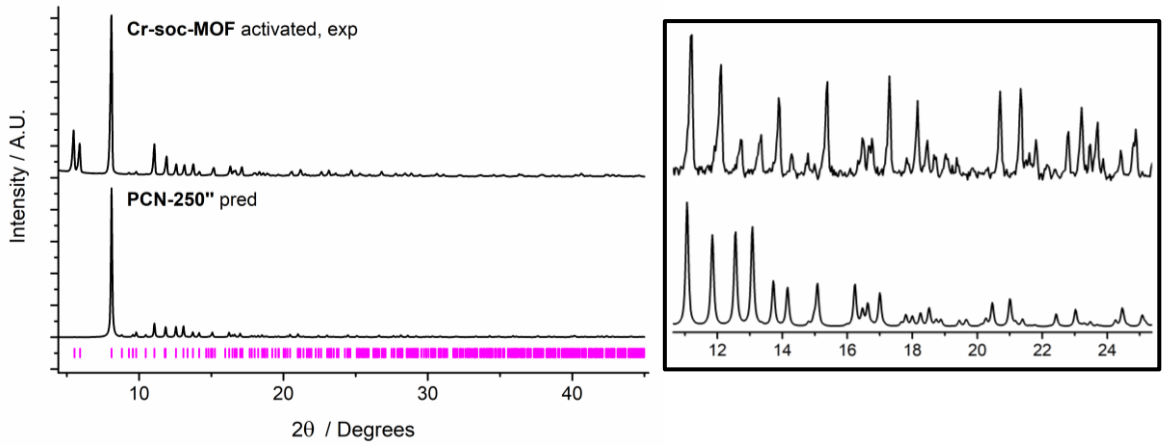

Figure 4.35. Stacked PXRD patterns of Cr-soc-MOF experimental compared with the predicted pattern for PCN-250″, with an expanded region at higher angle.

It is particularly surprising that this high-pressure form crystallises under the synthetic conditions used, as PCN-250″ is formed under an extrusion pressure of 150 MPa (Figure 4.36a) and the pressure that can build up inside the reaction vessel is significantly lower than that (the saturation pressure of water is ~2.55 MPa at 225 °C). PCN-250″ was reported to be kinetically stable and does not revert to PCN-250 once the pressure is relieved from the sample. The situation in the presence of solvent is quite different, however, with a full reversal back to PCN-250 when heating PCN-250″ in DMF at 150 °C for 12 hr.[45] Logically, I attempted to form PCN-250(Cr) by heating the sample in DMF at 150 °C overnight, but as can be seen from the PXRD patterns (Figure 4.36b), this did not induce transformation.

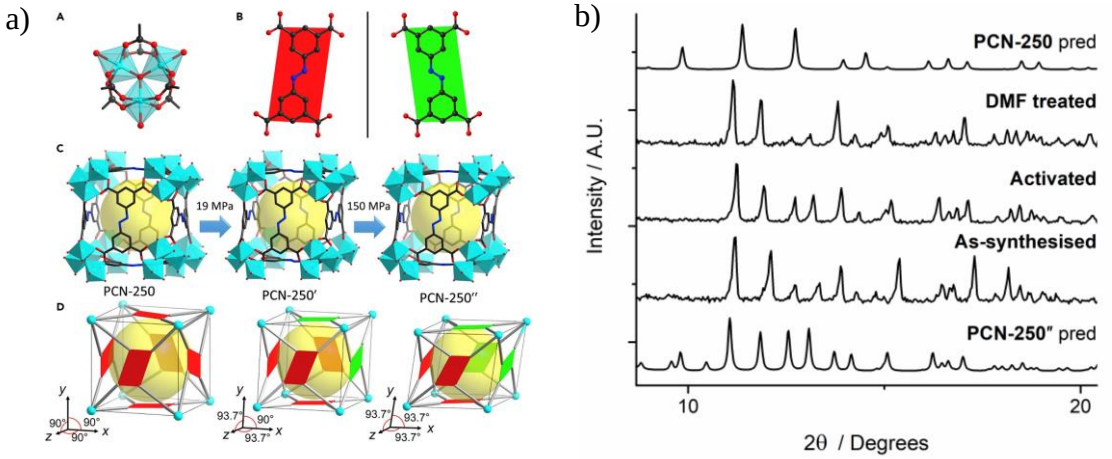

Figure 4.36. a) Schematic representation of the structural transformation including the inclination of unit cell and flipping of linkers.[45] b) Stacked PXRD patterns of Cr-soc-MOF treated under various conditions, compared to the predicted patterns for PCN-250″ and PCN-250.

Attempts to grow larger crystals by using more acetic acid generally failed, either not producing a crystalline product or causing no significant increase in size. In an attempt to find conditions which may yield larger crystallites, a longer synthesis time of 72 hours was explored, along with using other chromium precursors. When the quantity of acetic acid is kept constant, highly crystalline material can be obtained with all of the chromium sources used. Increasing, the synthesis time appears to make no significant difference to the crystal size or shape. The $Cr_3O(OAc)_6$ cluster, which worked well with many of the other linkers and yielded large crystals of MIL-88B(Cr)_1,4-NDC, appears almost identical to the products formed using the nitrate salt. However, it is notable that the same crystalline phase can be formed efficiently from a range of different precursors, which is not the case for all the Cr-MOFs reported here.

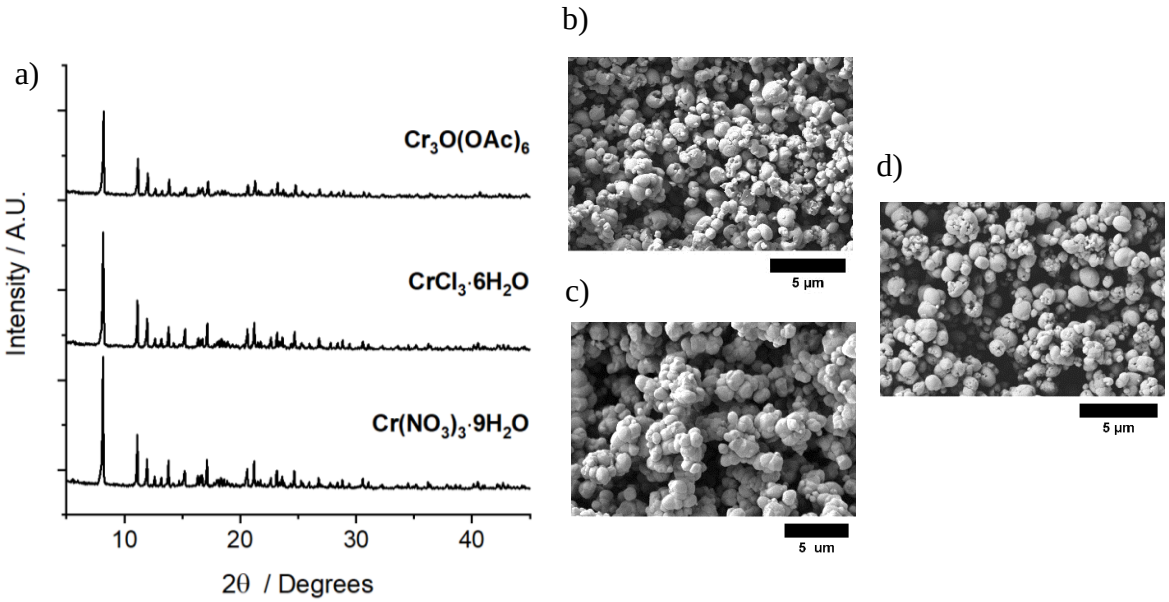

Figure 4.37. a) Stacked PXRD patterns of Cr-soc-MOF prepared using different chromium (III) sources, and SEM images of Cr-soc-MOF prepared using b) $Cr(NO_3)_3 \cdot 9H_2O$, c) $CrCl_3 \cdot 6H_2O$, d) $Cr_3O(OAc)_6$.

The porosity of Cr-soc-MOF prepared using each of these three chromium sources ($Cr(NO_3)_3 \cdot 9H_2O$, $CrCl_3 \cdot 6H_2O$, and $Cr_3O(OAc)_6$) was investigated using N_2 adsorption isotherms (77 K). The samples display Type 1 isotherms with pseudo plateaus, and exhibit similar uptake (271-288 cm^3g^{-1}), with a slight hysteresis evident in the sample prepared from $CrCl_3 \cdot 6H_2O$ (Figure 4.38a-b). The BET surface areas (Figure 4.38b) are all are lower than expected: the Fe-analogue is reported to possess values between 1310 and 1700 m^2g^{-1}.[41,42] Even considering the smaller hexagonal cell, only a slightly smaller uptake would be expected for a pristine sample.[45] Elemental analysis on one of the samples shows that it has a higher organic content than would be expected for a pristine sample with formula $Cr_3O(OH)(H_2O)_2(ABTC)_{1.5}$: Expected C, 38.10; H, 1.85; N, 5.88. Found C, 41.71; H, 2.42; N, 6.41. This could be due to residual DMF, pyridine, or unreacted linker not removed by the activation protocol, which accounts for the much lower than expected porosity.

a)

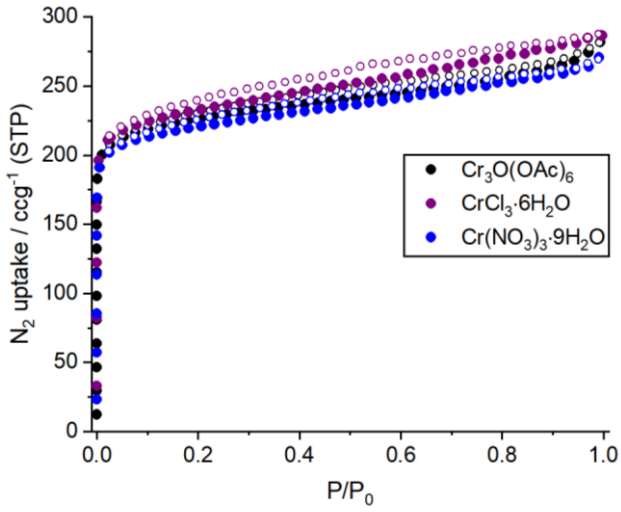

b)

Cr-source	S_{BET} (m^2g^{-1})	Total N_2 uptake (cm^3g^{-1})
$CrCl_3·6H_2O$	909	288
$Cr(NO_3)_3·9H_2O$	861	271
$Cr_3O(OAc)_6$	884	282

Figure 4.38. a) N_2 adsorption isotherms (77 K, filled symbol adsorption, empty desorption) of samples of Cr-soc-MOF prepared from different Cr-sources, b) gas sorption properties for each sample.

4.7.2 Summary

In this section I have demonstrated that our synthetic method works not only for dicarboxylates-containing frameworks, but also for an archetypical M^{3+}-tetracarboxylate framework with **soc** topology. The abovementioned MOF, Cr-soc-MOF, adopts a rare contracted structure with lower symmetry than the cubic ones adopted by other **M**-soc-MOFs, and has only previously been observed when the Fe-analogue was placed under pressure. Cr-soc-MOF retains its trigonal lattice upon treatment in hot DMF, which suggests much greater lattice stability than the Fe-analogue. Cr-soc-MOF can be synthesised with high crystallinity from a number of Cr-precursors, and these samples all exhibit permanent porosity. The porosity is lower than expected, but TGA and EA results suggest that this is due to insufficient activation, which can be further developed to enhance their porosity.

4.7.3 Mixed and Single Linker Frameworks Containing BTB

In order to target more rigid frameworks whose pores can remain accessible to nitrogen upon activation, I attempted to synthesise mixed linker MOFs containing 1,3,5-benzenetribenzoate (BTB) and various ditopic linkers (shown in Figure 4.39a-b). There are two relevant MOF topologies which have been reported with these ligand combinations and Fe^{3+}, namely MIL-142 and MIL-143. MIL-142 has a two-fold interpenetrated structure with hexagonal symmetry, and consists of superoctahedra formed from six $Fe_3O(RCO_2)_6$ SBUs, connected by three BDC and four BTB linkers (Figure 4.39c). The series of MIL-142 frameworks includes MIL142A with BDC, MIL142B with 2,6-NDC, MIL-142C with BPDC and MIL-142D with 1,4-phenylenediacrylate (PDAC).[46] MIL-142A has a kinetic isomer known as MIL-143 which was observed as a transient intermediate during the synthesis of MIL-142A,[46] and consists of two types of supertetrahedra which are identical to those found in MIL-101 and MIL-100_BTB, respectively. These supertetrahedra connect to form a non-interpenetrated cubic structure with two types of mesopores and possesses high porosity (theoretical SA_{BET} = 3430 m^2g^{-1}).[46] To target these frameworks, the H_2O/py/AcOH synthesis route was employed, which has proven to be very reliable at yielding $Cr_3O(RCO_2)_6$ SBUs, which are necessary to form the aforementioned topologies.

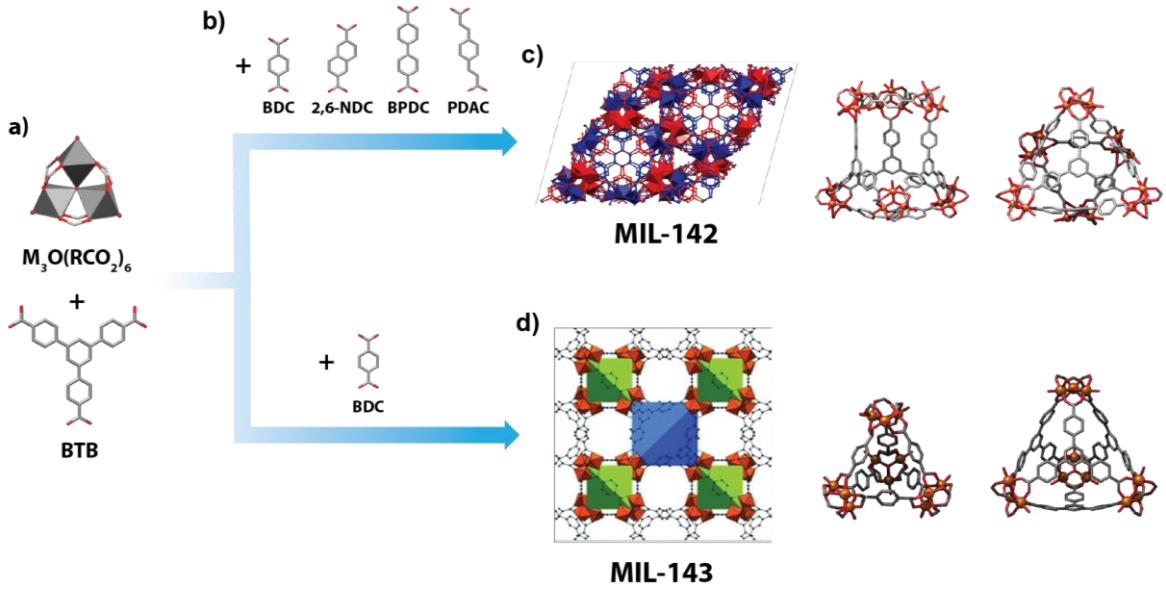

Figure 4.39. Schematic representation of the synthesis of mixed-linker MOF formed from a) Trigonal $M_3O(RCO_2)_6$ SBU and 1,3,5-benzenetribenzoate (BTB) combined with b) dicarboxylate linkers: BDC, 2,6-NDC, BPDC, or 1,4-phenylenediacrylic acid (PDAC) to form c) MIL-142,[46] and d) MIL-143.[46]

Synthesis was conducted using a 1:1:2 ratio of BTB:L_2:Cr^{3+}, where L_2 is the ditopic linker and the Cr^{3+} source is $Cr_3O(OAc)_6$, in a H_2O/py/AcOH mixture as per the previous Cr-MOF syntheses. Synthesis with each of the ditopic linkers and BTB was attempted and the samples are named as follows: BTB + BDC (**1**), BTB + 2,6-NDC (**2**), BTB + BPDC (**3**), and BTB + PDAC (**4**). PXRD of these four samples (**1**, **2**, **3**, and **4**) reveal that, apart from **3**, all of them are highly crystalline and display XRD peaks below 2θ = 5 ° (Figure 4.40a), which is an indication that they possess relatively large unit cells. **1** and **2** have similar PXRD patterns, with the peaks in **2** at relatively lower angle, suggesting these frameworks are isoreticular. Neither of these samples corresponds to the respective MIL-142 framework, nor MOF-907 - another mixed-linker Fe-MOF containing BTB and 2,6-NDC[47] - in the case of **2** (Figure 4.40b). The product of **4** is significantly different to both of these materials and also does not correspond to MIL-142D. SEM revealed that **1**, **2**, and **4** consist of large aggregates of intergrown octahedral crystallites (Figure 4.40c-e), consistent with face-centred cubic structures, further excluding MIL-142A and B which have trigonal space groups.

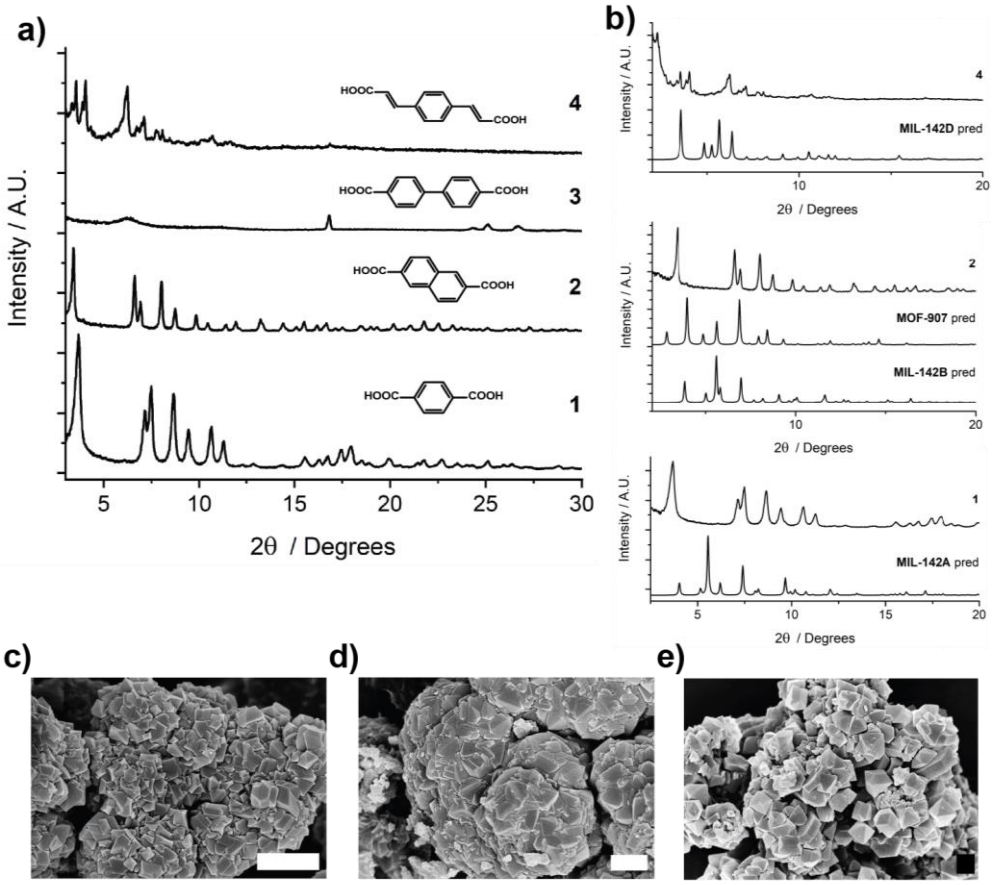

Figure 4.40. a) Stacked PXRD patterns of mixed-linker MOF samples **1-4** (the L_2 used is provided above each pattern), b) stacked PXRD patterns of each sample compared to predicted patterns of potential phases,[46,47] SEM images of c) **1**, d) **2**, e) **4**. Scale bars = 1 μm.

Visual inspection of the PXRD pattern of **1** suggests that it is isostructural to MIL-143, the kinetic product obtained during the synthesis of the Fe-MOF MIL-142A (Figure 4.41). The similarity in PXRD patterns between **1** and **2** suggests that **2** is an extended variant of MIL-143 and such a framework is thus far unreported – most likely due to the faster kinetics of reaction of Fe^{3+} relative to Cr^{3+}.

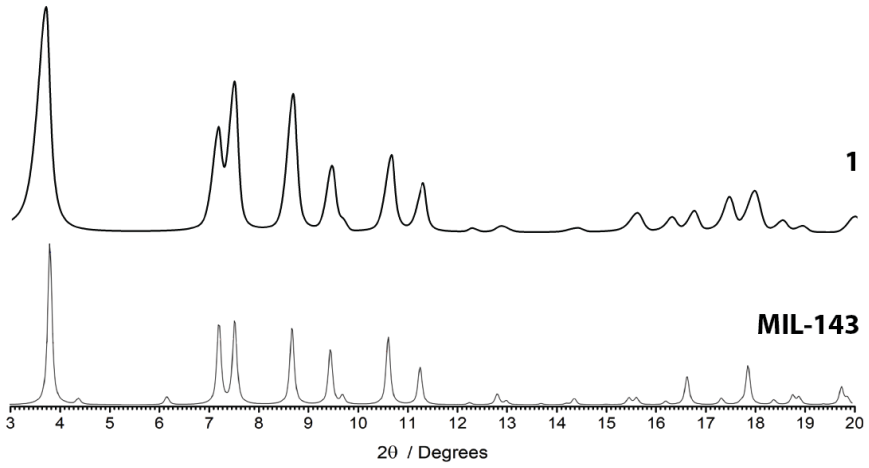

Figure 4.41. Stacked PXRD patterns of the mixed linker Fe-MOF MIL-143[46] and **1**.

To determine lattice parameters for **1** and **2**, data was collected for two hours and then refined using the Pawley method. The reported unit cell of MIL-143 was used for the starting parameters and the obtained fits can be seen in Figure 4.42a-b. This refinement strategy worked well for **1** (R_{wp} = 6.76%) while for **2** the unit cell had to be increased first in order to perform a successful refinement (from 40.6 to 43.86 Å for the *a* parameter).

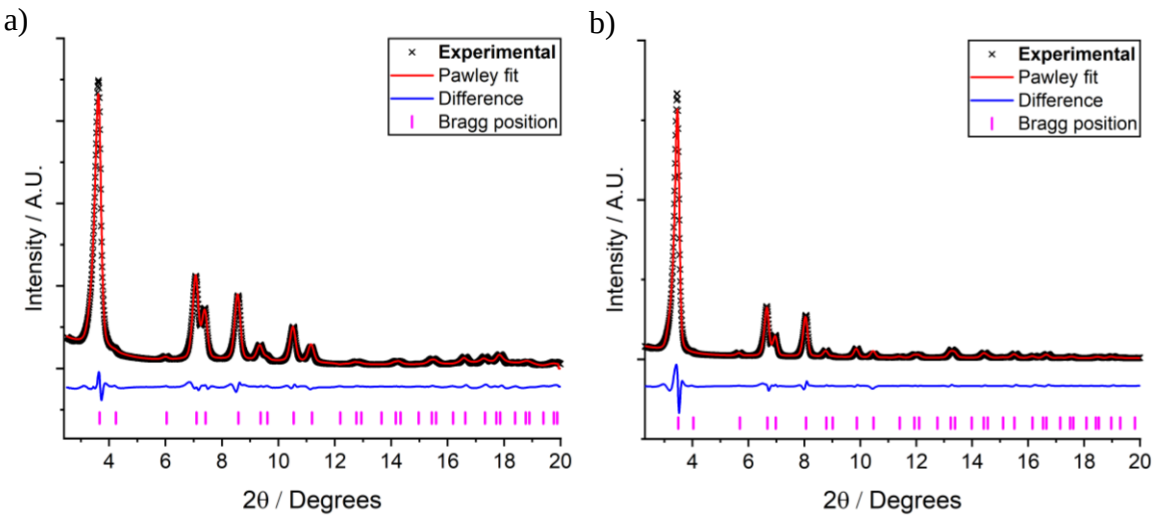

Figure 4.42. Pawley fits for a) **1** and b) **2**.

Both samples were fitted in the cubic space group *F*23 and the extracted lattice parameters are presented in Table 4.1. The unit cell of **1** is very similar to MIL-143 (volumes are within

0.6% of each other) and this supports our theory that they are isostructural. The final fit for **2** was also of a good quality (R_{wp} = 9.48%) and revealed that the unit cell is ~24% larger than MIL-143, consistent with **2** being an extended isoreticular analogue.

Table 4.1. Extracted unit cell parameters for **1** and **2** compared to the reported parameters for MIL-143.[46]

Phase	*a* (Å)	*V* (Å^3)
MIL-143	40.8635(1)	68235(N/A)
1	40.695(11)	67396(54)
2	43.852(41)	84329(24)

Nitrogen adsorption isotherms revealed that both samples are highly porous (Figure 4.43a), which is consistent with their rigid structures. Both samples exhibit Type 1 isotherms which are typical for microporous materials, and their BET surface areas are correspondingly high (Figure 4.43b). The higher uptake of N_2 for **2** compared to **1** is consistent with it being an extended isoreticular analogue, as has already been determined from Pawley fitting. It was possible to increase the porosity of **1** by heating in DMF (120 ˚C overnight) followed by refluxing in methanol overnight (denoted as **1^{ii}**). This increased the BET surface area to 1850 m^2g^{-1}, however, these values fall short of the experimental and theoretical values reported for the Fe-analogue (2150 m^2g^{-1} and 3540 m^2g^{-1}).[46] The BET surface area of **2** was greater than both the theoretical and experimentally obtained values for MIL-142B and MOF-907, respectively, which is further evidence that **2** is not isoreticular to these frameworks. No improvement was seen for **2** after a similar treatment.

a)

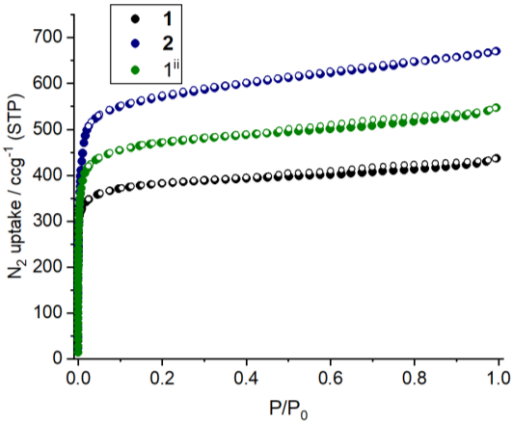

b)

Sample	S_{BET} (m^2g^{-1})
1	1500
1^{ii}	1850
MIL-142A	1850
MIL-143	3430
2	2266
MIL-142B	2085
MOF-907	2000

Figure 4.43. a) N_2 isotherms of 1 and 2, b) gas sorption data for **1, 1^{ii}** and **2**, compared to the values reported for similar Fe-based mixed-linker frameworks.[46,47]

Comparison to PXRD patterns obtained from the literature revealed that **4** possesses a similar structure to PCN-333(Al)[48], which is an extended isoreticular framework of MIL-100 that contains 4,4',4''-s-triazine-2,4,6-triyl-tribenzoate (TATB) as linker (Figure 4.44a). The PXRD patterns of our material and PCN-333(Al) have very similar reflections (Figure 4.44b), confirming its identity – the octahedral morphology of the crystals is also consistent with the face-centred cubic symmetry of PCN-333.

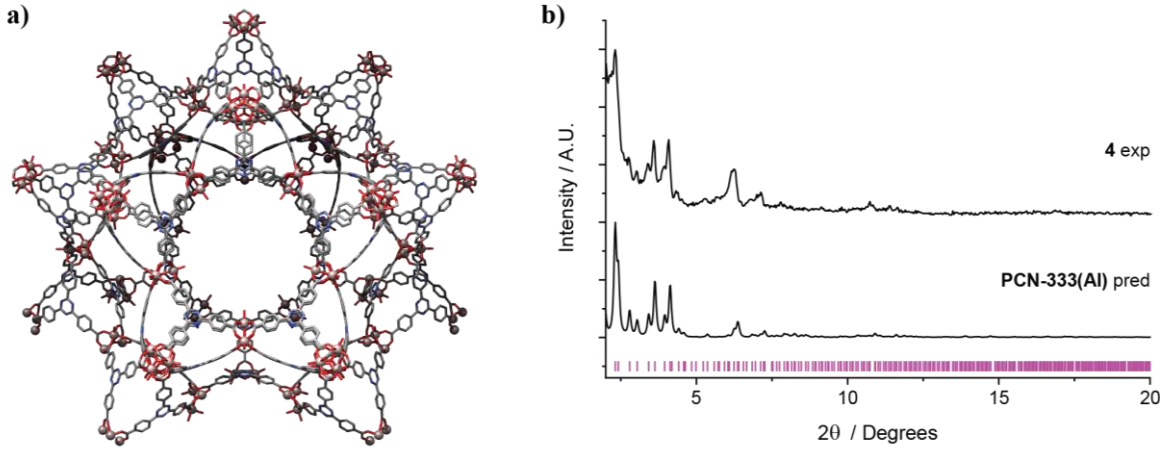

Figure 4.44. a) Structure of PCN-333(Al)[48] and b) stacked PXRD patterns of **4** and the predicted pattern for PCN-333(Al).

The failure to incorporate PDAC into product **4** was unexpected but PDAC is likely oxidised as was seen previously with SDC. Attempts were then made to synthesise this material without using the second ligand PDAC, however these were unsuccessful when using $Cr_3O(OAc)_6$ as Cr-source, as can be seen by PXRD (Figure 4.45a). The material, which will be referred to as MIL-100(Cr)_BTB, could only be successfully synthesised using nitrate or chloride, and in each case octahedral crystallites of very small size (< 200 nm) were obtained (Figure 4.45b-c).

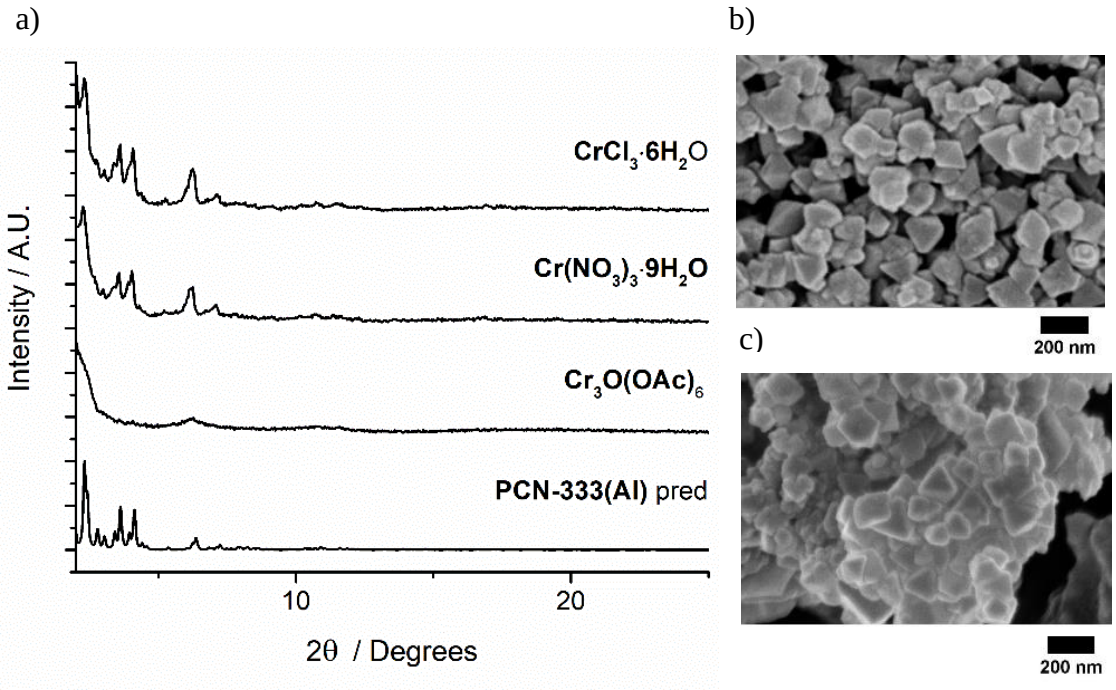

Figure 4.45. a) Stacked PXRD patterns of MIL-100(Cr)_BTB prepared using different Cr-sources, and SEM images of MIL-100(Cr)_BTB prepared using b) $Cr(NO_3)_3 \cdot 9H_2O$, c) $CrCl_3 \cdot 6H_2O$.

Nitrogen adsorption/desorption isotherms were measured for the MIL-100(Cr)_BTB prepared from $CrCl_3 \cdot 6H_2O$. Two activation methods were attempted in order to find the optimum conditions. The first method was to soak a sample in DMF at RT for 2 days, exchanging the DMF each day, followed by the same protocol with methanol. Finally, the sample was left to dry at room temperature before outgassing at 150 °C for 20 hours immediately prior to gas-sorption measurement. Nitrogen adsorption isotherms at 77 K reveal that the sample is highly porous, with total N_2 uptake of 1588 cm^3g^{-1} and a total pore volume of 2.46 cm^3g^{-1}. The true surface area of the framework cannot be reliably estimated using the BET method as most of the void space is in the form of mesopores, however, there are multiple satisfactory plots that can be obtained using points in the valid range defined by BET theory ($0.05 \leq P/P_0 \leq 0.35$) which give SA_{BET} = 2129-2791 m^2g^{-1}. Despite the high porosity of the sample, the nitrogen uptake and surface area were still much lower than those obtained for PCN-333(Fe).

a)

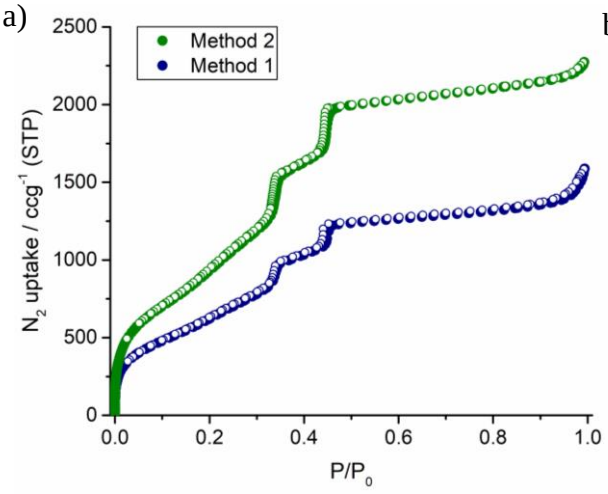

b)

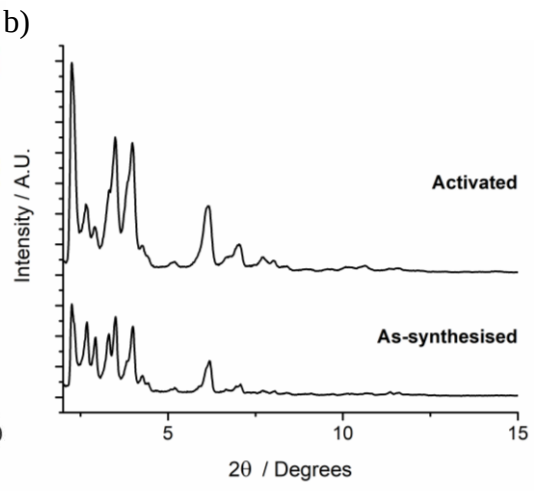

c)

Sample	PCN-333(Al)	MIL-100(Cr)_BTB	
		Method 1	Method 2
Total N_2 uptake (cm^3g^{-1})	2490	1588	2273
S_{BET} (m^2g^{-1})	4000	2129-2791	3090-4340
Total pore volume (cm^3g^{-1})	3.81	2.46	3.52

Figure 4.46. a) N_2 isotherms of MIL-100(Cr)_BTB activated using both methods, b) Stacked PXRD patterns of MIL-100(Cr)_BTB before and after activation, c) gas sorption properties of MIL-100(Cr)_BTB activated using each of the methods, compared to PCN-333(Al).

The second method consisted of heating a sample in DMF at 120 ˚C overnight in order to dissolve unreacted starting material and remove it from the pores. Afterwards the suspension was separated by centrifuging and washed once with DMF and then once with methanol. Then the sample was refluxed overnight in methanol, collected by centrifuging and washed with fresh methanol before allowing to to dry at room temperature. The same outgassing protocol (150 ˚C for 20 hours) was used prior to gas sorption analysis. The total N_2 uptake is 2273 cm^3g^{-1} and the total pore volume is 3.52 cm^3g^{-1}, which are comparable to those reported for PCN-333(Al): 2490 cm^3g^{-1} and 3.81 cm^3g^{-1}, respectively. The range of surface areas which can be obtained using the BET method are SA_{BET} = 3090-4340 m^2g^{-1}, which is comparable to the 4000 m^3g^{-1} reported for PCN-333(Al).

The fact that it is possible to crystallise a stable and highly porous extended MIL-100 framework using BTB is remarkable, as previous studies have suggested it is unfavourable for the BTB linker to adopt the necessary conformation to form the structure. This highlights the stabilising effect of using a kinetically inert metal such as Cr^{3+} as opposed to the more labile members of the M^{3+} family.

4.7.4 Summary

In this section I have demonstrated that our synthetic method is successful not only for synthesising flexible frameworks, but also for synthesising rigid and highly porous frameworks containing the $Cr_3O(RCO_2)_6$ SBU. By utilising mixtures of tri- and di-topic linkers, I have successfully synthesised the novel framework **1** which is isostructural to the Fe-MOF MIL-143. Its extended analogue **2** appears to be isoreticular, and represents a novel BTB/2,6-NDC containing framework. Both frameworks are highly porous and together represent the first examples of mixed-linker Cr-MOFs constructed from linkers of different connectivity.[33] Attempts to synthesise an upper analogue using PDAC as the ditopic linker yielded **4** which, unlike **1** and **2**, corresponds to the single linker framework MIL-100(Cr)_BTB. Further optimisation enabled the phase-pure synthesis of MIL-100(Cr)_BTB which, unlike the reported Fe-analogue, is stable to desolvation and thus exhibits exceptional permanent porosity, with total pore volume = 3.52 cm^3g^{-1}. This is significant as the isoreticular analogue PCN-333(Cr) can only be synthesised via metathesis from the Fe-analogue and possesses a lower N_2 uptake (total pore volume = 2.30 cm^3g^{-1}). It should be restated that prior to the work carried out in this chapter, only a handful of permanently porous Cr-MOFs could be synthesised directly, and out of them only MIL-101(Cr) exhibits comparably high N_2 uptake.[13] This combination of high stability and permanent porosity make all these novel Cr-MOFs highly desirable for a range of applications.

4.8 Conclusions

To conclude, the modulated synthesis of Cr-MOFs has been investigated, and reliable synthetic routes to different framework topologies have been established. For the first time there is a HF-free synthesis route to MIL-88D(Cr), a highly flexible framework, which uses acetic acid to control the self-assembly process and promote crystallisation. In addition, a whole series of novel frameworks containing $Cr_3O(RCO_2)_6$ SBUs and ditopic linkers has been successfully synthesised using the same method, which possess either MIL-88 or two-fold interpenetrated MIL-88-int topology. The high crystallinity and phase-purity of these materials has enabled me to study their flexibility using in-house PXRD techniques. I found that the DMF-solvated frameworks, which adopt open pore conformations, gradually and spontaneously close when not immersed in solvent, and I believe this is due to evaporation of the solvent from inside the pores. By applying various treatments to these solids, I found that the swelling amplitude - the increase in unit cell volume between the dry and solvated states – of the interpenetrated Cr-SDC is relatively high (100%) and comparable to the non-interpenetrated MIL-88 frameworks.[23] To the best of my knowledge this is the first example of a highly flexible interpenetrated MOF containing the trigonal $M_3O(RCO_2)_6$ SBU.

My synthetic efforts have yielded the first single-crystal structure of a directly-synthesised Cr^{3+} framework, MIL-88B(Cr)_1,4-NDC, which provides useful insight into the crystal structure that would not be possible from structure determination merely from PXRD, namely that the 1,4-NDC linker is disordered equally between four possible positions in the crystal structure. I have been able to extend this general methodology to obtain single crystal structures of two other Cr-MOFs, MIL-53(Cr) and MIL-53_Br(Cr), the latter of which has never previously been synthesised. This paves the way for future studies of the flexibility of these frameworks using both PXRD and SCXRD techniques, which will allow fine details of the structure to be elucidated during structural transformations.[17,31]

The ideal conditions for synthesising MIL-53(Cr) - with water as solvent and HCl as a modulator - are very general for $[Cr(OH)(RCO_2)_2]$ frameworks, and highly-crystalline material can be obtained with a range of dicarboxylate linkers. Future work will involve further attempts to obtain single crystals of more of these frameworks using the methodology I have established, as well as discovering new isoreticular analogues. The gas sorption properties of these frameworks have only been briefly investigated but for MIL-53(Cr) and MIL-53(Cr)_Br will first require development of a reliable protocol to remove the strongly interacting terephthalic acid from their pores.

I have been able to synthesise a novel Cr^{3+} MOF with a tetratopic linker, Cr-soc-MOF, which crystallises with lower symmetry than the Fe-analogue (PCN-250) and corresponds to the phase obtained upon applying pressure (PCN-250″). Cr-soc-MOF is highly stable and, unlike PCN-250″, does not relax to a cubic symmetry upon treatment in hot DMF. A more in-depth investigation of its behaviour is warranted and will likely require *in situ* PXRD studies under non-standard conditions. The porosities of these samples are lower than expected, but appears to be due to inefficient activation, and thus these conditions can be optimised further in future work.

Finally, I have synthesised a series of novel frameworks containing the BTB linker, both with single and mixed linkers, which are all highly porous. The mixed linker frameworks with BDC and 2,6-NDC as second linker are isoreticular analogues of MIL-143, an Fe framework containing both BTB and BDC linkers. MIL-143 is a transient phase relative to the more stable MIL-142A framework, which further exemplifies the slow kinetics of Cr^{3+} relative to Fe^{3+}. As expected, both frameworks are highly porous despite their porosities being somewhat lower than expected. The single linker framework, MIL-100(Cr)_BTB, is the first example of an extended MIL-100 framework formed with the BTB linker that can maintain its high porosity (SA_{BET} ~ 4000 m^2g^{-1}) upon desolvation. This is a perfect example of a Cr^{3+} framework that exhibits much higher stability and porosity than its Fe^{3+} analogue, which is imparted by its chemical inertness. This combination of high porosity and stability will make these materials well-suited and desirable for a wide range of potential applications.

To give a final summary, I have been able to synthesise a large number of phase-pure Cr-MOFs using HF-free synthesis routes that use either acetic or hydrochloric acid as modulators, demonstrating the extraordinary generality of my synthetic strategies. The two synthesis routes are highly selective for particular SBUs: synthesis in water and pyridine with acetic acid as modulator yields frameworks with the $[Cr_3O(RCO_2)_6(H_2O)_2X]$ SBU, while synthesis in water with HCl as a modulator yields those with $[Cr(OH)(RCO_2)_2]$. The ability to control the SBU in this manner is extremely useful and should enable the design of more novel Cr-MOFs with high gas uptake and/or flexibility: properties which I propose will lead to their development into real-world applications such as gas-storage and drug delivery. In the next chapter I will investigate the cytotoxicity and internalisation of a number of these materials to test their viability as potential drug delivery platforms.

4.9 Experimental

4.9.1 General Experimental Methods

All starting materials were purchased from commercial sources and used without further purification.

Powder X-Ray Diffraction (PXRD): PXRD measurements were carried out at 298 K using primarily a Rigaku MiniFlex diffractometer (λ (CuKα1) = 1.54056 Å, (CuKα2) = 1.54439 Å) on a spinning zero-background holder made of silicon, all other measurements were carried out using a PANalytical X'Pert PRO diffractometer (λ (CuKα) = 1.5405 Å) on a mounted bracket sample stage. All indexing and Pawley fitting was carried out using GSAS-II.[49]

DMF-solvated samples of the MIL-88 frameworks were collected by loading into a uncovered zero-background holder with a shallow cavity and packing with a glass slide immediately before collecting data so as to minimise solvent loss. The same procedure was used to prepare samples for the desolvation studies, in these cases the data was collected consecutively (5 minutes per measurement) up to 200 times.

Single Crystal X-Ray Diffraction (SCXRD): Data for MIL-53(Cr) and MIL-53(Cr)_Br were collected using a Bruker D8 VENTURE diffractometer (MoK_α = 0.71073 Å).

Scanning Electron Microscopy (SEM): Powders were deposited onto carbon tabs mounted on aluminium stubs, these were subsequently coated with Pd for 150 seconds using a Polaron SC7640 sputter coater. Samples were then imaged using a Carl Zeiss Sigma variable Pressure Analytical SEM with Oxford Microanalysis.

Thermogravimetric Analysis (TGA): Measurements were carried out using a TA Instruments Q500 Thermogravimetric Analyser.

Gas Uptake: N_2 adsorption and desorption isotherms were carried out at 77 K on a Quantachrome Autosorb iQ gas sorption analyser. Samples were typically degassed under vacuum at 150 °C for 20 hours using the internal turbo pump. BET surface areas were calculated from the isotherms using the Micropore BET Assistant in the Quantachrome ASiQwin operating software.

GCMC Gas Sorption Isotherm Simulations: Simulations of the nitrogen adsorption of MIL-53(Cr)_Br were carried out by Ignas Pakamore at the University of Glasgow using the RASPA2 program.[34] The Monte Carlo N_2 uptake was modelled using grand canonical

ensemble (GCMC) with 100,000 equilibration and 10,000 production cycles. Charges for framework atoms were obtained using charge equilibration method implemented in RASPA2. For simulations the 2x4x2 supercell was used. The forcefield for framework atoms was modelled using UFF parameters and Trappe for N_2.

4.9.2 General Synthesis of Cr-BPDC MOFs.

Biphenyl-4,4′-dicarboxylic acid (242 mg) and chromium(III) nitrate nonahydrate (238 mg) were added to a 50 mL Pyrex jar, water (4 mL) and pyridine (6 mL) were added along with any modulator. The mixture was sonicated until a homogeneous suspension was obtained, then this was transferred to a 23 mL capacity Teflon-lined stainless-steel autoclave and sealed tightly before placing in a solvothermal oven at 220 °C. After heating for the desired length of time, the autoclave was removed and allowed to cool naturally to room temperature. The solid was collected by centrifugation and washed 3 times with DMF (20 mL) to dissolve unreacted linker. The as-synthesised form of the material is subsequently obtained by washing 3 times with DCM (20 mL) and then drying in air at room temperature.

4.9.3 Synthesis of $[Cr_3O(CH_3COO)_6(H_2O)_3]NO_3 \cdot 6H_2O$ clusters

$[Cr_3O(CH_3COO)_6(H_2O)_3]NO_3 \cdot 6H_2O$ was synthesised following a modified procedure.[27] $Cr(NO_3)_3 \cdot 9H_2O$ (12 g, 0.03 mol) was dissolved in 10 mL hot water (50 °C). $CH_3COONa \cdot 3H_2O$ (8.16 g, 0.06 mol) was dissolved separately in 10 mL hot water (50 °C). The solutions were mixed and stirred at 50 °C for 10 minutes, before leaving to crystallise at room temperature. After 1-2 weeks, dark green crystals were collected by filtration and washed with diethyl ether, the remaining filtrate was left longer to precipitate more of the product. To remove any sodium nitrate, the solid was dissolved in acetone and filtered. The filtrate was dried by rotary evaporation to give a green solid which was characterised by PXRD (Figure 4.47). A typical synthesis yields ~2 g of material (~27%).

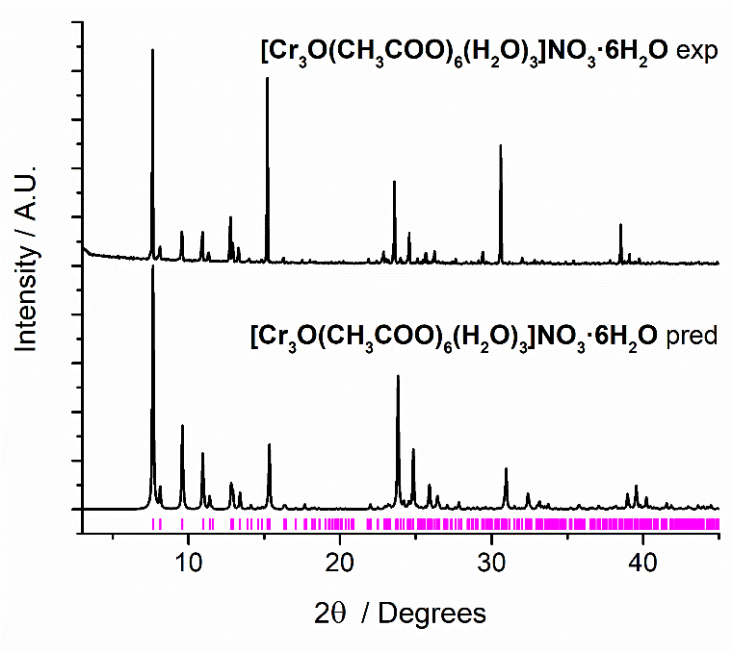

Figure 4.47. Stacked PXRD patterns of $[Cr_3O(CH_3COO)_6(H_2O)_3]NO_3{\cdot}6H_2O$ compared to the reported crystal structure (CCDC refcode XAYDUZ).[27]

4.9.4 General Synthesis of Isoreticular MIL-88 Series

The ligand and chromium source were added to a 50 mL Pyrex jar, water (4 mL) and pyridine (6 mL) were added along with a given quantity of glacial acetic acid. The mixture was sonicated until a homogeneous suspension was obtained, then this was transferred to a 23 mL capacity Teflon-lined stainless-steel autoclave and sealed tightly before placing in a solvothermal oven at 220 °C. After heating for the desired length of time, the autoclave was removed and allowed to cool naturally to room temperature. The open form of the material was obtained by washing 3 times with DMF (20 mL) and then keeping the sample sealed in a centrifuge tube to prevent solvent loss. The 'as-synthesised' material was collected by centrifugation and washing with DMF (3 x 20 mL) followed by DCM (3 x 20 mL) before drying in air at room temperature. The exact quantities of ligand and chromium source used to synthesise each MOF are given in Table 4.2.

Table 4.2. Cr-MOF synthesis details.

MOF	Ligand	Quantity of ligand (mg)	$Cr_3O(CH_3CO_2)_6$ (mg)	Acetic acid (mL)
MIL-88B(Cr)_1,4-NDC	1,4-Naphthalenedicarboxylic acid	216	250	0.572
MIL-88C(Cr)	2,6-Naphthalenedicarboxylic acid	216	250	0.572
Cr-SDC	4,4′-Stilbenedicarboxylic acid	268	250	0.4

4.9.5 Single-Crystal Synthesis of MIL-88B(Cr)_1,4-NDC

Naphthalene-1,4-dicarboxylic acid (216 mg) and $Cr_3O(OAc)_6$ (250 mg) were added to a 50 mL Pyrex jar, water (4 mL) and pyridine (6 mL) were added along with glacial acetic acid (0.8 mL). The mixture was sonicated until fully dissolved, then transferred to a 23 mL capacity Teflon-lined stainless-steel autoclave and sealed tightly before placing in a solvothermal oven at 220 °C. After heating for 72 hours, the autoclave was removed and allowed to cool naturally to room temperature. The green hexagonal-rod crystals were transferred to a glass vial and the solvent was replaced with acetone and then retained in this solvent for SCXRD.

4.9.6 Crystal data for MIL-88B(Cr)_1,4-NDC

$CrO_3(C_{10}H_6O_4)$, M_r = 230.61, crystal dimensions 0.02 × 0.01 × 0.01 mm, Hexagonal, $a = b$ = 14.2017 (14) Å, c = 17.189 (2) Å, V = 3002.35 (7) Å^3, T = 100 K, space group $P6_3/mmc$ (No. 194), Z = 8, 7448 measured reflections, 636 independent reflections (R_{int} = 0.116), which were used in all calculations. The final R_1 = 0.143 for 636 observed data $R[F^2 > 2\sigma(F^2)]$ and $wR(F^2)$ = 0.400 (all data).

4.9.7 Synthesis of MIL-53(Cr)

Terephthalic acid (166 mg) and chromium (III) chloride hexahydrate (266 mg) were added to a 23 mL Teflon autoclave liner and water (10 mL) was added along with any modulator. The mixture was stirred at room temperature for ~10 mins before sealing in a stainless-steel autoclave and placing in a solvothermal oven at 220 °C for 72 hours. The autoclave was removed and allowed to cool naturally to room temperature. The solid was collected by centrifugation and washed with ethanol multiple times before drying in a desiccator at room temperature. Samples prepared for SCXRD were transferred to glass vials and kept in solvent.

4.9.8 Crystal data for MIL-53(Cr).

$Cr(C_8H_4O_4)(OH)$, M_r = 810.18, crystal dimensions 0.06 × 0.04 × 0.04 mm, Orthorhombic, a = 17.5739 (9) Å, b = 6.8259 (3) Å, c = 11.8443 (6) Å, V = 1420.81 (12) Å^3, T = 273 K, space group *Pnna*, (No. 62), Z = 2, 1996 measured reflections, 1996 independent reflections (R_{int} = 0.099), which were used in all calculations. The final R_1 = 0.149 for 1996 observed data $R[F^2 > 2\sigma(F^2)]$ and $wR(F^2)$ = 0.497 (all data).

4.9.9 Synthesis of MIL-53_Br(Cr)

2-Bromoterephthalic acid (245 mg) and chromium (III) chloride hexahydrate (266 mg) were added to a 23 mL Teflon autoclave liner and water (10 mL) along with HCl (250 µL). The mixture was stirred at room temperature for ~10 mins before sealing in a stainless-steel autoclave and placing in a solvothermal oven at 220 °C for 72 hours. The autoclave was removed and allowed to cool naturally to room temperature. The green block crystals were transferred to a glass vial and kept in solvent for SCXRD. Elemental analysis: Found C, 32.99; H, 1.44; N, 0.67. Expected based on [Cr(OH)(BDC-Br)]·0.15DMF: C, 31.41; H, 1.56; N, 0.65. Expected based on [Cr(OH)(BDC-Br)]·0.15DMF·0.3BDC-Br: C, 32.85; H, 1.65; N, 0.53.

4.9.10 Crystal data for MIL-53(Cr)_Br

$Cr(C_8H_3O_4Br)(OH)$, M_r = 312.02, crystal dimensions 0.07 × 0.04 × 0.03 mm, Orthorhombic, a = 16.861 (5) Å, b = 6.8523 (19) Å, c = 13.003 (4) Å, V = 1502.3 (8) Å^3, T = 150 K, space group *Imma*, (No. 74), Z = 4, 1052 measured reflections, 1052 independent reflections (R_{int} = 0.110), which were used in all calculations. The final R_1 = 0.077 for 1052 observed data $R[F^2 > 2\sigma(F^2)]$ and $wR(F^2)$ = 0.212 (all data).

4.9.11 Synthesis of Cr(OH)(1,4-NDC)

Naphthalene-1,4-dicarboxylic acid (108 mg) and chromium (III) chloride hexahydrate (266 mg) were added to a 23 mL Teflon autoclave liner and water (10 mL) was added along with any modulator. The mixture was stirred at room temperature for ~10 mins before sealing in a stainless-steel autoclave and placing in a solvothermal oven at 220 °C for 72 hours. The autoclave was removed and allowed to cool naturally to room temperature. The solid was collected by centrifugation and washed with DMF (3 x 20 mL) and DCM (3 x 20 mL), then dried in a desiccator at room temperature.

4.9.12 Synthesis of Cr(OH)(2,6-NDC)

Naphthalene-2,6-dicarboxylic acid (108 mg) and chromium (III) chloride hexahydrate (266 mg) were added to a 23 mL Teflon autoclave liner and water (10 mL) was added along with any modulator. The mixture was stirred at room temperature for ~10 mins before sealing in a stainless-steel autoclave and placing in a solvothermal oven at 220 °C for 72 hours. The autoclave was removed and allowed to cool naturally to room temperature. The solid was collected by centrifugation and washed with DMF multiple times before drying in a

desiccator at room temperature. TGA and elemental analysis are consistent with a formula of Cr(OH)(2,6-NDC)·2DMF. TGA: 1st mass loss = 35.4 % (expected = 34.1 %), 2nd mass loss = 47.7 % (expected = 48.3 %). EA: Expected C, 50.34; H, 4.90; N, 6.53. Found C, 50.07; H, 5.225; N, 6.87. DMF could be partially removed to form the hydrated phase via heating at 220 °C in air overnight. Elemental analysis based on formula Cr(OH)(2,6-NDC)·H_2O: Expected C, 47.84; H, 2.99; N, 0.00. Found C, 48.67; H, 2.76; N, 0.18.

4.9.13 General Synthesis of Cr-soc-MOF

3,3',5,5'-Azobenzene tetracarboxylic acid[41] (179 mg) and chromium source (0.5 mmol) were added to a 50 mL Pyrex jar, water (4 mL) and pyridine (6 mL) were added along with a given quantity of glacial acetic acid. The mixture was sonicated until a homogeneous suspension was obtained, then this was transferred to a 23 mL capacity Teflon-lined stainless-steel autoclave and sealed tightly before placing in a solvothermal oven at 220 °C. After heating for the desired length of time, the autoclave was removed and allowed to cool naturally to room temperature. The solid was collected by centrifugation and washed 3 times with DMF (20 mL) and then 3 times with DCM (20 mL) before drying at room temperature in a desiccator. Elemental analysis on one of the samples shows that it has a higher organic content than would be expected for a pristine sample with formula $Cr_3O(OH)(H_2O)_2(ABTC)_{1.5}$: Expected C, 38.10; H, 1.85; N, 5.88. Found C, 41.71; H, 2.42; N, 6.41.

4.9.14 Synthesis of Mixed Linker MOFs

1,3,5-Tris(4-carboxyphenyl)benzene (219 mg), the second ligand (0.5 mmol) and chromium source were added to a 50 mL Pyrex jar, water (4 mL) and pyridine (6 mL) were added along with glacial acetic acid (1 mL). The mixture was sonicated until a homogeneous suspension was obtained, then this was transferred to a 23 mL capacity Teflon-lined stainless-steel autoclave and sealed tightly before placing in a solvothermal oven at 220 °C. After heating for 72 hours, the autoclave was removed and allowed to cool naturally to room temperature. The solid was collected by centrifugation and washed 3 times with DMF (20 mL) and then 3 times with DCM (20 mL) before drying at room temperature in a desiccator.

4.9.15 Synthesis of MIL-100(Cr)_BTB

1,3,5-Tris(4-carboxyphenyl)benzene (219 mg) and chromium source (1 mmol) were added to a 50 mL Pyrex jar, water (4 mL) and pyridine (6 mL) were added along with a given quantity of glacial acetic acid. The mixture was sonicated until a homogeneous suspension

was obtained, then this was transferred to a 23 mL capacity Teflon-lined stainless-steel autoclave and sealed tightly before placing in a solvothermal oven at 220 °C. After heating for 72 hours, the autoclave was removed and allowed to cool naturally to room temperature. The solid was collected by centrifugation and washed 3 times with DMF (20 mL) and then 3 times with DCM (20 mL) before drying at room temperature in a desiccator.

4.10 References

(1) Devic, T. and Serre, C., *Chem. Soc. Rev.*, **2014**, *43*, 6097-6115.

(2) Shuai, Y., Liang, F., Kecheng, W., Jiandong, P., Matheiu, B., Christina, L., Yujia, S., Junsheng, Q., Xinyu, Y., Peng, Z., Qi, W., Lanfang, Z., Yingmu, Z., Liangliang, Z., Yu, F., Jialuo, L. and Hong-Cai, Z., *Adv. Mater.*, *0*, 1704303.

(3) Furukawa, H., Cordova, K. E., O'Keeffe, M. and Yaghi, O. M., *Science*, **2013**, *341*.

(4) Yuan, S., Feng, L., Wang, K., Pang, J., Bosch, M., Lollar, C., Sun, Y., Qin, J., Yang, X., Zhang, P., Wang, Q., Zou, L., Zhang, Y., Zhang, L., Fang, Y., Li, J. and Zhou, H.-C., *Adv. Mater.*, **2018**, *30*, 1704303.

(5) Ding, M., Cai, X. and Jiang, H.-L., *Chemical Science*, **2019**, *10*, 10209-10230.

(6) Serre, C., Millange, F., Thouvenot, C., Noguès, M., Marsolier, G., Louër, D. and Férey, G., *J. Am. Chem. Soc.*, **2002**, *124*, 13519-13526.

(7) Millange, F., Serre, C. and Férey, G., *Chem. Commun.*, **2002**, 822-823.

(8) Mowat, J. P. S., Seymour, V. R., Griffin, J. M., Thompson, S. P., Slawin, A. M. Z., Fairen-Jimenez, D., Düren, T., Ashbrook, S. E. and Wright, P. A., *Dalton Trans.*, **2012**, *41*, 3937-3941.

(9) Millange, F., Guillou, N., Walton, R. I., Grenèche, J.-M., Margiolaki, I. and Férey, G., *Chem. Commun.*, **2008**, 4732-4734.

(10) El Osta, R., Carlin-Sinclair, A., Guillou, N., Walton, R. I., Vermoortele, F., Maes, M., de Vos, D. and Millange, F., *Chem. Mater.*, **2012**, *24*, 2781-2791.

(11) Guillou, N., Bourrelly, S., Llewellyn, P. L., Walton, R. I. and Millange, F., *CrystEngComm*, **2015**, *17*, 422-429.

(12) Bhattacharjee, S., Chen, C. and Ahn, W.-S., *RSC Advances*, **2014**, *4*, 52500-52525.

(13) Férey, G., Mellot-Draznieks, C., Serre, C., Millange, F., Dutour, J., Surblé, S. and Margiolaki, I., *Science*, **2005**, *309*, 2040-2042.

(14) Wang, J.-H., Zhang, Y., Li, M., Yan, S., Li, D. and Zhang, X.-M., *Angew. Chem. Int. Ed.*, **2017**, *56*, 6478-6482.

(15) Lian, X., Feng, D., Chen, Y.-P., Liu, T.-F., Wang, X. and Zhou, H.-C., *Chemical Science*, **2015**, *6*, 7044-7048.

(16) Chen, Z., Li, P., Zhang, X., Li, P., Wasson, M. C., Islamoglu, T., Stoddart, J. F. and Farha, O. K., *J. Am. Chem. Soc.*, **2019**, *141*, 2900-2905.

(17) Surble, S., Serre, C., Mellot-Draznieks, C., Millange, F. and Férey, G., *Chem. Commun.*, **2006**, 284-286.

(18) Shih, Y.-H., Lo, S.-H., Yang, N.-S., Singco, B., Cheng, Y.-J., Wu, C.-Y., Chang, I.-H., Huang, H.-Y. and Lin, C.-H., *ChemPlusChem*, **2012**, *77*, 982-986.

(19) Yang, F., Xu, G., Dou, Y., Wang, B., Zhang, H., Wu, H., Zhou, W., Li, J.-R. and Chen, B., *Nature Energy*, **2017**, *2*, 877-883.

(20) Férey, G., Serre, C., Mellot-Draznieks, C., Millange, F., Surblé, S., Dutour, J. and Margiolaki, I., *Angew. Chem. Int. Ed.*, **2004**, *43*, 6296-6301.

(21) Surblé, S., Millange, F., Serre, C., Düren, T., Latroche, M., Bourrelly, S., Llewellyn, P. L. and Férey, G., *J. Am. Chem. Soc.*, **2006**, *128*, 14889-14896.

(22) Horcajada, P., Salles, F., Wuttke, S., Devic, T., Heurtaux, D., Maurin, G., Vimont, A., Daturi, M., David, O., Magnier, E., Stock, N., Filinchuk, Y., Popov, D., Riekel, C., Férey, G. and Serre, C., *J. Am. Chem. Soc.*, **2011**, *133*, 17839-17847.

(23) Serre, C., Mellot-Draznieks, C., Surblé, S., Audebrand, N., Filinchuk, Y. and Férey, G., *Science*, **2007**, *315*, 1828-1831.

(24) Tan, B., Luo, Y., Liang, X., Wang, S., Gao, X., Zhang, Z. and Fang, Y., *Ind. Eng. Chem. Res.*, **2019**, *58*, 2983-2990.

(25) Horcajada, P., Chevreau, H., Heurtaux, D., Benyettou, F., Salles, F., Devic, T., Garcia-Marquez, A., Yu, C., Lavrard, H., Dutson, C. L., Magnier, E., Maurin, G., Elkaïm, E. and Serre, C., *Chem. Commun.*, **2014**, *50*, 6872-6874.

(26) Feng, D., Wang, K., Wei, Z., Chen, Y.-P., Simon, C. M., Arvapally, R. K., Martin, R. L., Bosch, M., Liu, T.-F., Fordham, S., Yuan, D., Omary, M. A., Haranczyk, M., Smit, B. and Zhou, H.-C., *Nat. Comm.*, **2014**, *5*, 5723.

(27) Peng, L., Asgari, M., Mieville, P., Schouwink, P., Bulut, S., Sun, D. T., Zhou, Z., Pattison, P., van Beek, W. and Queen, W. L., *ACS Appl. Mater. Interfaces*, **2017**, *9*, 23957-23966.

(28) Towsif Abtab, S. M., Alezi, D., Bhatt, P. M., Shkurenko, A., Belmabkhout, Y., Aggarwal, H., Weseliński, Ł. J., Alsadun, N., Samin, U., Hedhili, M. N. and Eddaoudi, M., *Chem*, **2018**, *4*, 94-105.

(29) Schaate, A., Roy, P., Godt, A., Lippke, J., Waltz, F., Wiebcke, M. and Behrens, P., *Chem. Eur. J.*, **2011**, *17*, 6643-6651.

(30) Schneemann, A., Bon, V., Schwedler, I., Senkovska, I., Kaskel, S. and Fischer, R. A., *Chem. Soc. Rev.*, **2014**, *43*, 6062-6096.

(31) Carrington, E. J., McAnally, C. A., Fletcher, A. J., Thompson, S. P., Warren, M. and Brammer, L., *Nat. Chem.*, **2017**, *9*, 882-889.

(32) Devic, T., Horcajada, P., Serre, C., Salles, F., Maurin, G., Moulin, B., Heurtaux, D., Clet, G., Vimont, A., Grenèche, J.-M., Ouay, B. L., Moreau, F., Magnier, E.,

Filinchuk, Y., Marrot, J., Lavalley, J.-C., Daturi, M. and Férey, G., *J. Am. Chem. Soc.*, **2010**, *132*, 1127-1136.

(33) Lammert, M., Bernt, S., Vermoortele, F., De Vos, D. E. and Stock, N., *Inorg. Chem.*, **2013**, *52*, 8521-8528.

(34) Dubbeldam, D., Calero, S., Ellis, D. E. and Snurr, R. Q., *Mol Simul*, **2016**, *42*, 81-101.

(35) Loiseau, T., Serre, C., Huguenard, C., Fink, G., Taulelle, F., Henry, M., Bataille, T. and Férey, G., *Chem. Eur. J.*, **2004**, *10*, 1373-1382.

(36) Volkringer, C., Loiseau, T., Guillou, N., Férey, G., Elkaïm, E. and Vimont, A., *Dalton Trans.*, **2009**, 2241-2249.

(37) Chen, J.-J., Chen, Y.-T., Senthil Raja, D., Kang, Y.-H., Tseng, P.-C. and Lin, C.-H., *Sci. Technol. Adv. Mater.*, **2015**, *16*, 054203.

(38) Comotti, A., Bracco, S., Sozzani, P., Horike, S., Matsuda, R., Chen, J., Takata, M., Kubota, Y. and Kitagawa, S., *J. Am. Chem. Soc.*, **2008**, *130*, 13664-13672.

(39) Senkovska, I., Hoffmann, F., Fröba, M., Getzschmann, J., Böhlmann, W. and Kaskel, S., *Microporous Mesoporous Mater.*, **2009**, *122*, 93-98.

(40) Loiseau, T., Mellot-Draznieks, C., Muguerra, H., Férey, G., Haouas, M. and Taulelle, F., *Comptes Rendus Chimie*, **2005**, *8*, 765-772.

(41) Chevreau, H., Permyakova, A., Nouar, F., Fabry, P., Livage, C., Ragon, F., Garcia-Marquez, A., Devic, T., Steunou, N., Serre, C. and Horcajada, P., *CrystEngComm*, **2016**, *18*, 4094-4101.

(42) Belmabkhout, Y., Pillai, R. S., Alezi, D., Shekhah, O., Bhatt, P. M., Chen, Z., Adil, K., Vaesen, S., De Weireld, G., Pang, M., Suetin, M., Cairns, A. J., Solovyeva, V., Shkurenko, A., El Tall, O., Maurin, G. and Eddaoudi, M., *J. Mater. Chem. A*, **2017**, *5*, 3293-3303.

(43) Liu, Y., Eubank, J. F., Cairns, A. J., Eckert, J., Kravtsov, V. C., Luebke, R. and Eddaoudi, M., *Angew. Chem. Int. Ed.*, **2007**, *46*, 3278-3283.

(44) Dhakshinamoorthy, A., Alvaro, M., Chevreau, H., Horcajada, P., Devic, T., Serre, C. and Garcia, H., *Catal. Sci.*, **2012**, *2*, 324-330.

(45) Yuan, S., Sun, X., Pang, J., Lollar, C., Qin, J.-S., Perry, Z., Joseph, E., Wang, X., Fang, Y., Bosch, M., Sun, D., Liu, D. and Zhou, H.-C., *Joule*, **2017**, *1*, 806-815.

(46) Chevreau, H., Devic, T., Salles, F., Maurin, G., Stock, N. and Serre, C., *Angew. Chem. Int. Ed.*, **2013**, *52*, 5056-5060.

(47) Nguyen, H. L., Vu, T. T., Nguyen, D.-K., Trickett, C. A., Doan, T. L. H., Diercks, C. S., Nguyen, V. Q. and Cordova, K. E., *Commun. Chem.*, **2018**, *1*, 70.

(48) Feng, D., Liu, T.-F., Su, J., Bosch, M., Wei, Z., Wan, W., Yuan, D., Chen, Y.-P., Wang, X., Wang, K., Lian, X., Gu, Z.-Y., Park, J., Zou, X. and Zhou, H.-C., *Nat. Comm.*, **2015**, *6*, 5979.

(49) Toby, B. H. and Von Dreele, R. B., *J. Appl. Crystallogr.*, *46(2)*, 544-549.

Chapter 5

Biocompatibility and Internalisation of Cr-MOFs

Contributions

Confocal microscopy, flow cytometry, and RTCA measurements were carried out with the assistance of Dr Nikolaos Panagiotou (University of Glasgow). TEM imaging was carried out by Dr Margaret Mullin (University of Glasgow). MIL-101(Cr) was synthesised by Panagiota Markopoulou (University of Glasgow).

Contents

Chapter 5 191

5.1 Introduction 194

5.2 Aims 195

5.3 Biocompatibility of Cr-MOFs 196

5.3.1 Effect of Cr^{3+} on Cells 196

5.3.2 Effect of Cr-MOFs on Cells 197

5.3.3 Internalisation 199

5.4 Conclusions 202

5.5 Experimental 204

5.5.1 Alamar blue assay 204

5.5.2 Real time cell analysis (RTCA) 205

5.5.3 Calcein Loading 208

5.5.4 Flow cytometry 208

5.5.5 Confocal microscopy 211

5.5.6 Scanning and Transmission Electron Microscopy 212

5.6 References 215

5.1 Introduction

The main purpose of the previous three chapters was to control the synthesis of Fe and Cr-MOFs to facilitate their future development as drug delivery systems (DDS). Initially we envisioned Fe-MOFs as ideal candidates for these applications, as has been identified in the literature,[1] however, in our work we have often obtained large crystallites (>20 μm) which are unsuitable for intravenous administration. Comparatively, our Cr-MOFs have been much easier to obtain as microcrystalline powders with uniform crystal size, due to the slow kinetics of Cr^{3+} and the success of our modulation strategy.

Typically, the MOFs which are considered viable for drug delivery are restricted to those containing relatively non-toxic metals such as Fe^{3+}, Zr^{4+}, and Zn^{2+}, while Cr^{3+} is generally considered to be toxic and thus unsuitable for these applications. The toxicity of hexavalent chromium is considerable, being both very toxic and mutagenic, and this has raised concern over the use of Cr-containing compounds in general.[2] On the other hand, trivalent chromium compounds are generally nontoxic and are present in small quantities in a wide range of food products.[3] Furthermore, Cr^{3+} is very inert and is the most stable form of chromium, and so a negligible amount of the toxic hexavalent form would be expected to be present in Cr^{3+}-MOFs. Considering these points, we reasoned that there is no clear reason for Cr-MOFs to be disregarded outright as long as they are not prepared from Cr^{6+} precursors.[4]

To the best of our knowledge, two Cr-MOFs have already been tested by *in vitro* studies: MIL-100(Cr)[5] and MIL-101(Cr)[6-8]. Both MOFs have demonstrated negligible negative cellular effects within the concentrations expected to be used in therapeutic applications, suggesting that they are indeed biocompatible. Furthermore, an *in vivo* study on mice orally administered with MIL-101(Cr) showed no acute toxicity, even at a daily dose of 1000 mg/kg for 28 days,[9] which suggests it could potentially be well-tolerated by patients. Based on these encouraging results, we decided to investigate the biocompatibility and internalisation efficacy of some of our Cr-MOFs to determine if this is a general trend and to aid in their development as DDSs.

5.2 Aims

The main aims of this chapter are:

1. To assess the *in vitro* biocompatibility of a number of Cr-MOFs and their components on healthy cells using both real time and end point measurements.
2. To investigate the internalisation efficacy of Cr-MOFs using multiple imaging techniques to assess cellular uptake and quantify the delivery of Calcein using MOFs as a transport mechanism.

For Cr-MOFs to be viable as drug delivery systems (DDSs), it is crucial that any cytotoxicity is properly characterised, and its origin isolated to narrow down the best possible candidates. To this end we have looked at the effects not only of the MOFs, but of their constituent components (Figure 5.1) in order to correlate their respective cellular effects. To comprehensively assess the biocompatibility of these MOFs, we looked at their effects on cell proliferation, cell viability, and cellular metabolic activity using healthy cell lines.

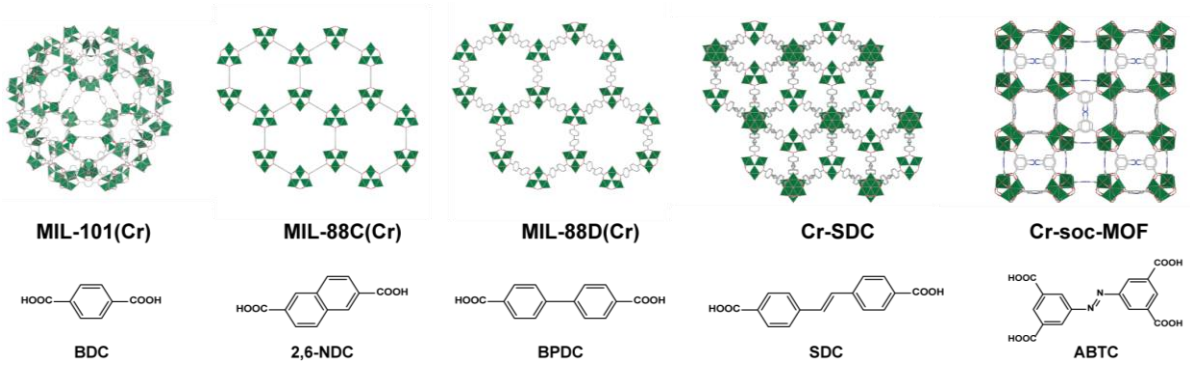

Figure 5.1. Cr-MOF structures and their linkers.

To ensure that these Cr-MOFs will be able to deliver drugs in human tissue, we assessed their internalisation into cells using scanning electron microscopy (SEM) and transmission electron microscopy (TEM). Additionally, Calcein (Cal) is loaded into the MOFs in order to investigate cellular uptake using flow cytometry and confocal microscopy on cells post Cal@MOF administration. This also enables the delivery of Calcein to be quantified, which will allow us to determine the effectiveness of using these MOFs as potential drug delivery mechanisms.

5.3 Biocompatibility of Cr-MOFs

5.3.1 Effect of Cr^{3+} on Cells

To assess the biocompatibility of Cr-MOFs, we first compared the toxicity of Cr^{3+} against some of the other metal ions commonly used in MOF synthesis. The impact of the metals on cell growth was measured using real-time cell analysis (RTCA) over a 72-hour period in primary Human Dermal Fibroblasts (HDFs), with varying doses of the metal salts (either the corresponding nitrate or chloride). RTCA monitors cell proliferation in real time over the course of the experiments via impedance measurements and thus enables the cell growth rate to be determined over a given time period. Subsequent slope analysis on our RTCA data suggested that Cr^{3+} is the least toxic and thus most biocompatible of the metals that were tested compared to Fe^{3+}, Zr^{4+}, and Zn^{2+} (Figure 5.2a), and was also the only metal that maintained a positive cell growth rate at the maximum dose tested. Additionally, the impact of Cr^{3+} on the metabolic activity of Human Embryonic Kidney (HEK-293) cells was investigated with Alamar blue assays, 72 hours after Cr^{3+} salt administration. Alamar blue is reduced by metabolically active cells to a fluorescent metabolite, and is thus added at the end point of the experiment (i.e. an end-point assay) to quantify metabolic activity.[10] Metabolic activity was significantly negatively impacted only at a remarkably high concentration of Cr^{3+} (Figure 5.2b) and this effect resulted in a drop of metabolic activity to only 76%. These results suggest that Cr^{3+} is well-tolerated by cells and so MOFs constructed from Cr^{3+} could be expected to exhibit similarly low toxicity.

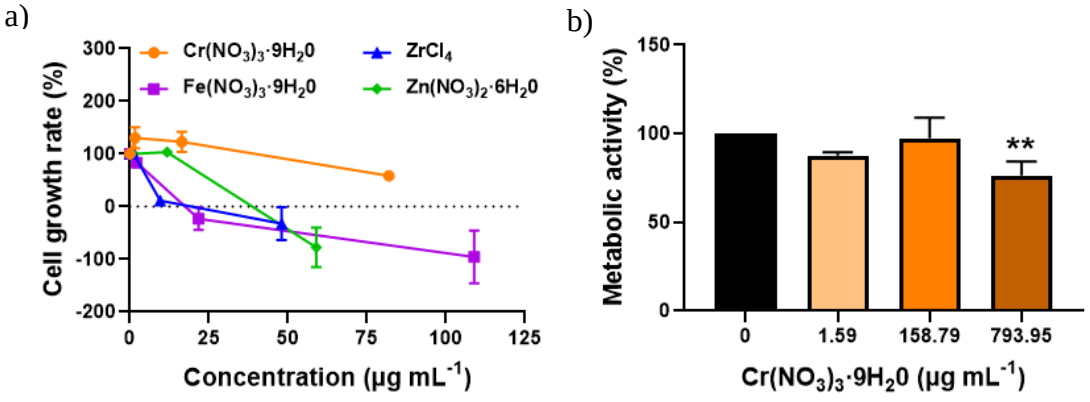

Figure 5.2. Cell viability following metal salt administration. a) RTCA: Rate of cell growth over a 72-hour period post administration of metal salts in HDFs measured by RTCA. Data are presented as mean ± SEM (n=3). b) Alamar blue: Cell metabolic activity 72 hours post Cr salt addition in HEK-293 cells determined using Alamar Blue assays. Data are presented

as mean ± SEM; One-way ANOVA with Dunnett's test (n=3). **p≤0.01.**Effect of Cr-MOFs on Cells**

To test this hypothesis, we investigated the biocompatibility of four of the Cr-MOFs synthesised in Chapter 4: Cr-soc-MOF, MIL-88C(Cr), MIL-88D(Cr) and Cr-SDC, along with MIL-101(Cr) for comparison. Initially, to observe their effect on cell proliferation, we employed real-time cell analysis, where HEK-293 cells were plated and incubated with the Cr-MOFs for a period of 72 hours. In line with the RTCA results with Cr^{3+}, no significant reduction in cell growth was observed for any of the MOFs at the two concentrations used (Figure 5.3a). Interestingly, a statistically significant increase in cell growth was seen for the lowest concentrations of Cr-soc-MOF, MIL-88C(Cr), and MIL-88D(Cr). This is likely due to internalisation of the MOF particles, leading to an overall increase in the size of the cells, rather than a true increase in cell proliferation. Further evidence for this is seen at the highest concentration, where this effect is absent as any increase in size is likely cancelled out by cell loss attributable to cytotoxicity.

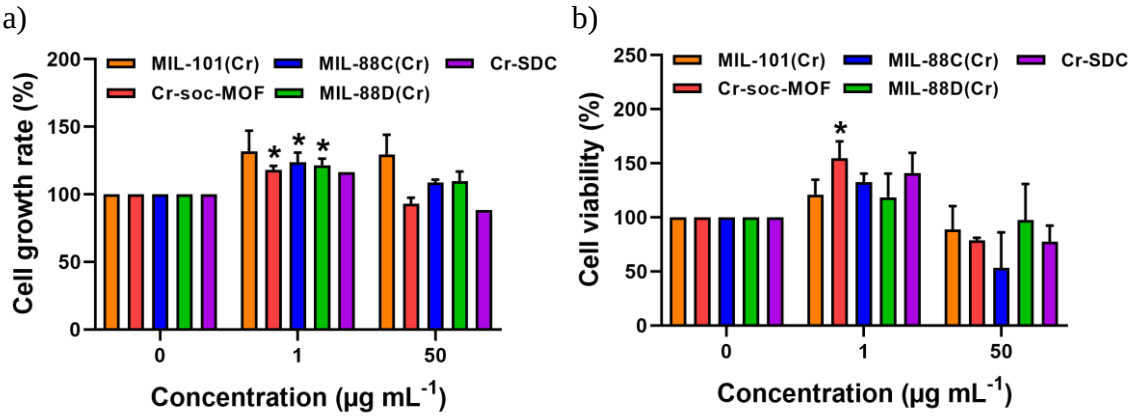

Figure 5.3. Cr-MOFs biocompatibility evaluation. a) RTCA: HEK-293 proliferative capacity, normalised to the untreated control, 72 hours post MOF administration. b) Flow cytometry: HEK-293 viability, normalised to the untreated control, 72 hours post MOF administration. Data are presented as mean ± SEM; One-way ANOVA with Dunnett's test (n=3). *p≤0.05.To further investigate this, we used flow cytometry to measure cell viability 72 hours post Cr-MOFs administration in HEK-293 cells. Flow cytometry is a technique that separates cells and passes them individually through a laser beam, with the direction of the scattered light enabling discrimination of individual cell. The dead cells were stained with a fluorescent dye and its signal could thus be detected by a channel in the flow cytometer, enabling the cell viability to be determined. Compared to the RTCA results, both MIL-88C(Cr) and MIL-88D(Cr) maintained cell viability at similar levels to the controls (Figure

5.3b), which is consistent with our suggestion that the increased cell growth rate is due primarily to cell size increase following MOF internalisation and not the outcome of increased proliferation. In contrast, Cr-soc-MOF increases cell viability at low concentration, suggesting an effect on cell proliferation. The data also suggest that a high concentration of MIL-88C(Cr) can induce a degree of cell loss which, although statistically insignificant in comparison to our control, could further support our previous observation with RTCA. The other Cr-MOFs that we investigated did not affect cell viability at either of the two concentrations.

Alamar blue assays were additionally carried out 72 hours post Cr-MOF administration in HEK-293 cells to measure the effect of varying MOF concentration on the metabolic activity of the cells. Apart from Cr-SDC, all the Cr-MOFs were biocompatible at both concentrations tested and did not affect cellular metabolic activity compared to the untreated controls (Figure 5.4a). The only MOF which caused a significant negative impact on metabolic activity was Cr-SDC at 50 μg mL^{-1}. This was a surprising outcome as our previous observations indicated that Cr^{3+} would not affect cell metabolic activity in these concentrations. Thus, we recognised that the linker (4,4′-stilbenedicarboxylate) in Cr-SDC could potentially have a negative effect towards metabolic activity. Similar cytotoxicity has been reported for a Zr-SDC framework, which was an outlier amongst isoreticular Zr-MOFs with different linkers,[11] suggesting that the ligand itself causes this toxicity.

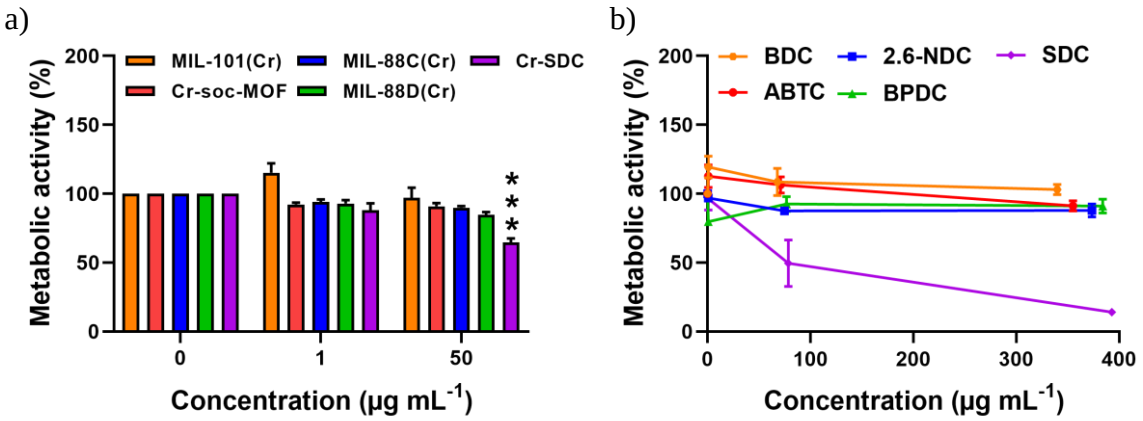

Figure 5.4. a) Alamar blue: HEK-293 metabolic activity, normalised to the untreated control, 72 hours post administration of MOFs. b) Alamar blue: HEK-293 metabolic activity, normalised to the untreated control, 72 hours post linker administration. Data are presented as mean ± SEM (n=3). One-way ANOVA with Dunnett's test (n=3). ***$p \leq 0.001$.

To investigate further, we incubated HEK-293 cells with each of the constituent linkers for 72 hours, then performed Alamar blue assays to assess cell metabolic activity. Over the range

of concentrations administered, SDC was the most cytotoxic by far and had a significantly negative impact upon metabolic activity (Figure 5.4d). Additionally, 2,6-NDC had a significant negative effect at medium and high doses, while BPDC had a negative effect when the small dose was administered. Aside from their inherent toxicities, differences in the solubility of each linker may also contribute to these results as the concentration is varied. Neither ABTC nor BDC had any significant effect on metabolic activity at the doses used.

5.3.3 Internalisation

To validate that Cr-MOFs sufficiently enter cells, we investigated their cellular internalisation. By doing so, we could verify whether the negligible cellular effects seen with MIL-101(Cr), MIL-88C(Cr), and MIL-88D(Cr) were truly due to biocompatibility or merely their absence from the cells. To this end, we utilised two complementary imaging techniques which would allow us to observe the crystals outside and inside the cells, comprising scanning electron microscopy (SEM) and transmission electron microscopy (TEM). We selected the highest concentration administered (50 μg mL^{-1}) to focus on for these experiments, as most of the Cr-MOFs were well-tolerated by cells at this concentration and this presented the best chance to observe cellular internalisation.

Each of the MOFs were administered to HEK-293 cells for 72 hours on plastic coverslips, which were then further prepared for the respective imaging techniques. The presence of MOF crystals outside the cells was evident by SEM (Figure 5.5a), both around the cells and on their surface. In some cases, crystals could be seen poking out of the cell membrane of the cells, indicating their likely presence inside as well. Cross-sections of the cells were also imaged using TEM to verify internalisation. In each case, crystals could be seen inside the cell cytoplasm; the electron density and hardness of the MOFs relative to the cell matter provided good contrast between the two phases. Clear evidence of internalisation was observed particularly with MIL-88D(Cr) where the crystal size was relatively large (> 2 μm) (Figure 5.5b) and the hexagonal morphology aided in identification. Smaller crystals would be expected to be internalised into cells more easily, and predictably a higher number of MIL-101(Cr) crystals could be seen inside the cells (see also Figure 5.17 in the experimental section).

a) b)

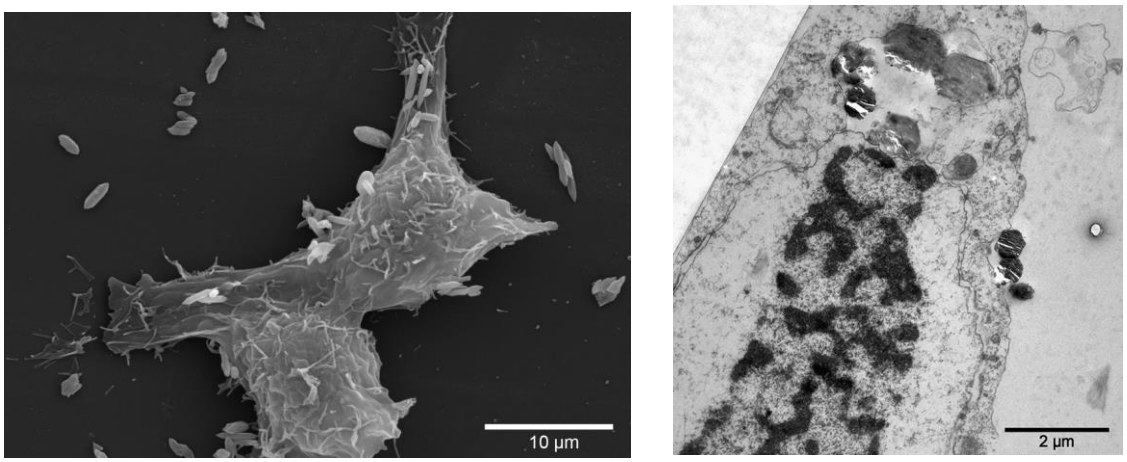

Figure 5.5. a) SEM of MIL-88D(Cr) treated HEK-293 cells. b) TEM of MIL-88D(Cr) particles located in an endosome inside the cytoplasm of a HEK-293 cell and exteriorly on the cell membrane.

Subsequently, we loaded the MOFs with the fluorophore Calcein to simulate drug delivery by soaking the MOFs in water/methanol (1:1) solutions of Calcein for 5 days; we have termed these Cal@MOF. Calcein is a hydrophilic molecule which does not pass through the cell membrane efficiently without a delivery system, and thus serves as a good proxy for the poorly soluble anti-cancer drugs which necessitate DDSs.[11] The loadings were determined by release in PBS pH 5.5 followed by UV-Vis measurement, and are provided in Table 5.1. Flow cytometry was used to quantify the Calcein delivery 72 hours post administration to cells for each of the Calcein-loaded MOFs against free Calcein. At 1 μgmL^{-1} of MOF there is a higher Calcein intracellular fluorescence from the Calcein-loaded MOFs compared to free Calcein (Figure 5.6a), evidence of effective internalisation, although the difference is only statistically significant for MIL-101(Cr), MIL-88C(Cr), and Cr-SDC. At higher concentration, MIL-101(Cr) performs very well and delivers the highest quantity of Calcein Figure 5.6b), consistent with its high internalisation seen previously by TEM. Comparatively, the other four MOFs all show a much lower delivery, although most still appear to perform better than free Calcein. The internalisation of these MOFs, which consist of much larger crystallites, is likely lower as indicated by TEM, explaining why they do not deliver as much Calcein. In addition, the Calcein binding, which necessarily can only be onto the outer surface of these four MOFs due to their small pores sizes, is also expected to be much weaker compared to MIL-101(Cr) which can easily fit molecules such as Calcein inside its pores.[12]

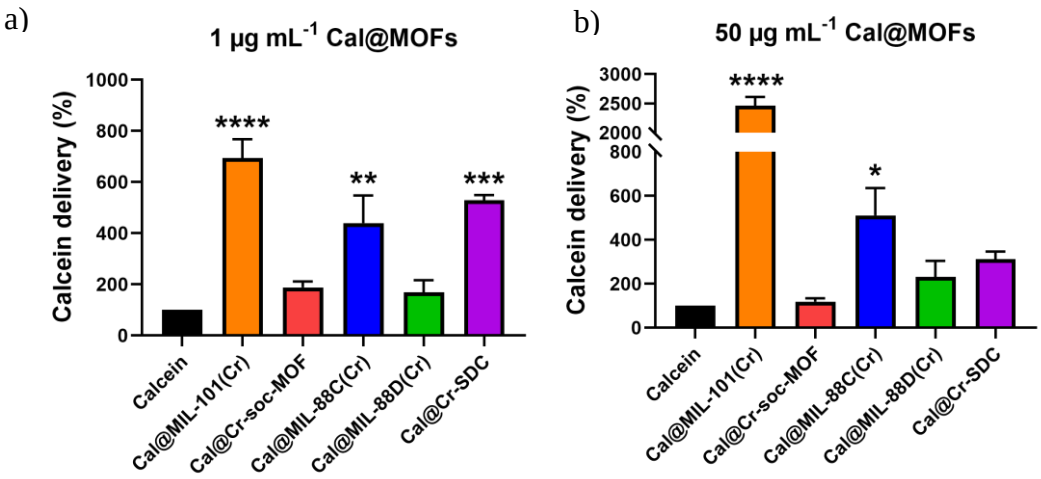

Figure 5.6. Delivery of Calcein from a) 1 µg mL^{-1} and b) 50 µg mL^{-1} Calcein@MOFs in HEK-293 cells, measured with flow cytometry 72 hours post administration. Data are presented as mean ± SEM; One-way ANOVA with Dunnett's test (n=3). *p≤0.05, **p≤0.01, ***p≤0.001, ****p≤0.0001.

Based on these results, Calcein loaded MIL-101(Cr) (Cal@MIL-101) was selected for further imaging via confocal fluorescence microscopy. After administering Cal@MIL-101 (50 µgmL-1) to cells for 72 hours, the cells were stained with 4′,6-diamidino-2-phenylindole (DAPI) for imaging the cell nuclei and Cell Mask™ Orange for imaging the cell membrane. Compared to free Calcein, there is a much higher colocalisation between the Calcein and the cell membrane stain (Figure 5.7) and higher fluorescence intensity when Cal@MIL-101 is used, confirming that it is efficiently delivered by the MOF into the cells.

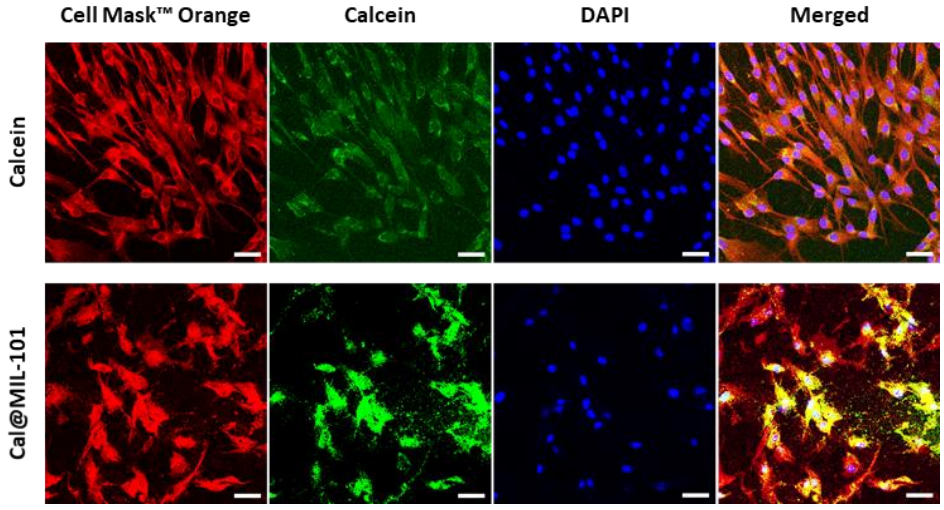

Figure 5.7. Confocal microscopy of free Calcein and Cal@MIL-101 (50 µg mL^{-1}) delivery in HDF cells 72 hours post administration. The concentration that was used for free Calcein corresponds to the amount of Calcein loaded in 50 µg mL^{-1} Cal@MIL-101. Red; cell membrane stain, Green; Calcein, Blue; nuclear DAPI stain. Scale bars are 50 µm.

5.4 Conclusions

We have comprehensively investigated the biocompatibility of several Cr-MOFs using *in vitro* techniques and have gained valuable insight into their effects on cells. The most significant finding in this study is that Cr-MOFs are not inherently cytotoxic at any appreciable level, particularly not at the concentrations expected for use in drug delivery (< 10 μg/mL), and thus can potentially serve as biocompatible nanocarriers. Even where some cytotoxic effects are seen, such as with Cr-SDC, we have found that this is due primarily to the toxicity of the linker and even then only statistically significant when high concentrations of MOF are administered (50 μg/mL). These findings are particularly significant when we consider the fact that Fe^{3+} MOFs are generally considered to be the best candidates for drug delivery, and yet Fe^{3+} showed very poor biocompatibility by RTCA even at low concentrations. When also considering that Fe^{3+} MOFs are less hydrolytically stable than Cr^{3+} MOFs, and therefore will likely exhibit more metal leaking under biological conditions, it seems that Cr^{3+} MOFs could be better candidates for these applications.

Our internalisation studies show that all the MOFs are internalised, albeit to varying degrees, confirming that they can be taken up and retained in cells over a reasonable period (72 hours). This is particularly encouraging as internalisation is a prerequisite for effective therapy, and it confirms that our biocompatibility results arise from minimal cytotoxicity and not just a separation between the cells and MOFs. Out of the MOFs studied, MIL-101(Cr) appears to be internalised the most, as evidenced by TEM imaging, likely owing to its very small crystal size (< 200 nm). By using Calcein as an imaging agent, we can see that the internalisation is very efficient as the vast majority of Calcein colocalises within the cell membrane. Small crystal size (< 200 nm) is already considered to be a requirement for effective dispersion in the bloodstream when administering MOFs intravenously as DDSs but these results suggest they may also be beneficial for internalisation. As such, future work should be aimed towards reducing the crystal size of the other Cr-MOFs or selecting those which can already be obtained easily with appropriately small crystal size.

Finally, by using Calcein as a model molecule for drug delivery (Figure 5.8), we have shown that all the MOFs can act as effective drug delivery platforms, as evidenced by a higher cargo delivery into cells vs. free Calcein. As expected, based on its higher internalisation and large porosity, MIL-101(Cr) demonstrated the highest delivery of Calcein to cells, which was verified by both flow cytometry and confocal microscopy. These suggest that large pore and nanoscaled Cr-MOFs are ideal candidates to further investigate MOF-assisted drug delivery

and potentially use as drug delivery systems, once further research is conducted with these underlooked materials in animal models; accumulation of Cr^{3+} in the body and conversion to Cr^{6+} are potential sources of off-target toxicity.

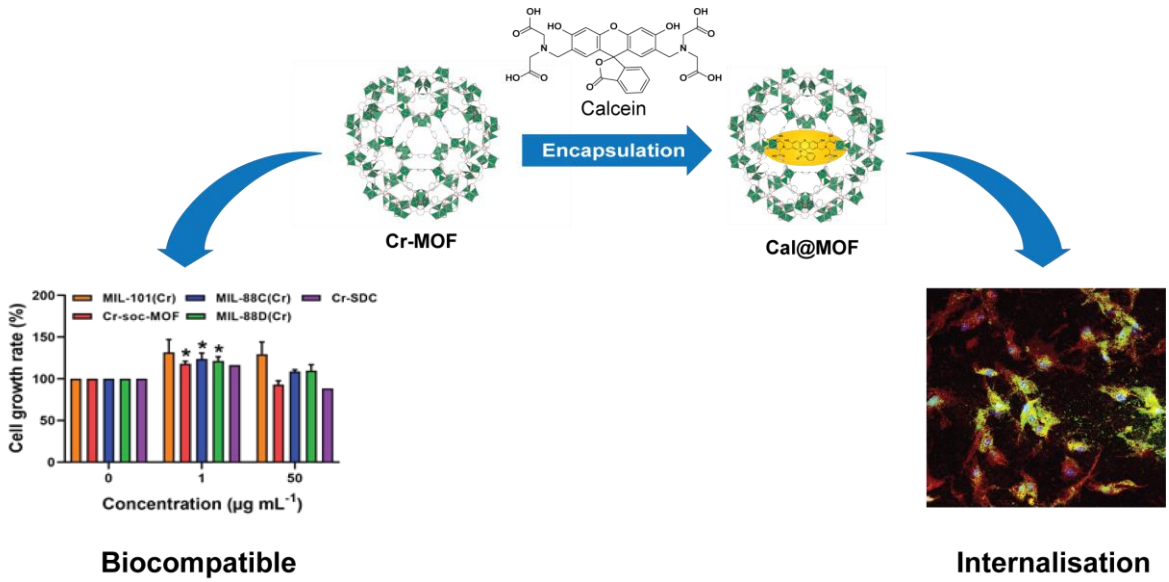

Figure 5.8. Schematic representation of the biocompatibility, Calcein loading, and cellular internalisation of Cr-MOFs.

The main challenge for diversifying Cr-MOFs will be their slow ligand substitution kinetics, which will make it hard to post-synthetically modify them, and therefore appropriate functionalization techniques will need to be explored in future in order to attach molecules for targeting and/or controlling release. Out of the MOFs synthesised in the previous chapter, MIL-100(Cr)_BTB represents the best candidate for future work as the pores are exceptionally large (~ 66 Å) and the crystal size is appropriately small (< 200 nm), and thus future work will be focused on attempting to load drugs in this MOF. Based on the results of this study, we expect that this will prove to be fruitful and such work could lead to the future development of more effective cancer therapy.

5.5 Experimental

5.5.1 Alamar blue assay

Cells were seeded into a VWR treated 96 well plate at a density of 5×10^3 cells per well (200 μL media per well). The cells were incubated for 24 hours in a humidified incubator atmosphere maintained at 5% CO_2. The MOF nanoparticles were suspended in complete media and were sonicated for 5 minutes in the various concentrations. The media was aspirated from the cells and the MOF suspension treatment was added (200 μL per well) – 3 to 6 replicates for each concentration. Complete media was added in the cases of untreated controls (200 μL per well) – 6 replicates. The cells were incubated for 24 or 72 hours in a humidified incubator atmosphere maintained at 5% CO_2. To measure the metabolic activity 20 μL per well Alamar Blue™ Cell Viability Reagent were added and the cells were incubated for 3.5-5 hours (depending on the cell line) in a humidified incubator atmosphere with 5% CO_2. Then the fluorescence intensity was measured on the plate reader (λ_{exc}=557±10 nm, λ_{ems}=593±10 nm).

Figure 5.9 shows the results of individual Alamar blue assays for different concentrations of linker, where the values are normalised against the control (which is set to 100%). The concentrations that were tested correspond to the concentration of the respective linker that would be present in 1, 100 and 500 μg mL^{-1} of the Cr-MOFs Cr-soc-MOF(ABTC), MIL-88C(Cr)(2,6-NDC), MIL-88D(Cr)(BPDC), Cr-SDC(SDC) and MIL-101(Cr)(BDC).

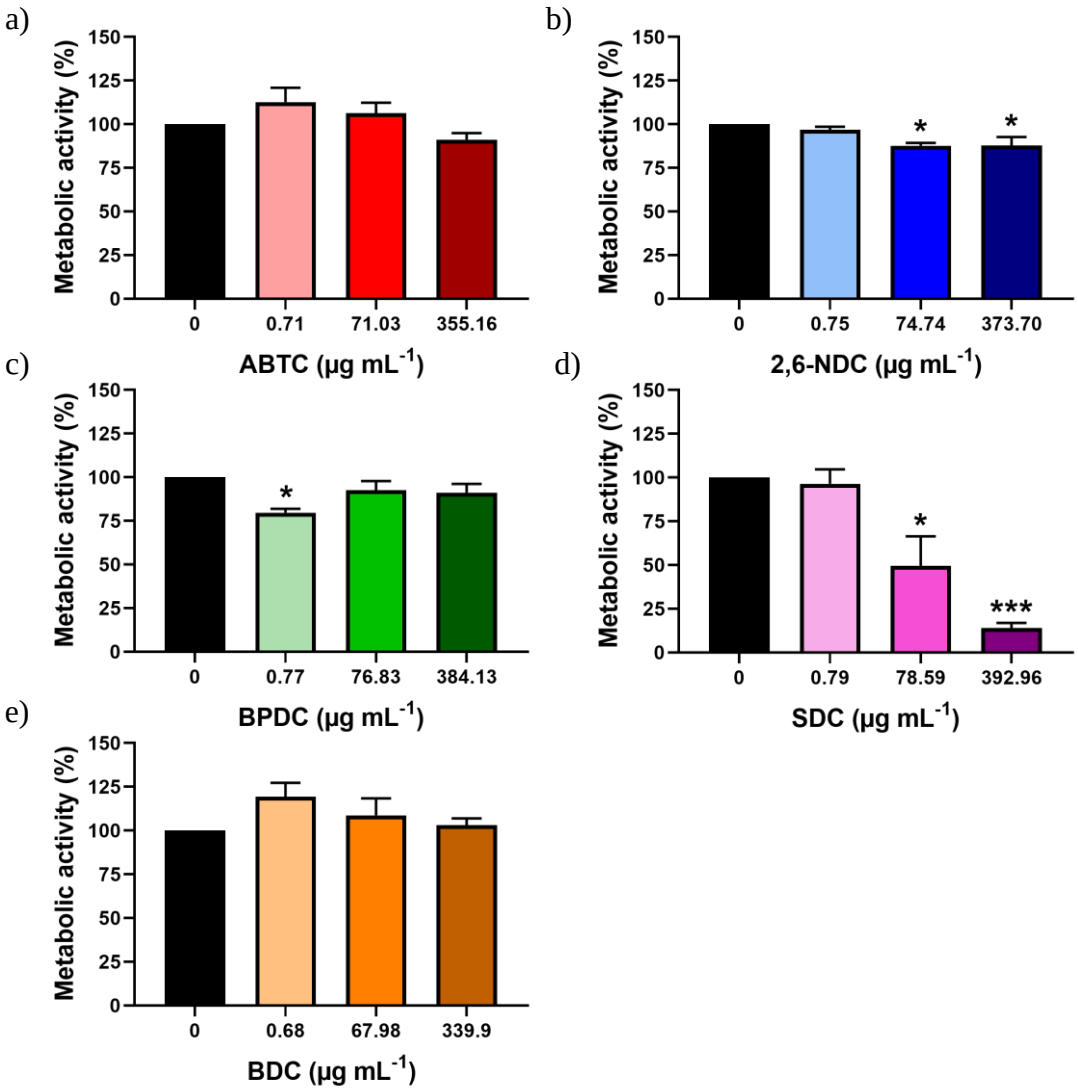

Figure 5.9. Cell metabolic activity following linker administration measured by Alamar blue assays. Metabolic activity of HEK-293 cells, normalised to the untreated control, 72 hours post administration of a) ABTC, b) 2,6-NDC, c) BPDC, d) SDC and e) BDC. Data are presented as mean ± SEM; One-way ANOVA with Dunnett's test (n=3). *$p \leq 0.05$, ***$p \leq 0.001$.

5.5.2 Real time cell analysis (RTCA)

100 µL of cell media per well were added to the E-plate VIEW and it was incubated at room temperature for 10 minutes. The plate was added to the RTCA instrument in the incubator (37˚C, 5% CO_2), to measure background impedance. The cells were counted and added to the plate at a concentration of 5×10^3 cells per well to a total volume of 200 µL per well. The plate was returned to the RTCA instrument and the cells were allowed to sediment for 30 minutes before the start of the measurement. After 24 hours of incubation, the media was carefully aspirated. The MOF nanoparticles were suspended in complete media and were

sonicated for 5 minutes in the various concentrations. The media was aspirated from the cells and the MOF suspension treatment was added (200 µL per well) – 6 replicates for each concentration. Complete media was added in the cases of untreated controls (200 µL per well) – 6 replicates. The plate was returned to the RTCA instrument where cell proliferation/loss was recorded for 72 hours.

RTCA cell proliferation assays were performed on an xCELLigence® RTCA MP machine, with E-plate VIEW 96. The RTCA normalised cell index over time data, which were collected and analysed with the use of the RTCA software version 1.2.1 (ACEA Biosciences Inc.). Figure 5.10 shows the real time cell proliferation of HDFs with the metal salts investigated, while the cellular growth rates post administration of the metal are given in Figure 5.11. Real time cell proliferation of HEK-293 cells after addition of the Cr-MOFs are shown in Figure 5.12; these data were used to derive cellular growth rates in Figure 5.3a.

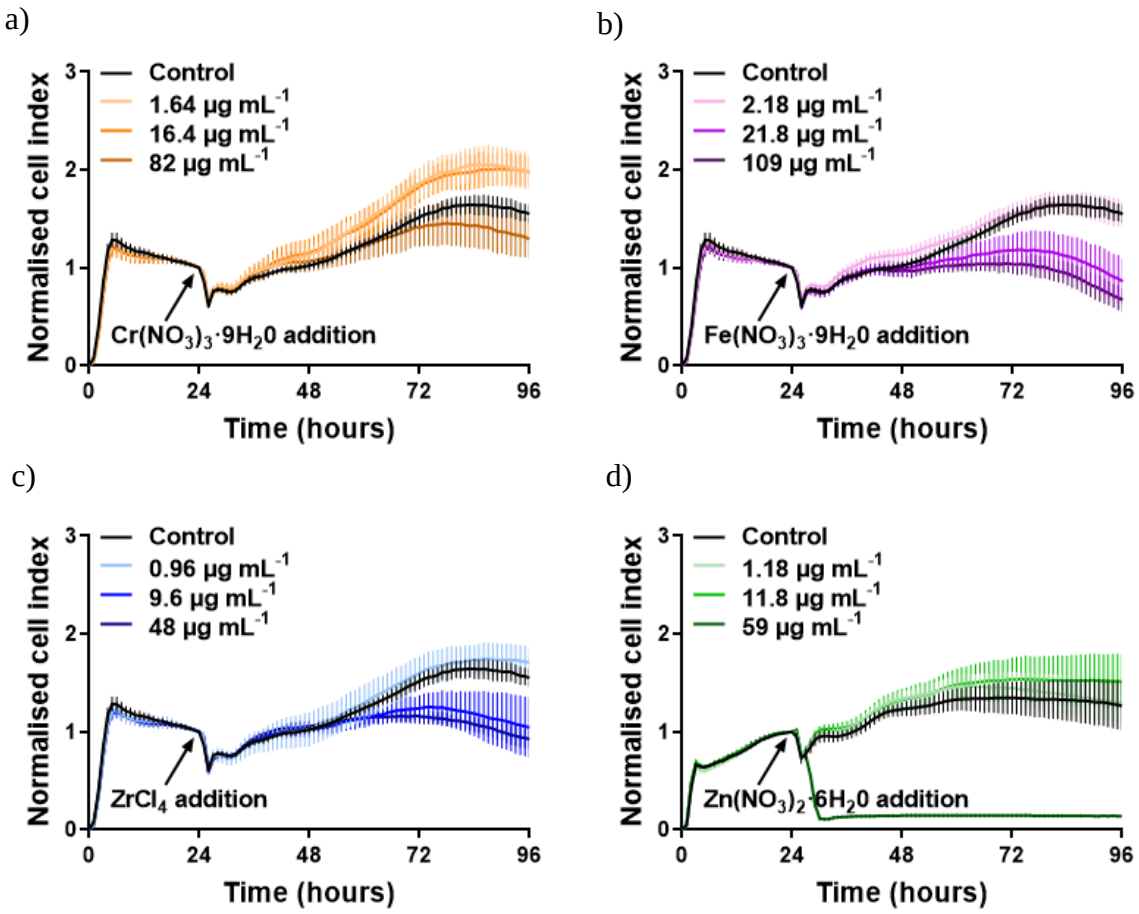

Figure 5.10. Real time cell analysis of HDF cells after addition of a) $Cr(NO_3)_3 \cdot 9H_2O$, b) $Fe(NO_3)_3 \cdot 9H_2O$, c) $ZrCl_4$ and d) $Zn(NO_3)_2 \cdot 6H_2O$. Data are presented as mean ± SD (n=6).

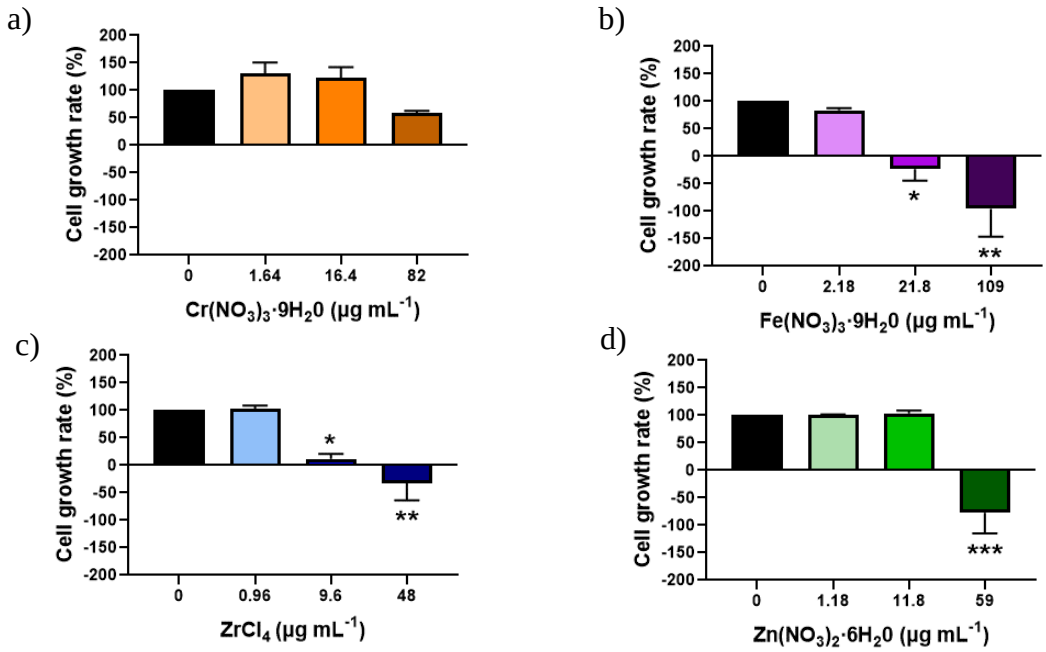

Figure 5.11. Cellular proliferative capacity following metal salt administration. HDF cell growth rate, normalised to the untreated control, 72 hours post administration of a) $Cr(NO_3)_3 \cdot 9H_2O$, b) $Fe(NO_3)_3 \cdot 9H_2O$, **c)** $ZrCl_4$ and d) $Zn(NO_3)_2 \cdot 6H_2O$. Data are presented as mean ± SEM; One-way ANOVA with Dunnett's test (n=3). *p≤0.05, **p≤0.01, *** p≤0.001.

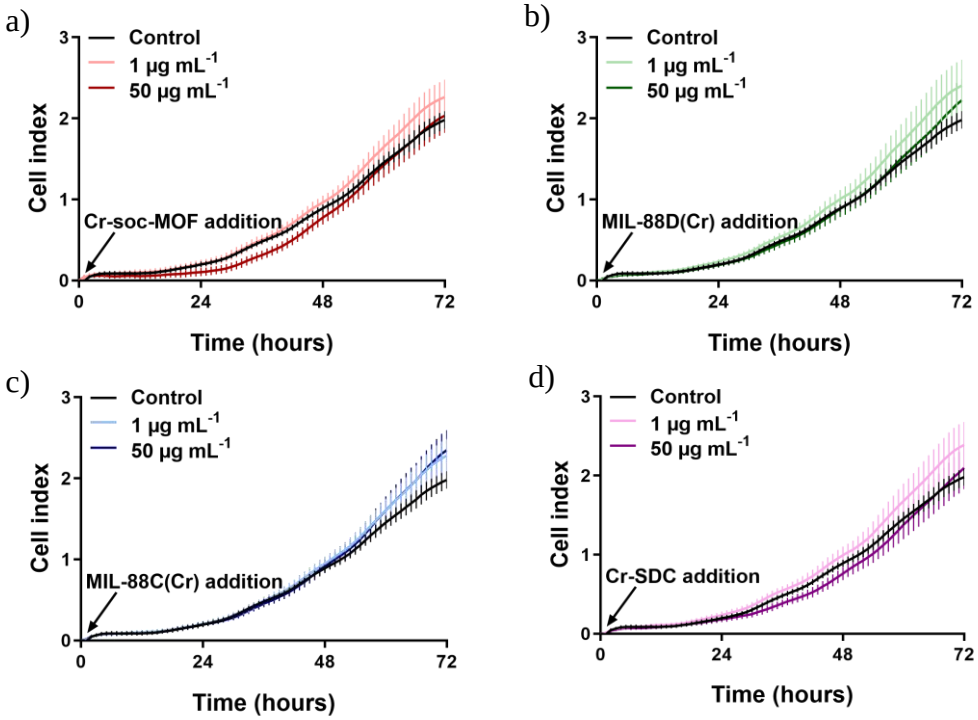

Figure 5.12. Cell proliferation following Cr-MOFs administration. a) Cr-soc-MOF, (B) MIL-88C(Cr), c) MIL-88D(Cr) and d) Cr-SDC administered in HEK293 cells. Data are presented as mean ± SD (n=6).

5.5.3 Calcein Loading

Approximately 20 mg of MOF were suspended in 10 mL of a water/methanol (1:1) solution of Calcein (5 $mgmL^{-1}$). This was covered with foil and left stirring at room temperature for 5 days. The suspensions were separated by centrifuging, followed by multiple washings with methanol before drying at room temperature in a desiccator. The solids were then dried overnight at 120 $^{\circ}C$. To calculate the loading wt.%, 0.5 $mgmL^{-1}$ of Cal@MOF were degraded in PBS pH 5.5 and the resulting Calcein concentration was determined using UV-Vis spectroscopy. The wt.% was subsequently calculated and is presented in Table 5.1.

Table 5.1. Calcein loadings of Cr-MOFs.

MOF	Calcein loading (wt.%)
Cr-soc-MOF	18.6
MIL-88D(Cr)	9.8
MIL-88C(Cr)	5.6
Cr-SDC	7.9
MIL-101(Cr)	7.2

5.5.4 Flow cytometry

Cells were seeded into a VWR treated 96-well plate at a density of 5×10^3 cells per well (200 μL media per well). The cells were incubated for 24 hours in a humidified incubator atmosphere maintained at 5% CO_2. The Cal@MOF nanoparticles were suspended in complete media and were sonicated for 5 minutes in the various concentrations. The media was aspirated from the cells and the MOF suspension treatment was added (200 μL per well) – 3 to 6 replicates for each concentration. Complete media was added in the cases of untreated controls (200 μL per well) – 6 replicates. The cells were incubated for 24 or 72 hours in a humidified incubator atmosphere maintained at 5% CO_2. The media was carefully aspirated and 50 μL per well Trypsin-EDTA (0.25%) were added. The plate was incubated (37˚C, 5% CO_2) for 5 minutes. 150 μL per well fresh media were added and the cells were

resuspended by pipetting and transferred to a Corning® 96 round bottom well plate. Then, the cells were centrifuged at 1200 rpm for 10 minutes. The supernatant media was removed by flipping the plate over a piece of tissue paper. 200 µL of the Flow Buffer (PBS 1X, 2% FBS and 2 mM EDTA diluted in PBS 1X) per well were added with SYTOX™ AADvanced™ Dead Cell Stain at a concentration of 1 µL of 1 mM stain per mL of Flow Buffer. In the samples of untreated cells and BL3-H channel control, used for the compensation of the instrument, the Flow Buffer solution added did not contain the SYTOX™ AADvanced™ Dead Cell Stain. For the sample used for the PeprCp-Cy5.5 channel control used for the compensation 160 µL of the Flow Buffer containing the SYTOX™ AADvanced™ Dead Cell Stain and 40 µL of DMSO were added per well.

The gating strategy used to determine cell viability and Calcein fluorescence is provided in Figure 5.13. The cell viability results determined by flow cytometry in Figure 5.14 were obtained from these experiments on the Cal@MOFs, but as we expect negligible cellular effects from Calcein, we have assumed any cytotoxicity will be due to the MOFs and not Calcein. The absolute fluorescence intensities measured by flow cytometry for different concentrations of Cal@MOFs are given in Figure 5.14. A calibration curve of fluorescence intensity against Calcein concentration (Figure 5.15) was used to determine the Calcein delivery.

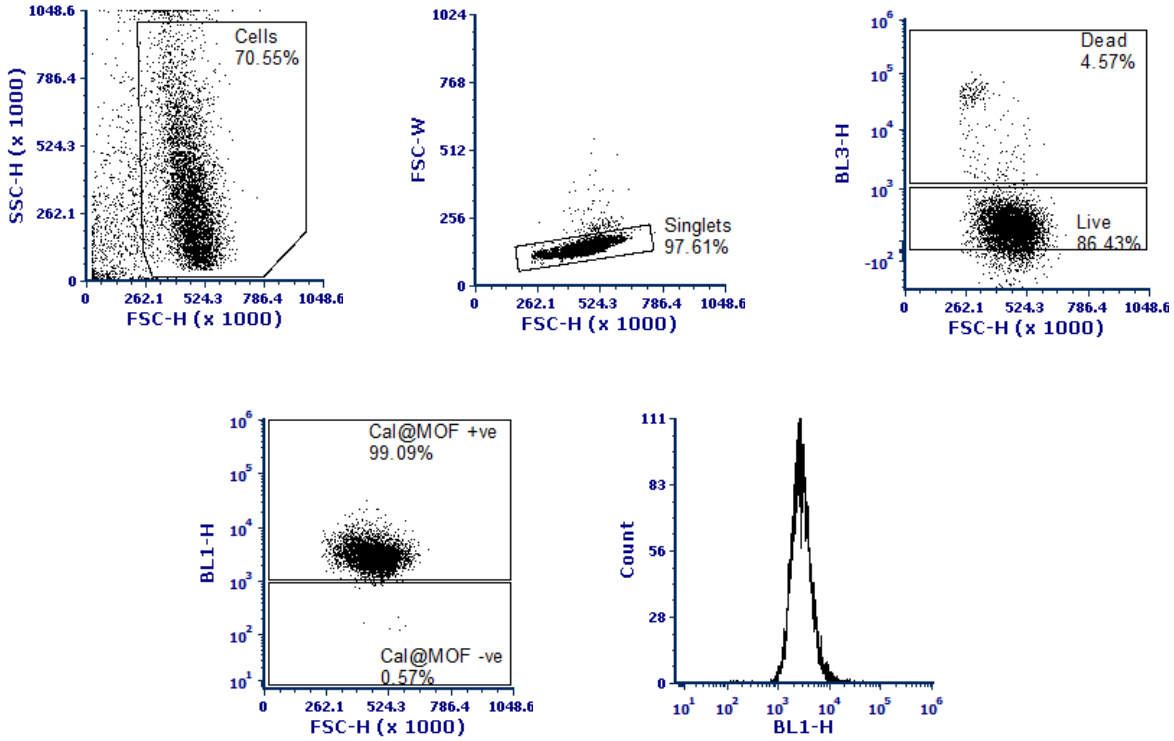

Figure 5.13. Flow cytometry gating strategy for HEK-293 cells.

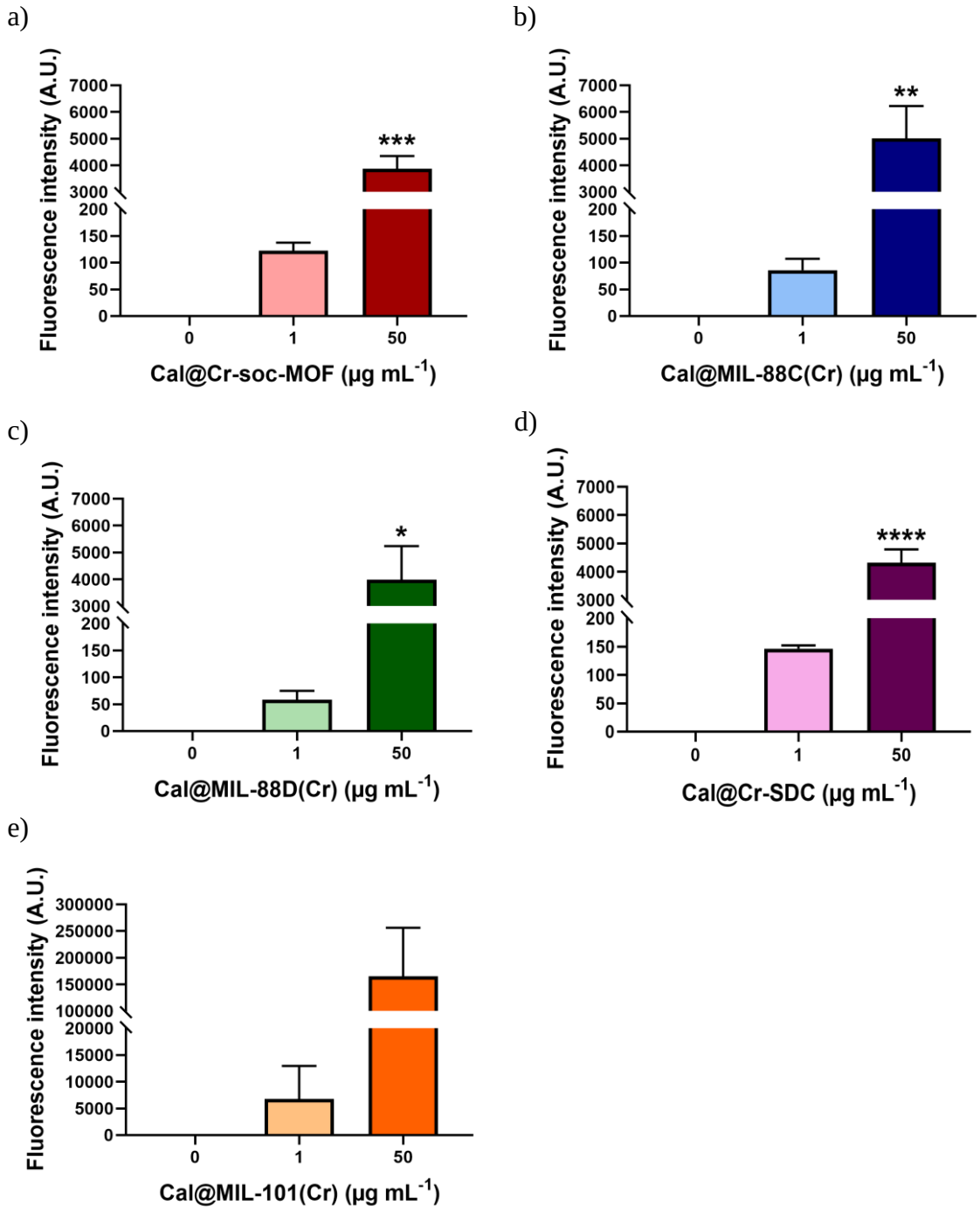

Figure 5.14. Intracellular fluorescence intensity measured with flow cytometry in HEK-293 cells 72 hours post administration of a) Calcein@Cr-soc-MOF b) Calcein@MIL-88C(Cr), c) Calcein@MIL-88D(Cr), d) Calcein@Cr-SDC and e) Calcein@MIL-101. Data are presented as mean ± SEM; One-way ANOVA with Dunnett's test (n=3). *p≤0.05, **p≤0.01, ***p≤0.001, ****p≤0.0001.

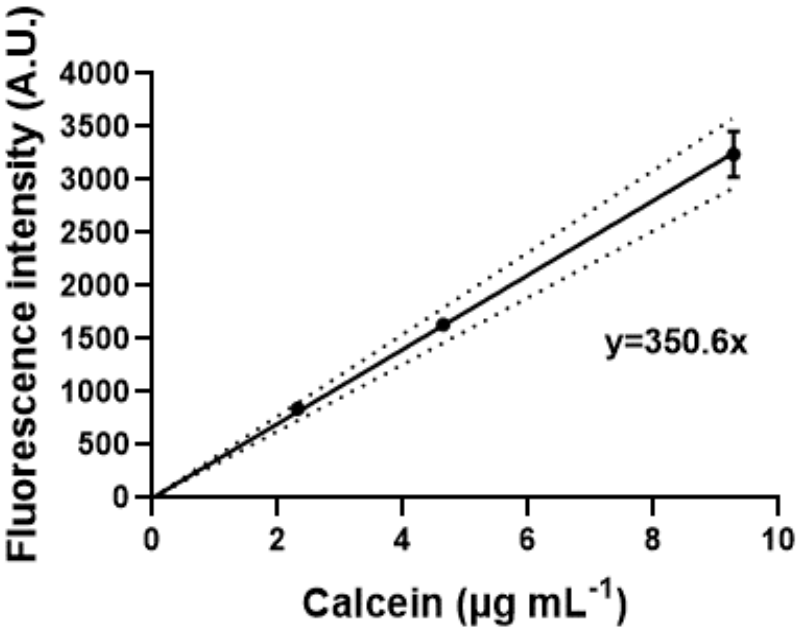

Figure 5.15. Calcein calibration curve. Calculated from free Calcein uptake measured with flow cytometry in HEK-293 cells, 72 hours post administration. Data are presented as mean ± SEM (n=3).

5.5.5 Confocal microscopy

HDF cells were seeded in a Nunc™ Lab-Tec™ II CC2™ Chaber Slide with removable walls system at a density of 2×10^5 cells per well (400 µL media per well). The cells were incubated for 24 hours in a humidified incubator atmosphere maintained at 5% CO_2. The Cal@Cr-MOF nanoparticles were suspended in complete media and were sonicated for 10 minutes in the appropriate concentrations. Free Calcein was dissolved in complete cell culture media at the appropriate concentration and was sonicated until complete dissolution. The media were removed from the wells by turning the slide over a beaker containing Virkon disinfectant. Complete cell culture media was added to the controls (400 µL per well) and the Cal@Cr-MOF suspension or Calcein solution was added to the samples (400 µL per well) – 2 replicates. The cells were incubated in a humidified incubator atmosphere maintained at 5% CO_2 for 4 and 8 hours. The media were removed from the wells by turning the slide over a beaker containing Virkon disinfectant. The cells were washed twice with PBS 1X with $CaCl_2$ and $MgCl_2$ (400 µL per well). Then 400 µL per well CellMask™ Green plasma membrane stain diluted 1:500 in warm media were added to all the samples apart from the nucleus stain controls where 400 µL of complete media were added. The cells were incubated for 30 min at 37°C in a humidified incubator atmosphere maintained at 5% CO_2. The stain was removed over Virkon disinfectant and the cells were washed twice with PBS

1X with $CaCl_2$ and $MgCl_2$ (400 µL per well). Subsequently, 100% methanol was added to the wells (400 µL per well) and the cells were incubated at room temperature for 5 minutes. The methanol was removed over Virkon disinfectant and the cells were washed twice with PBS 1X with $CaCl_2$ and $MgCl_2$ (400 µL per well). After the final washing, the wall framework of the slide was removed and one drop of ProLong™ Glass Antifade Mountant with DAPI nuclei stain was added over each sample and the slide was covered with a thin glass slide. The slide was let dry in the dark at room temperature overnight and then was stored at 4°C. The cells were imaged using a ZEISS LSM 780 Confocal Microscope and ZEN Black software.

5.5.6 Scanning and Transmission Electron Microscopy

Common procedure: Cells on coverslips were initially fixed in 2.5% Glutaraldehyde/2% Paraformaldehyde/0.1 M Sodium Cacodylate buffer for 1 hr at 4°C, and rinsed with 0.1 M Sodium Cacodylate buffer (3 x 5 mins) before post fixation in 1% Osmium Tetroxide for 1 hr. Osmium Tetroxide was removed with distilled water (3 x 10 mins). Samples were then block stained with 0.5% Uranyl Acetate/DH_2O for 1 hr in the dark (light sensitive). Samples were dehydrated with a series of aqueous ethanol solutions with concentrations of 30, 50, 70, and 90%, each of which was added for 10 mins. After these treatments, absolute ethanol was added and changed several times (5 mins each), followed by similar additions of dry ethanol (3Å Molecular sieve). After this, further treatments were applied for the different imaging techniques:

SEM: Cells/coverslips were given 3 x 5 mins incubation with Hexamethyldisilazane (HMDS) and left to dry overnight in a desiccator containing silica gel. Coverslips with dried cells were secured onto aluminium pin SEM stubs using conductive double-sided Carbon tape and Gold/Palladium coated (15-20 nm thick) using a QUORUM Q150T ES high vacuum coater. Cells were viewed on a JEOL IT 100 SEM and digital images captured using INTOUCH SCOPE version 1.05.

TEM: Cells/coverslips were given 3 x 5 mins changes of Propylene Oxide then dipped in Propylene Oxide: EPON 812 resin (1:1 mix) before placing the cell side down onto pure resin overnight. Samples were embedded the next day by placing coverslips cell side down onto embedding moulds and polymerised at 60 ºC for 24 hrs. Coverslips were fractured off by dipping in Liquid Nitrogen, leaving the cells in resin. A further layer of resin was added on top then polymerised for a further 24 hrs. Ultrathin sections (50-70 nm thick) were cut using a DRUKKER diamond ultratome Knife and a LEICA Ultracut. UTC sections were

collected on Formvar coated 100 mesh copper grids and contrast stained with 2% Uranyl Acetate (5 mins) and Reynolds Lead Citrate (5 mins). Cells were viewed on a JEOL 1200EX TEM running at 80 kV and digital images were captured using a Cantega camera and Olympus ITEM software.

Representative images for different Cr-MOFs are shown for SEM (Figure 5.16) and TEM (Figure 5.17).

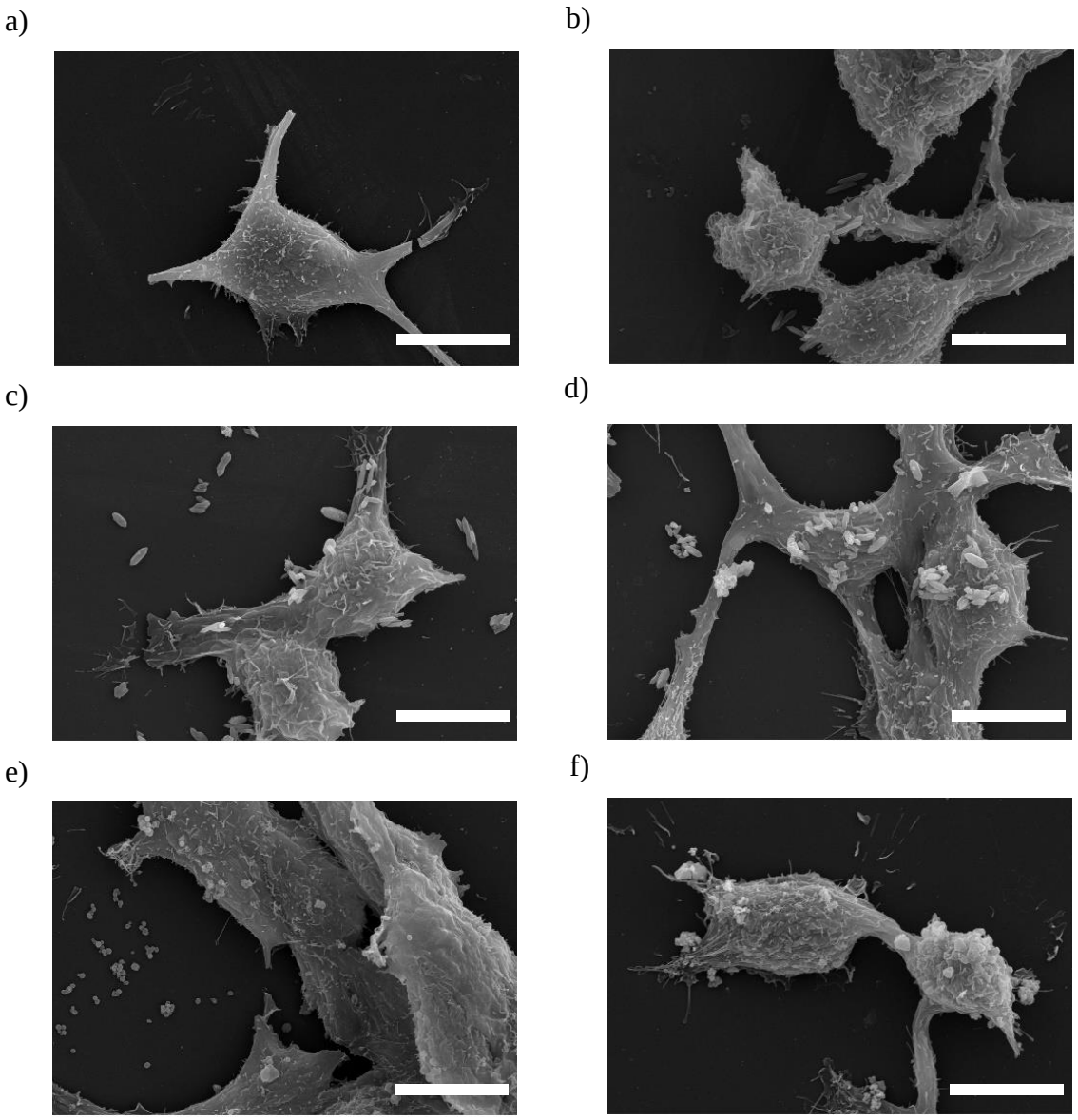

Figure 5.16. SEM of Cr-MOF treated HEK-293 cells: a) Control (no MOF), b) MIL-88C(Cr), c) MIL-88D(Cr), d) Cr-soc-MOF, e) Cr-SDC, f) MIL-01(Cr). Scale bar = 10 µm.

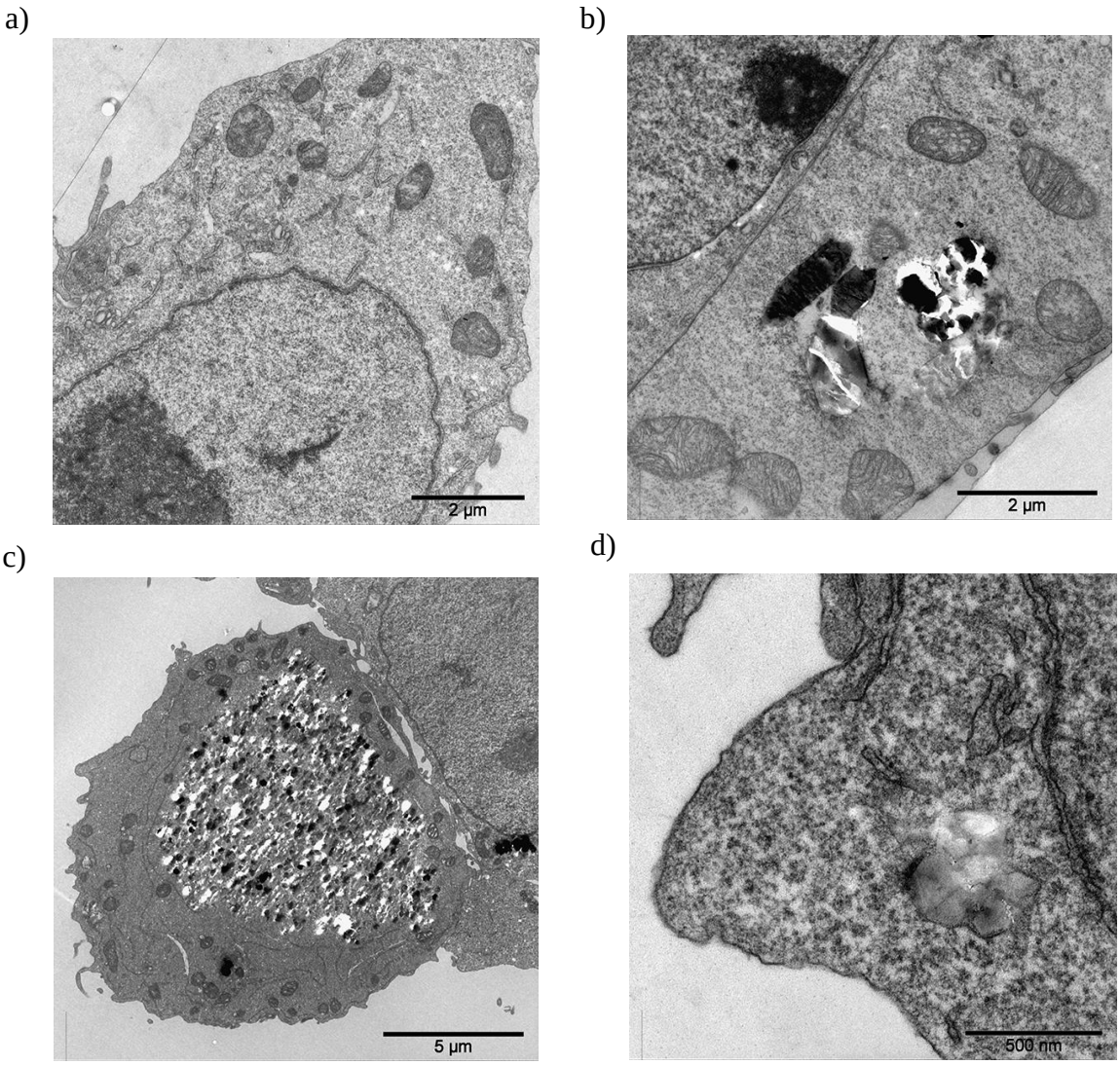

Figure 5.17. TEM of Cr-MOF treated HEK-293 cells: a) Control (no MOF), b) MIL-88C(Cr), c-d) MIL-101(Cr).

5.6 References

(1) Horcajada, P., Chalati, T., Serre, C., Gillet, B., Sebrie, C., Baati, T., Eubank, J. F., Heurtaux, D., Clayette, P., Kreuz, C., Chang, J.-S., Hwang, Y. K., Marsaud, V., Bories, P.-N., Cynober, L., Gil, S., Férey, G., Couvreur, P. and Gref, R., *Nat. Mater.*, **2010**, *9*, 172-178.

(2) Katz, S. A. and Salem, H., *J. Appl. Toxicol.*, **1993**, *13*, 217-224.

(3) Anderson, R. A., Bryden, N. A. and Polansky, M. M., *Biol. Trace Elem. Res.*, **1992**, *32*, 117-121.

(4) Vimont, A., Goupil, J.-M., Lavalley, J.-C., Daturi, M., Surblé, S., Serre, C., Millange, F., Férey, G. and Audebrand, N., *J. Am. Chem. Soc.*, **2006**, *128*, 3218-3227.

(5) Grall, R., Hidalgo, T., Delic, J., Garcia-Marquez, A., Chevillard, S. and Horcajada, P., *J. Mater. Chem. B*, **2015**, *3*, 8279-8292.

(6) Wuttke, S., Zimpel, A., Bein, T., Braig, S., Stoiber, K., Vollmar, A., Müller, D., Haastert-Talini, K., Schaeske, J., Stiesch, M., Zahn, G., Mohmeyer, A., Behrens, P., Eickelberg, O., Bölükbas, D. A. and Meiners, S., *Adv. Healthcare Mater.*, **2017**, *6*.

(7) Latifi, L. and Sohrabnezhad, S., *Polyhedron*, **2020**, *180*, 114321.

(8) Vinogradov, V. V., Drozdov, A. S., Mingabudinova, L. R., Shabanova, E. M., Kolchina, N. O., Anastasova, E. I., Markova, A. A., Shtil, A. A., Milichko, V. A., Starova, G. L., Precker, R. L. M., Vinogradov, A. V., Hey-Hawkins, E. and Pidko, E. A., *J. Mater. Chem. B*, **2018**, *6*, 2450-2459.

(9) Liu, C.-H., Chiu, H.-C., Sung, H.-L., Yeh, J.-Y., Wu, K. C. W. and Liu, S.-H., *Regul. Toxicol. Pharmacol.*, **2019**, *107*, 104426.

(10) Rampersad, S. N., *Sensors (Basel)*, **2012**, *12*, 12347-12360.

(11) Orellana-Tavra, C., Marshall, R. J., Baxter, E. F., Lázaro, I. A., Tao, A., Cheetham, A. K., Forgan, R. S. and Fairen-Jimenez, D., *J. Mater. Chem. B*, **2016**, *4*, 7697-7707.

(12) Horcajada, P., Serre, C., Vallet-Regí, M., Sebban, M., Taulelle, F. and Férey, G., *Angew. Chem. Int. Ed.*, **2006**, *45*, 5974-5978.

Chapter 6

Conclusions

Contents

Chapter 6 217

6.1 Conclusions 219

6.2 References..... 225

6.1 Conclusions

The use of modulation as a tool for phase-tuning in MOF synthesis was proposed at the end of Chapter 1 and has been the main theme of the subsequent chapters. In Chapter 2 we explored how modulation could be used to tune between interpenetrated MIL-126 and non-interpenetrated MIL-88D type MOFs based on Fe^{3+} and the linkers BPDC and BPYDC. The results of our synthetic study validated that coordination modulation can be used to kinetically control the phase space in this system, and operates by slowing the self-assembly process to favour the interpenetrated MIL-126(Fe) framework as the thermodynamic product, while the non-interpenetrated framework MIL-88D(Fe) is a kinetic product. These results were corroborated by DFT simulations which reveal a strong preference for the arrangement of capping species in MIL-126 that is not evident for MIL-88D, observed for both the Fe^{3+} and Sc^{3+} analogues, indicating that the thermodynamics of correlated anion disorder influence the formation of MIL-126(Fe). The phase-purity of MIL-126(Fe) samples could be enhanced by varying the quantity and identity of the modulator added during synthesis, and it was also possible to tune the size, morphology, and defectivity of this interpenetrated MOF.

The use of BPYDC in place of BPDC inhibits the formation of the interpenetrated MIL-126(Fe) phase as a consequence of the prohibitively distorted linker conformation required, as previously demonstrated for Sc^{3+} analogues, and confirmed by new DFT calculations and modulated experiments. In contrast to Sc^{3+}, Fe^{3+} can coordinate to the bipyridyl N-donors and form MOFs with different topologies to MIL-88D, which can also be isolated under specific modulation conditions. Both new structures are non-interpenetrated and possess significant potential void space, however, phase-pure samples of either MOF could not be obtained on a large enough scale for further investigation.

Finally, the use of an Fe^{2+} salt as starting material for the Fe^{3+} MOFs effectively slows the synthesis to favour interpenetration and, when combined with modulation, greatly enhances the porosity of the resulting MOF without inducing defectivity. Our results with the Fe-BPDC system suggest that oxidation modulation - the deliberate use of metal precursors in different oxidation states to that found in the resulting MOF - could be used in other MOF systems to favour thermodynamic products. In addition, the overall greater sample quality suggests that oxidation modulation could also be a simple and effective synthetic tool for preparing high quality MOFs with improved physical properties crystallinity and porosity.

In Chapter 3 we took the two methodologies that were developed in the previous chapter - coordination and oxidation modulation - and applied them to the Fe-terephthalate system, one of the most structurally diverse MOF systems, in order to further test their efficacy for phase-tuning. In this study we aimed to develop synthetic routes to various MOFs containing the common chain and trimeric SBUs, as well as gaining insight into the kinetic and thermodynamic relationships between these different phases.

I have demonstrated that MOFs with the trigonal SBU, MIL-88B(Fe) and MOF-235(Fe) can be best stabilised by the addition of a monocarboxylate modulator, such as acetic acid, while MOFs with the chain SBU, MIL-53(Fe) and [Fe(BDC)(DMF)], can best be obtained without modulator at higher temperature or by use of a mineral acid such as HCl. Compared to the previous chapter, the kinetic role of varying the oxidation state of the metal precursor is significantly more complex as the counterion dictates the nature of the phase to a far greater extent than the synthesis kinetics, suggesting a templating effect which we then further investigated.

One of the main aspects of this system that we identified from the outset were the similarities between the two Fe-terephthalates with **acs** topology – MOF-235(Fe) and MIL-88B(Fe) – and their frequent misidentification in the literature. Our results suggest that that MOF-235(Fe) is the thermodynamically preferred product that forms in DMF when using iron chloride precursors, while MIL-88B(Fe) can be obtained when both the synthesis time is relatively short and acetic acid is used as modulator. Through variation of the metal precursor, we have also identified a novel analogue of MOF-235(Fe) with formula $[Fe_3O(DMF)_3(BDC)_3][BF_4]$, which can be obtained when using $Fe(BF_4)_2$ and acetic acid as modulator. The formation of these $[Fe_3O(DMF)_3(BDC)_3][YX_4]$ frameworks can be entirely avoided by use of Fe-precursors which cannot provide the necessary YX_4 anions for their formation, and thus MIL-88B(Fe) can be more easily isolated. We propose that the most reliable strategy for researchers interested in synthesising MIL-88B(Fe) is to avoid the use of chloride or $[BF_4]^-$ containing precursors, as we have found that they display a strong preference to yield products with either MIL-53 or MOF-235 type structures.

As an additional side study, we also investigated the flexibility of MIL-53(Fe) using SCXRD and PXRD techniques to confirm and build upon the reported literature. MIL-53(Fe) undergoes stepwise framework transformations when the guest is exchanged, and we have been able to determine the crystal structures of five distinct solvates via solvent-exchanges on single crystals on the DMF solvate of MIL-53(Fe). The difficulty in obtaining single

crystal structures of most of the solvates is particularly notable, and we had to contend with the break-up of crystals upon solvent exchange, which is a non-trivial problem for this method of characterisation. However, further study into this system could reveal a more effective solvent-exchange strategy, which will be particularly valuable given the dearth of single-crystal structures of MIL-53(Fe) solvates. Interestingly, we found that while DMSO and DMF will remain in the pores of MIL-53(Fe) crystals even after removal from their mother liquor, volatile solvents such as acetone and DCM rapidly evaporate to yield the hydrated form of MIL-53(Fe), MIL-53(Fe)_lt, when exposed to air. These practical considerations (solvent loss, crystal break-up) are particularly important to understand when attempting to study the structural transformation of these types of MOFs *in situ*, which is already underway.

In Chapter 4 I have explored the use of modulation to synthesise new and existing Cr-MOFs, with the aim of replacing HF with more benign modulators and to develop reliable protocols that enable control over framework topology. Initially I developed a HF-free synthesis route to MIL-88D(Cr), which uses acetic acid to control the self-assembly process and promote crystallisation, and this encouraged us to explore other linker systems. This synthesis route, which uses water and pyridine as solvent, yielded a whole series of novel frameworks containing $Cr_3O(RCO_2)_6$ SBUs and ditopic linkers, each of which possess either MIL-88 or two-fold interpenetrated MIL-88-int topology. Further refinement of the synthesis conditions enabled us to obtain the first single-crystal structure of a directly synthesised Cr^{3+} MOF, MIL-88B(Cr)_1,4-NDC. This is significant as it indicates the feasibility to determine Cr-MOF structures from single-crystal X-ray diffraction, which is the least time-consuming method, and I expect this will facilitate future studies into their synthesis.

The flexibility of these materials has also been investigated, enabled by the high crystallinity and phase purity achieved by my synthetic procedure. It was found that the DMF-solvated frameworks, which adopt open pore conformations, gradually and spontaneously close when not immersed in solvent, a phenomenon not mentioned in the literature but which arises from evaporation of the solvent from inside the pores. This is true even for Cr-SDC, a two-fold interpenetrated MIL-88 framework that, unlike MIL-126, is highly flexibility and exhibits a swelling amplitude - the increase in unit cell volume between the dry and solvated states - comparable to the non-interpenetrated MIL-88 frameworks.[1] To the best of my knowledge this is the first example of a highly flexible interpenetrated MOF containing the trigonal $M_3O(RCO_2)_6$ SBU.

Additionally, I have established a route to frameworks with the same topology as MIL-53, by using water as solvent and HCl as a modulator. This enabled us to obtain single crystal structures of two other Cr-MOFs, MIL-53(Cr) and MIL-53_Br(Cr), the latter of which has never previously been synthesised. The ideal conditions for synthesising these two MOFs are very general for $[Cr(OH)(RCO_2)_2]$ frameworks, and highly crystalline material can be obtained with a range of dicarboxylate linkers. Synthesis with 2,6-napththalenedicarboxylate (2,6-NDC), which yielded MIL-88C(Cr) when using pyridine and acetic acid, provides a novel extended analogue of MIL-53(Cr) which displays a impressive degree of flexibility upon the adsorption and removal of guest molecules. Based on these results, I expect that further efforts to synthesise isoreticular analogues of MIL-53 containing Cr^{3+} will yield even more novel frameworks which possess exceptional flexibility and could be particularly useful for encapsulating small molecules.

When I focused attention to higher connectivity linkers, I was able to synthesise a novel Cr^{3+} MOF containing a tetratopic linker, Cr-soc-MOF. Interestingly, this framework crystallises with lower symmetry than the Fe-analogue (PCN-250) and corresponds to the phase obtained upon applying pressure (PCN-250″). Attempts to relax this structure to a cubic symmetry, as has been demonstrated for PCN-250″, revealed that Cr-soc-MOF is much more stable and may require different conditions to enable this structural transformation. A more in-depth investigation of this behaviour is warranted and will comprise any future study into this framework. The porosities of samples of Cr-soc-MOF are lower than expected, but this appears to be due to inefficient activation, and thus these conditions can also be optimised further in future work.

In a similar vein, I attempted to synthesise mixed-linker frameworks containing both benzene-1,3,5-tribenzoate (BTB) and dicarboxylate linkers. The obtained mixed linker frameworks with BDC and 2,6-naphthalenedicarboxylate (2,6-NDC) are isoreticular analogues of MIL-143, an Fe framework containing both BTB and BDC linkers. These frameworks are stable to activation and exhibit high permanent porosity (SA_{BET} >1800 m^2g^{-1}). Synthesis attempts with 1,4-phenylenediacrylate (PDAC) as second linker led to the discovery of the single linker framework MIL-100(Cr)_BTB, an extended analogue of MIL-100. Strikingly, this solid appears to be stable to desolvation and displays remarkable permanent porosity (SA_{BET} ~ 4000 m^2g^{-1}), properties not shared by the previously synthesised Fe-analogue.[2] The combination of high porosity and stability should make these materials well-suited for a wide range of potential applications, and future work should include stability testing of these solids to confirm this.

The two Cr-MOF synthesis routes developed herein are highly selective for particular SBUs: synthesis in water and pyridine with acetic acid as modulator yields frameworks with the $[Cr_3O(RCO_2)_6(H_2O)_2X]$ SBU, while synthesis in water with HCl yields those with $[Cr(OH)(RCO_2)_2]$. The ability to control the SBU in this manner is extremely useful and should enable the design of more novel Cr-MOFs with high gas uptake and/or flexibility, properties which we propose will lead to their development into real-world applications such as gas-storage and drug delivery. Future work will include further characterisation of the porosity and flexibility of each of these frameworks, which will be an essential step in their development for potential applications.

MOFs have been widely studied for their potential use in biomedical applications, however these have typically been limited to frameworks consisting of either Zr^{4+} or Fe^{3+}, with those consisting of Cr^{3+} largely neglected due to an associated stigma. In Chapter 5 we investigated the biocompatibility of several of the Cr-MOFs developed in Chapter 4 using *in vitro* techniques. We found no significant cytotoxic effect arising from Cr^{3+}, when administering the corresponding metal salt to cells, and in fact it displayed much better biocompatibility than other metals which have been considered suitable for biomedical applications. As for the Cr-MOFs, in general they did not display any inherently cytotoxic at the concentrations expected for use in drug delivery (< 10 μg/mL), and thus we propose their suitability as biocompatible nanocarriers pending further *in vivo* studies.[3] Even where some cytotoxic effects are identified, such as with Cr-SDC, they arise primarily due to the toxicity of the linker and are only statistically significant when high concentrations of MOF are administered (50 μg/mL). Our results are particularly relevant as Fe^{3+} MOFs are generally considered to be the best candidates for drug delivery, and yet Fe^{3+} showed very poor biocompatibility by real-time cell analysis (RTCA) even at low concentrations. When also considering that Fe^{3+} MOFs are much less hydrolytically stable than Cr^{3+} MOFs, and therefore will likely exhibit more metal leaking under biological conditions, it seems that Cr^{3+} MOFs could be better candidates for these applications.

Our internalisation studies show that all the MOFs are internalised, albeit to varying degrees, confirming that they can be taken up and retained in cells over a reasonable period (72 hours). This confirms that our biocompatibility results arise from minimal cytotoxicity and not just a separation between the cells and MOFs. MIL-101(Cr) appears to be internalised the most, as evidenced by TEM imaging, likely owing to its very small crystal size (< 200 nm). When using Calcein as an imaging agent, we can see that the internalisation is very

efficient as the vast majority of Calcein colocalises within the cell membrane, indicating excellent cargo delivery.

When I explored the use of Calcein as a model molecule for drug delivery it was found that all the MOFs can act as effective drug delivery platforms, delivering a higher cargo into cells compared to. the equivalent amount of free Calcein. MIL-101(Cr) demonstrated the highest delivery of Calcein to cells, which was verified by both flow cytometry and confocal microscopy and is in line with the higher internalisation observed by TEM. Based on these results I can suggest that the best candidates for further investigation are nanoscaled Cr-MOFs containing large pores, potentially serving as benign and efficient carriers in MOF-assisted drug delivery. As such, future work could focus on MIL-100(Cr)_BTB, one of the MOFs synthesised in Chapter 4, which possesses both suitably small crystal size (< 200 nm) and exceptionally high permanent porosity.

To conclude, I have developed novel synthetic strategies for phase-tuning in Fe^{3+} and Cr^{3+} carboxylate systems and have confirmed that modulation is a powerful tool for controlling the kinetics of self-assembly and for templating phases. The enhanced synthetic protocols developed in this study have enabled discovery of a number of new phases, and investigation of the flexibility, gas sorption, and biocompatibility of these and existing materials has revealed that Cr-MOFs are highly promising candidates for biomedical applications.

6.2 References

(1) Serre, C., Mellot-Draznieks, C., Surblé, S., Audebrand, N., Filinchuk, Y. and Férey, G., *Science*, **2007**, *315*, 1828-1831.

(2) Horcajada, P., Chevreau, H., Heurtaux, D., Benyettou, F., Salles, F., Devic, T., Garcia-Marquez, A., Yu, C., Lavrard, H., Dutson, C. L., Magnier, E., Maurin, G., Elkaïm, E. and Serre, C., *Chem. Commun.*, **2014**, *50*, 6872-6874.

(3) Liu, C.-H., Chiu, H.-C., Sung, H.-L., Yeh, J.-Y., Wu, K. C. W. and Liu, S.-H., *Regul. Toxicol. Pharmacol.*, **2019**, *107*, 104426.